FUNDAMENTALS OF AMBIENT METASTABLE-INDUCED CHEMICAL IONIZATION MASS SPECTROMETRY AND ATMOSPHERIC PRESSURE ION MOBILITY SPECTROMETRY

A Dissertation
Presented to
The Academic Faculty

by

Glenn A. Harris

In Partial Fulfillment
of the Requirements for the Degree
Doctor of Philosophy in the
School of Chemistry & Biochemistry

Georgia Institute of Technology

August 2011

FUNDAMENTALS OF AMBIENT METASTABLE-INDUCED CHEMICAL IONIZATION MASS SPECTROMETRY AND ATMOSPHERIC PRESSURE ION MOBILITY SPECTROMETRY

Approved by:

Dr. Facundo M. Fernández, Advisor
School of Chemistry & Biochemistry
Georgia Institute of Technology

Dr. Thomas M. Orlando
School of Chemistry & Biochemistry
Georgia Institute of Technology

Dr. Lawrence Bottomley
School of Chemistry & Biochemistry
Georgia Institute of Technology

Dr. M. Cameron Sullards
School of Chemistry & Biochemistry
Georgia Institute of Technology

Dr. Greg Huey
School of Earth and Atmospheric Sciences
Georgia Institute of Technology

Date Approved: May 26th, 2011

I’m smart enough to know that I’m dumb.

— Richard Feynman

This is dedicated to…

my parents, Martin and Mary Ann Harris, for advice beyond description, teaching me how to work hard and reminding me to enjoy the ride,
my brother, Craig M. Harris, for being a great role model and friend,
and my grandma, Mary Quattrocki, for always being supportive.

To those listed above, and the rest of my family and friends, thank you for your unconditional love and support.

ACKNOWLEDGEMENTS

First I would like to express my gratitude to my advisor, Dr. Facundo M. Fernández, for guidance and support during the past four years. Under your supervision, my training and growth as a scientist has been outstanding. I am grateful for the financial and professional support needed to pursue the work outlined in this dissertation. I look forward to many years of friendship and collaboration. In addition, I would like to thank my committee members Dr. Thomas M. Orlando, Dr. Lawrence Bottomley, Dr. M. Cameron Sullards and Dr. Greg Huey for their advisement and interest in my graduate research.

My fellow group members deserve significant thanks. Our past group members, Dr. Christina Y. Hampton, Dr. Leonard Nyadong, Dr. Arti Navare, Dr. Mark Kwasnik and Dr. Carrie Pierce set the expectations high upon my arrival. Current group members including Jose Perez, Christina Jones, Dana Hostetler, Deanna Synder, Rachel Bennett, Joel Keelor and my undergraduate researcher Caitlin E. Falcone, provided the day-to-day assistance required for the completion of my work. Also, I would like to thank Dr. Asiri S. Galhena and Dr. Manshui Zhou for their research insight as excellent post doctoral and research scientist colleagues.

My collaborators and funding agencies have provided invaluable help for many of the projects I pursued. Special thanks is given to Dr. David Powell, Dr. Gary Eiceman, Dr. Jennifer Brodbelt, Dr. Douglas Henderson and Northrop Grumman, Dr. Joe Chipuk and Signature Science, Dr. Katrin Fuhrer, Dr. Marc Gonin and Dr. Richard Knochenmuss at Tofwerk AG, Dr. Michael Greene, Dr. Paul Newton, the National Science Foundation and the Department of Homeland Security. I am also grateful for the services of Sam

Mize at the College of Science machine shop as well as Richard Berdell and Jose Fonts in the School of Chemistry and Biochemistry electronics shop.

I have been lucky to have many friends while studying at Georgia Tech. I must thank Michael and Sarah Stollar Smith for being a never ending source of fun, excitement and memories. Please give Betty a belly rub and a few treats for me when I leave. My roommate and friend, Nick Haase, has been a great research colleague and fellow concert and fine-dining companion while in Atlanta. I am sure Nick's cat Sherman will enjoy life more without my constant pestering. My coffee breaks and late night adventures will never be the same without Susan Orwig. I wish you and your family my best. Other friends here in Atlanta (Jessica Peters, Lauren-Christine Orwig, Craig Clark, James Goeders, William "Chip" Humphries IV, Anthony Baldrige, Nicole Marrotta, and Meg Mackey) and old friends (Dane Lewis, Pierce Wolfinbarger, Dr. Diana Tadros, Julia Shaw, Dr. Anne Shearrow and Erica Turner) should also be thanked for their humor and support over the years.

Finally and most importantly, I would like to thank my family for their unconditional love. To my parents, Martin and Mary Ann Harris, you have raised two sons better than any parents could wish for. This degree is as much yours as it is mine. Thank you for your patience, and I promise to get a real job someday. To my brother, Craig M. Harris, who would have thought that I would be the scientist in the family and you the lawyer? I look forward to your wedding later this year with M. Ashley Cain, seeing Kosmo and Clarence (the dogs) and spending many more fun weekend trips with you. Also, thank you to the rest of my family. Without you all, this task would not be possible.

TABLE OF CONTENTS

ACKNOWLEDGEMENTS……... v

LIST OF TABLES……..... xiii

LIST OF FIGURES……... xiv

LIST OF SCHEMES……. xxi

LIST OF SYMBOLS……..... xxii

LIST OF ABBREVIATIONS……... xxiii

SUMMARY……..... xxvi

CHAPTER 1. RECENT DEVELOPMENTS WITH AMBIENT MASS SPECTROMETRY……..... 1

1.1. Abstract……. 1

1.2. Emerging Ionization Techniques: An Introduction to Ambient MS…..... 1

1.3. Overview of Plasma-Based Techniques……... 3

1.4. Direct Analysis In Real Time (DART)……..... 5

1.4.1. Fundamentals……..... 5

1.4.2. Instrumentation……..... 11

1.4.3. Applications…….. 14

1.5. Conclusion……... 25

CHAPTER 2. Simulations and Experimental Investigation of Atmospheric Transport In an Ambient Metastable-Induced Chemical Ionization Source…….. 26

2.1. Abstract……... 26

2.2. An Introduction to Direct Analysis In Real Time…….…. 26

2.2.1. Physicochemical Properties of DART……..... 26

2.3. Experimental……... 28

2.3.1. Instrumentation……..... 28

2.3.2. Computer Simulations……..... 30

2.3.3. Procedure……. 31

2.4. Finite Element Analysis of the Ionization Source…….. 32

2.5. Combined Fluid-Thermal Dynamic and Electrostatic Simulations With Experimental Validation of the Spatial Variations Within The DART Ionization Region……. 34

2.6. The Role of Sample Geometry In Space On the Observed Experimental Sensitivities With DART…….. 45

2.7. Conclusion……... 49

CHAPTER 3. Comparison of the Internal Energy Deposition of Direct Analysis In Real Time and Electrospray Ionization Time-of-Flight Mass Spectrometry……... 50

3.1. Abstract……... 50

3.2. Internal Energy Deposition……. 50

3.2.1. Internal Energy Deposition During Ionization……. 50

3.3. Experimental Determination of the Internal Energy Deposition……..... 52

3.3.1. Synthesis and Preparation of Para-Substituted Benzylpyridinium Salts……... 52

3.3.2. DART-MS Sampling, Instrumentation and Data Acquisition……... 53

3.3.3. ESI-MS Experiments, Instrumentation and Data Acquisition……... 55

3.3.4. Survival Yield Method and Data Analysis……..... 56

3.3.5. Computational Fluid Dynamic Simulations……..... 58

3.4. Determination of the Internal Energy Deposition of DART

Compared to ESI……..... 59

3.5. Thermal Activation Pathways of Internal Energy Deposition……... 62

3.6. Collisional Activation Effects of Internal Energy Deposition……... 67

3.7. Influence of Fluid Dynamics on Internal Energy Deposition……..... 68

3.8. Metastable-Stimulated Desorption Effects on Internal Energy Deposition……... 69

3.9. Conclusion…….. 70

CHAPTER 4. Ion Yield "Hot Spots" and Suppression Effects In Direct Analysis In Real Time Mass Spectrometry of Nerve Agent Simulants…….. 71

4.1. Abstract……... 71

4.2. Physicochemical Effects In the DART Ionization Region……. 72

4.3. Experimental Set-Up of Continuous DART Sampling…….. 73

4.3.1. Chemicals and Gases……... 73

4.3.2. DART-MS Instrumentation……. 73

4.3.3. DART-MS of Continuous Liquid Samples……. 74

4.4. Sampling Region Temperature Gradients…….. 76

4.5. Spatial Sensitivity and Dynamic Range……. 79

4.6. Ion Suppression…….. 84

4.7. Conclusion…….. 92

CHAPTER 5. Direct Analysis In Real Time Coupled To Multiplexed Drift Tube Ion Mobility Spectrometry……..... 94

5.1. Abstract……... 94

5.2. Chemical Detection Systems…….. 94

5.2.1. Recent Developments With Chemical Detection Platforms... 94

5.2.2. Ionization Techniques Used With Drift Tube Ion Mobility

Spectrometry……..... 95

5.3. Experimental Development of the DART-DTIMS Platform…….. 96

5.3.1. Drift Tube Ion Mobility Spectrometer and DART Instrumentation Setup……... 96

5.3.2. DART-IMS Sample Analysis……... 98

5.3.3. Determination of Reduced Mobility Terms…….. 100

5.4. Initial Assessment of DART-DTIMS Platform……... 101

5.5. Probability of Detection of Toxic Industrial Chemicals…….. 103

5.6. Transmission-Mode DART-DTIMS……... 105

5.7. Reliability of Detection of Conventional and TM DART-DTIMS……. 106

5.8. Sensitivity Gains Obtained From Multiplexed DART-DTIMS…….. 108

5.9. Conclusion……... 114

CHAPTER 6. Direct Analysis In Real Time In Transmission and Imaging Modes……. 115

6.1. Abstract……... 115

6.2. Alternate Implementations of Direct Analysis In Real Time…….. 115

6.2.1. Transmission-Mode Geometry……..... 115

6.2.2. IR-LAMICI……... 116

6.3. Experimental……..... 117

6.3.1. Instrumentation……..... 117

6.3.2. Computer Simulations…….. 119

6.3.3. Procedure……..... 120

6.4. Comparison of Helium and Nitrogen TM DART……..... 121

6.5. Effect of Flow Rates on TM DART……..... 125

6.6. Quantitative Assessment of TM DART……. 128

6.7. Investigating the Fluid Dynamic Contributions to IR-LAMICI……. 130

6.8. Direct Analysis With IR-LAMICI…….. 131

6.9. Mass Spectrometry Imaging Utilizing IR-LAMICI……... 133

6.10. Conclusion…… 134

CHAPTER 7. Conclusions and Future Outlook……..... 136

7.1. Abstract……... 136

7.2. Accomplishments In the Characterization and Implementation of Ambient Sampling/Desorption Ionization Insights……..... 136

7.2.1. Fundamental Insights……... 136

7.2.2. Instrument Development and Applications……. 138

7.3. Proposed Future Directions…… 140

7.3.1. Fundamental Insight Awaiting To Be Explored and Exploited…….. 140

7.3.2. Direction For Current Applications…….…. 141

7.3.3. Emerging Applications…….… 141

APPENDIX A. Application of Direct Analysis In Real Time Mass Spectrometry to Pharmaceutical Forensics……... 143

A.1. Abstract…….. 143

A.2. Substandard and Counterfeit Antimalarials……... 143

A.2.1. Outline of Counterfeit Drugs' Impact on Sensitivity…….. 143

A.2.2. Counterfeit Antimalarials…… 145

A.3. Experimental…….. 146

A.3.1. DART MS Analysis……..... 146

A.4. Detection of Counterfeit Medicines Acquired In South East Asia

And Cameroon……..... 147

A.5. Combining Two-Dimensional Diffusion-Ordered Nuclear Magnetic Resonance Spectroscopy, Imaging Desorption Electrospray Ionization Mass Spectrometry and Direct Analysis In Real Time Mass Spectrometry for the Integral Investigation of Counterfeit Pharmaceuticals……. 148

A.6. Conclusion..... 150

APPENDIX B. Enhanced Direct Ambient Analysis By Differential Mobility-Filtered Desorption Electrospray Ionization Mass Spectrometry….. 151

B.1. Abstract…….. 151

B.2. Introduction…… 152

B.2.1. Desorption Electrospray Ionization…… 152

B.2.2. Differential Mobility Spectrometry…… 153

B.3. Experimental…….. 153

B.3.1. DESI Instrumentation Setting……. 153

B.3.2. DMS-TOF MS Instrumentation Settings…… 154

B.4. Improving the Signal-to-Noise Ratio……. 155

B.5. Incorporating Collision Induced Dissociation With DMS Separation.. 159

B.6. DMS Separation of Isoberic Ions……... 160

B.7. Conclusion…….. 161

REFERENCES……..... 162

LIST OF PUBLICATIONS……..... 180

VITA…….. 183

LIST OF TABLES

Table 3.1: Pirani gauge pressure for first TOF differentially-pumped chamber under various experimental blank DART and ESI conditions……... 68

LIST OF FIGURES

Figure 1.1: An overview of DC and radiofrequency electrical discharge ambient desorption techniques..... 5

Figure 2.1: Top panel: Photograph of the uninsulated ambient metastable-induced chemical ionization source. Device regions: (i) gas inlet and corona discharge (7.5 cm long); (ii) plasma heating (2.0 cm); (iii) grid electrode/plasma exit (3.5 cm). Bottom panel: Two-dimensional representation of the ion source depicting: (a) temperature gradients of both the ion source and environment (ºC), and (b) gas velocity contour map (m s^{-1}). The purple to light blue lines correspond to the gas velocity contour map, while red lines represent simulated gas streamlines denoting directional flow of the exiting gas..... 29

Figure 2.2: Zoomed image of the ionization region. Tablet positions correspond to the "upright-below" position at different distances between the ion source and inlet orifice: **(x)** adjacent to the ion source (0 cm); **(y)** between the ion source and the inlet orifice (1.5 cm); and **(y)** adjacent to the inlet orifice (3 cm). Legends on left show the temperature scale (above) and the particle velocity scale (m s^{-1}) (below)..... 35

Figure 2.3: Simulated (black circles) and measured (red triangles) temperatures along the "below" sampling line..... 37

Figure 2.4: SIMION simulated electric field values on the straight line linking the center of the ion source gas exit and the orifice inlet cone at various grid potentials of (a) 50 V, (b) 100 V, (c) 150 V, (d) 200 V, (e) 250 V and (f) 300 V. In each case, these calculations were repeated for orifice potentials between 20 and 40 V... 39

Figure 2.5: Calculated ion velocities in the ambient sampling region of a straight line between the center of the ion source gas exit and the spectrometer orifice inlet determined from the reduced ion mobility constant of the protonated acetaminophen molecule $[M+H]^+$ and SIMION-simulated electric field values at defined grid potentials, and at specified orifice potentials of (a) 20 V, (b) 25 V, (c) 30 V, (d) 35 V and (e) 40 V..... 41

Figure 2.6: Experimentally determined intensities of the (a) protonated acetaminophen molecule $[M+H]^+$ and (b) protonated dimer $[2M+H]^+$ at specified grid and orifice potentials (n = 5). Fragment ions were not detected in any of the assayed conditions..... 43

Figure 2.7: Distance-dependent sensitivity of the upright tablet orientation of both the acetaminophen protonated molecule $[M+H]^+$ and dimer $[2M+H]^+$ under (a) normal (grid 250 V orifice 30 V) and (b) low electric field (grid 50 V orifice 20 V) conditions for 5 measurement replicates..... 44

Figure 2.8: (a) Particle tracing simulations of circular tablets showing simulated particle velocities (m s^{-1}) and (b) temperatures (ºC). The temperature scale is shown in b). Top row: Above position for sideways (i), flat (ii) and upright (iii) orientations; middle row: inline position for sideways (iv), flat (v), and upright (vi) orientations; bottom row: below position for sideways (vii), flat (viii) and upright (ix) orientations..... 46

Figure 2.9: Average signal intensities of (a, c) acetaminophen protonated molecule (*m/z* 152.07) and (b, d) proton-bound dimer (*m/z* 303.14) for the flat (black), sideways (red), and upright (green) orientations in the above (1), inline (2), and below (3) positions under high (grid 250 V orifice 30 V, left panels) and low field (grid 50 V orifice 20 V, right panels) conditions. Error bars indicate the standard deviation of replicate measurements (n=5)..... 48

Figure 3.1: (a) electron ionization mass spectrum of reserpine showing $M^{+\cdot}$ and significant fragmentation (reproduced from the NIST database). (b) ESI quadrupole ion trap mass spectrum of 1 µM reserpine in 50:49.9:0.1 (v:v:v) methanol:water:acetic acid showing $[M+H]^+$ and fragments at *m/z* 196 and 396 (10 µL min^{-1}, 5000 V_{DC})..... 52

Figure 3.2: Sample placement for DART-TOF MS analysis of thermometer compounds. Samples were applied to Dip-it™ (diameter 0.16 cm) sample capillaries affixed to a stable sampling arm. Sample positioning distances: (i) center of MS orifice to capillary, 0.60 cm, (ii) capillary depth below center of MS orifice, 0.16 cm and (iii) capillary to center of gas outlet distance, 0.74 cm..... 54

Figure 3.3: Schematic of pneumatically-assisted ESI source used in this work: a) cross-section view of the ionization source enclosure, and b) zoomed region of the desolvation chamber depicting the i. heating block, ii. electrospray needle with nebulizing gas, and iii**.** cross flow drying gas..... 56

Figure 3.4: Mean E_{int} ($<E_o>$) distributions for DART and ESI with helium gas heater (DART) or desolvation chamber (ESI) temperature set points of a) 175 ºC, b) 250 ºC and c) 325 ºC..... 61

Figure 3.5: Measured gas temperature at the bottom of the sample capillary in the DART ionization region at experimental set temperatures of a) 175 ºC, b) 250 ºC and c) 325 ºC. Time t = 0 sec corresponds to the instant the gas flow is turned on in the preheated DART source..... 63

Figure 3.6: Mean E_{int} surface contour maps for a) ESI and b) DART. Temperatures plotted on the x-axis correspond to set temperature in the ion source control software..... 64

Figure 3.7: Observed absolute abundances of protonated water clusters with

"*n*" water molecules ($(H_2O)_nH^+$) at set DART temperatures of a) 175 °C, b) 250 °C and c) 325 °C and different glow discharge gas flow rates. The electrical current on the discharge needle monitored from the DART controller software remained constant throughout these experiments..... 66

Figure 3.8: Normalized $Py^{+\bullet}$ to ($Py^{+\bullet}$ + $[Py+H]^+$) intensities observed during E_{int} DART-MS experiments at various flow rates and set temperatures..... 67

Figure 3.9: Particle tracing plots showing simulated trajectories of neutral particles originating on the bottom surface of the sample capillary at helium gas flow rates of a) 2 L min^{-1}, b) 4 L min^{-1} and c) 6 L min^{-1}..... 69

Figure 4.1: DART-MS ionization region depicting the DART gas nozzle, GIST sampling tube to the MS inlet, and the sample grid matrix with the sampling probe in the B2 position..... 74

Figure 4.2: Day-to-day quality control runs for sensitivity-in-space (Figure 3) and dynamic range DART-MS experiments..... 76

Figure 4.3: Direct probe temperature maps of the DART ionization region at gas temperatures of a) 200 °C, b) 300 °C and c) 400 °C..... 78

Figure 4.4: Sensitivity-in-space maps at different DART gas temperatures and concentrations of DMMP: maps a) 50 μM, b) 100 μM, and c) 500 μM were tested l at 200 °C, maps d) 50 μM, e) 100 μM, and f) 500 μM were tested at 300 °C, and maps g) 50 μM, h) 100 μM, and i) 500 μM were tested at 400 °C. All averaged (n = 5) intensities were normalized to the B2 (center) position..... 79

Figure 4.5: DART-MS dynamic range of DMMP in column B at positions a) B3 (close to MS inlet), b) B2 (middle of region) and c) B1 (close to DART gas nozzle) at concentrations of 25 μM - 1 mM and software control temperatures of 200, 300 and 400 °C..... 83

Figure 4.6: The effect of different boiling points but the same proton affinity on ion suppression in different sampling spots of equimolar mixtures of DMMP (BP: 181 °C, PA 902 kJ mol^{-1}) and *p*-anisidine (BP: 243 °C, PA: 900 kJ mol^{-1}) at DART gas temperatures of: a) 100 °C, b) 200 °C, c) 300 °C and d) 400 °C..... 85

Figure 4.7: The effect of different proton affinities but the same boiling points on ion suppression in different sampling spots of equimolar mixtures of isoquinoline (BP: 242 °C, PA 952 kJ mol^{-1}) and *p*-anisidine (BP: 243 °C, PA: 900 kJ mol^{-1}) at DART gas temperatures of: a) 200 °C, b) 300 °C and c) 400 °C..... 87

Figure 4.8: Average intensities of protonated water clusters of "*n*" size observed during the experiments of equimolar isoquinoline and *p*-anisidine at solution concentrations of a) 50 μM, b) 100 μM, c) 250 μM and d) 500 μM..... 89

Figure 4.9: Ion suppression competition between isoquinoline and *p*-anisidine in different molar ratios and sampling spots at a DART gas temperature of 300 °C. In the legend, the labeled position on the left refers to isoquinoline and the labeled position on the right refers to *p*-anisidine..... 91

Figure 5.1: Schematic of the DART-DTIMS system: drift tube (i.), entrance tube (ii.), entrance electrode (5 mm split) (iii.), DART gas and sampling tube (iv.), DART ion source (v.), adjustable rails (vi.). The inset shows the TM DART assembly mounted on the front of the instrument (vii.). Not shown is the 0.2 cm thick aluminum Faraday cage surrounding the DTIMS tubes..... 99

Figure 5.2: Direct measurements (n = 5) of the temperature gradient at the tip of the sample capillary when the DART gas and DTIMS drift gas temperatures were set to 400 °C and 150 °C, respectively..... 100

Figure 5.3: DART-DTIMS spectrum (400 sweeps averaged) of 2,4-lutidine (10 % v/v) showing two peaks at drift times of 28.8 ms (K_0 = 1.73 cm^2 V^{-1} s^{-1}) and 35.6 ms (K_0 = 1.40 cm^2 V^{-1} s^{-1}) at a field strength of 381.9 V cm^{-1} (9.93 kV applied to entrance of the drift tube)..... 102

Figure 5.4: DART-DTIMS spectra (400 sweeps averaged) of 2,4-lutidine (10 % v/v) at field strengths (applied voltage) of a) 255 (8 kV), b) 286.5 (9 kV), c) 318.1 (10 kV) and d) 349.6 V cm^{-1} (11 kV). The drift times of the first and second peaks were a) 42.8 and 53.7 ms, b) 37.9 and 47.2 ms, c) 34.2 and 43.0 ms and d) 31.0 and 38.6 ms..... 103

Figure 5.5: Probability of detection (POD) curves for a) DMMP, b) 2-CEES, c) methamidophos and d) TM DART analysis of DMMP tested at various concentration levels (n = 8 at each concentration level)..... 105

Figure 5.6: Sample spectra collected at the 95% POD with corresponding average drift time values (n = 24) for a) DMMP, b) 2-CEES, c) methamidophos and d) TM DART analysis of DMMP. Four hundred sweeps were averaged in every case..... 107

Figure 5.7: Box plot of the interquartenary ranges of recorded drift times of each analyte at their POD concentration levels (n = 24). Solid lines inside the boxes are the median values and the dots are outlier values..... 107

Figure 5.8: Illustration describing multiplexing theory using a basic 16 element sequence as an example. a) In conventional signal averaging mode, the gate is opened only for the first element (*r* = 1) and ions travel until they are detected

(6.25 % duty cycle). In digitally-multiplexed methods, ions can be injected any place along the sequence for a predetermined amount of elements: b) three potential sequences (12.5 % duty cycle) out of a possible 120 total sequences, c) ions are injected during four elements (25 % duty cycle) five of a total of different 1820 sequences are shown, d) ions are injected for eight elements (50 % duty cycle) eight of 12870 different sequences are shown above..... 109

Figure 5.9: Comparison of DMMP spectra at the 95% POD concentration level acquired with a 400 µs gate pulse width: a) conventional signal averaging (~0.4 % duty cycle), and digital sequences with duty cycles of b) 2 %, c) 5 %, d) 10 %, e) 30 % and f) 50 % (400 sweeps averaged)..... 110

Figure 5.10: Comparison of DART-DTIMS spectra of DMMP at the POD level with 200 µs gate pulse width. Spectrum collected using a) conventional signal averaging (~0.4 % duty cycle) and arbitrary digital sequences with duty cycles of b) 2 %, c) 5 %, d) 10 %, e) 30 % and f) 50 %. All experiments consisted of 400 sweeps..... 111

Figure 5.11: Signal-to-noise ratio gains observed for digitally-multiplexed experiments over traditional signal averaging mode during the DART-DTIMS analysis of DMMP at the 95% POD concentration level carried out with a) 200 µs and b) 400 µs gate pulse widths and 20 (●), 100 (▼) or 400 (■) averaged sweeps..... 112

Figure 5.12: DART-DTIMS spectra acquired using HT multiplexing. Spectra acquired with 200 µs gate pulse widths for a) 20 sweeps, b) 100 sweeps and c) 400 sweeps. Spectra acquired with 400 µs gate pulse widths for d) 20 sweeps, e) 100 sweeps and f) 400 sweeps. SNR gains over conventional signal averaging mode runs were a) 2.6x, b) 3.3x, c) 3.2x, d) 1x, e) 1.4x and f) 1.5x..... 113

Figure 6.1: Schematics of the custom-made sample holder used for TM-DART analysis. Top: exploded view of the sample holder. Bottom: top-view of the sample holder assembly mounted in the ionization region of the TM-DART time of flight (TOF) mass spectrometer interface..... 118

Figure 6.2: Schematic of the IR-LAMICI ion source coupled to a quadrupole ion trap mass spectrometer. The inset shows the total ion current trace observed for the analysis of an acetaminophen tablet with the laser turned off and on..... 119

Figure 6.3: Helium DART MS spectra of a neat deltamethrin standard obtained at 225°C (a) and 150°C (b) with 1.5 L min^{-1} gas flow rate. Fragmentation is observed when helium is used as the ionizing gas, increasing with increasing temperature. The nitrogen-induced mass spectrum shown in (c) presents a predominant $[M+NH_4]^+$ ion with little-to-no fragmentation (225°C, 7.0 L min^{-1}). The insets in panel (c) show the experimental and theoretical isotopic structures of the deltamethrin $[M+H]^+$ ion observed in the helium-induced spectra..... 122

Figure 6.4: Helium induced DART MS spectra of a neat permethrin standard obtained at 225°C (a) and 150°C (b) with 1.5 L min^{-1} gas flow rate. Significant fragmentation exists when helium is used as the ionizing gas, increasing only slightly with increasing temperature. The nitrogen induced (225°C, 7.0 L min^{-1}) mass spectrum (c) results in an abundant $[M+NH_4]^+$ ion but also considerable fragmentation compared to that of deltamethrin (see Figure 2). Insets in panel (c) show the chemical and isotopic (experimental and theoretical) structures of the permethrin pesticide. The inset showing the isotopic distribution corresponds to the $[M+NH_4]^+$ ion of the nitrogen-induced spectra..... 124

Figure 6.5: Effect of helium gas flow rate on the absolute intensity of the deltamethrin $[M+H]^+$ ion during TM-DART analysis of a 55 mg m^{-2} conventionally-treated bed net. The adjustable distance between the gas exit of the DART source and the sample holder (see Figure 6.1) allowed two settings to be examined at various gas flow rates: in contact with one another (▲) and 4 mm apart (×). Set gas temperature was 150°C in all cases..... 126

Figure 6.6: CFD simulations at a) 0.5, b) 1.0, c) 1.5 and d) 2.0 L min^{-1} helium at 150 ºC when the DART gas nozzle is positioned 4 mm away from the sample holder. The images on the left show a 3D perspective of the system, the middle images show the gas flow from above, and the heat map scales on the right are the gas velocities in m s^{-1}..... 127

Figure 6.7: CFD simulations at a) 0.5, b) 1.0, c) 1.5 and d) 2.0 L min^{-1} helium at 150 ºC when the DART gas nozzle is positioned in contact with sample holder. The images on the left show a 3D perspective of the system, the middle images show the gas flow from above, and the heat map scales on the right are the gas velocities in m s^{-1}..... 128

Figure 6.8: Extracted ion chronograms for the DART analysis of bed nets coated with increasing levels of deltamethrin using the custom-made sample holder. Experiments were performed using helium (0.5 L min^{-1} (top) and 2.0 L min^{-1} (center) at 150°C) and nitrogen (7.0 L min^{-1} at 225°C (bottom)). Insets show integrated peak areas as a function of bed net insecticide concentration. The $[M+H]^+$ and $[M+NH_4]^+$ ions are plotted for helium and nitrogen, respectively..... 129

Figure 6.9: Three-dimensional CFD simulations of the IR-LAMICI setup: (a) 150 particles were simulated originating from a 300 µm-diameter laser spot; (b) gas velocity map and velocities; (c) particle trajectories originating from the positions outlined in (a). The laser spot diameter was measured by taking an optical image (Olympus BX41, optical microscope) of a single shot laser ablation spot..... 131

Figure 6.10: IR-LAMICI MS analyses of (a) a counterfeit artesunate antimalarial drug tablet collected in Cameroon; (b) a red macroalga, *Callophycus serratus*, showing the presence of bromophycolides; and (c) a Tylenol® tablet (325 mg acetaminophen). The inset in (b) shows a typical negative ion mode DESI MS spectrum of a similar tissue sample, with the peak at *m/z* 665 corresponding to [bromophycolide A/B - H]$^-$ and the peak at *m/z* 583 to [bromophycolide A/B – HBr]$^-$ and/or [bromophycolide E - H]$^-$). The insets in (c) show false-color scale IR-LAMICI MS images of the distribution of acetaminophen monomer and dimer ions on the tablet..... 132

Figure A.1: Positive mode DART spectrum of sample Cam S5/07. The insert shows the isotopic signature of the ion at *m/z* 320.1891..... 148

Figure A.2: Analyses of a sample by: (A) 2D DOSY 1H NMR in DMSO-d_6 with TMPS as internal reference standard (S_{DMSO} represents DMSO satellite signals), (B) DART MS in positive ion mode and (C) DESI MS in positive ion mode..... 150

Figure B.1: DESI-DM-TOF MS mounting assembly composed of the DESI spray probe, heated transfer region, DMS assembly, and TOF MS orifice..... 154

Figure B.2: Analysis of a counterfeit antimalarial pharmaceutical tablet by DESI-DM-MS: (a) DMS-off mode (no voltages applied) and DMS-on mode for the isolation of: (b) sodiated lactose excipient (*m/z* = 365.1061, SV = 1300 V, CV = -1.7 V), (c) sodiated artesunic acid (*m/z* = 407.1082, SV = 1300 V, CV = -0.7 V), and (d) R6G (*m/z* = 443.2335, SV = 1300 V, CV = 1.7 V). The inset shows the normalized selected ion trace for each ion in the MS acquisition time scale with a CV sweep rate of 0.25 V step^{-1}..... 156

Figure B.3: Separation of a mixture of sodiated lactose (*m/z* 365.106), sodiated artesunic acid (*m/z* 407.108) and R6G (*m/z* 443.233) in the presence of a) 20 % helium in nitrogen and b) pure nitrogen as the transport gas..... 158

Figure B.4: Application of DESI-DM-MS to the analysis of chemical standards on PTFE surfaces. Mixture of 0.5 mM pyrimethamine (mono-isotopic MW = 248.083) and 1 mM polyethylene glycol (PEG 400): (a) DMS-off (no voltages applied), and (b) DMS-on mode (SV = 1300, CV = 1.2V). The inset of (b) shows the DESI-DM-CID-MS mode of operation at orifice voltage of 120 V. (c) The analysis of a binary mixture of pyrimethamine (100 μM) and 5-HMF (100 μM) in DMS-on mode (SV = 900 V, CV = -15 V to 5 V). Inset shows the total ion trace in the MS time scale, while the CV was scanned..... 159

LIST OF SCHEMES

Scheme 3.1: p-Substituted benzylpyridinium cation structure and fragmentation pathway..... 57

Scheme 3.2: Proposed energy deposition pathways for the compounds analyzed by DART-TOF MS..... 60

LIST OF SYMBOLS

λ	Mean free path
2^3S_1	Helium metastable atom excited to the triplet state
Da	Dalton
eV	Electronvolt
$\langle E_0 \rangle$	Mean internal energy
E_0	Critical energy (minimum energy needed by an ion to overcome the dissociation energy barrier and form product ions)
He*	Helium metastable atom
i	Current
i.d.	Inner diameter
I_{prec}	Precursor ion intensity
I_{prod}	Product ion intensity
K_0	Reduced ion mobility
m/z	mass-to-charge ratio
o.d.	Outer diameter
P(E)	Internal energy distribution
Py	Pyridine
S/N	Signal-to-noise ratio
V	Voltage

LIST OF ABBREVIATIONS

AC	Alternating current
ACT	Artemisinin-derivative combination therapy
AP	Atmospheric pressure
APCI	Atmospheric pressure chemical ionization
API	Active pharmaceutical ingredient
AP-MALDI	Atmospheric pressure matrix-assisted laser desorption ionization
APPI	Atmospheric pressure photo-ionization
APTDI	Atmospheric pressure thermal desorption ionization
BP	Boiling point
CFD	Computational fluid dynamics
CI	Chemical ionization
CID	Collision-induced dissociation
CV	Compensation voltage
CWA	Chemical warfare agent
DAPCI	Desorption atmospheric pressure chemical ionization
DART	Direct analysis in real time
DBDI	Dielectric barrier discharge ionization
DC	Direct current
DCBI	Direct corona beam ionization
DESI	Desorption electrospray ionization
DM	Differential mobility
DMS	Differential mobility spectrometry

DOSY	Diffusion ordered spectroscopy
DTIMS	Drift tube ion mobility spectrometry
EI	Electron ionization
ELISA	Enzyme-linked immunosorbent assay
ESI	Electrospray ionization
FAIMS	Field asymmetric waveform ion mobility spectrometry
FAPA	Flowing atmospheric-pressure afterglow
FEM	Finite element method
FT-ICR	Fourier transform ion cyclotron resonance
GC	Gas chromatography
GIST	Gas-ion separation tube
H/D	Hydrogen/deuterium exchange
HPLC	High performance liquid chromatography
HT	Hadamard transform
IM	Ion mobility
IMS	Ion mobility spectrometry
IR	Infrared
IR-LAMICI	Infrared-laser ablation metastable induced chemical ionization
ITN	Insecticide treated nets
LC	Liquid chromatography
LTP	Low temperature plasma
MALDI	Matrix assisted laser desorption ionization
MICI	Metastable induced chemical ionization

MS	Mass spectrometry
MS/MS	Tandem mass spectrometry
MSD	Metastable stimulated desorption
MSI	Mass spectrometry imaging
Nd:YAG	Neodymium yttrium aluminum garnet
NMR	Nuclear magnetic resonance
OPO	Optical parametric oscillator
PA	Proton affinity
PAH	Polycyclic aromatic hydrocarbon
PEG	Polyethylene glycol
PI	Photoionization
POD	Probability of detection
Q-TOF	Quadruple-time of flight
RTD	Resistance temperature detector
SNR	Signal-to-noise ratio
SV	Separation voltage
SY	Survival yield
TIC	Toxic industrial chemical
TM	Transmission mode
TOF	Time of flight
UPLC	Ultra performance liquid chromatography
UV	Ultraviolet
WHO	World Health Organization

SUMMARY

Molecular ionization is owed much of its development from the early implementation of electron ionization (EI). Although dramatically increasing the library of compounds discovered, an inherent problem with EI was the low abundance of molecular ions detected due to high fragmentation leading to the difficult task of the correct chemical identification after mass spectrometry (MS). These problems stimulated the research into new ionization methods which sought to "soften" the ionization process. In the late 1980s the advancements of ionization techniques was thought to have reached its pinnacle with both electrospray ionization (ESI) and matrix-assisted laser desorption/ionization (MALDI). Both ionization techniques allowed for "soft" ionization of large molecular weight and/or labile compounds for intact characterization by MS. Albeit pervasive, neither ESI nor MALDI can be viewed as "magic bullet" ionization techniques. Both techniques require sample preparation which often included native sample destruction, and operation of these techniques took place in sealed enclosures and often, reduced pressure conditions.

New open-air ionization techniques termed "ambient MS" enable direct analysis of samples of various physical states, sizes and shapes. One particular technique named Direct Analysis In Real Time (DART) has been steadily growing as one of the ambient tools of choice to ionize small molecular weight (< 1000 Da) molecules with a wide range of polarities. Although there is a large list of reported applications using DART as an ionization source, there have not been many studies investigating the fundamental properties of DART desorption and ionization mechanisms.

The work presented in this thesis is aimed to provide in depth findings on the physicochemical phenomena during open-air DART desorption and ionization MS and current application developments. A review of recent ambient plasma-based desorption/ionization techniques for analytical MS is presented in Chapter 1. Chapter 2 presents the first investigations into the atmospheric pressure ion transport phenomena during DART analysis. Chapter 3 provides a comparison on the internal energy deposition processes during DART and pneumatically assisted-ESI. Chapter 4 investigates the complex spatially-dependent sampling sensitivity, dynamic range and ion suppression effects present in most DART experiments. New implementations and applications with DART are shown in Chapters 5 and 6. In Chapter 5, DART is coupled to multiplexed drift tube ion mobility spectrometry as a potential fieldable platform for the detection of toxic industrial chemicals and chemical warfare agents simulants. In Chapter 6, transmission-mode DART is shown to be an effective method for reproducible sampling from materials which allow for gas to flow through it. Also, Chapter 6 provides a description of a MS imaging platform coupling infrared laser ablation and DART-like phenomena. Finally, in Chapter 7 I will provide perspective on the work completed with DART and the tasks and goals that future studies should focus on.

CHAPTER 1: PLASMA-BASED AMBIENT DESORPTION/IONIZATION TECHNIQUES FOR ANALYTICAL MASS SPECTROMETRY

1.1. Abstract

This chapter describes some of the latest breakthroughs, developments and applications with a new class of emerging ionization techniques called ambient desorption/ionization mass spectrometry ("ambient MS" for short). Ambient ionization techniques enable the interrogation of a variety of samples in their native state by MS, and are rapidly advancing all fields where screening for the presence of various analytes in a broadband and/or high-throughput fashion is desirable. Within the past two years alone (January 2009 to January 2011), a PubMed and Scifinder Scholar electronic database search resulted in over 290 references referring to this field. For the scope of this chapter, a brief introduction of the current ambient MS field will be given to clarify how the techniques are unique from traditional MS ionization techniques, and how they are categorized from each other. Particular focus will be towards the select plasma ionization technique described in the subsequent chapters called Direct Analysis In Real Time (DART) and the latest fundamental, instrumental and application developments within the past two years.

1.2. Emerging Ionization Techniques: An Introduction to Ambient MS

The introduction of desorption electrospray ionization (DESI) by Cooks and coworkers in late 2004[1] followed by DART by Cody et al. in early 2005,[2] were the pivotal milestones in the recent development of a subfield of analytical MS known as "ambient MS", also referred to as "direct ionization MS".[3-13] The ambient MS field is

now past its initial hype period and is finding its application niche. It is also becoming increasingly clear that, with some important exceptions, the unique aspect about ambient MS technology is not necessarily the ionization mechanisms themselves, but the *format* in which the ion sources are designed/configured. Ambient MS techniques make use of well-established ionization principles such as electrospray ionization (ESI), chemical ionization (CI), photoionization (PI) etc., but in an open air direct ionization *format* which allows unique experiments to be performed on samples previously requiring significant sample preparation prior to MS analysis. Non-destructive surface analysis, spatially-resolved analyte detection, multi-analyte fingerprinting, matrix-less imaging and selective ionization enhancement by means of specific liquid or gas-phase chemical reactions are now possible with ambient MS, with most sample preparation needs effectively removed.

To distinguish ambient ionization MS approaches from atmospheric pressure (AP) ionization techniques, a set of basic traits should be present in techniques to be included in the ambient MS field. Ambient MS techniques should enable (a) ionization in the absence of enclosures such as those typically found in ESI, APPI, APCI, AP matrix-assisted laser desorption ionization (AP-MALDI) sources. This feature is critical when examining samples ("objects") of unusual shape or size that cannot fit easily inside of an ion source enclosure or that would be critically disrupted or damaged when placed under vacuum. In other words, the technique should operate in the open air or ambient environment. (b) Ambient MS techniques allow *direct* ionization with minimum sample pre-treatment such as preconcentration, extraction, derivatization, dissolution or chromatographic or electrophoretic separation. Although this requirement can be relaxed

to some extent in challenging applications of ambient MS, it is still one of the end goals of research in this field. (c) The techniques should be interfaceable to most types of mass spectrometers fitted with differentially pumped atmospheric pressure interfaces, without substantial modification to the ion transfer optics or vacuum interface. (d) Finally, ions should be generated softly, with amounts of internal energy deposited equal to or lower than those in ESI, AP-MALDI, APPI or APCI.

The rapid growth of the field of ambient MS has caused some difficulty in classification of the techniques due to minor differences in instrumental conditions and geometries. Based on their fundamental properties of ionization and desorption mechanisms, ambient MS techniques can be classified into the following categories: 1) spray and solid-liquid extraction-based techniques which involve ESI or similar mechanisms, 2) direct and alternating current (DC and AC) plasma based techniques involving CI mechanisms, 3) plasma-based techniques where chemical sputtering-like desorption steps are followed by CI, 4) multimode techniques involving two of the principles discussed in previous sections, 5) laser desorption/ablation methods, 6) acoustic desorption methods, and 7) other techniques that do not fit into previous categories. The majority of the research presented in this dissertation pertains to a DC plasma based techniques called DART. In the sections that follow, an introduction to DART will be presented.

1.3. Overview of Plasma-Based Techniques

Plasma based techniques comprise DART, flowing atmospheric-pressure afterglow (FAPA), low temperature plasma (LTP), dielectric barrier discharge ionization (DBDI), desorption atmospheric pressure chemical ionization (DAPCI), direct corona

beam ionization (DCBI) and microplasmas (Figure 1.1). They involve the generation of a DC or radiofrequency electrical discharge between a pair of electrodes in contact with a flowing gas such as nitrogen or helium, generating a stream of ionized molecules, radicals, excited state neutrals and electrons. Some or all the plasma species are directed towards the sample, with optional secondary heating of the plasma gas stream to enhance desorption. Plasma ambient sampling/ionization techniques have the advantages of simple instrumentation, rugged construction, no need for solvents and generation of singly charged analyte species that are more easily identifiable than for spray-based techniques, which also generate adducts and multimers. Their use is mainly limited to analytes in a reduced mass range, usually below 800-1000 Da.

Differences between plasma techniques are sometimes not obvious, as not all experimental conditions are sufficiently well described to understand similarities and differences. The main differences usually reside in one of the following points: (a) if the plasma species are or not removed from the flowing gas (nitrogen, helium or air) stream previous to interaction with the sample, (b) if the plasma gas stream is heated or not, and if the heating is performed by a supplementary heating element, or by Joule heating induced by the discharge current itself, (c) if the discharge is operated in DC, AC pulsed mode etc., (d) the regime in the current-voltage curve (i-V) where the discharge is operated, (e) if the discharge is in the point-to-plane or annular configuration, and (f) if the plasma is established within a macro (several mm or more) or micron-sized gap. Of the five techniques included in this subgroup, only DART is currently commercially available explaining its growing popularity.

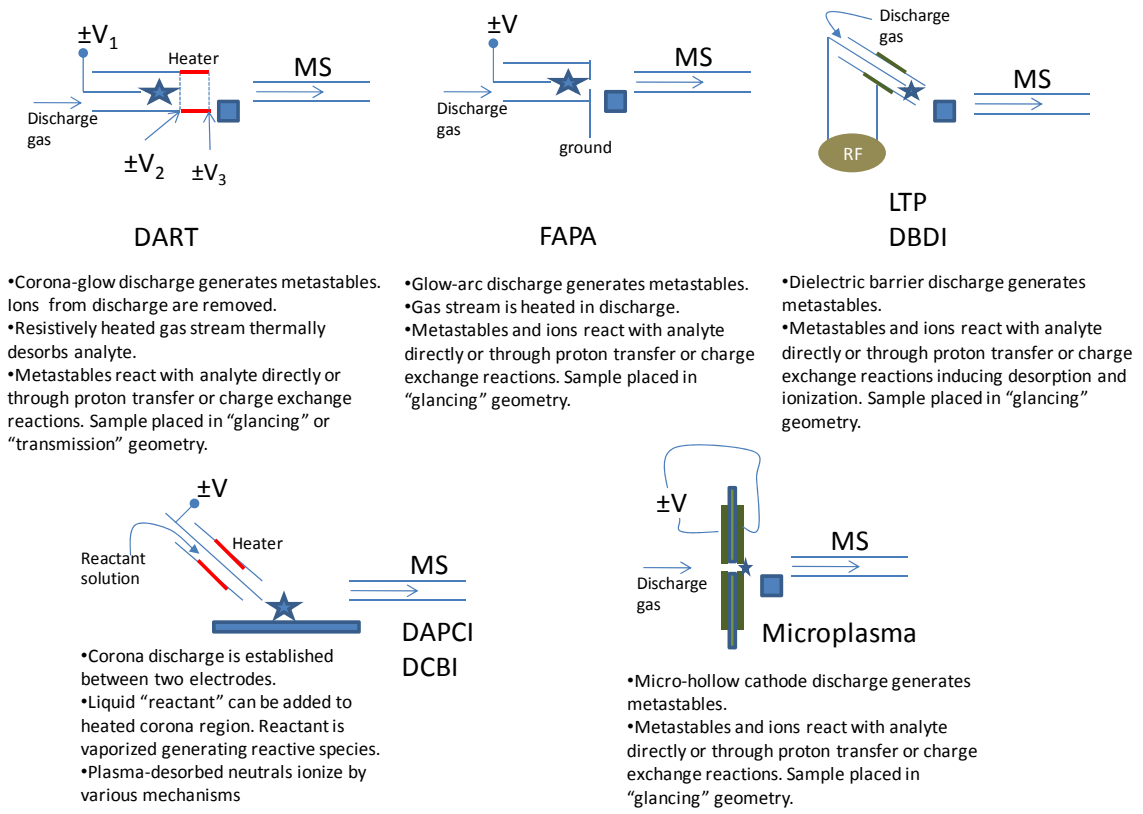

Figure 1.1: An overview of DC and radiofrequency electrical discharge ambient desorption techniques.

1.4. Direct Analysis In Real Time (DART)

1.4.1. Fundamentals

DART is a plasma-based ambient chemical ionization source encompassing an enclosed point-to-plane glow discharge physically separated from the ionization region. Atomic metastables (nitrogen or most commonly helium) produced in this discharge are heated and directed towards the sample held in between the ion source outlet and the mass spectrometer atmospheric pressure interface inlet. Cody *et al.* have suggested a mechanism where the heated gas stream of excited state helium metastables (He* $^3S_1$, 19.8 eV) induces Penning ionization of atmospheric water molecules upon exiting into the environment, generating protonated water clusters (eq. 1.1).[2]

$$He^{*}(g) + nH_2O(g) \rightarrow He(g) + (H_2O)_{n-1}H^{+}(g) + OH^{-}(g) \quad \text{(eq. 1.1)}$$

These clusters are believed to be the predominant reactant species in positive mode ionization of basic molecules,[2] as evidenced by the abundant $[M+H]^{+}$ ions observed in experimental mass spectra, and the array of protonated water clusters (n = 1-14) observed in the background.[2]

The mechanisms for analyte volatilization and interaction with reactant ions possibly involves thermal desorption (eq. 1.2) followed by proton transfer reactions with reactant ions leading to protonated analyte molecules according with Kebarle's water displacement mechanism.[14] This is followed by declustering during travel within the first differentially pumped stage of the mass spectrometer (eq. 1.3).

$$AB(s) \xrightarrow{heat} AB(g) \qquad \text{(eq. 1.2)}$$

$$(H_2O)_m H^{+}(g) + AB(g) \longrightarrow AB(H_2O)_{m-1}H^{+}(g) + H_2O(g) \xrightarrow{-(m-1)H_2O} ABH^{+}(g)$$

(eq. 1.3)

For low vapor pressure species, an alternate ionization mechanism resembling chemical sputtering[15] by reactive surface collisions with protonated water clusters has also been suggested (eq. 1.4). For example, N,N-diisopropylaminoethyl methylphosphonothioic acid (EA2192), a strong ionic salt could still be ionized by DART, despite its negligible vapor pressure under normal conditions.[2] This type of chemical sputtering mechanism has also been proposed for other plasma based ambient ionization methods such as surface desorption atmospheric pressure chemical ionization.[16]

$$(H_2O)_m H^{+}(g) + AB(s) \longrightarrow AB(H_2O)_{m-1}H^{+}(g) + H_2O(g) \xrightarrow{-(m-1)H_2O} ABH^{+}(g)$$

(eq. 1.4)

The DART proton transfer mechanism is not universal. Direct Penning ionization producing electron impact-like spectra (eq. 1.5) and charge exchange reactions with oxygen molecular ions (eq. 1.6 and 1.7) have also been reported.[17] The importance of these alternate ionization mechanisms is affected by the ionization potential and gas-phase basicity of *AB*, and by the ion source-to-mass spectrometer distance, which alters the reaction chemistry in the DART sampling region.

$$He^{*}(g) + AB(g) \rightarrow He(g) + AB^{+\cdot}(g) + e^{-} \qquad \text{(eq. 1.5)}$$

$$He^{*}(g) + O_2(g) \longrightarrow He(g) + O_2^{+\cdot} + He + e^{-} \qquad \text{(eq. 1.6)}$$

$$O_2^{+\cdot}(g) + AB(g) \longrightarrow O_2 + AB^{+\cdot} \qquad \text{(eq. 1.7)}$$

Comparison of finite element computational simulations with matching experiments carried out by our group have demonstrated that gas velocity and temperature gradients play a central role in successfully transmitting ions generated within the DART ionization region into the atmospheric pressure interface of the mass spectrometer (Chapter 2).[18] It was observed that optimum sample placement was a fine balance between adequate and rapid sample heating to induce efficient thermal desorption and an abundant population of neutrals, and the losses that may occur when the gas trajectory lines are disturbed by the presence of a macroscopic sample placed between the DART ion source outlet and the mass spectrometer inlet. An important limitation of these simulations was that, due to computational limitations, suction from the mass spectrometer interface was not included in the models. However, the experimental results seem to qualitatively agree well with predictions from particle tracing simulations. It was also observed that due to heat losses to the environment, the effective gas temperature measured at different points within the ionization region was

consistently lower than the DART gas temperature set through the software, an important point when considering the choice of experimental parameters, and for internal energy deposition studies described below.

DART in-source fragmentation of labile molecules is a phenomenon that has been known for a number of years[19] and has recently led to the discovery of unusual decay products of nucleotides an nucleosides.[20] It is well known that metastable gas temperature has a critical role in the appearance of fragment ions. For example, systematic studies with the antifungal voriconazole, demonstrated the increase in the relative abundance of fragment ions when DART gas temperatures were ramped from 50 to 500 °C.[21] The presence of these fragments may make peak assignment difficult, including false negatives and positives. To further investigate these processes, our group recently completed a comprehensive study that used ion thermometry and computational fluid dynamics to attempt to identify the main sources of internal energy deposition in DART under standard operation conditions, and compare the amount of internal energy deposited by this technique relative to benchmark softer techniques (Chapter 3). The internal energy distributions of a series of *p*-substituted benzylpyridinium ions generated by both DART and ESI were compared using the "survival yield" method. DART mean internal energy values at glow discharge gas flow rates of 2, 4 and 6 L min^{-1}, and at set temperatures of 175, 250 and 325 ºC were in the 1.92-2.21 eV range. ESI mean internal energy at identical temperatures in aqueous and 50 % methanol solutions ranged between 1.71-1.96 eV and 1.53-1.63 eV, respectively. The results indicated that ESI is a “softer” ionization technique than DART, but that there was a certain degree of overlap between the two techniques for the particular time of flight mass (TOF) spectrometer used in this

work. As a whole, when helium was used to sustain the glow discharge, there was an increase in DART internal energy with increasing gas temperatures and flow rates, indicating thermal ion activation and increased in-source activation within the first differentially pumped region of the mass spectrometer. There was no evidence of internal energy deposition pathways from metastable-stimulated desorption or excess energy released from large differences in proton affinities, but fragmentation induced by high-energy helium metastables was observed at the highest glow discharge gas flow rates and effective gas temperatures.

In atmospheric pressure ion sources, ionization does not occur by a single, clearly defined mechanism as with vacuum techniques such as electron ionization (EI). For example, fundamental studies by Cody have shown that, although positive ions in DART are generally formed by proton transfer, molecular ions can be produced as well by charge exchange mechanisms under very specific experimental conditions.[22] DART shares some similarities with APPI in the sense that molecular ions are involved in the very first steps, which further react to produce charge or proton transfer products. The abundance of odd electron ions from a given analyte was found to correlate directly with the abundance of $O_2^{+\cdot}$, which was favored by small (3 mm or less) source-to-inlet distances, absence of excess moisture and high (650 °C) set gas temperatures. Another interesting shared characteristic between DART and APPI is that dopants can be used to selectively enhance the production of odd electron species. For example, fluorobenzene, a typical APPI dopant with an ionization potential of 9.2 eV, can be added as a vapor during DART ionization of non-polar analytes such as cholesterol. Under standard DART conditions (where $O_2^{+\bullet}$ is not abundant), cholesterol predominantly forms the dehydration

product $[M-H_2O + H]^+$. However, if fluorobenzene is added, a molecular ion is observed, in a similar fashion to that seen under conditions that maximize the abundance of $O_2^{+\bullet}$.

Bartmess, Song et al. have published a series of interesting papers[23, 24] investigating positive and negative ion generation mechanisms in DART beyond those proposed by Cody. A "transient microenvironment" effect consisting of nine gas-phase reactions accompanied by the respective thermochemical data was proposed to address matrix effects in positive mode DART ionization. It was observed that mixtures containing 1 μg ml^{-1} naphthalene, 1,2,4,5-tetramethylbenzene, decanoic acid, 1-naphtol, anthracene, 1,3-dimethoxybenzene, 9-methylantracene, 12-Crown-4, N,N-dimethylaniline, and tributylamine in solvents such as methanol, toluene, hexane and chloroform produced very different DART mass spectra depending on the solvent chosen. The proposed 9-step transient microenvironment mechanism suggests that analyte ionization, rather than proceeding by proton transfer from protonated water clusters, occurs by proton transfer from protonated microenvironment solvent clusters. Solvent molecular ions can also react with analyte molecules to produce both protonated analyte molecules and analyte molecular ions. This theory would also support the results described above regarding the use of fluorobenzene as a dopant, which would be part of the microenvironment of nascent DART ions. Negative ion formation mechanisms were also studied by Bartmess, Song et al., which compared DART with APPI, finding that the ionic products formed were similar, leading to four ionization mechanisms including electron capture, dissociative electron capture, proton transfer and anion attachment.[24]

1.4.2. Instrumentation

Recognizing that sample introduction plays a critical role in DART, many reports presenting alternative ways of exposing analytes to the metastable stream have been published. An automated linear rail auto sampler was used to map chemical plumes produced by accidental or intentional release of potentially toxic compounds using water-soaked cotton-swab wipe samples.[25] Another swabbing technique, this time involving foam swabs, was recently developed to detect 132 multiclass pesticides on the surface of grapes, apples and oranges entering the United States.[26] In this application, a transmission mode (TM) DART ionization approach was coupled to high-resolution non-targeted mass analysis using an Orbitrap mass spectrometer, mitigating the loss in peak capacity caused by the lack of chromatographic separation. Detection was achieved consistently for 86% of the analytes at levels ranging 2-10 ng g^{-1}. Partial separation was achieved by thermally ramping the DART gas temperature from 100-350 °C over 3 minutes. This thermal dependent release of volatiles has also been employed in various DART applications such as detection of compounds from eucalyptus,[27] and to resolve ions produced by the chemical warfare agent sarin from isobaric interferences.[28] TM DART analysis was first implemented to detect and quantify insecticides directly from insecticide treated bed nets, showing great promise due to increased ion transmission and reproducibility, as suggested by fluid dynamic simulations.[29] Because millions of insecticide treated bed nets are deployed worldwide for malaria prevention, detection of counterfeit products and assessment of the remaining amount of insecticide after prolonged environmental exposure are two applications that can gain from the high-throughput characteristics of DART ionization. TM operation is highly advantageous in the case of bed net samples, as

these can be “sandwiched” between two inert spacers and placed directly in between the ion source and the mass spectrometer inlet, allowing the DART plasma gas stream to interact with the sample in a flow-through fashion, therefore maximizing interaction with ionizing species.

Direct DART desorption/ionization from solid-phase extraction materials has been reported in both stir bar[30] and syringe formats.[31] Both of these approaches are highly appealing as they remove some of the manual steps and potential elution losses involved in any pre-concentration approach. DART coupled to stir bar sorptive microextraction was used to analyze environmental waters contaminated with UV filters. Semi-quantitation was possible from polydimethylsiloxane-coated bars with repeatabilities in the 5-30 %, and detection limits lower than 40 ng L^{-1}. DART results were in good agreement with thermal desorption gas chromatography (GC) MS, suggesting that this approach has the potential to be routinely used in environmental analysis.

A modification to a DART ion source that incorporates a micropyrolyzer stage to study primary vapors and char products of poplar biomass in a step-wise fashion has been recently implemented.[32] In this device, the stream of volatiles produced by the pyrolyzer was intersected with the DART metastable gas stream, enabling a direct decomposition/desorption/analysis experiment without sample preparation. In addition to DART MS analysis, the sample surface was also monitored at various pyrolysis stages using Fourier transform infrared photoacoustic spectroscopy. The importance of this application cannot be underestimated, as the analysis of complex biomass is of critical relevance to address increasing demands in the energy and fuels field.

DART has also been proposed as an ionization interface for liquid chromatography (LC) MS.[33] Although most applications covered in this review are directed at avoiding any sort of chromatographic or electrophoretic separation, this work is still of potential importance. The coupling of LC to MS via DART was achieved via a simple interface consisting of a stainless steel or fused silica capillary directing the LC eluent into close proximity to the ion source exit grid electrode. It was found that DART was highly tolerant to phosphate buffer concentrations up to 120 mM in the mobile phase at typical flow rates of 1 ml min^{-1}. Minimal contamination of the ion source or ion suppression was reported. Mixtures of parabenes and pyrazine derivatives were tested by LC-DART MS with good linearity and limits of detection in the μg L^{-1} to mg L^{-1} range.

One of the keys to the versatility of DART and other ambient ionization/sampling techniques has been the ability to be used on a variety of commercial mass spectrometers. DART was initially designed to work with cone/orifice atmospheric pressure inlets with no modification. However, many capillary inlet instruments could not handle the gas loads (especially of helium). As a result, a gas-ion separator tube assembly (GIST, a.k.a. Vapur™ tube) was designed to allow for the coupling of DART to these instruments. The GIST unit adds a small reduced-pressure region in front of the mass spectrometer capillary inlet to further reduce the vacuum load. The first demonstration of the GIST interface targeted improved quantitation of drugs in biological matrixes using automated sample delivery.[34] A coefficient of variance of 3.1 % was demonstrated with nine repeated injections of rat plasma containing 1 μM benzoylecgonine. In cases where the biological matrix suppressed the ion signal, as in the case of testosterone in raw rat plasma, a simple protein precipitation method was used to remove many of the

interferents. Additionally, pharmacokinetic experiments involving the oral administration of 25 mg kg^{-1} of a proprietary compound to mice were used as a test bed for investigating differences observed between LC MS/MS and DART MS/MS results. Plasma samples taken over seven time points in three animals revealed the mean difference of concentrations between the methods ranged from 4.7-16.4 %.

With the exception of the Orbitrap,[26] DART has been primarily coupled to mass analyzers of low to medium resolving power such as quadrupoles and TOF. Powell et al. described the first coupling of a custom-built DART ion source to two different (4.7 and 9.4 T) FT-ICR mass spectrometers. DART FT-ICR MS was successfully applied to the detection with baseline resolution of mixtures of theophylline and diisopropyl methylphosphonate separated by only 27 mDa. Analysis of two simple food products (grapefruit flesh and habanero pepper) and a crude oil sample (NIST Heavy Sweet crude oil) demonstrated that the combined rapid screening capabilities of DART and the ultra-high resolving power offered by FT-ICR MS result in an extremely powerful tool for rapid characterization of complex mixtures.

1.4.3. Applications

DART has been used for a multitude of applications due to both its ease of use, versatility and commercial availability. The major driving force behind its widespread use was to develop alternatives to traditional GC and LC MS methods. DART methods may not yield reproducibility as high as conventional GC and LC MS, but the time and cost savings may ultimately balance out. Furthermore, DART accurate mass measurements can be rapidly obtained since external mass scale calibration is quasi-instantaneously performed through direct analysis of various calibrant compounds, and

because DART was initially preferentially marketed as a companion for orthogonal TOF-MS instrumentation. The most common DART calibrant in positive ion mode is diluted PEG 600, which provides good coverage over the typically acquired mass range (50-800 Da) and can be sampled easily after dipping a melting point capillary tube in the calibrant solution.

DART has been identified in the homeland security field as a promising technique for surface and volatile analysis of explosives,[35] biotoxins,[36] and chemical warfare agents.[37] For these applications, the ability to nondestructively sample from various surfaces and substrate materials allows for a quick first screening tool while more time consuming, but complementary investigations can be pursued in parallel. In an extensive study investigating the analysis of explosives (ethylene glycol dinitrate (EGDN), propylene glycol dinitrate (PGDN), Tetryl, pentaerythritol tetranitrate (PETN), mononitroglycerin (MNG), dinitroglycerin (DNG), trinitroglycerin (TNG), HMX, RDX, dinitrotoluene (DNT), amino-DNT, TNT, dinitrobenzene (DNB), trinitrobenzene (TNB) and picric acid) sampled from surfaces (glass, polyurethane foam, steel, wood and asphalt shingle) and liquids (diesel fuel, creek water and sea water), DART was shown to produce informative and simple spectra of the targeted analyte.[35] The explosives were rubbed onto the substrates after deposition and drying on aluminum foil (<2 μg) to simulate how explosive residues might be found on materials after an explosion. For liquids, the explosives were diluted to 100 ng mL^{-1}. The DART source was run in negative ion mode with dichloromethane as a dopant to produce mainly the chlorinated adducts or molecular anions with little background. Without the dopant, small amounts of nitrite and nitrate adduct anions were observed. The explosives were also simultaneously

detected on the five surfaces in mixtures containing DNB, DNT, amino-DNT, TNB and TNT, although no quantitation was attempted.

A quantitative biotoxin activity assay for ricin was developed as a means to eliminate timely multistep analysis of ricin activity.[36] Ricin is a large (>60 kDa) enzyme so direct analysis is not possible with DART. However, one can monitor the secondary processes that ricin invokes on eukaryotic cells, in particular, the release of adenine from the nucleic acid. Herring sperm DNA was used as a model substrate for ricin exposure, with uracil as an internal standard. Linearity for adenine was in the 2.9-740 μM range with the lowest concentration of adenine (2.9 μM) detected well above the limit of detection (SNR > 350). Time-dependent ricin activity was observed for 50 h showing linearity in adenine production for the first 4 h at 53 ± 2 pmol adenine $pmol^{-1}$ ricin h^{-1}.

Quantitative analysis of chemical warfare agents showed similar promising results.[37] Linear calibration curves over 3 orders of magnitude for nerve agents (tabun, sarin and VX) and a blister agent (sulfur mustard) were demonstrated. VX was detected as the protonated molecule and tabun and sarin as the ammonium adducts. Interestingly, the hydroxyl adduct cation was the base peak ion for sulfur mustard. This is an odd species to observe with DART. For confirmation of this species, negative mode analysis of sulfur mustard revealed the chlorinated adduct. For all compounds linearity exceeded $R^2 > 0.99$ and quantitative percent errors often averaging no worse than 3 %.

Food and beverage testing has seen its share of DART-related applications for both quality control and forensic purposes. Gamma-hydroxybutyric acid (GHB, "date rape drug") was detected from 50 drink matrices such as juices, sodas, wines and liquors, and proposed as a more reliable test than colorimetric assays.[38] A lower limit of detection

was set at 0.05 mg mL^{-1} which was lower than typically encountered GHB concentrations in real life samples (1.7-21.1 mg mL^{-1}). Similar analytical merits were seen for fungal mycotoxins in cereals using either matrix-matched standards or ^{13}C-labeled internal standards.[39] A variety of mycotoxin standards (n = 24) were tested in both positive and negative modes. Not all mycotoxins were detected (DON-3-Glc, OTA, FB1, FB2, ergocornine, ergocristine and ergosine), and it was believed that low volatility could be the cause since these compounds were heavier than other successfully analyzed mycotoxins (400-700 Da). Derivatization or alternative desorption methods could remedy this issue in future studies. Common anions and cations observed were the chlorinated (ADON, DON, Deepoxy-DON, FUS-X, NIV, ZEA, altenuene, alternariol and alternariol-met) and deprotonated (ZEA, altenuene, alternariol and alternariol-met) adducts and protonated (DAS, AFB1, AFB2, AFG1, AFG2 and sterigmatocystin) and ammonium (HT-2, T-2 and DAS) adducts, respectively. Comparative analysis of certified reference materials of DON or ZEA mycotoxins in maize flour, wheat flour, and ground millet by DART MS and UPLC MS showed that DART offered comparable results. For example, the mean amount of the mycotoxin DON in maize flour measured via external calibration and isotope dilution with DART was 459 and 486 μg kg^{-1} with relative standard deviations of 9.0 and 5.9 %, respectively. Compared to the mean value (500 μg kg^{-1} maize flour) and relative standard deviation (4.1 %) obtained by UPLC, the results obtained with DART are certainly similar.

Food packaging was tested for additives like plasticizers, anti-oxidants, colorants, grease-proofers and ultraviolet light stabilizers.[40] Attention should be drawn to the detection of some high molecular weight (~1000 Da) compounds in this study. For

instance, a plasticizer (epoxidized soybean oil) and an antioxidant (Irganox 1010) were both detected as the protonated water adducts (*m/z* 992.8 and 1196, respectively). The epoxidized soybean oil contained a mixture of epoxidized triglycerides, diglycerides and fatty acids with the base peak belonging to the epoxidized triglyceride of linoleic acid. The protonated water peak for Irganox 1010 was also accompanied with a less intense protonated molecule peak (*m/z* 1177.7).

DART has also been applied to the detection of melamine contamination in milk powder. In one study, melamine and cyanuric acid were detected from powdered milk samples.[41] Limits of detection for melamine and cyanuric acid were 170 and 450 μg kg^{-1}, respectively. Isotopically-labeled standards ($^{13}C_3$-melamine and $^{13}C_3$-cyanuric acid) were used for quantitation. Instant H/D exchange occurred with deuterated melamine analogues (melamine-d_6). The limit of quantitation was 450 and 1200 μg kg^{-1} for melamine and cyanuric acid, respectively, with relative standard deviation in the 5-7 % range for standard mixtures. In real life samples of dried milk, condensed milk and dried cheeses, good agreement was seen amongst DART and LC MS/MS methods with poorer results seen for an ELISA assay comparable to both MS metrics. The DART MS and LC MS/MS results for condensed milk analysis showed comparable mean values (4140 and 3958 μg kg^{-1}) and relative standard deviations (6.2 and 2.8 %).

Differentiation between 5-hydroxymethylfurfural (5-HMF) and melamine can be difficult without tandem MS or high resolution MS capabilities since they share the same nominal *m/z* (127). In a clever experiment, Dane and Cody[42] operated DART with argon as the discharge gas, and acetylacetone and pyridine reagent "dopant" gases to selectively ionize melamine. The metastable energy states of argon (11.55 eV $^3P_2$ and 11.72 $^3P_0$) are

lower than the ionization energy of water (12.6 eV), therefore no Penning ionization of water occurred. Direct Penning ionization of either compound was not observed so a multistep reaction sequence involving dopant gases introduced into the ionization region was used to selectively protonate melamine. First, metastable argon Penning-ionized acetylacetone. This molecular ion then reacted with a neutral acetylacetone molecule protonating it. The proton affinity of the acetylacetone molecule was lower than pyridine (873.5 vs. 930 kJ mol^{-1}), and pyridine thus captured the proton. Finally, the protonated pyridine transferred the proton to melamine. Although no literature values were found for the proton affinity of melamine and 5-HMF, these results demonstrate that melamine must have a proton affinity greater than pyridine, and both have affinities greater the 5-HMF. As noted earlier, this study utilized argon as the metastable gas and has been the first and only reference to date that uses this DART approach.

An unique investigation of the release kinetics of a chewing gum flavor agent (WS-3, cyclohexanecarboxamide) in saliva was pursued with DART and compared to LC MS.[43] A custom sample probe was made to reproducibly hold the sample in the gas stream. The probe consisted of a 0.12 mm diameter metal (nickel chromium) wire wrapped around a 0.80 x 0.80 mm disposable syringe needle with a sealed hole. This probe could be rapidly made and reproducibly placed with the help of a custom assembly attached to the DART source. The sample probe provided a medium that conduced heat efficiently, provided surface "roughness" for liquid to adhere, and was small so that the reactive gas dynamics were not severely disturbed. Compared to conventional melting point capillary probes, maximum signal intensity was higher for the new probe, and the relative standard deviation was improved 3-fold over 4-decades of concentration range

(0.1-1000 ng mL^{-1}). In regards to the release kinetics of WS-3, four subjects gave 10 saliva samples over an hour of both free and encapsulated WS-3 in an extruded carbohydrate carrier. The levels of free WS-3 started low (1 μg g^{-1} saliva) and seemed to stay constant or gradually increase after 10 minutes of chewing (maximum level of 10 μg g^{-1} saliva shown in one subject). Conversely in encapsulated form, WS-3 levels spiked within the first 3 minutes to levels of 5-25 μg g^{-1} saliva. A sudden decrease in levels was then observed in the next few minutes until stabilization after 10 minutes near 3-10 μg g^{-1} saliva. These results reflect the differences in saliva secretion between the subjects and the release of flavor quickly in encapsulated forms.

Polymers and additives have been also investigated by DART since most low-molecular weight polymer subunits, side chains and initiators contain functional groups that readily protonate. Additive stabilizing agents such as those from the Irganox, Irgafos and Tinuvin types, amongst others, were investigated in both toluene extracts and directly from polypropylene polymer samples.[44] For these stabilizers, common observed ions were the deprotonated anions and the protonated molecules. Positive mode ionization provided the best sensitivity with limits of detection below 1 mg L^{-1} except for one of the 21 tested samples (Tinuvin 328, 50 mg L^{-1}). Intact polymer samples (0.5 x 0.5 cm pieces) with multiple additives were all successfully investigated. For example, the additives Tinuvin 770, Tinuvin 234, Irgafos 38 and Chimassorb 81 at concentrations of 10 mg per 5 g base polymer (polypropylene) were successfully detected as the protonated molecules at *m/z* 481.4017, 448.2373, 515.3637 and 327.1931, respectively.

Additives in poly(vinyl chloride) lid gaskets were targeted for detection since their introduction into food products is regulated.[45] Toluene extracts of gaskets were used

to identify numerous compounds such as phthalates, fatty acid amides, tributyl *O*-acetylcitrate, dibutyl sebacate, bis(2-ethylhexyl) adipate, 1,2-diisononyl 1,2-cyclohexane-dicarboxylate, acetylated mono- and diacylglycerides, epoxidised soybean oil and polyadipates. Similarly, phthalic acid esters were detected from poly(vinyl chloride) toys.[46] Phthalic acid esters are under safety scrutiny for potential toxic effects against the health of children. Limits of detection for benzyl butyl phthalate, bis(2-ethylhexyl) phthalate and diisononyl phthalate were 0.05 %. Other additives such as dibutyl phthalate, di-*n*-octyl phthalate and diisodecyl phthalate had a slightly higher limit of detection of 0.1 %. Both studies were able to demonstrate that the detection of additives could be conducted from intact polymer samples or liquid extracts which required minimal time for preparation. Compared to traditional verification techniques which may exceed 16 h for preparation alone, complete analysis with DART took only 8 min.

Environmental contaminants such as polycyclic aromatic hydrocarbons (PAH) are insoluble and incompatible with many typical analysis methods. DART was able to quickly (3-5 s sample^{-1}) screen for pure PAHs off of melting point capillary tubes.[47] The protonated molecules of 1,2,5,6-tetrabromocorannulene (*m/z* 566.7236), diacenaphtho[1,2-*a*:1',2'-*g*]-corannulene (*m/z* 499.1484), diphenanthro[9,10-*a*:9',10'-*g*]-corannulene (*m/z* 551.1797), tetraindenocorannulene (*m/z* 547.1502), decachlorocorannulene (*m/z* 594.6904), 1,3,5,7,9-pentachlorocorannulene (*m/z* 421.8809) and *peri*-bis-dibenzo[*a,g*]corannulene (*m/z* 697.1947) were detected with mass accuracies better than 3 ppm. Protonated molecules and molecular ions were also detected from headspace vapor from organometallic compounds containing As, Fe, Hg, Pb, Se and Sn.[48] Additionally, protonated metal ions for some of the compounds were observed. For

example, tetraethyllead sampled in helium showed the protonated lead ion (*m/z* 209) in addition to the molecular ion of ethyllead (*m/z* 237), protonated diethyllead (*m/z* 267), the molecular ion of triethyllead (*m/z* 295) and the water adduct of the protonated molecule (*m/z* 343). Sulfur containing species in drywall products were detected in negative ion mode.[49] S_2^- (*m/z* 64), SO_3^- (*m/z* 80) and S_3^- (*m/z* 96), amongst others, were only detected from samples of drywall made in China.

The high-throughput surface sampling qualities of DART have been exploited for forensic pharmaceutical drug screening. The detection of counterfeit antimalarials with DART has also been performed and briefly reviewed previously in the DESI applications section.[50] In a validation analysis of illegal drugs,[51] limits of detection for target compounds (heroin, alprazolam, cocaine, testosterone propionate and trazodone) were determined to be 0.05 mg mL^{-1}. Then, 553 case specimens were tested by DART and compared to GC MS. For identification/screening purposes the results for all but one sample were identical. The one sample exception contained heroin and the unusual cutting additive yohimbine ($[M+H]^+$, *m/z* 355.2001). Although this ion does not interfere with the detection of heroin ($[M+H]^+$, *m/z* 370.1654) *per se*, the isotopic (^{13}C) peak of an unidentified concomitant species at *m/z* 369.2147 positively interfered.

The pharmaceutical industry has utilized DART in preclinical trials and for the quantitation of drugs in biological fluids. For example, photo degradation analysis of encapsulated photosensitive active ingredients was completed with DART.[52] Although the active ingredient was not identified in the text by name, the corresponding protonated molecule and dimer were detected in control (not exposed to UV light) and exposed in different capsule colors (white, orange and green, increasing in UV protection). A

degradation product was detected in UV-exposed capsules with relative increases in intensity corresponding to the lowest protective colors (white and orange) compared to the green colored capsule where the degradation product ion was detected in very low levels. Similar experiments would take hours with LC-UV analysis. The same study also demonstrated that a similar improvement in throughput could be achieved for the determination of specific activity of radio labeled compounds used in drug metabolism studies. Four isotopically labeled active ingredients showed very similar specific activities in both LC MS and DART. Less than a 5 % error was observed amongst the four samples with DART analysis. Additionally, DART did not require the addition of a solvent modifier for efficient ionization like in ESI. As a result, there was almost no radioactive waste to be concerned with after DART experiments.

Metabolite screening has been targeted by DART for rapid investigation of volatile and non-volatile compounds. An insect hormonal regulator in insects, juvenile hormone III and its corresponding terpene precursors farnesol, farnesoic acid and methyl farnesoate were detected to create a quick screening method for insect terpenoids.[53] Careful optimization of DART conditions resulted in detection limits ranging from femtomole to sub-picomole levels with accurate mass determination below 5 ppm. These merits would allow for detection of the compounds from the endogenous production in most insects. In-source collision-induced dissociation (CID) was used to distinguish between two farnesol isomers, an important merit since only one isomer is biologically active. When orifice one voltages were set between 40-80 V, the breakdown curves revealed that the fragmentation efficiency of the EE-farnesol isomer was greater than the

ZZ-farnesol isomer. The differences in fragmentation highlight the different configurations of the carbon-carbon double bond at C-2 of farnesol.

Traditional metabolomics screening methods using LC MS and GC MS require significant time to conduct the analysis. Alternative rapid techniques may allow for larger sample sets and replicates to be screened if the sample prep steps can be parallelized. In this context, DART human serum metabolomic fingerprinting was first developed and optimized[54] before implementation in a broader ovarian cancer detection study.[55] Optimized DART runs required as little as 1.2 min, however it should be noted that the method still required derivatization to increase the volatility of sample constituents. Throughout DART runs, more than 1500 different spectral features could be detected. These spectral features do not individually represent separate metabolites as some are most likely fragment and various adduct ion species. However, the quantity and the resultant detected overall peak patterns can all be used in building metabolite screening databases. Most importantly, a 4.1-4.5 % repeatability was obtaining using a custom built sampling arm to introduce samples for DART ionization.

In a pilot study, DART metabolomic fingerprinting of blood serum samples from 44 patients diagnosed with serous papillary ovarian cancer (stages I-IV) and 50 healthy patients with or without benign conditions were differentiated.[55] Samples were subject to protein precipitation and derivatized by silanization prior to analysis. The predictive performance of the DART mass spectra was evaluated through a 64-30 split validation with and without different feature selection methods and with leave-one-out cross validation. Modified support vector machine models were used to obtain predictive rules. One hundred and fifty three estimated elemental formulae were obtained by accurate

mass measurements which were tentatively mapped to 25 metabolic pathways. The method was able to distinguish between cancer and control groups with 99-100 % accuracy. This study demonstrated the potential powerful role that DART screening can have as a diagnostic tool, but more samples are required to further validate these findings and to translate this approach into a routine clinical tool.

1.5. Conclusion

The extensive list of newly developed ambient MS ionization techniques has sparked significant interest and new applications in the field of analytical MS. One technique in particular, DART, offers not only the advantages of speed and ease-of-use, but may be instrumental in the continuing growth of specific fields such as rapid quantitative screening. Further, it is expected that DART will continue to contribute to established fields like environmental monitoring, homeland security and food safety along with emerging fields such as metabolomics. Nevertheless, much remains to be learned about the fundamental mechanisms and properties of DART which should allow for the discovery of new applications and the optimization of existing methods.

CHAPTER 2. SIMULATIONS AND EXPERIMENTAL INVESTIGATION OF ATMOSPHERIC TRANSPORT IN AN AMBIENT METASTABLE-INDUCED CHEMICAL IONIZATION SOURCE

2.1. Abstract

A prototype metastable-induced chemical ionization source (MICI) was designed and constructed to perform some of the first fundamental experiments investigating DART. Specifically, atmospheric transport of desorbed molecules and ions was probed in a strictly designed manner and compared to static finite element method fluid and thermal dynamic and SIMION ion trajectory simulations. The complex coupled fluid dynamics, heat transfer, and electrostatic phenomena within the sampling region all contribute to the variability in ion transmission efficiencies and ultimately, the overall sensitivity of analysis. Particle tracing plots mapping neutral particles on the outer perimeter of the simulated tablet in different positions and orientations yielded insight into optimal sample placement and evidence for sweet spots conducive to better ion transport. Experiments in a wide range of electric field conditions were performed revealing that under optimum sample placement, sensitivity could be improved if ion mobility contributions were minimized.

2.2. An Introduction to Direct Analysis In Real Time

2.2.1. Physicochemical Properties of DART

Generally absent from the discussion of DART ionization are the phenomena affecting ion transport within the ionization region and their influence on sensitivity and

reproducibility. Heat dissipation from the helium gas stream and from the ion source itself should result in marked temperature gradients. These gradients not only can affect the energy transfer rates that surface-bound analytes are exposed to, but also produce convective currents which are superimposed to the forced gas flow from the ion source outlet. From the practical point of view, two sources of signal variance are tightly coupled to these transport phenomena: (a) the sample orientation and relative position with respect to the convective gas flow lines and (b) the sample proximity to the ion source inlet resulting in different placements within the thermal gradients and variable heating. Commercial and home-built sample introduction devices have been implemented to aid in reproducible sample positioning within the ionization region maintaining these sources of variability constant,[17, 19, 56-61] but no rationale yet exists as to which sample placement and orientation are preferable in terms of analytical performance.

In addition to convective gas fluid dynamics and thermal gradients, ions within the DART ionization region are exposed to the electric field created between the exit grid electrode and the mass spectrometer inlet. Under atmospheric pressure, this field impinges an additional electric force onto the ions, which is balanced by drag forces generated while traveling in and colliding with gas molecules in the fluid media.[62] Although the electric fields are mild compared to those used in other atmospheric pressure techniques such as electrospray ionization, the extent to which these contribute to atmospheric ion transport also remains unexplored. This is partly because the combined contribution of electric mobility, diffusion and convection makes modeling ion motion under atmospheric pressure conditions computationally intensive and more

cumbersome than in vacuum.[63] Recent advances in this field include the modeling of ion transport in atmospheric pressure drift cells[64] and ion mobility spectrometers[65] using advanced SIMION[66] ion optics simulations.

2.3. Experimental

2.3.1. Instrumentation

A DART-type metastable-induced chemical ionization ion source was built in house so the physical dimensions and gas flows were accurately known and could be modeled by finite element simulations. This ion source consists of three regions (Figure 2.1, top panel): (i) gas inlet and corona discharge, (ii) gas heating, and (iii) grid electrode/ion source exit. The gas inlet (5 cm o.d., 1 cm i.d.) and ion source exit (3.5 cm o.d., 0.7 cm i.d.) regions were constructed out of Macor (Astro Met Inc., Cincinnati, OH). The glow discharge (4.5 cm o.d., 2.5 cm i.d.) and plasma heating (1.5 cm o.d., 1.25 cm i.d.) regions were constructed out of stainless steel (McMaster-Carr, Atlanta, GA). A tungsten corona discharge needle (2.8 cm long, 0.1 cm o.d., sharpened to a tip) was secured internally within the glow discharge region.

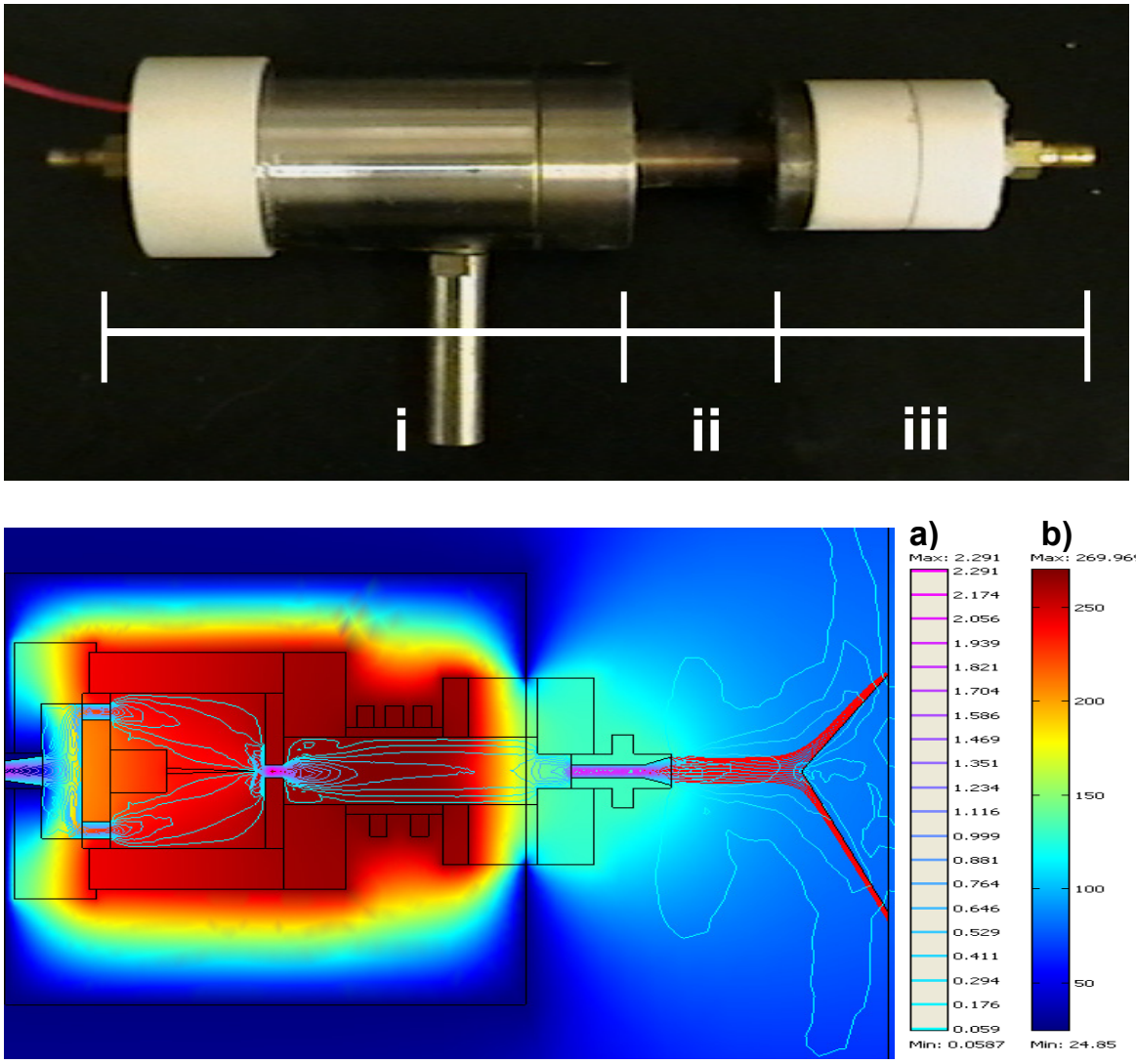

Figure 2.1: Top panel: Photograph of the uninsulated ambient metastable-induced chemical ionization source. Device regions: (i) gas inlet and corona discharge (7.5 cm long); (ii) plasma heating (2.0 cm); (iii) grid electrode/plasma exit (3.5 cm). Bottom panel: Two-dimensional representation of the ion source depicting: (a) temperature gradients of both the ion source and environment (ºC), and (b) gas velocity contour map (m s^{-1}). The purple to light blue lines correspond to the gas velocity contour map, while red lines represent simulated gas streamlines denoting directional flow of the exiting gas.

The discharge was established between a 1.2 cm gap separating the needle and the grounded stainless steel chamber housing it. A single steel grid electrode (0.6 cm o.d., McMaster-Carr, Atlanta, GA), necessary for filtering ionic species produced in the corona discharge was held between the two Macor plates in the exit region. Glow

discharge and grid electrode voltages were supplied via model 10R and 03R high voltage power supplies, respectively (Bertran Associates, Inc., Hicksville, NY). A 1.0 MΩ ballast resistor was placed in series with the corona discharge high voltage power supply. A rope heater wrapped around region (ii) (not pictured, Omega Engineering, Inc., Stamford, CT) was connected to a Thermoworks temperature controller (Cole Palmer Co., Vernon Hills, IL) while a RTD temperature sensor element (Omega Engineering, Inc., Stamford, CT) monitored the temperature for consistent heating. Aluminum-lined fiberglass insulation was tightly wrapped around the ion source to minimize heat losses. Focusing of the heated gas stream was facilitated via a male-to-male straight type brass tube fitting (Swagelok, Solon, OH) attached to the front Macor plate of the exit region. The helium gas flow was controlled with a Scienware Riteflow® 150 mm Flowmaster flow controller (Bel-Art, Pequannock, NJ).

2.3.2. Computer Simulations

Schematics of the metastable-induced chemical ionization source were translated into a two-dimensional cross sectional geometry file in the computer aided design program within the COMSOL Multiphysics® (COMSOL, Inc., Burlington, MA) finite element analysis environment. This geometry file was imported into the heat transfer convection-conduction and the incompressible fluid dynamics Navier-Stokes steady-state models within COMSOL. Material properties of the ion source components were selected from a predefined built-in materials database. Modeled flow rate and temperature settings were those used in routine DART experiments performed in our lab using a commercial DART ion source (IonSense Inc., Saugus, MA) as detailed below. All models were built in the absence of electric fields as discussed in the results section. Virtual pharmaceutical

tablets were placed at various positions and orientations with respect to the ion source gas outlet. Particle tracing plots were generated from twenty particles randomly placed on the external perimeter of the virtual tablet surface by the finite element modeling software. The temperature of the simulated surrounding environment was fixed to 23.6º C. The influence of the reduced pressure transport originating at the inlet of the mass spectrometer was neglected.

Electric field electrostatic modeling was performed in SIMION 7.0 (SIS, Ringoes, NJ). The SIMION geometry file modeled both the circular grid electrode and the atmospheric pressure MS inlet cone to the best possible exactness. The only irregularity to the simulated geometry was the exclusion of the small orifice of the inlet cone. Electric field values were obtained along a simulated ion flight path from the center point of the gas exit of the ion source to the tip of the inlet orifice. The reduced ion mobility constants (K_0) for protonated acetaminophen species used to calculate the electric field-dependent ion velocities were obtained from the literature.[67]

2.3.3. Procedure

Time-of-flight mass spectrometric analysis was performed with a JMS-100TLC (AccuTOF™) orthogonal mass spectrometer (JEOL, USA, Peabody, MA). The metastable-induced chemical ionization source was aligned with the MS orifice to match the latitudinal and longitudinal geometry spacing from the reference COMSOL computer model. All experiments were performed in positive ion mode. Ion optics settings were as follows: inlet orifice voltage: 30 V (unless stated otherwise), ring electrode voltage: 5 V, orifice 2: 5 V, ion guide bias voltage: 29 V, ion guide peaks voltage: 300 V. The detector voltage was set to 2650 V. The DART-type ion source settings were as follows: helium

gas (7.1 L min^{-1}), heater temperature: 270º C, glow discharge needle voltage: 1000 V, grid electrode voltage: 250 V (unless stated otherwise), distance between ion source and the spectrometer inlet: 3 cm. Mass calibration was performed by placing a 1.5 mm o.d. x 90 mm long glass capillary dipped in PEG in front of the helium stream for 60 s, and obtaining a reference mass spectrum. Glass capillaries inserted into the acetaminophen tablets were used to hold them manually in place, increasing the stability and reproducibility of sample positioning. Tablets were held into the sampling region for 60 s. The last 10 s of data following signal stabilization were averaged and used for all steady-state sensitivity studies. Mass spectral data processing, calibration, and background subtraction were performed using the built-in mass spectrometer software (MassCenter, v. 1.3). The voltages on both the exit grid electrode and orifice 1 plate were measured against ground. The temperature gradient within the sampling region was determined with an 80BK temperature probe connected to a multimeter (Fluke 179-True RMS, Everett, WA).

2.4. Finite Element Analysis of the Ionization Source

Finite element analysis is a widely used simulation approach in engineering. It is based on a numerical technique known as the finite element method (FEM), which evolved over several decades and was introduced in its present form in the late 1950's. Since then, it has been implemented as a robust mathematical modeling procedure to solve multivariate problems in a wide variety of disciplines.[68] Briefly, a system is "discretized" into many subdomains of an unstructured grid. Partial differential equations termed shape functions relating to the variable of interest are solved for each grid element in an iterative manner to determine the solution of the non-linear equation system. FEM

accuracy can be increased by refining the model mesh, at the cost of increased computing requirements. Detailed explanations of FEM can be found elsewhere.[69-71] Software packages which combine FEM with computer-aided design have streamlined FEM analysis, enabling the simulation of heat transfer and fluid dynamics phenomena simultaneously, yielding insightful computer-generated graphics that facilitate the intuitive understanding of complex coupled systems.

Steady state FEM simulations provided a framework to investigate the gas flow velocity field (Figure 2.1a) and temperature gradients (Figure 2.1b) both within the ion source, and the ionization region between the gas outlet and spectrometer inlet cone. The heater temperature in the model was set to 270 ºC to correspond with the settings used in the experiments, and the fiberglass insulation cover was included in the simulation with a thermal conductivity value of 0.04 W m^{-1} K^{-1}. The maximum simulated temperature reached within the insulated model was 269.959 ºC suggesting negligible heat loss at the core of the ion source body, leading to efficient heating of the gas in the internal cavity of the ion source (Figure 2.1b). The highest temperature regions of the ion source were those closest to the heaters, and the temperature gradient was fairly uniform throughout the ion source body until these parts contacted the non-insulated ceramic ends in the gas inlet and outlet regions. There, heat losses and convective cooling due to the forced helium flow were observed. Although low thermal conductivity (1.46 W m^{-1} K^{-1}) machinable ceramic was used in the fabrication of the gas outlet region, FEM models showed that the non-insulated portion of the ion source still dissipated a certain amount of heat into the surrounding environment. The gas temperature within the ionization

region was much lower than the setting chosen for region (ii), and pronounced temperature gradients were observed in this region.

The velocity contour map describes the gas flow through the ion source (blue and purple lines, Figure 2.1a). As expected, the flow through the ion source was at a higher velocity through geometrically narrower passages (purple lines) as opposed to lower velocity regions that were unobstructed and open (light blue lines). The magnitude of the gas velocity at the ion source exit was computed to be 1.05 m s^{-1}. Simulations also indicated that gas streamlines (red lines) flowing upwards were more numerous. The most logical explanation pertains to the generation of a lower gas density region as a result of the heated helium gas and the dissipated heat from the ion source, resulting in a pocket of higher-velocity upward gas flow above the ion source sampling region.

2.5. Combined Fluid-Thermal Dynamic and Electrostatic Simulations With Experimental Validation of the Spatial Variations Within the DART Ionization Region

In order to ascertain the combined role of temperature gradients and convective gas currents on ion transport, virtual pharmaceutical tablet samples were positioned along the ion source exit-spectrometer inlet axis. Qualitative particle tracing simulations were first generated for a tablet placed upright and 0.6 mm below the ion source exit-spectrometer inlet axis (Figure 2.2, top panel). Three cases were considered: (**x**) near the ion source exit, (**y**) half way between the ion source and inlet orifice, and (**z**) in close proximity of the inlet orifice (Figure 2.2, bottom). Simulated particles were initially placed on the tablet surface and allowed to be carried by the ionizing gas, flowing in the local environment in a path determined by the gas velocity field. The particles were

chosen to have negligible mass since it was assumed that the species leaving the sample surface are either ions produced by chemical sputtering or neutrals produced by thermal desorption. Particle tracing plots display path lines of particles that are visualized trajectories of particles in a fluid dynamic field. The motion of the particles in the simulation does not affect the modeled fluid dynamic flow field.

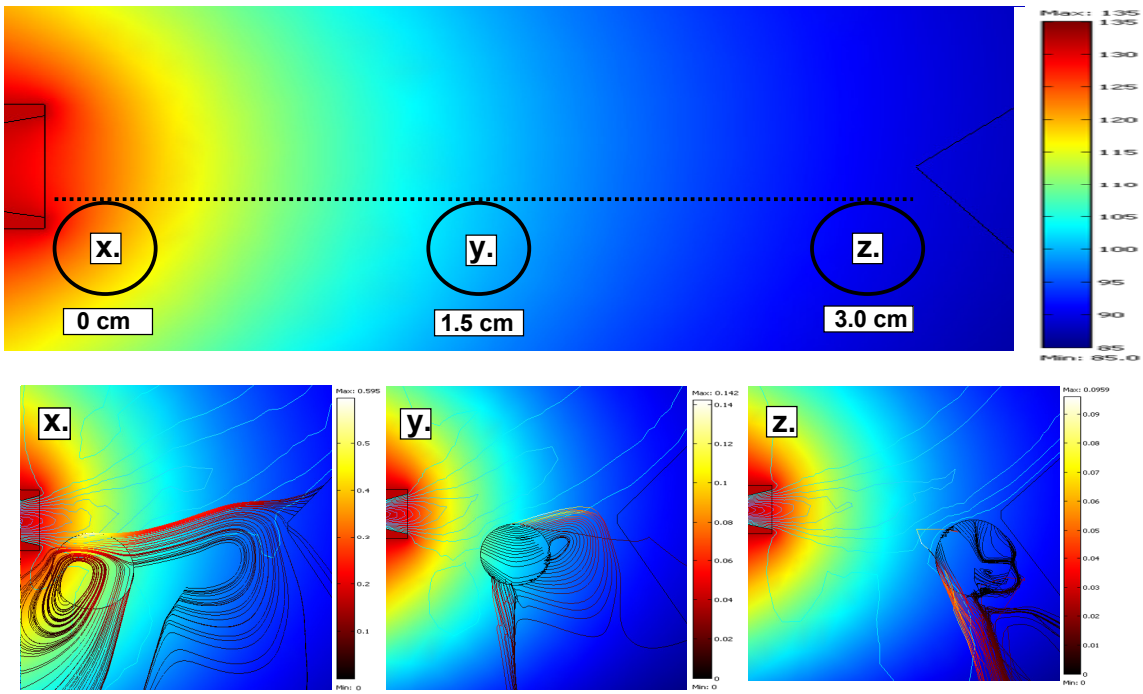

Figure 2.2: Zoomed image of the ionization region. Tablet positions correspond to the "upright-below" position at different distances between the ion source and inlet orifice: **(x)** adjacent to the ion source (0 cm); **(y)** between the ion source and the inlet orifice (1.5 cm); and **(y)** adjacent to the inlet orifice (3 cm). Legends on left show the temperature scale (above) and the particle velocity scale (m s^{-1}) (below).

Simulations showed that particle flow towards the inlet was the greatest when the sample was held in position **x**, compared to the positions **y** and **z** (Figure 2.2, bottom panels). Position **x** not only was conducive to the most efficient particle transport, but also exposed the tablet to the highest temperatures from the heat radiating off the ion source and the gas plume. This temperature was experimentally determined to be in the

124.2 - 116.9°C range measured on the left to right ends of the tablet, a finding that was also supported by the modeled thermal gradient (Figure 2.3). Particle flow simulations for position **y** showed a disadvantageous downwards particle flow, and exposure to lower temperatures (106.1 - 99.9°C, Figure 2.3), which may experimentally translate into reduced sensitivity. When the tablet was placed in position **z**, minimal particle flow towards the inlet orifice was predicted. This effect is attributed to the downwards streamline gas flow beneath the orifice depicted in Figure 2.1 (bottom panel). In addition, even less pronounced sample heating would be expected (94 - 90.1°C, Figure 2.3). The combined effect of these two phenomena should result in the lowest signal intensities. It was observed that some particles appeared to travel inside the virtual tablets. This is a mathematical artifact caused by the finite tolerance of the differential equation solver at the boundaries of the curved tablet surface. Lowering the tolerance factor decreased the apparent flow through the tablet. The lowest tolerance factor was used, but particle flow through the virtual tablets could not be completely eliminated, the power of our computing hardware being the limiting factor. Other limitations of these simulations include lack of three-dimensional information, and neglecting the suction from the spectrometer inlet. Despite these limitations, comparison of simulations and experiments showed the former to qualitatively describe ambient ion transport in the ionization region, as described below.

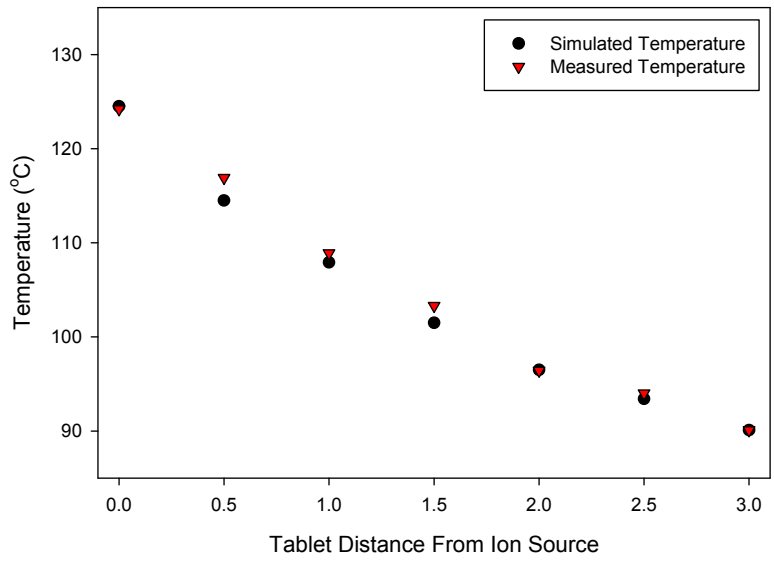

Figure 2.3: Simulated (black circles) and measured (red triangles) temperatures along the "below" sampling line.

The above simulations did not account from the forces exerted by the electric field formed between the perforated grid electrode and inlet orifice. Traditionally, a potential has been applied to the grid electrode to prevent ion-ion recombination, and to filter ionic species formed in the corona discharge.[2] As a first step to investigate the magnitude of the electric field repelling effect, SIMION simulations were utilized to model the electric field gradients of a system with a geometry corresponding to that of our setup. Figures 2.4 (a-f) depict the average electric field in the sampling region defined along the ion source-inlet axis. The calculated average values along this axis ranged from 0.0288 V cm^{-1} for a grid electrode voltage of 50 V to 18.6 V cm^{-1} for a grid voltage of 300 V. Based on these results, ion velocity magnitudes induced solely by the electric field were calculated using the literature value for the protonated acetaminophen ion reduced ion mobility (1.70 cm^2 V^{-1} s^{-1}), a laboratory atmospheric pressure (P) of 732.8

Torr, and temperatures (T) calculated at various points along the sampling region. The reduced ion mobility is directly related to the ion velocity (v) by:

$$K_0 = \frac{v}{E} \times \frac{P}{760} \times \frac{273}{T} \quad \text{(eq. 2.1)}$$

where

$$v = \frac{d}{t} \qquad \text{(eq. 2.2)}$$

and d is the distance traveled by the ion, E is the average electric field in a given point in space calculated by SIMION (Figure 2.4), and t is the time required to travel such a distance.

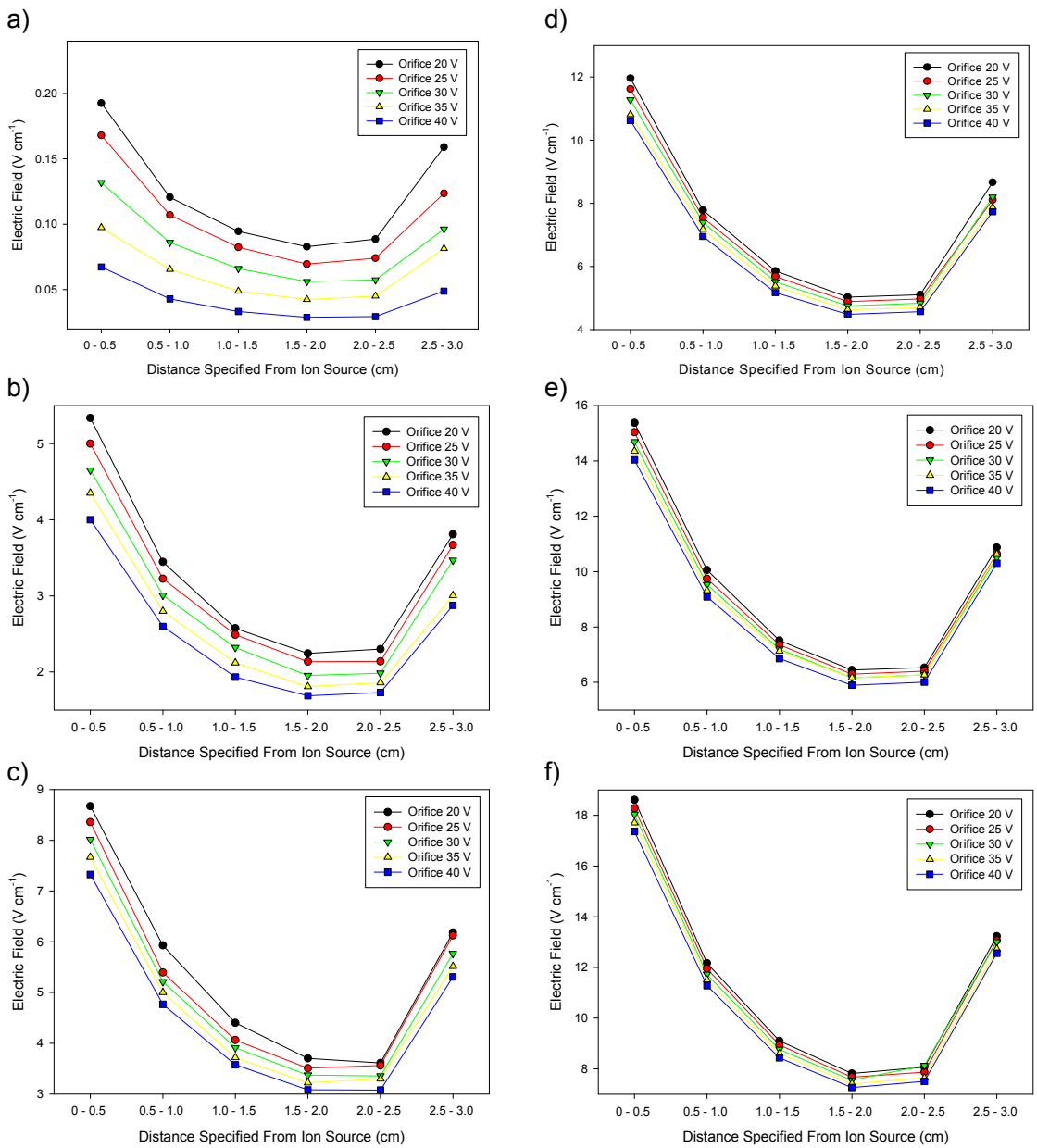

Figure 2.4: SIMION simulated electric field values on the straight line linking the center of the ion source gas exit and the orifice inlet cone at various grid potentials of (a) 50 V, (b) 100 V, (c) 150 V, (d) 200 V, (e) 250 V and (f) 300 V. In each case, these calculations were repeated for orifice potentials between 20 and 40 V.

The calculated ion velocity magnitudes under various conditions are shown in Figures 2.5 (a-e). Velocities ranged from $6.95 \cdot 10^{-3}$ m s^{-1} to $4.74 \cdot 10^{-1}$ m s^{-1}, and were greatest at the highest grid electrode potential and closest to the ion source exit or

spectrometer inlet. Under higher field conditions (grid voltages of 250 V – 300 V), the field-induced ionic mobility could be expected to be deleterious for sensitivity, as due to the conical shape of the inlet electrode, ions would be directed in trajectories not converging towards the orifice. If the sample is placed in an optimum position, it would be expected that lower field conditions (grid voltages of 50 V – 100 V) could result in improved ion transport driven mostly by fluid dynamics, and that this effect should be more marked for smaller ions, with higher K_0 values.

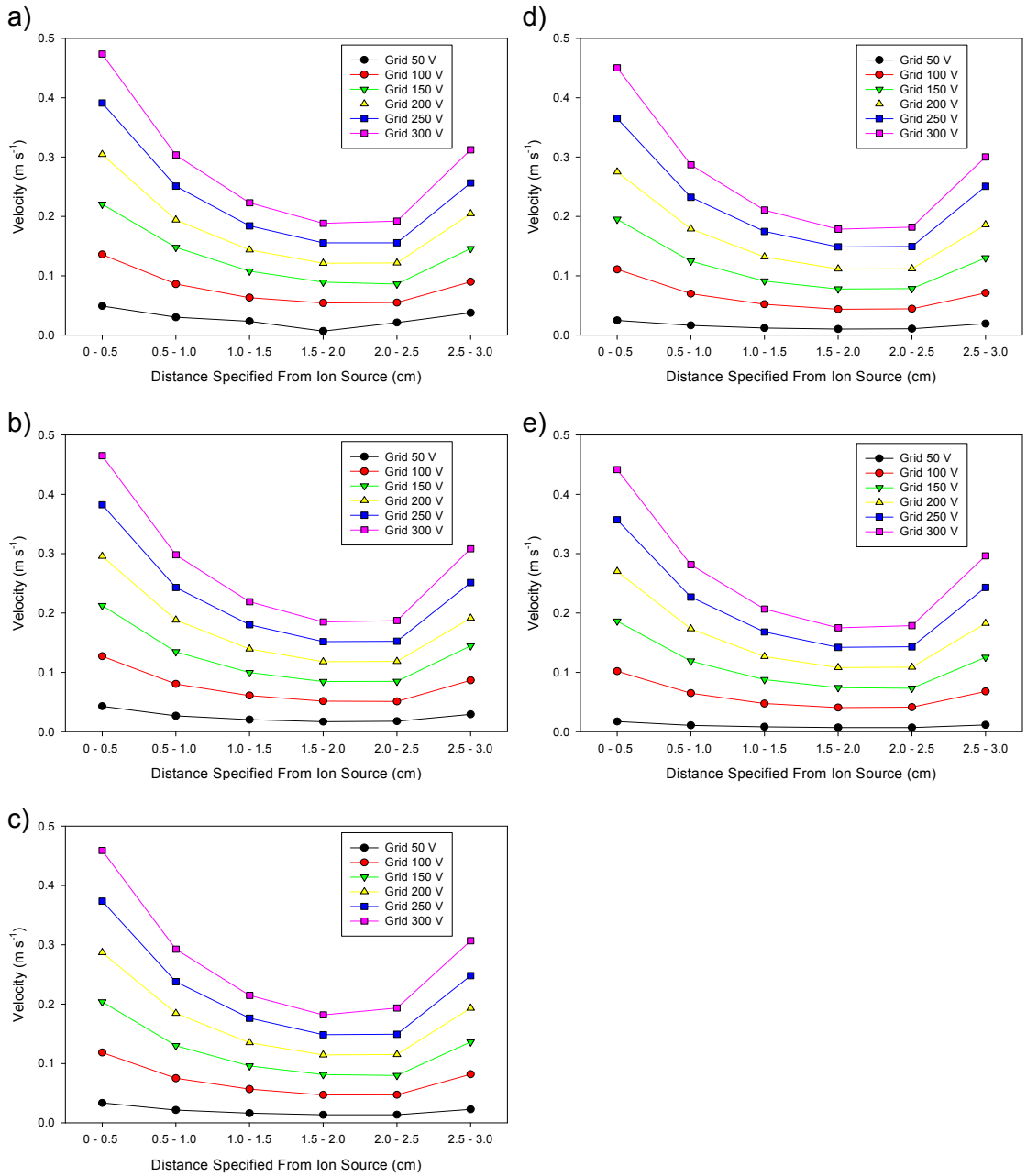

Figure 2.5: Calculated ion velocities in the ambient sampling region of a straight line between the center of the ion source gas exit and the spectrometer orifice inlet determined from the reduced ion mobility constant of the protonated acetaminophen molecule $[M+H]^+$ and SIMION-simulated electric field values at defined grid potentials, and at specified orifice potentials of (a) 20 V, (b) 25 V, (c) 30 V, (d) 35 V and (e) 40 V.

The overall contribution of the grid and orifice electrode potentials to the sensitivity for both the protonated acetaminophen molecule (Figure 2.6a) and dimer (Figure 2.6b) was experimentally explored for all electric field values previously modeled. Tablets were manually held in the "upright-below" position matching FEM simulations (Figure 2.2, bottom panel, **x**). Experimental results confirmed that sensitivity was greatly improved at lower grid and orifice voltages, both for the protonated monomer and dimer ions. These findings support the hypothesis of a decreased amount of focusing towards the orifice inlet when greater electrostatic forces are present.

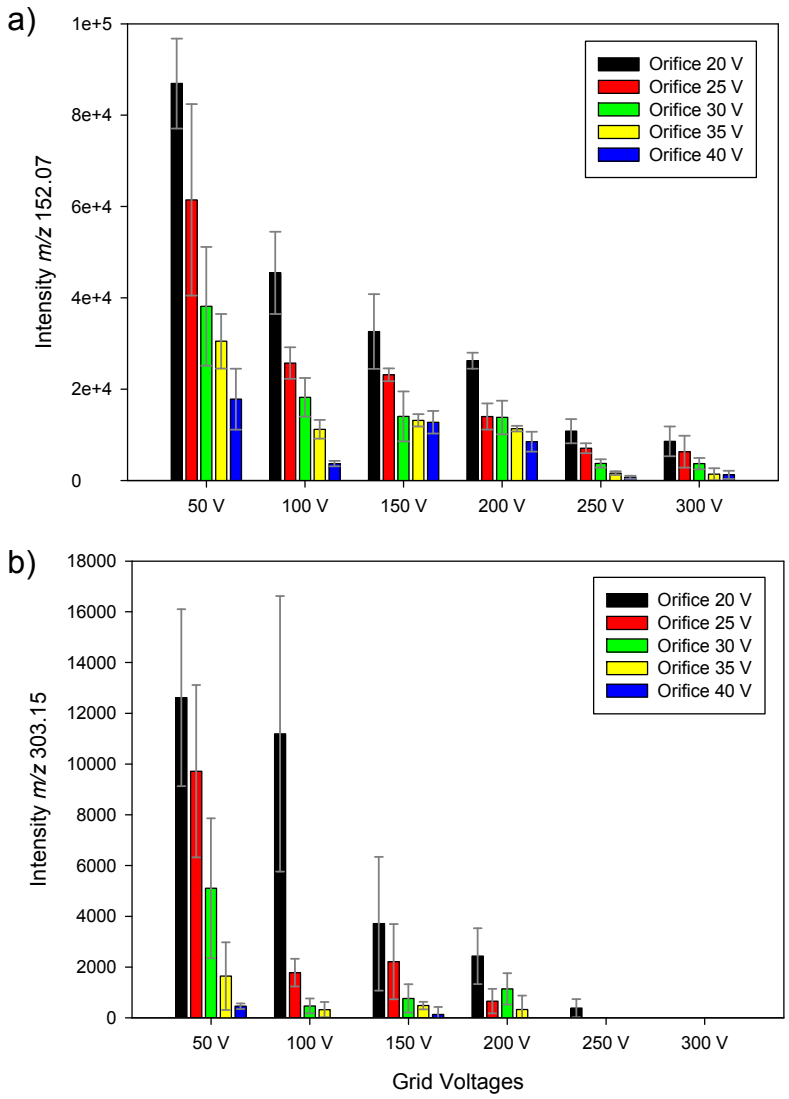

Figure 2.6: Experimentally determined intensities of the (a) protonated acetaminophen molecule $[M+H]^+$ and (b) protonated dimer $[2M+H]^+$ at specified grid and orifice potentials (n = 5). Fragment ions were not detected in any of the assayed conditions.

The sensitivity as a function of distance from the ion source under normal (grid 250 V, orifice 30 V) and low field (grid 50 V orifice 20 V) ion source settings is depicted in Figure 2.7 a and b, respectively. Sensitivity decreased with respect to increased distance from the ion source outlet, and at the higher grid and orifice electrode potential settings. The sensitivity in the upright tablet orientation of the acetaminophen protonated

molecule in the **x**, **y**, and **z** positions was improved under the low-field settings by 128%, 220% and 160%, respectively. The overall distance-dependent drop off in sensitivities under both normal and low-field settings can be attributed to both the decrease in net particle flow towards the inlet (Figure 2.2) and the decrease in the overall temperature in the sampling region (Figure 2.3).

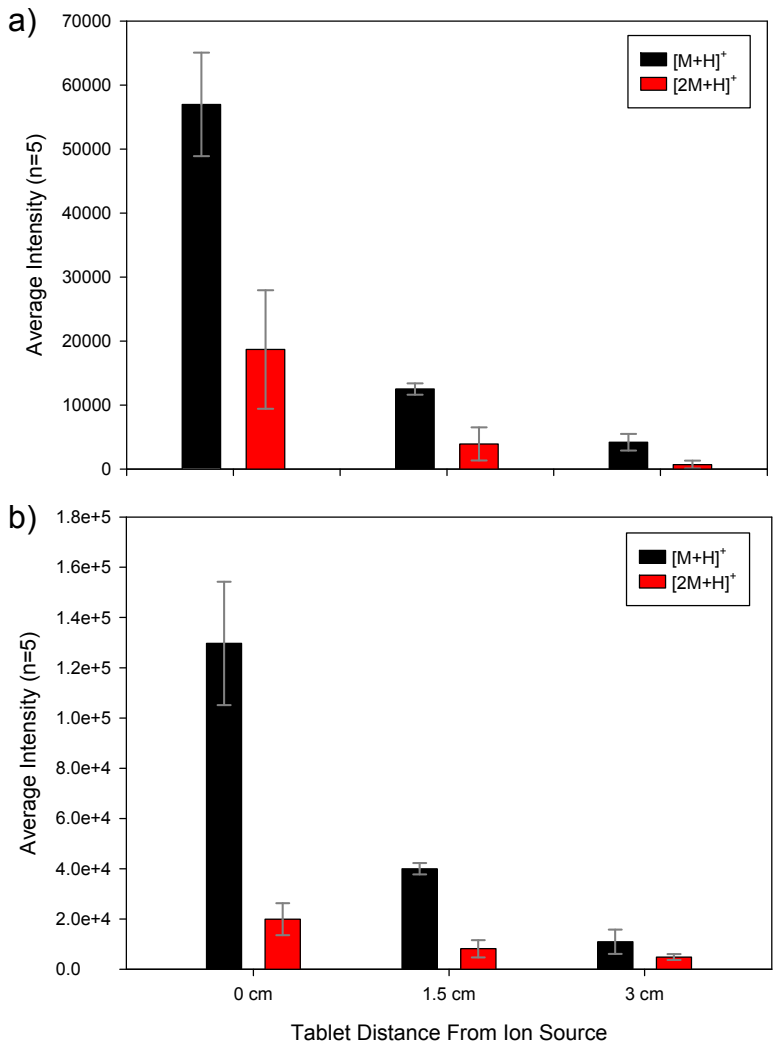

Figure 2.7: Distance-dependent sensitivity of the upright tablet orientation of both the acetaminophen protonated molecule $[M+H]^+$ and dimer $[2M+H]^+$ under (a) normal (grid 250 V orifice 30 V) and (b) low electric field (grid 50 V orifice 20 V) conditions for 5 measurement replicates.

2.6. The Role of Sample Geometry In Space On the Observed Experimental Sensitivities With DART

The previous findings confirmed that marked spatial variations in the local sampling environment exist within the ionization region. Different sample orientations within this region should also result in variable ion transport efficiencies. FEM models of a circular virtual tablet exposed to the helium stream emanating from the ion source were generated in multiple orientations and positions to further investigate this hypothesis (Figure 2.8). Three tablet orientations (left column: sideways, center column: flat, right column: upright), in three different heights respect to the ion source (above, inline, below) were modeled to reflect several possible sample placements in space. The "sideways" and "flat" sample geometries were represented by rectangles since this was the projected shape of a cylindrical tablet visualized from the side. The effect of the tablet curvature from this perspective can not be simulated in two dimensional models, and is a limitation of these simulations.

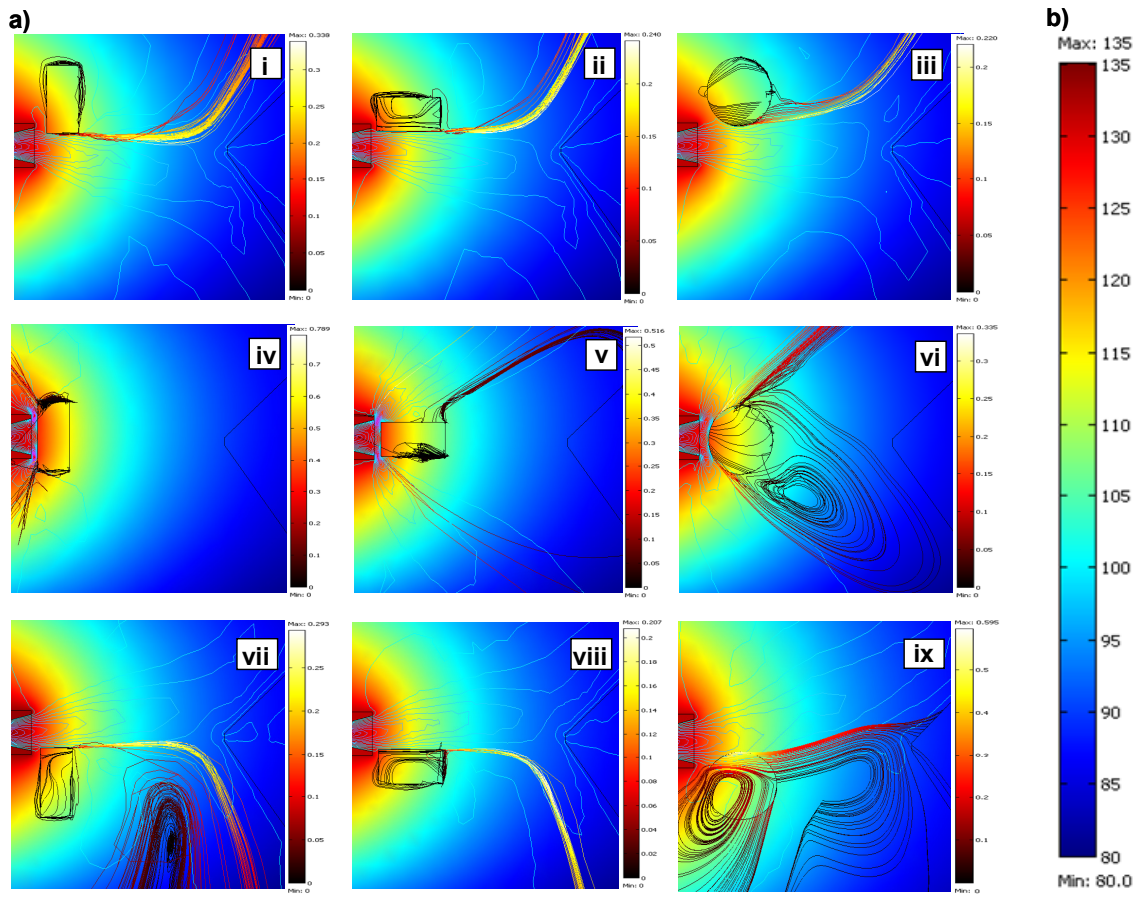

Figure 2.8: (a) Particle tracing simulations of circular tablets showing simulated particle velocities (m s^{-1}) and (b) temperatures (ºC). The temperature scale is shown in b). Top row: Above position for sideways (i), flat (ii) and upright (iii) orientations; middle row: inline position for sideways (iv), flat (v), and upright (vi) orientations; bottom row: below position for sideways (vii), flat (viii) and upright (ix) orientations.

Top row images depict the various sample orientations above the central sampling axis (Figure 2.8 i-iii). All three simulations portray no particles flowing towards the inlet orifice. Instead, particle flow was longitudinally upwards, as supported by the more numerous gas streamlines and gas velocity contour map previously described (Figure 2.1b). Low sensitivity is predicted for experiments with a sample placed in such positions. The middle row images have the samples directly in line with the gas outlet and inlet orifice (Figure 2.8 iv-vi). Particle flow again shows desorbed particles flowing

longitudinally upwards, similarly to the "above" sample position. Although tablet heating rate should be improved in this "inline" position due to the placement within higher-temperature areas, it should also result in little to no signal since the tablet was blocking most, if not all, helium gas flow towards the inlet orifice. The bottom row images represent sampling below the central line (Figure 2.8 vii-ix). Here, the greatest particle flow towards the mass spectrometer was observed. Simulation **ix** show particles traveling directly onto the mass spectrometer orifice, and simulations **vii** and **viii** have significant latitudinal (left to right) flow towards the inlet. There was also reduced upward particle flow, with many particles flowing longitudinally downwards. These models seem to suggest that a sweet spot exists where the position of the sample placed in the "below" position can be slightly adjusted to find a balance between the latitudinal and longitudinal flows, directing a greater percentage of particles into the mass spectrometer. In addition, the spiraling of particles in all the "below" sample positions may contribute to increased ion yield since particles are shown to recycle back into the ionization region by gas whirlpools, increasing their residence time, and the probability of reactive collisions with ionizing species. In summary, these simulations suggest the "below" position reflects the optimum situation for tablet sampling in terms of sensitivity.

Experimental validation of the previously described simulations was accomplished using acetaminophen tablets with identical dimensions as those utilized in the FEM models. Using normal (high field) ion source settings (Figure 2.9a and b), experimental results for five repeat measurements indicated that signal intensity was greatest in the "below" (**3**) position for both the protonated acetaminophen molecule (Figure 2.9a) and dimer (Figure 2.9b), in comparison to the above (**1**) and inline (**2**)

positions. Again, low field settings demonstrated a significant increase in sensitivity for both the protonated molecule (Figure 2.9c) and dimer (Figure 2.9d). An increase in sensitivity with the low field settings compared to normal settings at the various tablet positions and orientations occurs for both protonated molecule and dimer ions, respectively: **i)** 173% and 1853%, **ii)** 43% and 561%, **iii)** 150% and 367%, **iv)** 75% and 475%, **v)** 0% and 0%, **vi)** 59% and 88%, **vii)** 94% and 150%, **viii)** 23% and 45%, and **ix)** 128% and 7%.

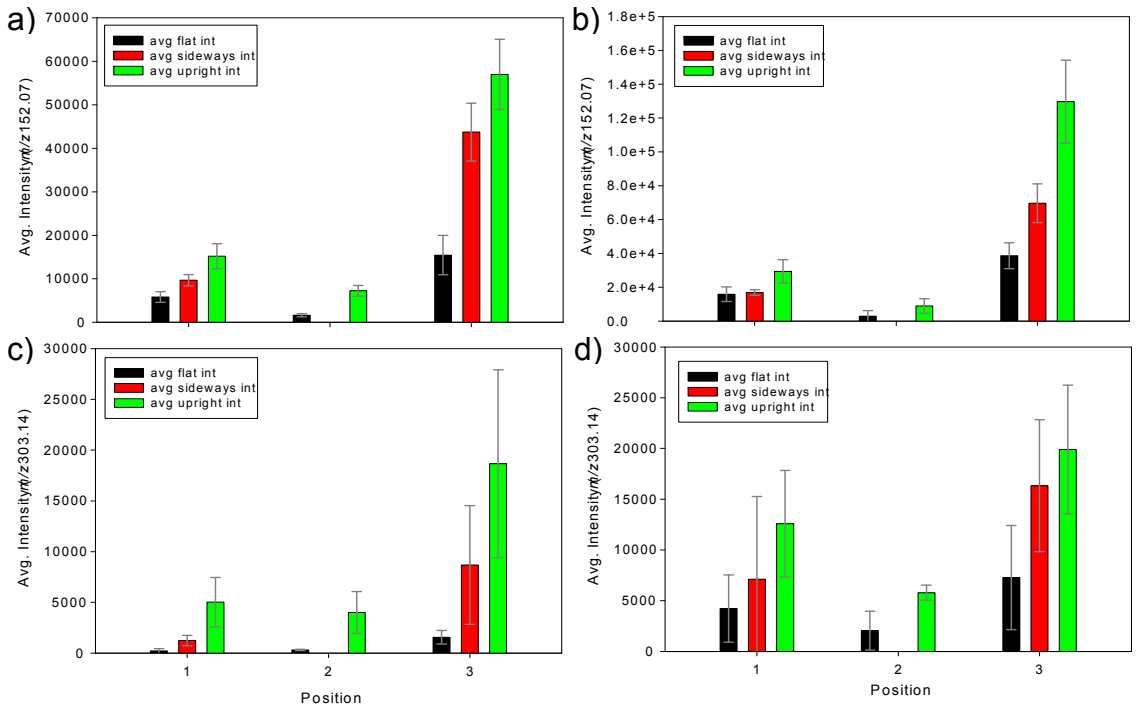

Figure 2.9: Average signal intensities of (a, c) acetaminophen protonated molecule (*m/z* 152.07) and (b, d) proton-bound dimer (*m/z* 303.14) for the flat (black), sideways (red), and upright (green) orientations in the above (1), inline (2), and below (3) positions under high (grid 250 V orifice 30 V, left panels) and low field (grid 50 V orifice 20 V, right panels) conditions. Error bars indicate the standard deviation of replicate measurements (n=5).

As the experiments and simulations demonstrate, orientation **ix** results in the greatest overall signal intensity, while any "upright" orientation results in greater signal

intensity for any given tablet position. This effect may be attributed to buoyancy of the hot gas flowing off the surface of the tablet affording the sample surface to be subjected to the gas plume in a position that facilitates maximum particle flow towards the mass spectrometer inlet orifice, while not being placed directly inline with the gas causing blockage and/or deflection of desorbed particles, or having desorbed species travel out of the ionization region.

2.7. Conclusion

The FEM simulations and validation experiments presented here provide a first insight into the complex coupled fluid dynamics, heat transfer, and electrostatic phenomena within the ionization region of an ambient metastable-induced chemical ionization ion source. These result in variable transmission efficiencies affecting the overall sensitivity. For the circular tablet geometry used in this study, we have found that placement close to the ion source outlet, in an upright position, and slightly below the centerline of the gas plume is most favorable for sampling. We have also confirmed, both theoretically and through direct experimental measurements, the presence of steep thermal gradients and electric fields within the ionization source region which could partially contribute to the lower ion yields at several positions along the axis linking the ion source outlet and the mass spectrometer inlet. Our simulations also suggest that there is still much room for improvement in terms of ion transmission for this type of ambient ion sources, which will certainly benefit from advances in ion focusing technologies effective under atmospheric pressure conditions.

CHAPTER 3. COMPARISON OF THE INTERNAL ENERGY DEPOSITION OF DIRECT ANALYSIS IN REAL TIME AND ELECTROSPRAY IONIZATION TIME-OF-FLIGHT MASS SPECTROMETRY

3.1. Abstract

This study aimed to improve the performance of DART by probing the energy transfer processes during ionization leading the fragmentation via "ion thermometry" experiments. The internal energy (E_{int}) distributions of a population of *p*-substituted benzylpyridinium ions generated by both DART and pneumatically-assisted ESI were compared using the survival yield (SY) method. As a whole, there was an increase in E_{int} with increasing gas temperature for both ESI and DART indicating thermal fragmentation of ions. Three-dimensional time resolved computational fluid dynamic simulations in combination with direct temperature measurements of the DART ionization region revealed complex inversely related fluid-thermal gradients which may affect ion E_{int} values during atmospheric transport. There was no evidence of E_{int} deposition pathways from metastable-stimulated desorption, but fragmentation induced by high-energy helium metastables was observed at the highest gas flow rates and temperatures.

3.2. Internal Energy Deposition

3.2.1. Internal Energy Deposition During Ionization

Uncontrolled ion activation within the ion source leads to an increase in the ions' E_{int}.[72] Defined by Vékey as the "amount of energy an ion contains above the ground

electronic, vibrational, and rotational states".[73] E_{int} is a significant factor in determining ion fragmentation yields.[74] The areas where ions receive unwanted E_{int} the most readily is during ion generation and the transmission from atmospheric pressure to the reduced pressure regions within the mass spectrometer through the atmospheric pressure inlet. It should be noted, that although ions can receive additional E_{int} within the mass analyzer portion of the instrument, this is usually a controlled process and does not affect the initial E_{int} of the ions. Therefore, it is beyond the scope of this chapter and will not be included.

When concerned with just the initial E_{int} deposition, the factors that must be taken into consideration are: 1) the E_{int} of the molecule before ionization, 2) the number of degrees of freedom of the molecule, and 3) the amount of energy deposited into the molecule during ionization and transmission. A *hard* ionization technique is one which deposits an excess of energy resulting in a spectra of extensive fragment ions from the precursor ion. Conversely, a *soft* ionization technique produces low E_{int} ions which are typically detected intact with little to no fragmentation. Soft ionization is typically desired for fragile organic and biological compounds including non-covalent complexes. Figure 3.1 a and b shows two spectra of reserpine when it is ionized by electron ionization (70 eV, hard ionization) and pneumatically-assisted ESI (soft ionization), respectively. It is clear with this example how the ESI spectrum is dominated by the intact protonated molecule whereas the electron ionization spectrum is filled with fragments which would make the identification of an unknown very difficult.

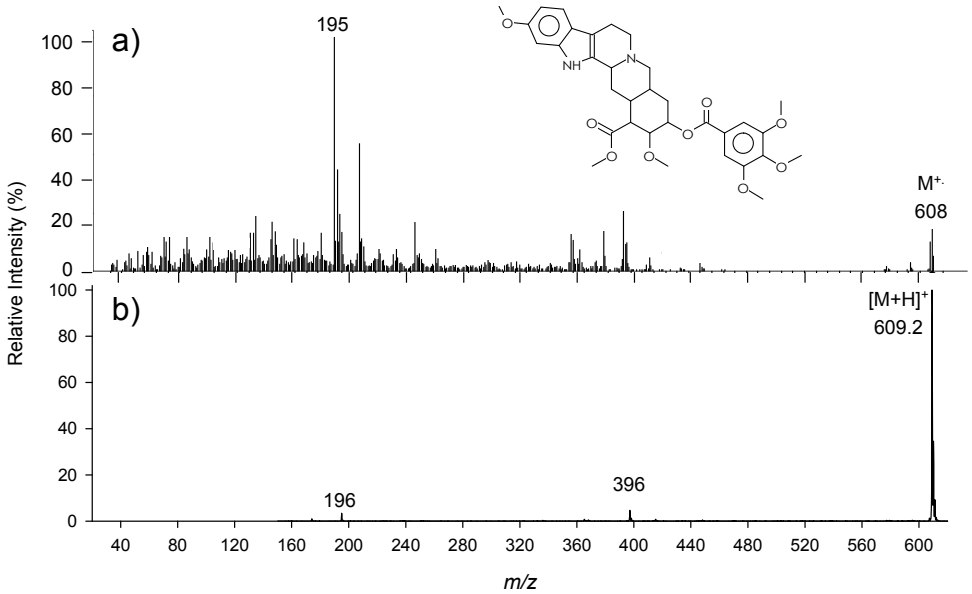

Figure 3.1. (a) electron ionization mass spectrum of reserpine showing $M^{+\cdot}$ and significant fragmentation (reproduced from the NIST database). (b) ESI-quadrupole ion trap mass spectrum of 1 μM reserpine in 50:49.9:0.1 (v:v:v) methanol:water:acetic acid showing $[M+H]^+$ and fragments at *m/z* 196 and 396 (10 μL min^{-1}, 5000 V_{DC}).

3.3. Experimental Determination of the Internal Energy Deposition

3.3.1. Synthesis and Preparation of Para-Substituted Benzylpyridinium Salts

The *p*-substituted methyl- (CH_3), chloro- (Cl), cyano- (CN), and nitro (NO_2) benzylpyridinium compounds were synthesized by condensation of the *p*-substituted benzyl halide with pyridine followed by recrystalization from diethyl ether as described by Katritzky *et al.*.[75] Pyridine, nitromethane, anhydrous diethyl ether, anhydrous ethanol, and the benzyl halide starting reagents were all used without further purification (Sigma-Aldrich, St. Louis, MO, USA). The methoxy- (OCH_3) substituted compound was purchased (Arkat USA, Inc. Gainesville, FL, USA). All samples were stored in a $^{-}$80 °C freezer when not in use to minimize degradation. For DART experiments, an equimolar thermometer ion mixture (100 μM) was prepared in nanopure water (Barnstead International, Dubuque, IA, USA), while for ESI experiments, a 1 μM mixture was

prepared in either a nanopure water or 50% methanol (Sigma-Aldrich, St. Louis, MO, USA) solution.

3.3.2. DART-MS Sampling, Instrumentation and Data Acquisition

DART samples were prepared by pipetting 5 μL aliquots of the sample mixture onto the tips of Dip-it™ sample capillaries (IonSense, Inc. Saugus, MA, USA) and allowing the drops to dry for 30 minutes. Sample deposition was repeated eight times so that a total of 4 nanomoles of each compound was deposited on the capillary. Capillaries were affixed to an in-house built sample holder attached to a hinged right-angle sample arm (Thorlabs, Newton, NJ, USA) for reproducible sample placement during all experiments.

MS analysis was performed with a commercial DART ionization source (IonSense, Inc. Saugus, MA, USA) and a JMS-100TLC (AccuTOF™) orthogonal acceleration TOF mass spectrometer (JEOL, USA, Peabody, MA). All experiments were performed in positive ion mode. Ion optics settings were as follows: inlet (orifice 1) temperature: 80 ºC, orifice 1 voltage: 20 V, ring electrode voltage: 10 V, orifice 2 voltage: 5 V, ion guide bias voltage: 27 V, ion guide peaks voltage: 300 V. The detector voltage was set to 2750 V. A lower orifice 1 voltage was required for DART than for ESI, since it improved sensitivity.[18] Preliminary experiments with DART at higher orifice 1 voltages (40 V and 60 V) resulted in overall low sensitivity, with the higher E_o ions remaining undetected, thus withholding the ability to conduct reliable E_{int} statistical calculations.

DART ion source settings were as follows: discharge needle voltage: 3600 V, discharge electrode voltage: 150 V, grid electrode voltage: 100 V, distance between ion

source and spectrometer inlet: 1.5 cm, distance of sample capillary to MS orifice: 0.60 cm, capillary depth below MS orifice: 0.16 cm, and capillary distance to the center of the DART gas nozzle: 0.74 cm (Figure 3.2). The rate of helium gas flow through the DART was 2, 4 or 6 L min^{-1}, and the set heater temperature was 175, 250 or 325 ºC.

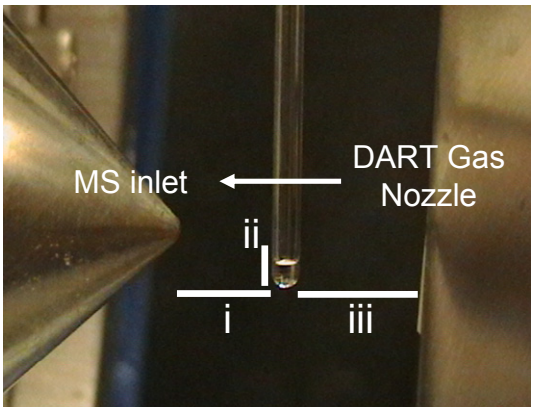

Figure 3.2: Sample placement for DART-TOF MS analysis of thermometer compounds. Samples were applied to Dip-it™ (diameter 0.16 cm) sample capillaries affixed to a stable sampling arm. Sample positioning distances: (i) center of MS orifice to capillary, 0.60 cm, (ii) capillary depth below center of MS orifice, 0.16 cm and (iii) capillary to center of gas outlet distance, 0.74 cm.

A solution of polyethylene glycol 600 (PEG, Sigma Aldrich, St. Louis, MO) prepared in 50% methanol was used as the mass calibration standard. A sample capillary dipped in the PEG solution was placed in front of the helium stream for 60 s, and a reference mass spectrum was obtained. Ultra high purity helium (99.999 %, Airgas, Atlanta, GA) was used in all DART experiments. Sample capillaries were held in the ionization region for 60 s. Mass spectral data processing, calibration, and background subtraction were performed using the built-in mass spectrometer software (MassCenter, v. 1.3). The temperature at the tip of the Dip-it™ capillary was determined with an 80BK temperature probe connected to a digital multimeter (Fluke 179-True RMS, Everett, WA). Ultra high purity nitrogen (99.995 %. Airgas, Atlanta, GA) was used following the

exact procedure as helium experiments, but only the low dissociation energy compounds (*p*-OCH_3, *p*-CH_3, and *p*-Cl) were detected in this case. This result made E_{int} calculations impossible due to the lack of data points on the fitted survival yield curves (see below). The lower vibronic metastable energy level of nitrogen, and its lower thermal conductivity are believed to be the primary responsible factor for the low sensitivity.[2]

3.3.3. ESI-MS Experiments, Instrumentation and Data Acquisition

For ESI-TOF MS experiments, the DART ion source mounted onto the TOF mass spectrometer was replaced by the a pneumatically-assisted micro-ESI source (JEOL, USA, Peabody, MA). In this source, the nebulizing gas flows orthogonally (pointing downwards) to the MS inlet orifice, while the drying (desolvating) gas is applied coaxially to the ESI needle assembly passing through a heated metal block (Figure 3.3) to enhance desolvation. All mass spectrometer settings were identical to those used for DART-TOF MS experiments, with the exception that the orifice 1 voltage was set to 50 V for ESI, the minimum setting that produced sufficient sensitivity. A 1 μM solution containing all five *p*-substituted benzylpyridinium compounds prepared in either nanopure water or 50% methanol was delivered to the ion source with a liquid handling pump (Valco Instruments Co., VICI M6, Houston, TX). For the 50% methanol solution, the flow rate used was 200 μL min^{-1}. Due to the difficulty of desolvating aqueous droplets, however, a lower flow rate (150 μL min^{-1}) was required to produce a stable spray from the aqueous solution. A 1:10 000 dilution of the PEG solution was used as the mass calibration standard. Ion source settings were as follows: desolvation and nebulizing gas: nitrogen (99.995%, Airgas, Atlanta, GA), desolvation gas flow rate: 1 L min^{-1}, nebulizing gas flow rate: 2.5 L min^{-1}, desolvating chamber temperature: 175, 250 or 325

ºC, and needle voltage: 2500 V. Mass spectral data acquisition, processing, and calibration settings were identical to those used in DART-TOF MS experiments.

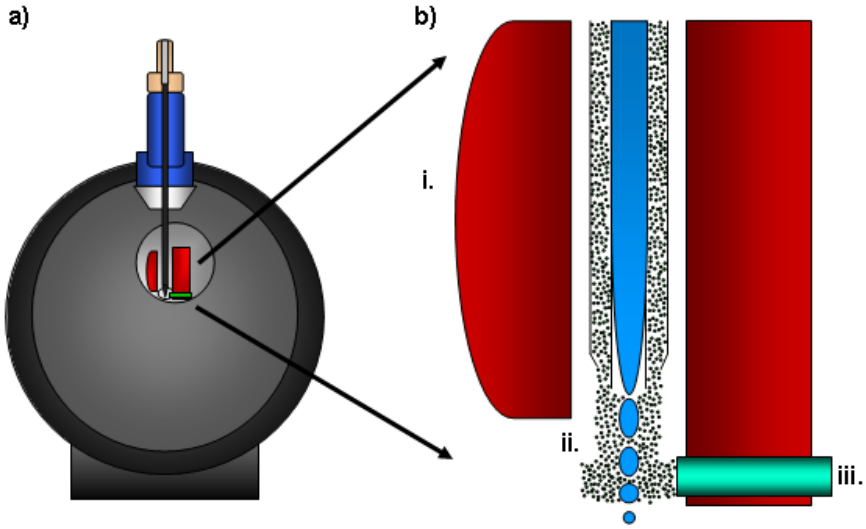

Figure 3.3: Schematic of pneumatically-assisted ESI source used in this work: a) cross-section view of the ionization source enclosure, and b) zoomed region of the desolvation chamber depicting the i. heating block, ii. electrospray needle with nebulizing gas, and iii**.** cross flow drying gas.

3.3.4. Survival Yield Method and Data Analysis

Because of the heterogeneity of the processes occurring in atmospheric pressure and ambient ionization, the extent of ion activation is better described by P(E), the normalized probability distribution that an ion has a given $E_{int.}$[73, 74] Many methods have been developed to determine P(E) including the "thermometer molecule" method,[76] the "deconvolution method,"[77] and the method used in this study, the "survival yield" (SY) method.[78, 79] The SY method assumes that: (1) all ions with E_{int} below a critical energy, E_o, do not dissociate and appear as intact ionic species, and (2) all ions with E_{int} above E_o will dissociate into fragment ions.[74, 80] Experiments are performed with a series of *p*-substituted benzylpyridinium salts with well characterized thermodynamic properties and a similar number of degrees of freedom. The prevailing fragmentation pathway

commonly observed for these salts is dissociation forming pyridine and a *p*-substituted benzyl cation at a known E_o (Scheme 3.1).

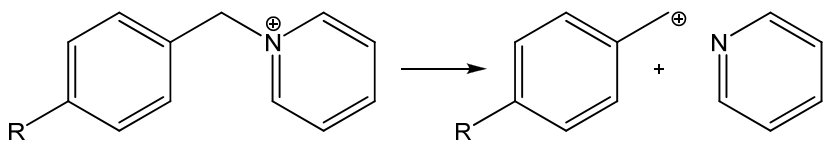

Para-substituted benzylpyridinium cation | Para-substituted benzyl cation | Pyridine

Scheme 3.1: p-Substituted benzylpyridinium cation structure and fragmentation pathway.

Following ionization, the ratio of the precursor (I_{prec}) and fragment (I_{frag}) ion intensities is calculated (eq. 3.1).[78, 79]

$$SY_{Exp} = \frac{I_{prec}}{I_{prec} + I_{frag}} \qquad \text{(eq. 3.1)}$$

SY values are then plotted against their respective E_o and two points corresponding to a SY value of 0 at 0 eV (indicating that no precursor ions would survive if the associated critical energy was 0 eV) and a SY value of 1 at 3.5 eV (indicating that at high critical energies, no fragment ions would be observed) are added prior to fitting the curve to a sigmoidal function (eq. 3.2).

$$SY_{Fitted} = \frac{a}{1 + \exp^{-}\left(\frac{Energy - x_0}{b}\right)} = \int_0^{\infty} P(E)dE \qquad \text{(eq. 3.2)}$$

The SY_{Fitted} curve parameters, a, b, and x_0, are experimentally fitted variables. The E_{int} distribution is determined by taking the first derivative of the sigmoid curve, generating the P(E) curve. The mean E_{int}, $\langle E_o \rangle$, is then calculated by determining the centroid of P(E) (eq. 3.3).

$$< E_o > = \frac{\int_0^\infty E \cdot P(E) dE}{\int_0^\infty P(E) dE} \qquad \text{(eq. 3.3)}$$

For data analysis, spectra were averaged for one minute using the built-in mass spectrometer software (MassCenter, v. 1.3) and exported into Excel (Microsoft, Auburn, WA, USA). After manually selecting peak maxima for the ions of interest, and calculating survival yields of each (eq. 3.1), the data were treated with an in-house programmed macro in SigmaPlot (Systat Software Inc., San Jose, CA, USA) to fit the survival yields to a sigmoid curve and to calculate the residual error of the fit, E_{int} distribution, mean E_{int}, and the full width half-maximum of the distribution.

3.3.5. Computational Fluid Dynamic Simulations

A three-dimensional design geometry file was created depicting the accurate dimensions of the DART gas exit nozzle, sample capillary and MS inlet orifice with the computer-aided design program within the COMSOL Multiphysics® (COMSOL, Inc., Burlington, MA, USA) finite element analysis environment. The modeled flow rate settings matched those used in the DART experiments. All models were built in the absence of electric fields and without regard to the influence of reduced pressure transport originating at the inlet of the mass spectrometer. The relative spacing between the ion source gas outlet, sample capillary, and MS orifice used during DART analysis were incorporated into the model. Particle tracing plots were generated from forty particles randomly placed on the external perimeter of the bottom capillary tip by the finite element modeling software. Time-resolved simulations of the first 100 ms of sampling were performed on a dual Intel Xeon quad core (2.66 GHz) computer with 8 GB memory and 1.5 GB video memory. Simulations required between 0.5 and 18 hours

to complete depending on the chosen conditions, with higher flow rates requiring longer due to the increased complexity of the fluid dynamics. Due to the mechanical complexity of the ESI source, it was not possible to accommodate the computational demand necessary to generate equivalent simulations.

3.4. Determination of the Internal Energy Deposition of DART Compared to ESI

Various energy-depositing processes occur during DART ionization. For the thermometer compounds tested here, potential energy deposition pathways begin with the thermal desorption of the solid neutral salt into the gaseous phase (Scheme 3.2i). The neutral salt undergoes charge splitting to form the halide anion and the precursor cation via atmospheric pressure thermal desorption ionization (APTDI),[81] and/or the effect of the electric field established between the needle electrode, grid electrode, and the mass spectrometer inlet orifice (Scheme 3.2ii). Further activation of the precursor cation proceeds through additional heating (Scheme 3.2iii), reactive collisions with metastable He species (He*) (Scheme 3.2iv), and/or deposition of excess energy released during proton transfer from protonated water clusters (Scheme 3.2v).

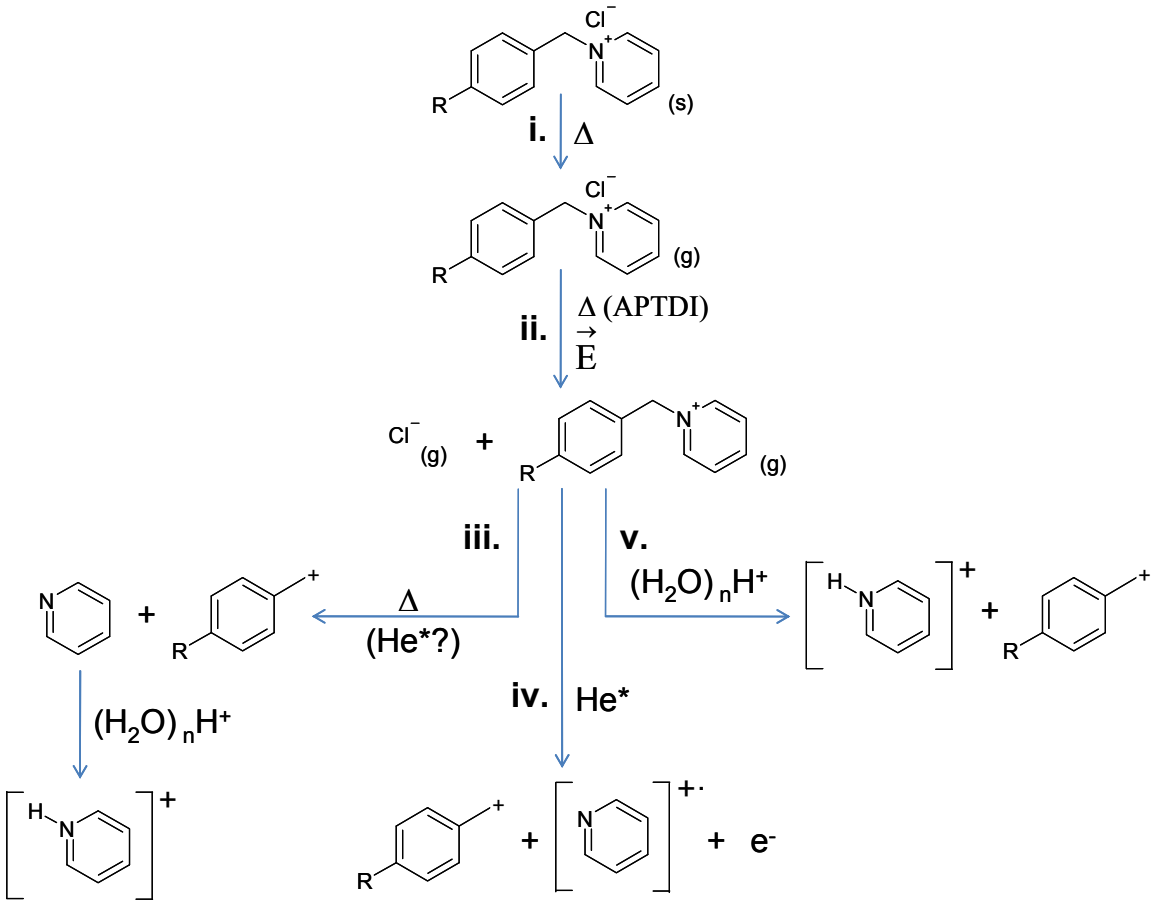

Scheme 3.2: Proposed energy deposition pathways for the compounds analyzed by DART-TOF MS.

At the lowest assayed helium gas heater (DART) or desolvating chamber (ESI) temperature set point (175 ºC), both aqueous and 50% methanol solutions probed by ESI had lower $<E_o>$ values (1.71 eV and 1.53 eV, respectively) compared to DART at all three gas flow rates tested (2 L min^{-1}: 1.92 eV, 4 L min^{-1}: 2.02 eV, and 6 L min^{-1}: 2.08 eV) (Figure 3.4a). In comparison to the softest ESI conditions with a 50% methanol solution, at 175 ºC, DART $<E_o>$ values were higher by 25%, 32% and 36% at 2, 4 and 6 L min^{-1}, respectively. The same trend followed at 250 ºC (Figure 3.4b), corresponding to DART $<E_o>$ values that were higher than 50% methanol ESI values by 30%, 34% and 38% at 2, 4 and 6 L min^{-1}, respectively. Furthermore, $<E_o>$ values at 325 ºC for DART (2

L min^{-1}: 2.09 eV, 4 L min^{-1}: 2.18 eV, and 6 L min^{-1}: 2.21 eV) were higher than the comparable experiments for the 50% methanol ESI values by 28%, 33% and 35% at 2, 4 and 6 L min^{-1}, respectively (Figure 3.4c). The shape of the E_{int} distributions displayed no asymmetric tailing at all temperatures tested.[82] These $<E_o>$ values indicated that under the tested conditions, ESI is a "softer" ionization technique compared to DART.

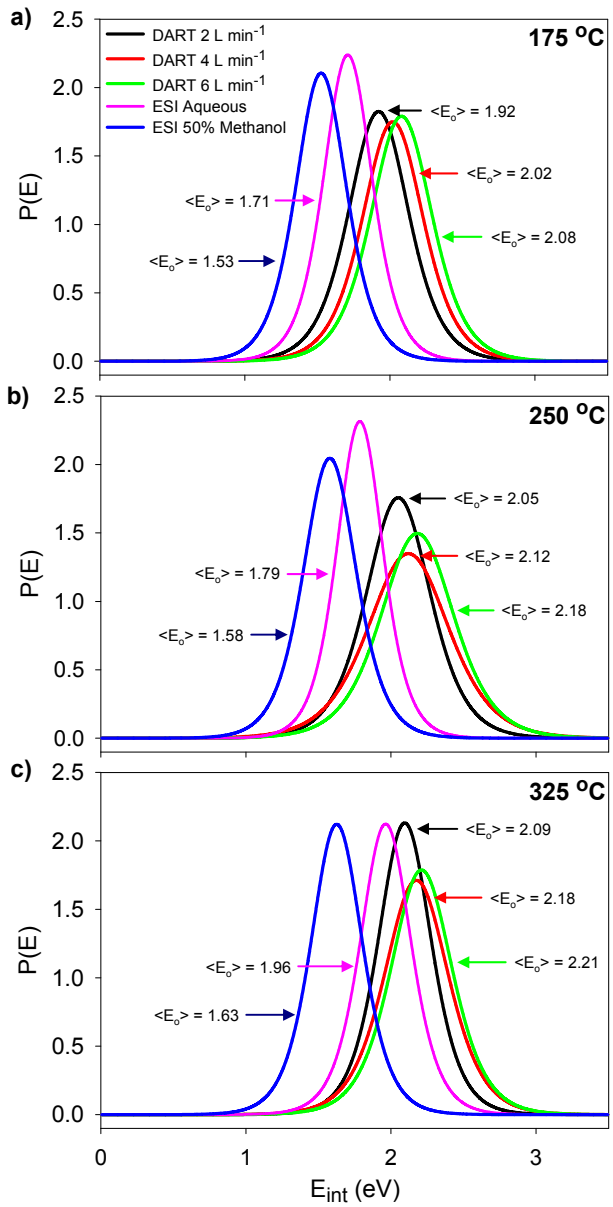

Figure 3.4: Mean E_{int} ($<E_o>$) distributions for DART and ESI with helium gas heater (DART) or desolvation chamber (ESI) temperature set points of a) 175 ºC, b) 250 ºC and c) 325 ºC.

The aqueous solution analyzed by ESI had higher $<E_o>$ values in comparison to the 50% methanol solutions by 12%, 13% and 20% at 175, 250 and 325 ºC, respectively. Due to the higher vapor pressure of methanol, droplets produced from a 50% methanol solution desolvate faster than aqueous droplets and cool more rapidly. The differences in E_{int} deposition observed between ESI experiments were consistent with prior investigations showing that P(E) could be altered by varying the solvent system vapor pressure, greatly affecting thermal and kinetic energy contributions.[78] Sprayed droplets acquire thermal energy by in-source heat conversion and friction with gas molecules to an extent that depends on droplet sizes.[78, 80, 83, 84] Kinetic energy from electric field-driven acceleration of charged droplets and ions can also be deposited into E_{int} modes, both in the atmospheric pressure region and within the various reduced pressure regions of the mass spectrometer interface.[74, 80, 85]

3.5. Thermal Activation Pathways of Internal Energy Deposition

In ESI, heated gas serves the role of improving charged droplet desolvation before entering the ion transfer optics region.[86, 87] This differs from the role of the heated gas used in DART experiments, which is to evaporate residual solvent and thermally desorb the analytes. If set high enough, high DART and ESI gas temperatures induce unwanted fragmentation of labile species. It is quite important to distinguish between the DART temperature set by software, and the actual temperature within the ionization region. Measured gas temperatures at the bottom of the sample capillaries rapidly decreased upon increasing the flow rate setting as a result of rapid convective cooling of the ionization source environment. Direct temperature measurements (Figure 3.5) indicated that the actual gas temperature was consistently lower than the set value, and that the difference

between the two increased with increasing flow rates. When the heater was set at 175 ºC (Figure 3.5a), the average steady-state gas temperatures at 2, 4 and 6 L min^{-1} were 163 ºC, 145 ºC and 136 ºC, respectively. This downward trend was the same for set temperatures of 250 ºC (2 L min^{-1}: 227 ºC, 4 L min^{-1}: 200 ºC, and 6 L min^{-1}: 187 ºC) (Figure 3.5b) and 325 ºC (2 L min^{-1}: 283 ºC, 4 L min^{-1}: 252 ºC, and 6 L min^{-1}: 236 ºC) (Figure 3.5c).

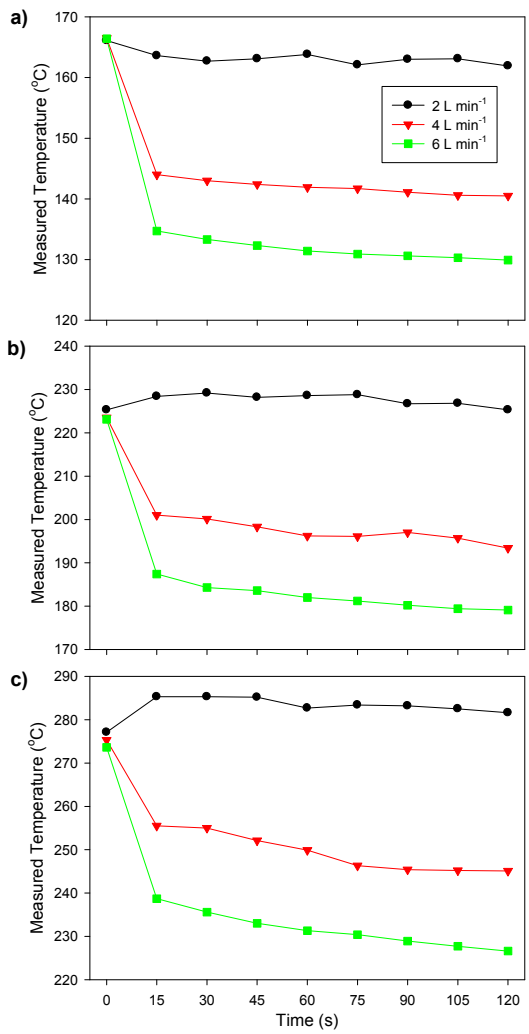

Figure 3.5: Measured gas temperature at the bottom of the sample capillary in the DART ionization region at experimental set temperatures of a) 175 ºC, b) 250 ºC and c) 325 ºC. Time t = 0 sec corresponds to the instant the gas flow is turned on in the preheated DART source.

The measured "effective" temperatures strongly influenced the extent of E_{int} deposition. Ions generated at a high flow rate (4 and 6 L min^{-1}) at any set gas temperature were created in a thermally cooler environment compared to those created at low flow rates (2 L min^{-1}). Ion formation in a locally cooler environment is expected to lead to a decrease in thermal-induced fragmentation.[82, 88, 89] Contour maps for the data in Figure 3.4 were created to assist in understanding the E_{int} deposition trends observed experimentally (Figure 3.6). The E_{int} contour map for ESI indicates a decrease in E_{int} deposition with increasing concentrations of methanol at lower temperatures (Figure 3.6a) as previously reported in similar work[78] and discussed above. The DART map shows that the least amount of energy was deposited at lower gas flow rates and temperatures (blue on the color scale), whereas the highest energy deposition occurred at high flow rates and set temperatures (orange and red color scale, Figure 3.6b). Because lower measured gas temperatures were found at higher flow rates, thermal ion activation could not account for the increase in E_{int} observed under those conditions.

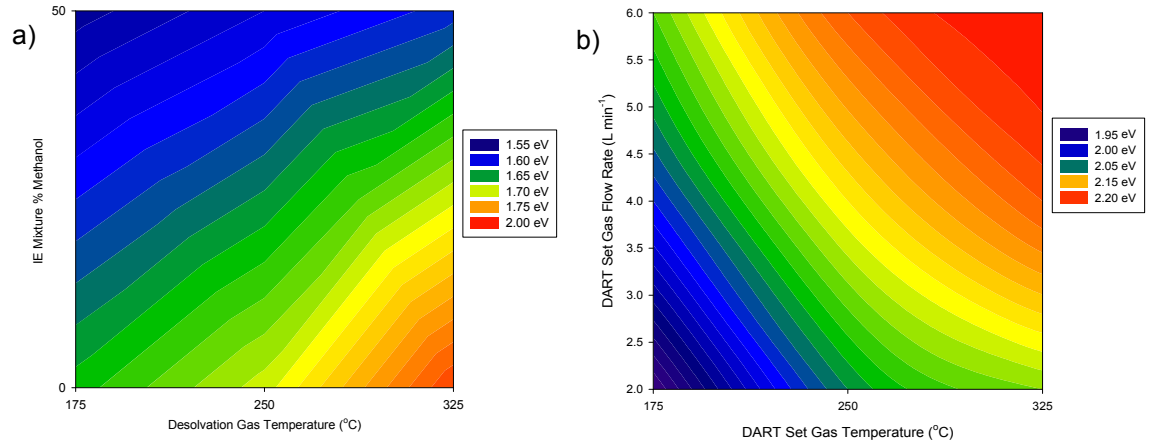

Figure 3.6: Mean E_{int} surface contour maps for a) ESI and b) DART. Temperatures plotted on the x-axis correspond to set temperature in the ion source control software.

Increase in $<E_o>$ may also result from the excess energy released during dissociative proton transfer reactions with protonated water clusters (Scheme 3.2v).[90] An increase in the intensities of protonated water cluster ions when increasing the set gas temperature was observed at all flow rates (Figure 3.7). At 175 °C (Figure 3.7a), 250 °C (Figure 3.7b) and 325 °C (Figure 3.7c), clusters with $n \leq 6$ were the most abundant. This suggests that the pathways shown in Scheme 3.2iii and 3.2v, may act concurrently. The abundance of clusters with $n \geq 8$ was observed to increase at low flow rates. This is to be expected, due to the increased hydrate thermodynamic stability at higher temperatures.[14] The trend was less clear for smaller hydrates. As a whole, however, the increase observed in protonated water cluster intensities as flow rate was decreased did not explain the changes in internal energy deposition.

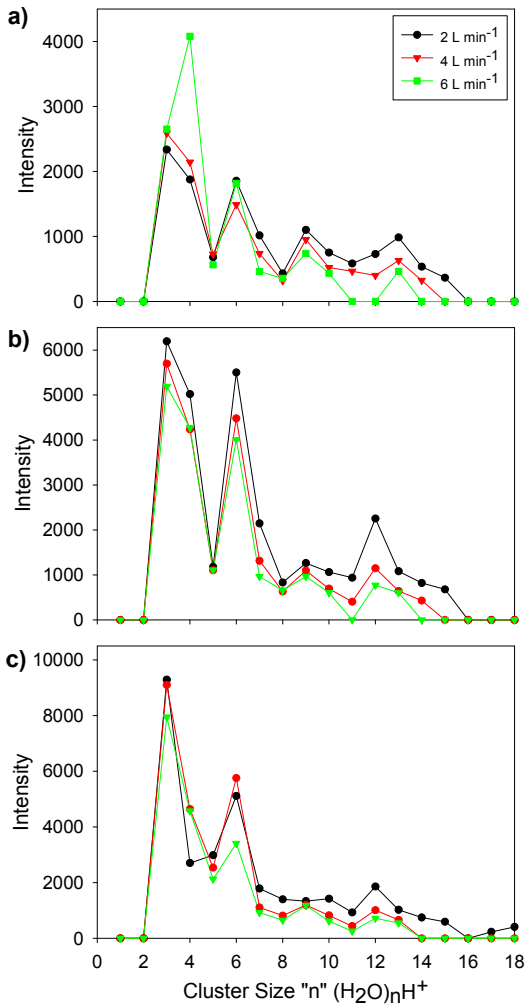

Figure 3.7: Observed absolute abundances of protonated water clusters with "*n*" water molecules ($(H_2O)_nH^+$) at set DART temperatures of a) 175 °C, b) 250 °C and c) 325 °C and different glow discharge gas flow rates. The electrical current on the discharge needle monitored from the DART controller software remained constant throughout these experiments.

This suggests that additional collisional activation during transit through the ion optics or other pathways, such as that shown in Scheme 3.2iv, may play a significant role in further determining $<E_o>$. This alternative activation pathway involves direct Penning ionization of thermometer ions with He* producing pyridine molecular ions ($Py^{+\cdot}$). This ionization pathway is not expected to be prevalent at low exit grid voltages and high ambient humidities (45%).[88] When DART mass spectra were examined in detail, $Py^{+\cdot}$

was detected in low abundance (Figure 3.8). As expected, protonation of the pyridine molecule was favored significantly over the formation of $Py^{+\cdot}$ at all tested flow rates and temperatures with a net increase in $Py^{+\cdot}$ abundance at higher effective temperatures. The relatively low abundance of $Py^{+\cdot}$ (0.61 % on average) suggests that under the present conditions, the pathway depicted in Scheme 3.2iv should not be considered a major contributor to changes in $<E_o>$.

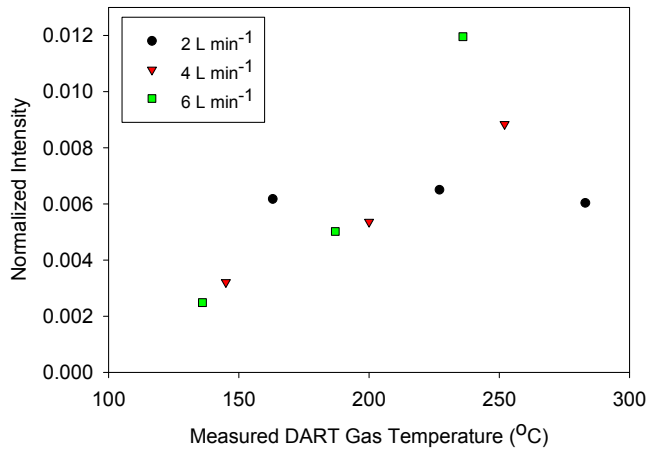

Figure 3.8: Normalized $Py^{+\bullet}$ to ($Py^{+\bullet}$ + $[Py+H]^+$) intensities observed during E_{int} DART-MS experiments at various flow rates and set temperatures.

3.6. Collisional Activation Effects of Internal Energy Deposition

In-source CID is generally performed by increasing the acceleration voltages applied to orifices and skimmers in the first stage of a differentially-pumped mass spectrometric system. Higher potential differences in the first differentially pumped regions produce more energetic collisions with gaseous molecules, inducing higher fragmentation yields during ion transport towards the mass analyzer. In-source CID yields can also be influenced by the gas pressure in the spectrometer's interface.[14] As pressure in this region increases, the mean free path (λ) decreases ($\lambda \alpha 1/P$) leading to a decrease in the collisional energy transfer.[91] Ultimately, this manifests into a reduction in

ion fragmentation and a decrease in the E_{int} deposition.[82] To investigate the existence of this type of effect, the pressure of the first differentially-pumped region was monitored via a Pirani gauge for all DART and ESI experiments (Table 3.1). A decrease in pressure was observed when both the DART ion source temperature and flow rate settings were increased. No changes were observed for ESI. It is thus highly likely that the increase in pressure in the first differentially pumped region as the DART gas flow rates were decreased is responsible for the lower E_{int} deposition observed a given set DART gas temperature.

Table 3.1: Pirani gauge pressure for first TOF differentially-pumped chamber under various experimental blank DART and ESI conditions.

Temperature Set Points	175 ºC	250 ºC	325 ºC
DART: 2 L min^{-1}	260 Pa	240 Pa	230 Pa
DART: 4 L min^{-1}	240 Pa	230 Pa	200 Pa
DART: 6 L min^{-1}	230 Pa	220 Pa	190 Pa
ESI: Aqueous blank	210 Pa	210 Pa	210 Pa
ESI: 50% methanol blank	210 Pa	210 Pa	210 Pa

3.7. Influence of Fluid Dynamics of Internal Energy Deposition

Previous ESI energy deposition studies have shown a correlation between the ion source design, and the mean value and width of the E_{int} distribution.[78] Using the DART ion source, design and experimental variables such as sample positioning, gas temperature and gas flow rates determine neutral and charged particle trajectories within the ionization region. Previous studies from our group have suggested that particle circulation may occur in some sampling geometries, decreasing experimental sensitivity.[18] In the present context, particle circulation may also lead to longer residence

times in elevated temperature regions and/or cause more collisions with energetic metastables, reactive ions, and neutral molecules.

Particle tracing plots (Figures 3.9) were generated to model the gas behavior in a commercial DART ion source. Simulated particle trajectories derived from these simulations showed that particles originating from the bottom surface of the sample capillary did not follow re-circulating trajectories, and thus E_{int} differences over various DART conditions are likely unrelated to differences in ion trajectories in the particular ion source geometry investigated here.

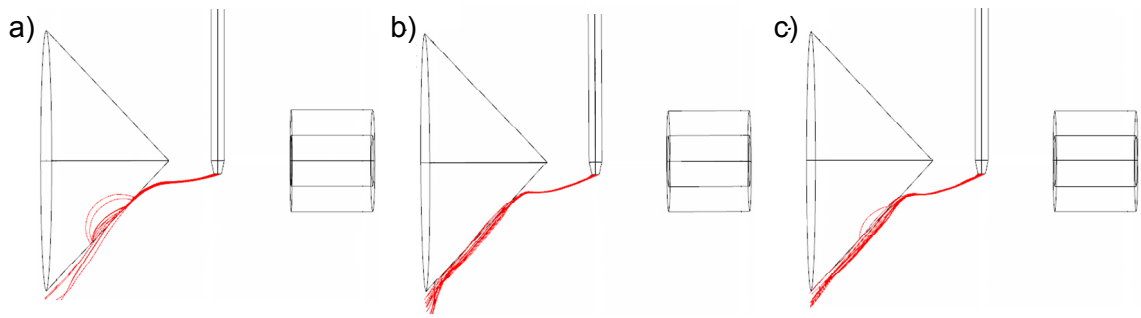

Figure 3.9: Particle tracing plots showing simulated trajectories of neutral particles originating on the bottom surface of the sample capillary at helium gas flow rates of a) 2 L min^{-1}, b) 4 L min^{-1} and c) 6 L min^{-1}.

3.8. Metastable-Stimulated Desorption Effects On the Internal Energy Deposition

Cody et al. have suggested that desorption in DART may include both thermal and non-thermal processes, such as bombardment of the sample surface by metastables or ions.[2] According to the results presented thus far, the former can be considered as being a predominant pathway for energy deposition. Example of the latter include reactive chemical sputtering,[15] and metastable-stimulated desorption (MSD). In MSD metastable rare gas atoms are directed at a surface *in-vacuo* and collide with the outermost surface of

the sample creating an electron hole via Auger de-excitation of the metastable.[92, 93] This process can create a repulsive potential between the surface and analyte stimulating desorption. To investigate the presence of these non-thermal desorption processes, survival yield experiments were attempted using ambient temperature helium metastables. Benzylpyridinium ions were not detected from either slurries, liquid solutions, or from completely dried salts under any of the conditions previously tested suggesting the absence of E_{int} deposition pathways involving non-thermal desorption processes.

3.9. Conclusion

Utilizing the "survival yield" method, the E_{int} distributions of a series of *p*-substituted benzylpyridinium ions was compared between ESI and DART-TOF MS. Although differences in some experimental settings were unavoidable to produce high quality data, ESI was the "softer" of the two ionization techniques with some overlap in energy distributions with DART. Thermal ion activation was a major contributor to E_{int} deposition in DART. Additionally, in-source CID in the first pumped region of the mass spectrometer contributed to DART E_{int} deposition as gas flow rates and temperatures increased.

CHAPTER 4. ION YIELD "HOT SPOTS" AND SUPPRESSION EFFECTS IN DIRECT ANALYSIS IN REAL TIME MASS SPECTROMETRY OF NERVE AGENT SIMULANTS

4.1. Abstract

Presented here are findings describing the spatially dependent levels of sensitivity and ion suppression with DART. Continuous liquid infusion of dimethyl methyl phosphonate (DMMP) revealed that ion yield "hot spots" did not always correspond with the highest temperature regions in space. For instance, at lower concentrations (50 and 100 μM) the highest sensitivities were in the middle of the ionization region where there was a shorter atmospheric pressure ion transport distance. Conversely, at higher DMMP concentrations (500 μM) the highest ion yield was directly in front of the DART source where it was exposed to the highest temperatures for thermal desorption. In corresponding experiments, differential analyte volatility played a smaller role in ion suppression than differences in proton affinity and the relative sampling positions of analytes. At equimolar concentrations sampled at the same position, suppression was as high as 26x between the average intensity of isoquinoline (proton affinity 952 kJ mol^{-1}, boiling point 242 °C) to *p*-anisidine (proton affinity 900 kJ mol^{-1}, boiling point 243 °C). This effect was exacerbated when sampling positions of the two analytes differed, reaching levels of suppression as high as 4543.0x ± 1406.0. To mitigate this level of ion suppression, sampling positions and molar ratios of the analytes were changed creating conditions in which almost no suppression was observed.

4.2. Physicochemical Effects In the DART Ionization Region

Despite the wide adoption of DART as a high-throughput screening tool for pharmaceuticals,[94-96] homeland security,[97-100] metabolomics[101, 102] and polymer analysis,[103, 104] the fundamental variables that effect DART analysis capabilities are still under investigation. The ionization region in DART-MS is a dynamic environment involving complex fluid dynamics, steep temperature gradients and weak electrostatic fields that are a result of the ion source geometry, sample position and orientation, and instrumental settings.[18] In situations where only qualitative information is required, spatial effects can be largely ignored. However, when highly reproducible and/or quantitative experiments are desired, sample positioning becomes critical to ensure homogeneity of the ionization conditions.

Ionization may proceed through several atmospheric pressure reaction pathways involving the primary reactive species formed by DART (metastables) and secondary reactive species such as protonated species from atmospheric gases. The factors that affect the prevailing ionization pathway depend on the presence and type of sample matrix, solvents and contaminants, the DART gas composition and the chemical properties of the analyte.[88] Even with optimized parameters, there is some evidence that DART may sometimes succumb to deleterious matrix effects involving ion suppression.[105] Ion suppression is present to some extent in all ion generation approaches, and affects the sensitivity and dynamic range of the experiment by preferentially decreasing a selected analyte signal. The major DART conditions to consider when mitigating ion suppression include the rates of neutral desorption (related to the temperature and flow rate of the DART gas and analyte boiling point,

BP), ionization efficiency (proton affinity, PA) and molar ratios of the analytes of interest respect to interfering species. These properties are compounded depending on the sampling position and orientation in space.

From our past experience, we believe that there may be differential levels of ion suppression in the ionization region. For instance, when a depletion point of reactive species has been reached, there will be competition amongst the analytes for charge.[106] To study what physicochemical processes and DART conditions contribute to sensitivity, ionization efficiency, ion suppression and dynamic range, a series of steady-state spatially-resolved experiments were devised to study these effects in more detail.

4.3. Experimental Set-Up of Continuous DART Sampling

4.3.1. Chemicals and Gases

All reagents were analytical grade (Sigma-Aldrich, St. Louis, MO, USA) and used without further purification. Solutions of dimethyl methylphosphonate (DMMP, 97 %), *p*-anisidine (99 %), and isoquinoline (97 %) were prepared in nanopure water (Barnstead International, Dubuque, IA, USA). High purity helium (99.999 % Airgas, Atlanta, GA) was used for the DART glow discharge gas.

4.3.2. DART-MS Instrumentation

MS analysis was performed with a commercial DART ionization source (IonSense, Inc. Saugus, MA, USA) coupled to a quadrupole-time of flight (Q-TOF) mass spectrometer (Bruker micrOTOF-Q I, Bremen, Germany). The Q-TOF mass spectrometer interface was modified to accommodate for the gas flow of the DART source through the addition of a custom gas-ion separator tube (GIST; IonSense, Inc. Saugus, MA, USA) connected to a Vacuubrand 2C diaphragm pump (Vacuubrand, Wertheim, Germany). The

DART source was operated with helium at 1 L min^{-1} at a gas temperature of 100–400 °C, discharge voltage of 3500 V and a grid electrode voltage of 50 V. The mass spectrometer settings were as follows: end plate offset -500V, capillary -2000V, dry gas (nitrogen) 2 L min^{-1}, dry gas temperature 150 °C, spectra acquired at 1 Hz in the 50-1000 *m/z* range.

4.3.3. DART-MS of Continuous Liquid Samples

DART-MS sensitivity, dynamic range and ion suppression experiments were performed via continuous liquid sampling to ensure a stable DART ion signal. A custom nylon sample holder was machined to ensure sampling reproducibility in discrete positions (Figure 4.1).

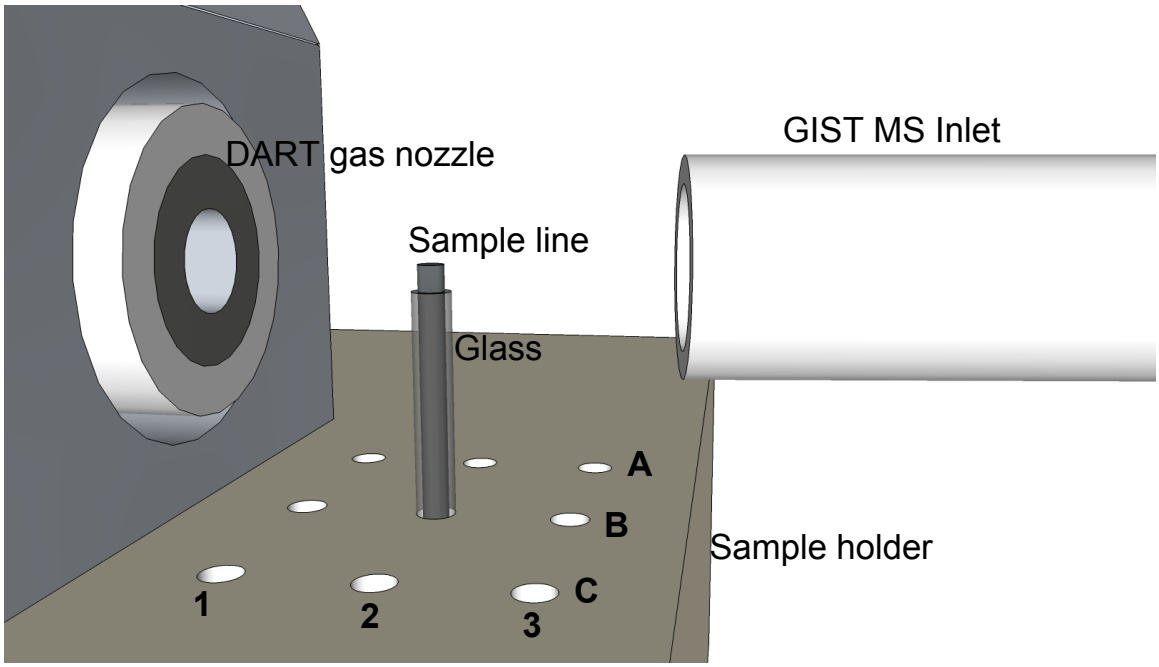

Figure 4.1: DART-MS ionization region depicting the DART gas nozzle, GIST sampling tube to the MS inlet, and the sample grid matrix with the sampling probe in the B2 position.

The sample holder contained 9 sampling holes in a 3 x 3 matrix separated from the center of each hole in row 1, 2 and 3 by 6.5 mm and across columns A, B and C by 4.5 mm. The sample matrix was set so that column B was in direct alignment with the

DART gas nozzle and the GIST. Each spot in space was probed by introducing a continuous flow (600 μL min^{-1}) of sample through a stainless steel capillary (o.d. 450 μm, i.d. 305 μm) inserted through the bottom of the sample holder. To prevent the stainless steel capillary from oscillating in the DART gas stream, a glass capillary protected the outside of the sampling line by providing a rigid base for support. The stainless steel sample line extended 1 mm above the glass capillary and was aligned with the center of the DART gas nozzle outlet. Steady-state experiments were recorded for all measurements. For each experiment, data was collected in a single day to ensure reproducibility except in the case of the sensitivity-in-space and dynamic range trials. Due to the length of time needed to conduct these experiment, day-to-day quality control runs were collected at set concentrations and positions to ensure a minimum ±10 % reproducibility (Figure 4.2). In all experiments, the average signal (protonated molecule in all cases) was acquired for five one-minute segments at each specified DART condition and spot-in-space. The average of all five acquired segments was reported in all cases below. Whenever sample concentrations were changed, the stainless steel capillary was thoroughly rinsed with pure methanol, 50/50 methanol-water and pure water three times. The line was reattached with pure water running through the line and the DART source on to insure no sample carryover was observed. Temperature mapping of the ionization region was determined with an 80 BK temperature probe connected to a digital multimeter (Fluke 179-True RMS; Everett, WA, USA). All data was processed using Sigma Plot 10.0 (Systat Software Inc., San Jose, CA, USA).

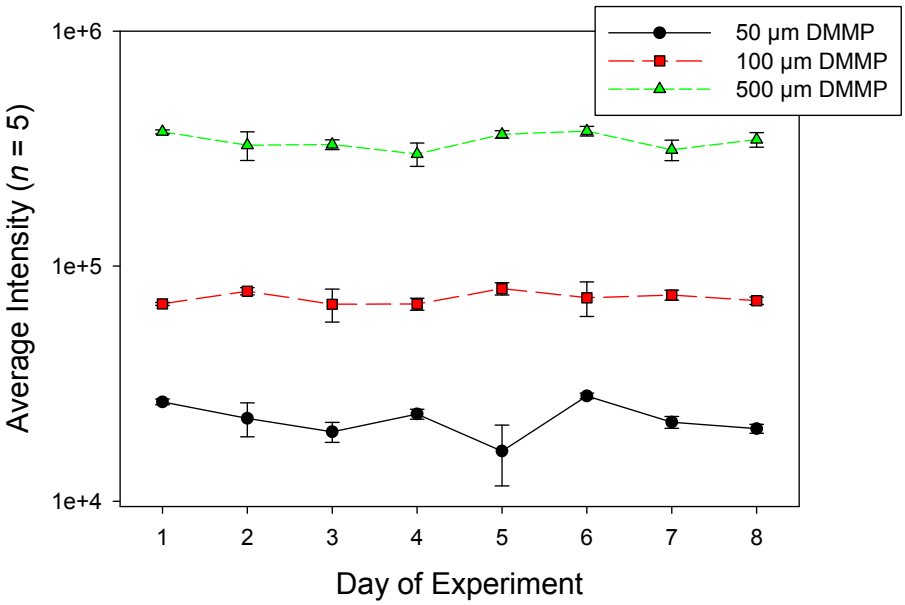

Figure 4.2: Day-to-day quality control runs for sensitivity-in-space (Figure 3) and dynamic range DART-MS experiments.

4.4. Sampling Region Temperature Gradients

Previous observations have shown that there is a steep temperature gradient along the line connecting the DART gas nozzle to the mass spectrometer inlet.[18, 107] However, given that sample surface areas may extend beyond the center-line of the ionization region and that peripheral sampling spots were machined in the sample holder (columns A and C, Figure 4.1), the temperature of the entire ionization region was now mapped to better understand the experimental conditions chosen for spatially mapping of relative sensitivities (Figure 4.3). For all DART temperature settings the hottest region was in the center-line (column B) aligned with the DART gas nozzle. The extent of temperature drop-off between this nozzle (sample spot B1) and the GIST MS inlet (sample spot B3) varied ranging from 30 °C (195 to 165 °C) with a software set temperature of 200 °C, 35 °C (285 to 250 °C) with a software temperature setting of 300 °C and 50 °C (365 to 315 °C) with a software temperature setting of 400 °C (Figure 4.3 a, b and c, respectively). In

the lateral sampling regions (columns A and C) the temperature decrease was less than at the center (column B), but overall temperatures were much lower. When the software temperature setting was 200 °C, the temperature drop-off was only 11 °C (56 to 45 °C) for column A and 12 °C (56 to 44 °C) for column C (Figure 4.3 a). The temperature drop-off was 16 °C (92 to 76 °C) for column A and 15 °C (91 to 76 °C) for column C when the temperature setting was set to 300 °C (Figure 4.3 b). When the temperature setting was 400 °C, the temperature drop-off was 20 °C (135 to 115 °C) for column A and 18 °C (134 to 116 °C) for column C (Figure 4.3 c). Although the overall temperatures in the lateral columns are much lower than in the central column B, the recorded temperature ranges in columns A and C were fairly identical. This result indicates a symmetric temperature contour map of the ionization region where little to no difference in thermal desorption efficiency should be observed between columns A and C.

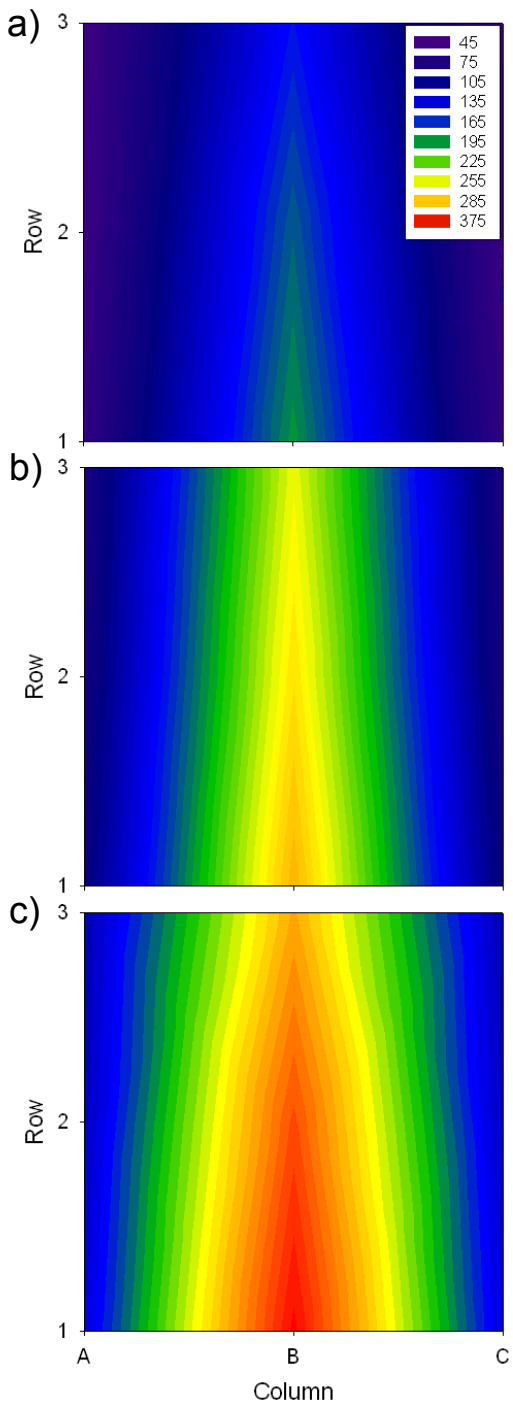

Figure 4.3: Direct probe temperature maps of the DART ionization region at gas temperatures of a) 200 °C, b) 300 °C and c) 400 °C.

4.5. Spatial Sensitivity and Dynamic Range

The symmetric temperature field observed in previous experiments supports the measured spatial sensitivity changes with respect to analyte (DMMP) concentration (Figure 4.4). Overall, the regions in space that yielded the highest ion intensity were mostly located in column B where the highest temperatures and therefore, the most effective thermal desorption was present.

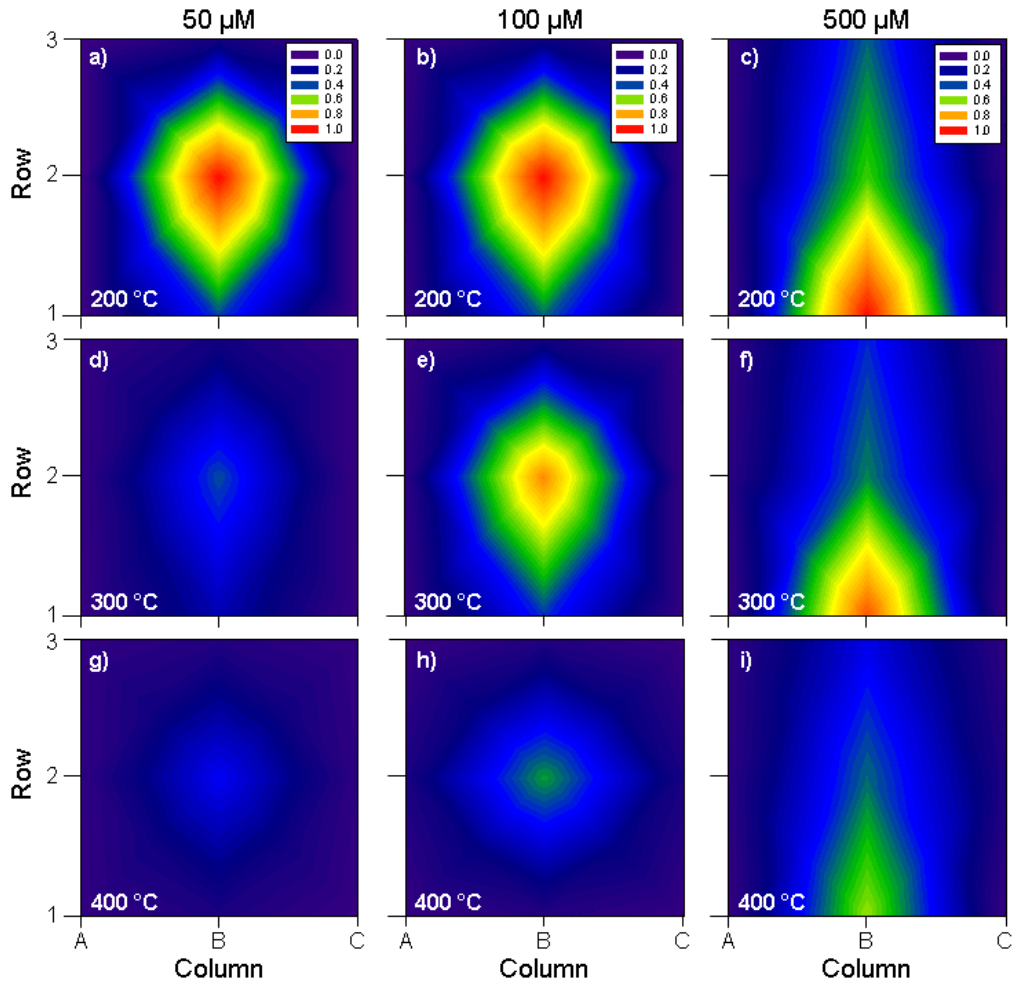

Figure 4.4: Sensitivity-in-space maps at different DART gas temperatures and concentrations of DMMP: maps a) 50 µM, b) 100 µM, and c) 500 µM were tested l at 200 °C, maps d) 50 µM, e) 100 µM, and f) 500 µM were tested at 300 °C, and maps g) 50 µM, h) 100 µM, and i) 500 µM were tested at 400 °C. All averaged (n = 5) intensities were normalized to the B2 (center) position.

At lower concentrations (50 and 100 μM), the most sensitive spot in space to sample from was B2 regardless of set DART gas temperature (Figure 4.4 a, b, d, e, g and h). Interestingly, this spot does not correspond to the highest observed temperature (Figure 4.3). B1, the hottest spot, had a 40-60 % lower relative intensity compared to B2 at lower DMMP concentrations. This suggests that at lower concentrations it may be beneficial to sample in the middle of the ionization region to also enhance ion transport. As noted in previous studies,[18] the high DART gas velocity in the ionization region may potentially result in sample being transported away from the mass spectrometer inlet, decreasing the concentration of neutrals in the ionization region. If sampling near the gas nozzle at B1, the analyte will be in the region of highest temperature but also of highest gas velocity. At this position, even if more total analyte is desorbed and ionized than B2, the higher gas velocity may blow neutrals and ions away from the inlet. Following this logic it may seem best to sample at B3 directly in front of the GIST MS inlet. However, B3 presented the lowest sensitivity by ~80 % compared to B2 and 40 % compared to B1. Row 3 was the region that suffered from the lowest measured temperature across any sampling column translating to the lowest amount of thermally desorbed neutrals. Coupled to this effect was the suction from the GIST MS inlet. Although inlet suction offsets neutral dilution by the DART gas, the rapid transit inside of the GIST MS inlet likely reduced the time for proton-transfer ionization reactions resulting in lower sensitivity.

The map of sensitivity differed at higher sampled concentrations (500 μM) with the highest sensitivity measured at position B1 (Figure 4.4 c, f and i). This sensitivity map corresponds well with the observed temperature gradients (Figure 4.3) and suggests

that dilution from the DART gas was not as significant of an effect. At such high concentration levels, the desorbed analyte was in excess to reactive species in the ionization region, and sensitivity will follow the relative rates of thermal desorption throughout the sampling grid. This was more pronounced at lower temperatures where the increase in relative intensity at B1 compared to B2 was 80 % and 100 % for DART gas temperatures of 200 and 300 °C, respectively (Figure 4.4 c and f). At these two temperature settings the relative drop-off of temperature from the software control to the actual measured temperature was the lowest. At a temperature setting of 400 °C, the increase in intensity was only 40 % due to the larger drop-off in temperature (35 °C) between the software and B1 measurement (Figure 4.4 i).

It is also important to point out that sensitivities were ~80-90 % lower in any row along column A and C compared to column B. The two major factors causing the low sensitivity were the lower overall temperature profile at these positions and poor ion transmission trajectories towards the inlet. Temperatures were lower by ~60-80 % on the outer columns A and C when compared to column B (Figure 4.3). Also, the sample positions along columns A and C were off axis to the GIST inlet. If ionized, the low quantity of desorbed molecules would have a more indirect and longer trajectory to the inlet. A possible means to further improve ion sampling would be to use a flared capillary inlet with a large entrance aperture at the opening of the GIST tube.

After it was clear that the best sensitivity resulted from column B, DMMP was sampled in all three positions (B1, B2, B3) and gas temperatures (200, 300 and 400 °C) over a wider concentration range (25 μM to 1 mM) to assess the dynamic range (Figure 4.5). The most even distribution of response was observed for B3 (Figure 4.5 a). This

position resulted in the poorest overall sensitivity at any tested concentration level which verifies the results presented previously. At lower concentrations (25, 50, 75 and 100 μM), the middle position, B2, had the highest sensitivity supporting the previous results (Figure 4.5 b). Position B1 also corresponds well to the previous sensitivity map showing the highest sensitivity for the highest tested concentrations (250 μM, 500 μM and 1 mM, Figure 4.5 c). Throughout all tested variables, there was a small decrease in overall sensitivity with an increase in DART gas temperature. This alludes to carefully tuning the rate of desorption to be sufficient enough to evaporate excess solvent (water), but not too high to induce pyrolysis and/or produce analyte neutrals faster than protonated reactive species. However, this may be a minor effect that compounds with a lower volatility may not experience due to the requirement for additional heat to thermally desorb.

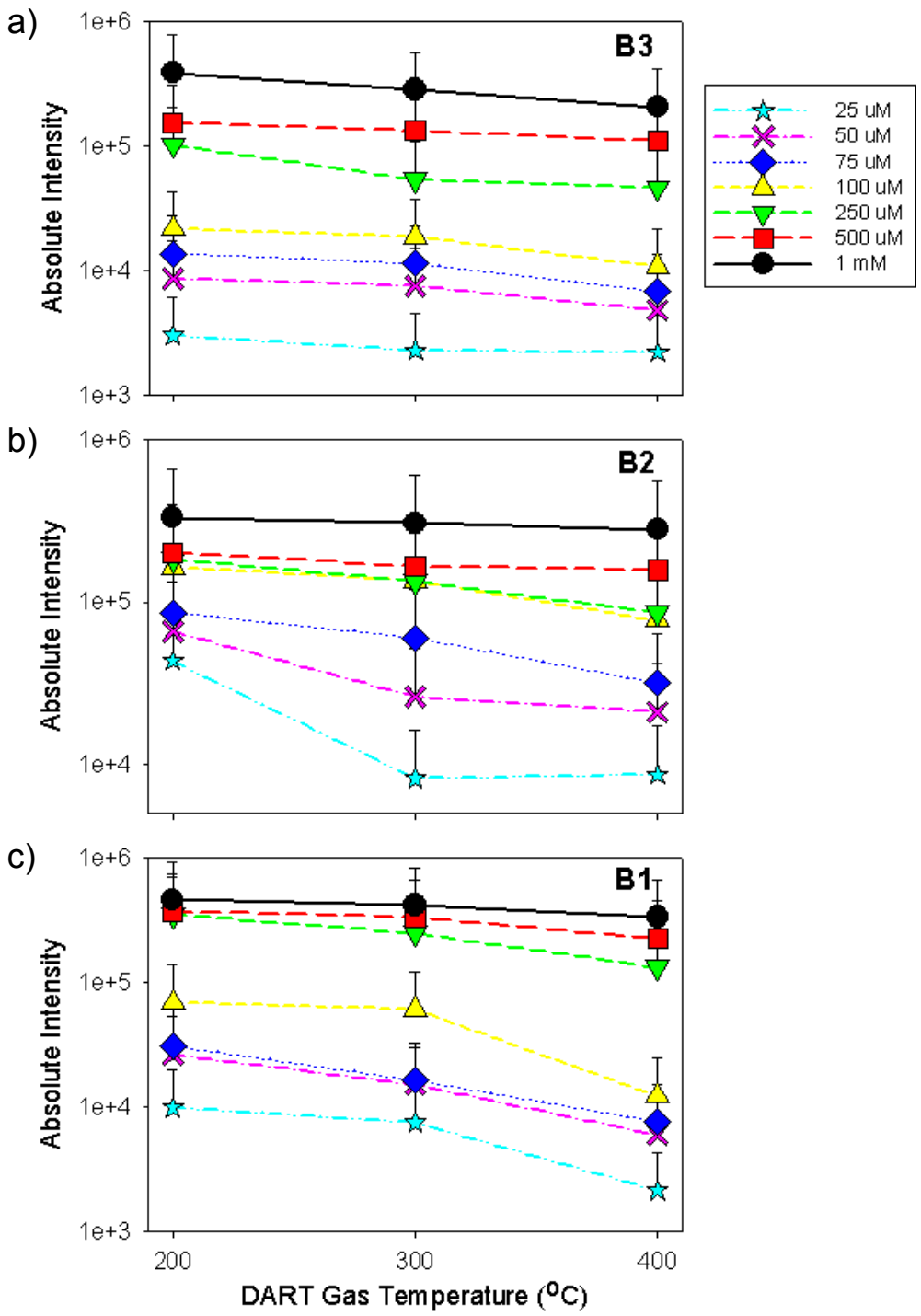

Figure 4.5: DART-MS dynamic range of DMMP in column B at positions a) B3 (close to MS inlet), b) B2 (middle of region) and c) B1 (close to DART gas nozzle) at concentrations of 25 µM - 1 mM and software control temperatures of 200, 300 and 400 °C.

4.6. Ion Suppression

A series of competitive ionization reactions were completed along column B to determine the effect of analyte BPs and PA in space. For the first set of experiments, equimolar solutions of DMMP (PA: 902 kJ mol^{-1}, BP: 181 °C)[108] and *p*-anisidine (PA: 900 kJ mol^{-1}, BP: 243 °C)[60] were simultaneously tested to determine whether volatility of analytes at different temperatures and sampling positions contributed to suppression.

When the DART set temperature was below the BPs of both compounds (100 °C), there was little observed suppression at low concentrations regardless of the sample position since very little of either analyte was thermally desorbed (Figure 4.6 a). Suppression increased with increasing concentration due to competition for protonated water clusters in the reaction region, as expected. Even in a low temperature environment, the compound with the lowest BP (DMMP) suppressed the compound with a higher BP (*p*-anisidine). This trend was more pronounced at higher DART temperatures (Figure 4.6 b, c and d). At the lowest concentration (50 μM) and at temperatures of 200-400 °C, 1.1-2.4 fold suppression was observed, regardless of the sample position. There was no clear trend regarding the effect of position on suppression at low concentrations (Figure 3). However at higher concentrations (100-500 μM), suppression was more pronounced in the B1 position (2.0-3.8x) across all temperatures in the 200-400 °C interval. Position B1 also showed to the best sensitivity at high concentrations (Figure 4.4 c, f and i), suggesting the region is rich with reactive species, and ion losses during transit were compensated by the overall higher rate of protonation. Suppression did not vary too much between positions B2 and B3 at higher concentrations, with position B2 having slightly higher suppression at 200 and 400 °C. Regardless, both positions produced lower

suppression in the higher concentration range compared to B1 due to their poorer overall sensitivity, indicative of a smaller population of desorbed neutrals, which minimized the effect of suppression.

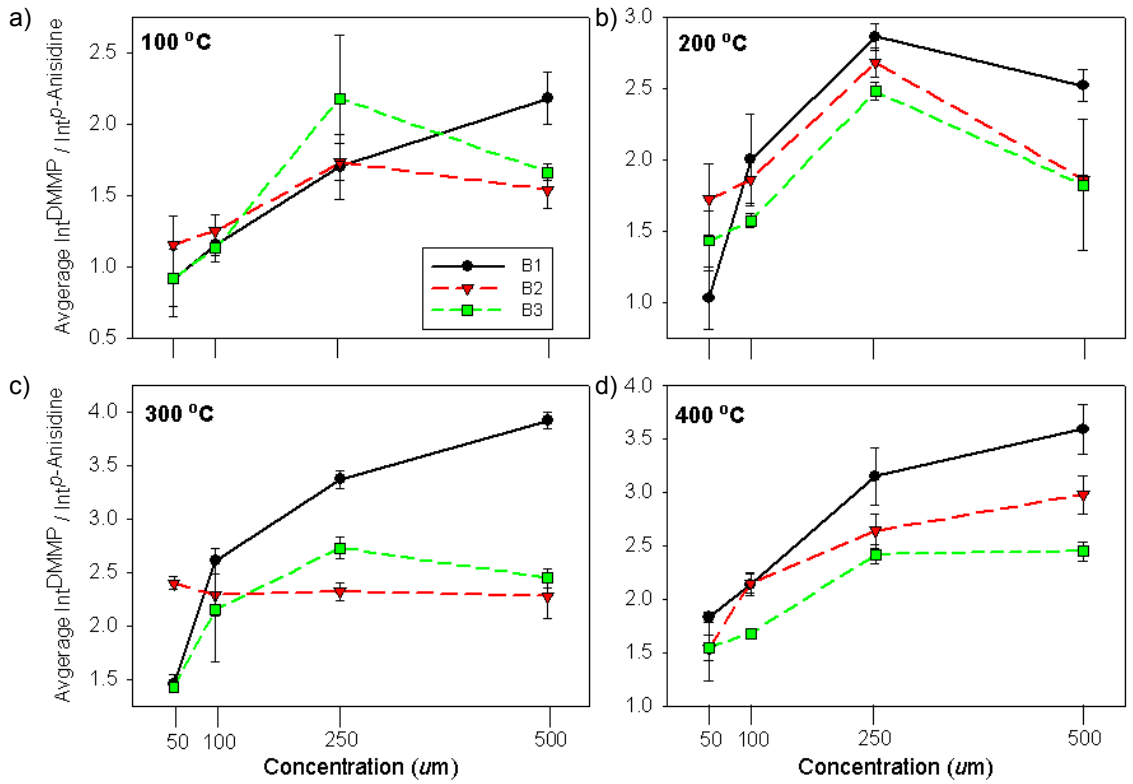

Figure 4.6: The effect of different boiling points but the same proton affinity on ion suppression in different sampling spots of equimolar mixtures of DMMP (BP: 181 °C, PA 902 kJ mol^{-1}) and *p*-anisidine (BP: 243 °C, PA: 900 kJ mol^{-1}) at DART gas temperatures of: a) 100 °C, b) 200 °C, c) 300 °C and d) 400 °C.

An identical experiment was carried out between isoquinoline (IsoQ, BP 242 °C, PA 952 kJ mol^{-1})[109] and *p*-anisidine where analyte BPs were almost equal and PAs were significantly different. Figure 4.7 demonstrates that observed levels of ion suppression for analytes at equimolar concentrations were temperature, position and concentration dependent. For all three tested temperatures (200, 300 and 400 °C), the average suppression was always greater than the previous results investigating differences in BP.

As a whole, the suppression observed at 200 °C was greater at all positions than at 300 °C and 400 °C indicating that proton exchange is more favorable for higher PA analytes at lower temperatures. This may be due to the lower thermodynamic stability of smaller protonated water clusters at lower temperatures, a phenomenon that has been observed with both DART[107] and APCI.[110] At 200 °C, ion suppression for position B1 ranged from 6x to 26x in the tested concentration range (50-500 μM), and was similar for positions B2 and B3, ranging from 7x to 19x (Figure 4.7 a). For both 300 °C and 400 °C, measured ion suppression did not vary much, ranging for B1 from 5x to 17x and for B2 and B3 from 7x to 17x (Figure 4.7 b and c).

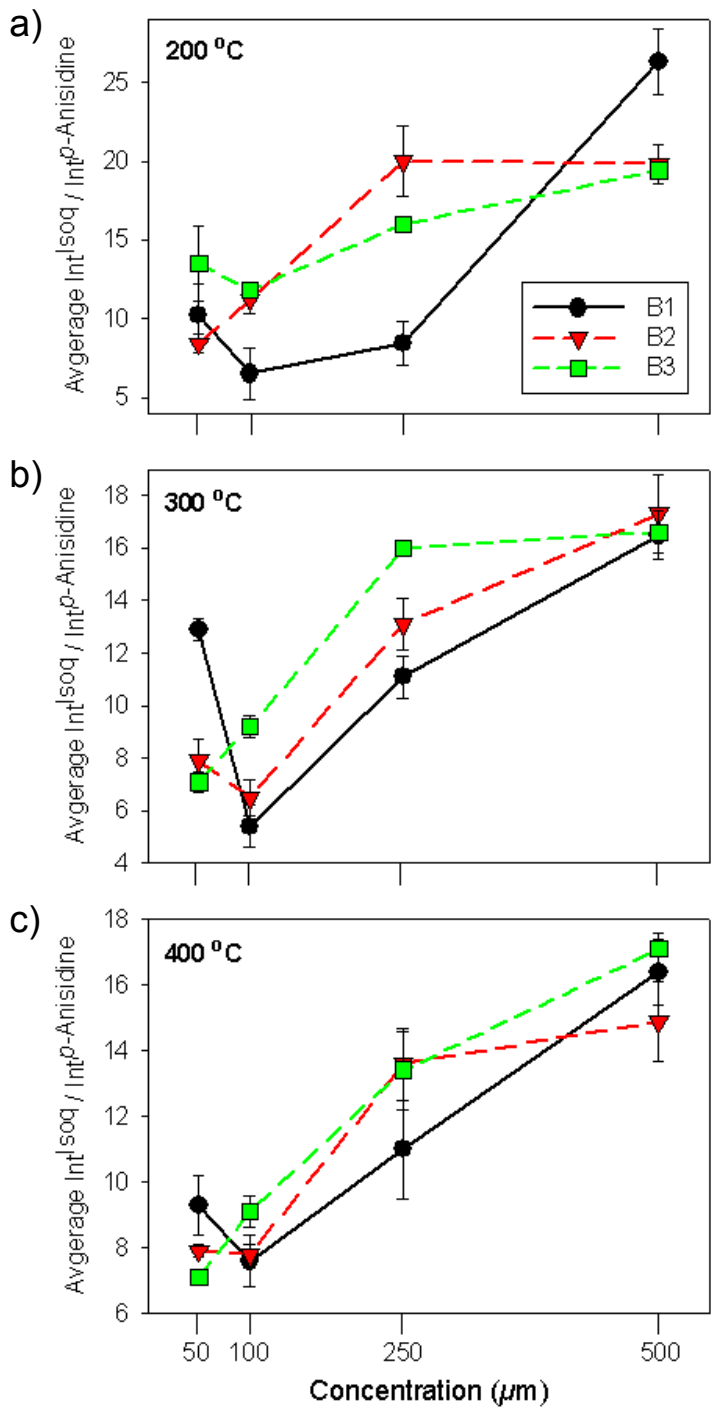

Figure 4.7: The effect of different proton affinities but the same boiling points on ion suppression in different sampling spots of equimolar mixtures of isoquinoline (BP: 242 °C, PA 952 kJ mol^{-1}) and *p*-anisidine (BP: 243 °C, PA: 900 kJ mol^{-1}) at DART gas temperatures of: a) 200 °C, b) 300 °C and c) 400 °C.

A decrease in detected protonated water cluster abundance during the experiments (Figure 4.8) was observed in correlation with the increase in suppression with overall concentration. For instance, at 500 μM the measured average intensities of protonated waters ranging in size from n = 7-19 decreased compared to the lower concentrations (Figure 4.8). Water clusters below n = 7 were not detected due to the data acquisition range used and the ion guide RF voltages chosen, which did not allow detection of low n clusters. A lower overall average intensity over the water cluster series indicated more protonation reactions preferentially to isoquinoline due to its higher PA compared to *p*-anisidine.

Oddly, for all three temperatures there was a dip in the level of suppression at the equimolar concentration of 100 μM. In most trials this dip was small and could be explained within experimental error, however position B1 suffered from the largest dips. This effect can not be explained by ion transmission or thermal dissipation effects since it would be expected that the relative ion transmission losses would be lower at higher concentrations (e.g. from 50 to 100 μM), and that position B1 experiences the highest temperatures (Figure 4.3). The dip may have been attributed to fluctuations in reactive species under those conditions. For clusters with n = 7-13, there was a slight increase in intensity for position B1 at 50 μM compared to 100 μM (Figure 4.8 a and b). The extreme dip at 300 °C, may have been caused from a gas turbulence disturbance between trials. Positioning could also have been slightly off in this one trial. Although the data presented in all the studies suggest very reproducible results, differences in sampling height by as little as 0.5 mm may have resulted in the observed set of results.

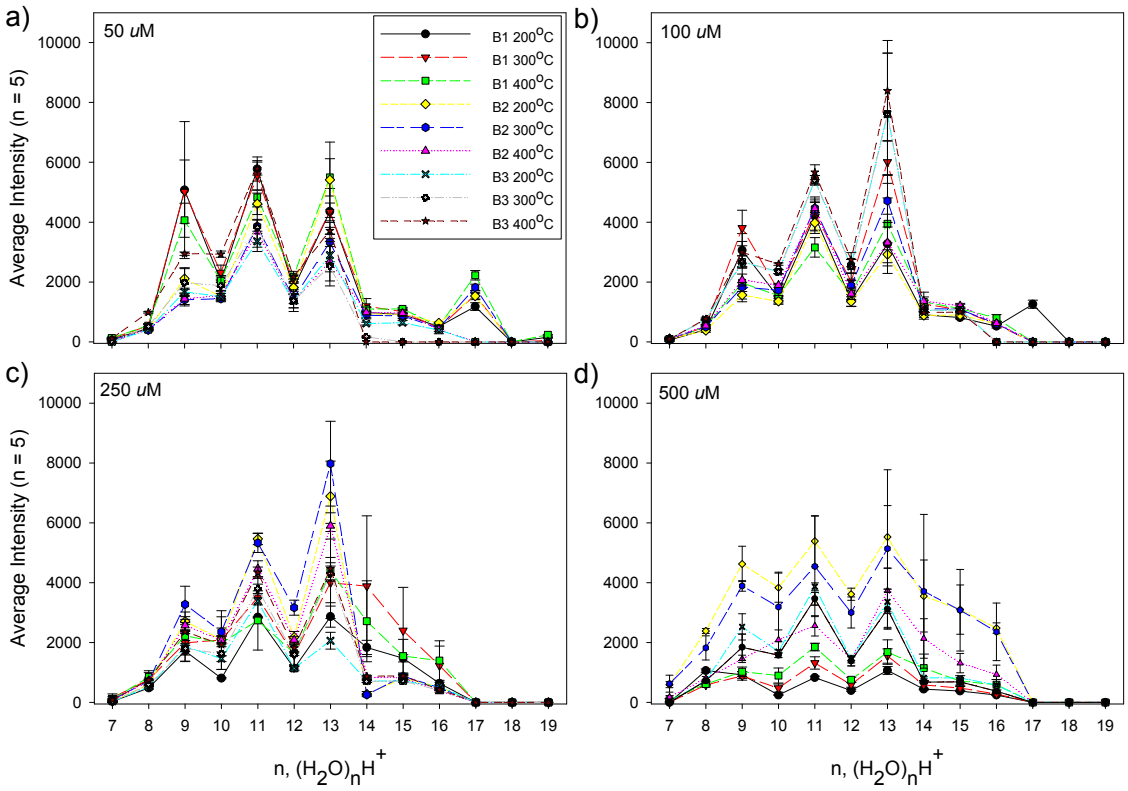

Figure 4.8: Average intensities of protonated water clusters of "*n*" size observed during the experiments of equimolar isoquinoline and *p*-anisidine at solution concentrations of a) 50 µM, b) 100 µM, c) 250 µM and d) 500 µM.

One other interesting, but currently unexplained phenomenon was the relative increase in midsized water cluster intensities at n = 9, 11, 13 and 17 in some trials (Figure 4.8). As a whole, the number of stable water cluster isomers increases exponentially with n.[111] The higher abundance of specific clusters has been observed previously with DART,[107] but that study showed relative higher levels of water clusters n = 3, 6, 9 and 12 for various temperatures (175, 250 and 325 °C) and flow rates (2, 4 and 6 L min^{-1}). Although there are no significant differences in binding energies[112] and bond dissociation energies[113] for water clusters in the range $9 \leq n \leq 17$, the atmospheric pressure interface in the instrument used in this study (GIST-capillary-dual ion funnel) is much more different than that in previous work (cone/skimmer orifice).[107] Therefore, we

believe that the observed differences in water cluster species is an effect caused more by the ion transfer optics design and reduced pressure region architecture, than the preferential formation or reactivity of particular species.

After observing that the major contributing factor to ion suppression was differences in PA rather than BP, conditions to reduce these effect were explored. The same analytes (*p*-anisidine and isoquinoline) were used in these tests, but not at equimolar concentrations as previously shown. Molar ratios were varied from 1 (50 μM each of *p*-anisidine and isoquinoline), to 10 (500 μM of *p*-anisidine and 50 μM isoquinoline) such that the lower PA analyte would have an increasing proportion of neutrals in the ionization region. These competition experiments were further compounded by changing the position where each individual analyte was simultaneously introduced to investigate how the relative increase of neutrals would be affected by ionization reactions in space.

As a whole, the highest suppression was at the lowest molar ratios regardless of sample position (1 and 2, Figure 4.9). Conversely, suppression was lowest at the highest molar ratio (5 and 10, Figure 4.9). The measured relative suppression did show considerable changes with respect to sample positioning. When *p*-anisidine was placed closest to the DART gas exit (B1) and isoquinoline was positioned in the middle (B2) of the ionization region, ion suppression for the molar ratios of 1, 2, 5 and 10 were 88.7x ± 34.8, 8.8x ± 6.5, 2.0x ± 0.6 and 2.2x ± 0.7, respectively (black line, Figure 4.9). At the same position for *p*-anisidine but with isoquinoline at B3, ion suppression for the molar ratios of 1, 2, 5 and 10 were 231.4x ± 51.2, 9.6x ± 0.5, 2.8x ± 1.1 and 0.8x ± 0.1, respectively (red line, Figure 4.9). Even though in the most extreme conditions *p*-

anisidine was 7 mm closer to the DART source and at 10x the relative concentration level, ion suppression still existed due to both the presence of excess protonated water clusters ionizing isoquinoline, and proton scavenging by the higher PA isoquinoline from the lower PA *p*-anisidine. As a result, suppression would only be minimized in environments where a lower PA analyte is both closer to the ionization source and in excess concentration respect to a higher PA analyte. These conditions would be difficult to control in a real world sample where shape and composition of the sample need to be considered, and the concentration, chemical and physical properties of the molecules can not be manipulated.

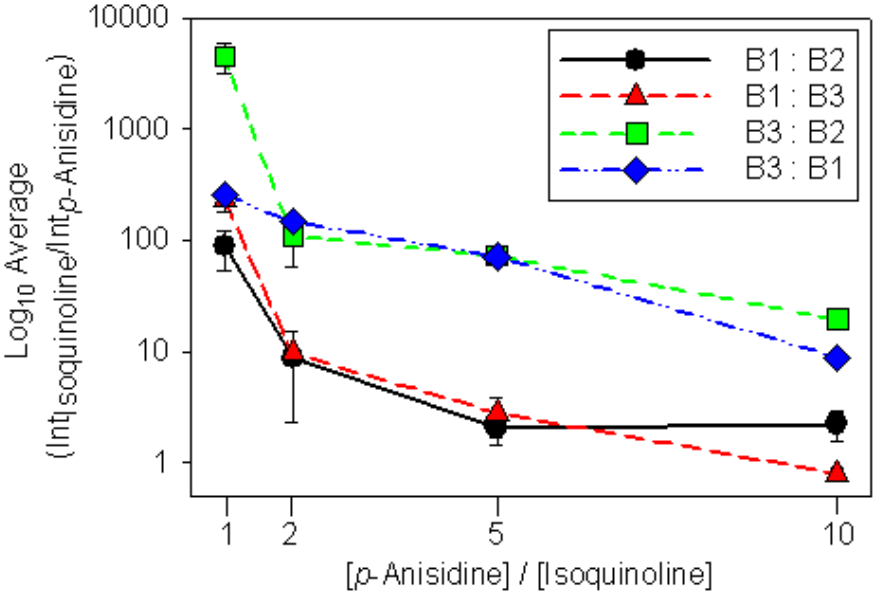

Figure 4.9: Ion suppression competition between isoquinoline and *p*-anisidine in different molar ratios and sampling spots at a DART gas temperature of 300 °C. In the legend, the labeled position on the left refers to isoquinoline and the labeled position on the right refers to *p*-anisidine.

A similar downward trend was observed when the positions were reversed such that the higher PA isoquinoline sample was continuously infused at B1 or B2 and the lower PA *p*-anisidine was injected at B3. Ion suppression levels were much higher in this

scenario, because the higher PA molecule was closer to the DART gas exit where it would undergo the majority of ionization reactions with protonated water clusters and scavenge protons from any PA *p*-anisidine protonated molecules in transit to the mass spectrometer inlet. When isoquinoline was at B2 and *p*-anisidine was at B3, a remarkably high suppression level of 4543.0x ± 1406.0 was observed at an equimolar ratio (green line, Figure 4.9). As the molar ratios increased to 2, 5 and 10 the ion suppression decreased to 107.8x ± 50.4, 73.1x ± 6.1 and 19.4x ± 2.2, respectively. The levels of suppression went down when the position of isoquinoline was moved closer to the DART source (B1) while *p*-anisidine remained at B3 thereby, increasing the distance between where the two molecules were introduced. For molar ratios of 1, 2, 5 and 10 ion suppression was 255.6x ± 13.3, 147.8x ± 7.5, 71.6x ± 3.7 and 8.8x ± 1.2, respectively (blue line, Figure 4.9). In this sampling configuration, there was a higher likelihood that isoquinoline would ionize from reactions with protonated water clusters and not from proton scavenging. Nevertheless, there would always be suppression in the concentration range tested since isoquinoline was closer to the ionization source.

4.7. Conclusion

Spatial sensitivity and ion suppression effects are often overlooked in applications involving ambient desorption/ionization techniques, however the results presented here demonstrate the magnitude that these can reach in certain sampling conditions. Although temperature gradients play a role in thermal desorption, concentration-dependent ion yield “hot-spots” where sensitivity was optimal may not coincide with the hottest regions in space. Additionally, differential analyte volatility plays a smaller role in ion suppression than differences in PAs. Suppression due to different PAs may be

exacerbated by the spatial location of sampling. Although the experiments outlined here used continuous infusion of liquids to acquire steady-state signals, it is expected that solid samples placed within the ionization region for rapid screening purposes would show similar, if not more ion suppression due to matrix composition and flow instabilities in the ionization region. Future investigations of ion suppression in DART should investigate multicomponent mixtures, higher molecular weight compounds to determine if the mass of analytes may affect ion suppression, and time-resolved observation of ion signals in space if a rapid and reproducible sampling mechanism is developed.

CHAPTER 5. DIRECT ANALYSIS IN REAL TIME COUPLED TO DRIFT TUBE ION MOBILITY SPECTROMETRY

5.1. Abstract

Atmospheric pressure drift tube ion mobility spectrometry (DTIMS) is a widely used analytical detection tool for ionized compounds. Fundamentally, DTIMS is a gas-phase electrophoretic separation where ions are pulsed into the drift tube against a counter flow of a drift gas. Separation of the ion packet is dictated by differences in the ions' mass, charge and cross-section before detection. This rapid separation occurs on the millisecond timescale which makes DTIMS a very attractive high-throughput tool for analyte identification. A radioactive (β-electron) ionization source (e.g. ^{63}Ni) is typically used with DTIMS due to its maintenance-free and reliable performance. As a result, these instruments require procedural mandates on their placement, use, and disposal resulting in increased costs and overhead. To address these problems a commercial DART ion source was coupled to a resistive glass monolithic DTIMS as the basis for a low maintenance, versatile, and robust chemical monitoring system. The instrument used nitrogen as both the DART discharge and DTIMS drift gases, allowing for a high electric field to be used for ion separation while keeping cost-of-use low.

5.2. Chemical Detection Systems

5.2.1. Recent Developments With Chemical Detection Platforms

In order to address current and future chemical vapor and aerosol threats to homeland security, chemical detection systems should be versatile and robust to identify hazardous chemicals ranging from chemical warfare agents (CWA) to toxic industrial

chemicals (TIC). Detection instrumentation should operate in an efficient, simple, and safe manner so that users can obtain reliable and reproducible readings with minimal training. These instruments should also be flexible to meet changing homeland security targets for chemical analysis, and have the ability to aid first responders with the identification of unknowns in the event of a successful terrorist attack targeting the chemical industry infrastructure[114] or in the case of intentional dissemination of CWAs.[115]

Detection technologies including chemical sensor arrays,[116] electrophoresis-based lab-on-a-chip devices,[117] impedance measurements via modified carbon nanotubes,[118] piezoresistive microcantilevers[119] and micro gas analyzers[120] have been shown to be potential fieldable technologies capable of chemical agent detection. Solid phase microextraction coupled to GC,[121] fast GC[122] and LC[123] are also common approaches to detection of CWAs and TICs in both laboratory and field environments. DTIMS has been shown to be one of the most popular tools for field detection of CWAs and TICs due to its low maintenance and rapid response,[124] with thousands of portable DTIMS units now distributed throughout the world for aviation security and battlefield detection applications.

5.2.2. Ionization Techniques Used With Drift Tube Ion Mobility Spectrometry

DTIMS instruments often use a radioactive ionization source (e.g. ^{63}Ni) due to its maintenance-free and reliable performance. However, procedural requirements involving the placement, use, and disposal of radioactive sources result in additional costs and regulatory overhead. Electrospray,[125] corona[126] and glow discharges,[127] laser,[128] X-ray[129] and photo ionization[130] techniques are other common ion generation approaches used for

DTIMS. Newer, ambient operation, direct ionization techniques,[4, 131] being rapidly developed for MS have also been coupled to IM spectrometers. For example, DESI has been coupled to reduced-pressure IM-MS for the analysis of pharmaceuticals, peptides and proteins.[132-136] More recently, a study involving DESI IM-MS detection of CWAs has been published focusing on the detection of organophosphorus compounds directly from solid phase microextraction fibers and Dacron swabs.[137] These DESI investigations utilized reduced pressure ion funnels and other ion optics elements to transport ions into the IM cell prior to MS analysis, and thus required sizeable vacuum systems which hampered the development of portable versions of these analytical platforms.

Largely absent from these efforts has been the coupling of ambient operation plasma-based ion generation techniques to atmospheric pressure DTIMS. One of the primary reasons being the difficulty in transporting ambient-generated ions against the uphill electric field at the entrance of atmospheric pressure DTIMS instruments while maintaining safe direct ionization capabilities without electrical shock risk for the operator. Overcoming this difficulty is expected to yield a new generation of fieldable chemical agent monitoring platforms without any vacuum requirements.

5.3. Experimental Development of the DART-DTIMS Platform

5.3.1. Drift Tube Ion Mobility Spectrometer and DART Instrument Setup

The resistive glass DTIMS instrument used in this study was described in our previous work,[138] with only minor changes discussed below. The entrance (12 cm) and drift (26 cm) regions (3 cm i.d., 4 cm o.d.) were constructed out of monolithic resistive glass (PHOTONIS USA, Sturbridge, MA) with a 0.45 GΩ cm^{-1} resistance. A Bradbury-Nielsen-type ion gate was placed between the two DTIMS tubes. When closed, the ion

gate had ± 35 V applied to adjacent wire sets. The entrance and drift tubes were wrapped with silicone heating tape (Minco, Minneapolis, MN), supported in a custom made PEEK mounting assembly, and mounted within a protective Faraday cage for safe operation and for electromagnetic insulation against interferences. Two grid electrodes were used in this set-up. One was positioned in front of the iridited aluminum (2.6 cm diameter) Faraday plate detector (TOFWERK AG, Thun, Switzerland). The second grid electrode was placed at the entrance of the entrance first tube. This grid had a 0.5 cm slit in the middle for the DART glass gas tube to pass through (described below). A high-voltage power supply (FUG HCL 14-2000, Magnavolt Technologies, Plattsburgh, NY) was connected to a voltage divider to supply the potentials for the drift tube entrance and exit, the ion gate and grid electrodes. Drift gas entered the instrument behind the detector plate and was controlled by a precision flow meter (PMR1, Bel-ART/Scienceware, Pequannock, NJ). Data acquisition and ion gate timing was controlled by in-house developed software coded in LabView 7.0 (National Instruments, Austin, TX).

A DART-SVP ion source (IonSense, Inc. Saugus, MA, USA) operated in positive ion mode was used for all experiments. The DART gas nozzle was connected to a 15 cm long glass tube (0.15 cm i.d., 0.3 cm o.d.) used to inject nitrogen metastable species directly into the entrance tube. A melting point glass capillary tube where liquid samples were deposited was affixed to the glass tube extending 2 cm past the tube exit. This entire assembly was easily pulled into and out of the entrance tube through a 0.5 cm wide open slit on the grid electrode with the assistance of the built-in ion source rail assembly. For transmission mode (TM) DART experiments, the entrance grid was removed, and a custom circular stainless steel mesh (1.1 cm diameter) coated with absorbent graphitized

carbon material (Carbopack X, Supelco) was placed in a stainless steel fitting support in electrical contact to the opening of the entrance tube.

5.3.2. DART-IMS Sample Analysis

DTIMS settings for typical experiments were as follows: entrance tube grid held at 12 kV, drift tube entrance held at 9.93 kV, a 381.9 V cm^{-1} electric field within the drift tube, 400 μs gate pulse width, 200 μs data acquisition window, 400 spectral sweeps averaged per analysis, 150 °C drift tube temperature and nitrogen drift gas at 1 L min^{-1}. Each 400 μs gate pulse comprised the first element in an n = 256 element sequence. For multiplexing experiments, both 200 and 400 μs arbitrary binary (n = 512 and 256, respectively) and Hadamard (n = 511 and 255, respectively) gating sequences were used. These were created following the procedure described in our previous work.[139] A constant 50 μs data acquisition window was used in all multiplexing experiments. In all cases, DART settings were as follows: grid voltage +500 V, 2.5 L min^{-1} nitrogen flow rate and 400 °C heater temperature.

A schematic of the experimental setup is shown in Figure 5.1. During analysis of various samples, the DART ion source was set to stand-by mode and 2 μL of the liquid sample were deposited on the melting point capillary tube tip with the sample introduction assembly pulled out of the DTIMS entrance tube. Following deposition of the liquid, the sample introduction assembly was moved into the entrance tube such that the gas transfer tube extended 1.5 cm inside this region (approximately 5 seconds for set-up). Once in position, the tip of the melting point capillary was 3.5 cm inside of the entrance tube and 8.5 cm away from the ion gate. Immediately, the glow discharge and heating element in the DART ion source were turned on and the data acquisition started.

For TM DART experiments, a similar method was used except that the entrance grid was replaced by a stainless steel mounting bracket (Figure 5.1 vii). The sample was applied directly to an absorbent screen mounted on this bracket, and allowed to dry. The heated gas stream from the DART ion source was then allowed to pass through the screen and into the entrance tube of the IM spectrometer, causing analyte desorption and ionization.

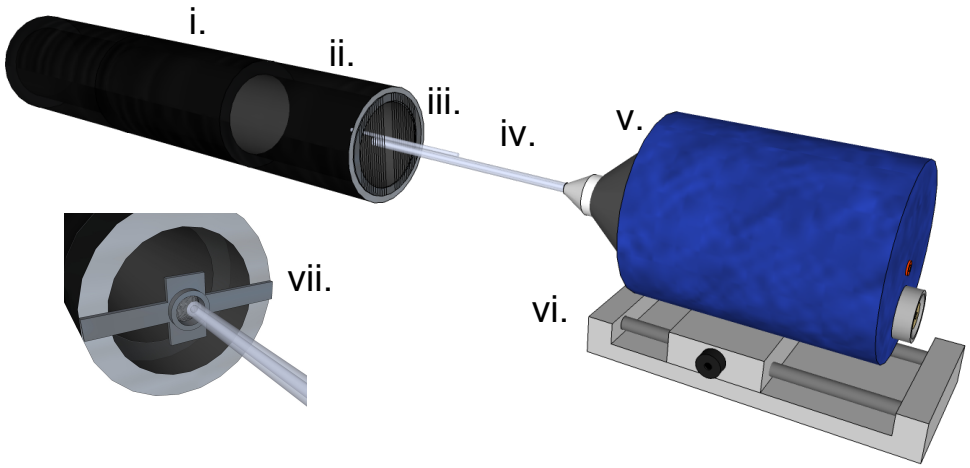

Figure 5.1: Schematic of the DART-DTIMS system: drift tube (i.), entrance tube (ii.), entrance electrode (5 mm split) (iii.), DART gas and sampling tube (iv.), DART ion source (v.), adjustable rails (vi.). The inset shows the TM DART assembly mounted on the front of the instrument (vii.). Not shown is the 0.2 cm thick aluminum Faraday cage surrounding the DTIMS tubes.

An 80BK temperature probe connected to a multimeter (Fluke 179-True RMS, Everett, WA) was used to measure the temperature gradient at the tip of the capillary where sample was deposited (Figure 5.2). A steep rise in the measured temperature from 0-60 seconds was observed when the gas tube was placed inside the IM spectrometer entrance tube and the DART heater was turned on. From this point until the end of the data acquisition period (180 sec) the temperature remained fairly steady between 68.7 to 70.2 °C.

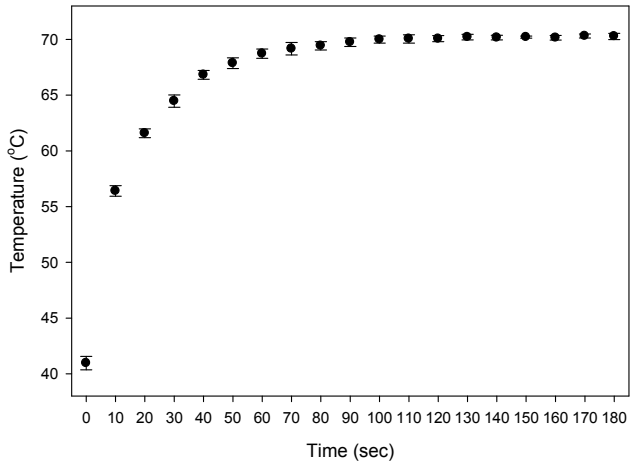

Figure 5.2: Direct measurements (n = 5) of the temperature gradient at the tip of the sample capillary when the DART gas and DTIMS drift gas temperatures were set to 400 °C and 150 °C, respectively.

Due to the temperature changes suffered by the sample during DART-DTIMS analysis, sequential averaged spectra were saved to monitor the response with respect to time for a total of 3 minutes. For example, a data file with the first 400 spectral sweeps took approximately 41 seconds to acquire. After the computer averaged individual sweeps and saved this file (19 seconds) the next acquisition window was started. Acquisition was repeated for a total of 3 averaged runs requiring 1 minute each. For all experiments, solvent blanks were run before each individual replicate to ensure a clean baseline signal and to verify no false positives were detected. Data smoothing of the raw DTIMS files was carried out in Origin v.7.5 using a Savitzky-Golay filter (OriginLab Corporation, Northampton, MA). All spectra were plotted in Sigma Plot v.10.0 (Systat Software, Inc., San Jose, CA).

5.3.3. Determination of Reduced Mobility Terms

In standalone DTIMS, the reduced mobility (K_0, in units of $cm^2\ V^{-1}\ s^{-1}$) values are calculated to aid in the identification of ionic species (eq. 5.1):

$$K_0 = \frac{d}{Et_d}\frac{P}{760}\frac{273}{T} \quad \text{(eq. 5.1)}$$

where d is the distance the ion drifts from the gate to the detector, t_d is the drift time of the ion, E is the electric field strength, P is the ambient pressure and T is the drift tube temperature. In some cases, reported reduced mobility values may be inaccurate due to impurities, cluster formation, and/or thermal expansion or contraction of the drift tube, amongst other factors.[124, 140] In these cases, standard compounds with well known and stable reduced mobility values are used to better determine the reduced mobilities of unknowns following eq. 5.2:[140]

$$K_0(\text{unknown}) = \frac{K_0(\text{standard})t_d(\text{standard})}{t_d(\text{unknown})} \quad \text{(eq. 5.2)}$$

During the course of our experiments, 2,6-D*t*BP was used as the calibration compound to correct K_0 values. This molecule has been shown to be a reliable compound since it gives an intense, stable protonated molecule signal under various experimental conditions with $K_0 = 1.42\ cm^2\ V^{-1}\ s^{-1}$.[140-142]

5.4. Initial Assessment of DART-DTIMS Platform

The nature of the ion species observed in DART-DTIMS was tested using 2,4-lutidine, following correction of K_0 values with 2,6-D*t*BP. At a field strength of 381.9 V cm^{-1}, two peaks were observed at t_d = 28.8 and 35.6 ms with K_0 = 1.73 and 1.40 $cm^2\ V^{-1}\ s^{-1}$, respectively (Figure 5.3). Literature K_0 values for the protonated molecule and dimer of 2,4-lutidine are 1.95 and 1.43 $cm^2\ V^{-1}\ s^{-1}$, respectively.[140, 143] Therefore, the second (slower) peak can be assigned to the protonated dimer of 2,4-lutidine with good certainty, but the first observed peak has a reduced mobility value indicative of an ion size larger

than the protonated molecule but smaller than the dimer. The first peak could be potentially attributed to $[M+H]^+(H_2O)_n$ ions of 2,4-lutidine.

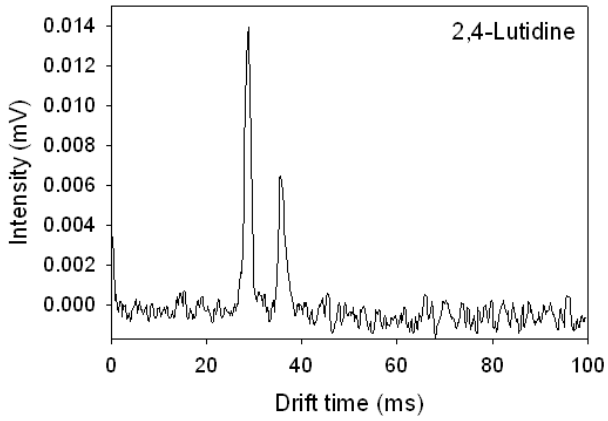

Figure 5.3: DART-DTIMS spectrum (400 sweeps averaged) of 2,4-lutidine (10 % v/v) showing two peaks at drift times of 28.8 ms (K_0 = 1.73 cm^2 V^{-1} s^{-1}) and 35.6 ms (K_0 = 1.40 cm^2 V^{-1} s^{-1}) at a field strength of 381.9 V cm^{-1} (9.93 kV applied to entrance of the drift tube).

These cluster species have previously been observed with atmospheric pressure DTIMS and are in agreement with ionization mechanisms believed to be predominant during DART and other atmospheric pressure chemical ionization techniques.[144] Protonated molecule-water clusters would form from a reaction similar to Kebarle's water displacement mechanism[14] (eq. 5a),

$$(H_2O)_n H^+(g) + M(g) \longrightarrow M(H_2O)_n H^+(g) \qquad \text{(eq. 5a)}$$

whereas dimer ions would arise from subsequent reactions between these cluster species and neutrals (eq: 5b): [144]

$$M(g) + M(H_2O)_n H^+(g) \xrightarrow{heat} (2M + H)^+(g) + (H_2O)_n \qquad \text{(eq. 5b)}$$

Additional experiments at field strengths of 255, 286.5, 318.1, and 349.6 V cm^{-1} indicated that the same ionic species in the same relative ratios were formed in all cases, suggesting that the generation of protonated clusters and dimers was likely occurring during ionization, and not from posterior reactions during the ion drift time (Figure 5.4).

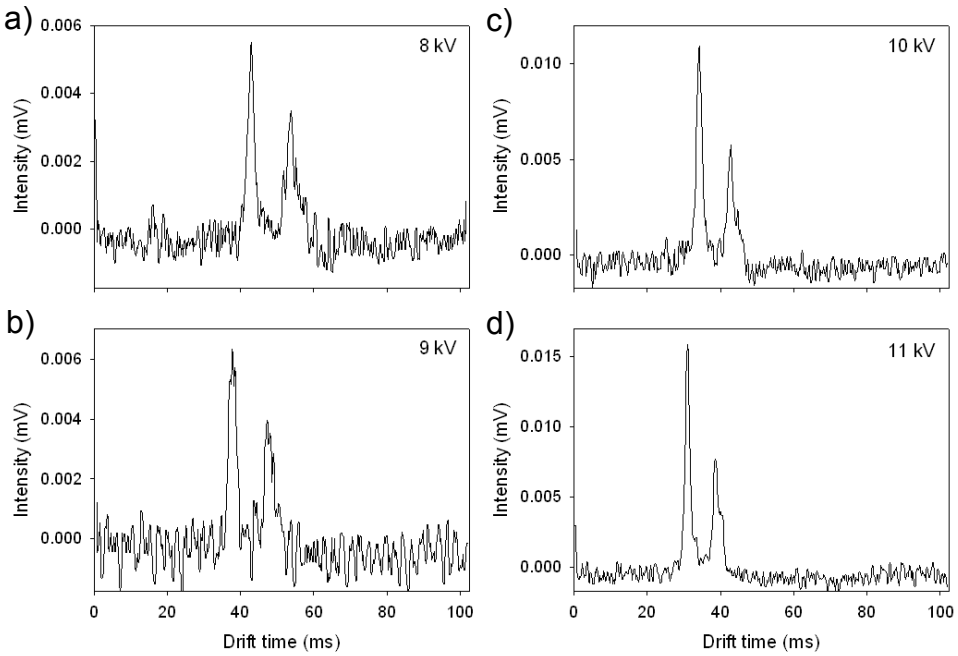

Figure 5.4: DART-DTIMS spectra (400 sweeps averaged) of 2,4-lutidine (10 % v/v) at field strengths (applied voltage) of a) 255 (8 kV), b) 286.5 (9 kV), c) 318.1 (10 kV) and d) 349.6 V cm^{-1} (11 kV). The drift times of the first and second peaks were a) 42.8 and 53.7 ms, b) 37.9 and 47.2 ms, c) 34.2 and 43.0 ms and d) 31.0 and 38.6 ms.

Because protonated water ion cluster formation derived from metastable-induced Penning ionization is always observed in background DART MS spectra,[2] these species have been suggested to have a significant role in DART ion formation via a transient microenvironment concept.[145] Therefore, molecule-water cluster ions are more likely to survive in DART-DTIMS than in DART MS where extensive declustering occurs during travel within the first differentially-pumped stage of the mass spectrometer.

5.5. Probability of Detection of Toxic Industrial Chemicals

Following these experiments, the baseline performance of the DART-DTIMS system was investigated by testing several model analytes. DMMP (Chemical Weapons Convention Schedule 2 substance used in the synthesis of Sarin) and 2-CEES (mustard gas analog) were chosen for both being chemical warfare simulants. Methamidophos, a

low vapor pressure harmful pesticide, was chosen as an additional test molecule. Detection limits were evaluated using a probability of detection (POD) methodology.[146, 147] POD values were calculated from the frequency of positive detections observed for replicate sample runs (n = 8) at increasing concentration values. The number of successful detections with SNR ≥ 3 as a function of analyte concentration was then fitted to a logistic function defined by (eq. 5.4):

$$y = \frac{A_1 - A_2}{1 + (x / x_o)^p} + A_2 \qquad \text{(eq. 5.4)}$$

where, A_1 and A_2 are the lower and upper asymptote values, respectively, x_o is the point of inflection and p is the rate of the curve steepness. The chosen POD was the point on the curve where the likelihood of detection was at least 95 % (the level at which there was less than a 5 % false negative rate).

Using a melting point capillary tube sample introduction method (Figure 5.1), the calculated PODs for DMMP, 2-CEES, and methamidophos were 11.81 % (v/v), 1.13 % (v/v), and 10.61 mM, respectively (Figure 5.5). Considering fmol amounts of reserpine have been detected with this instrument using nanoESI[138] and ppm and ppb levels are routinely detected with other DTIMS systems,[124] the nanomol 95% POD amounts detected by DART suggested that inefficient analyte desorption and/or insufficient ion transmission into the drift tube could be limiting sensitivity in this particular configuration. One key factor affecting DART sensitivity is the lower thermal conductivity of nitrogen (25.83×10^{-3} $W \cdot m^{-1} K^{-1}$) compared to helium (15.13×10^{-2} $W \cdot m^{-1} K^{-1}$), which is more typically used in DART experiments.

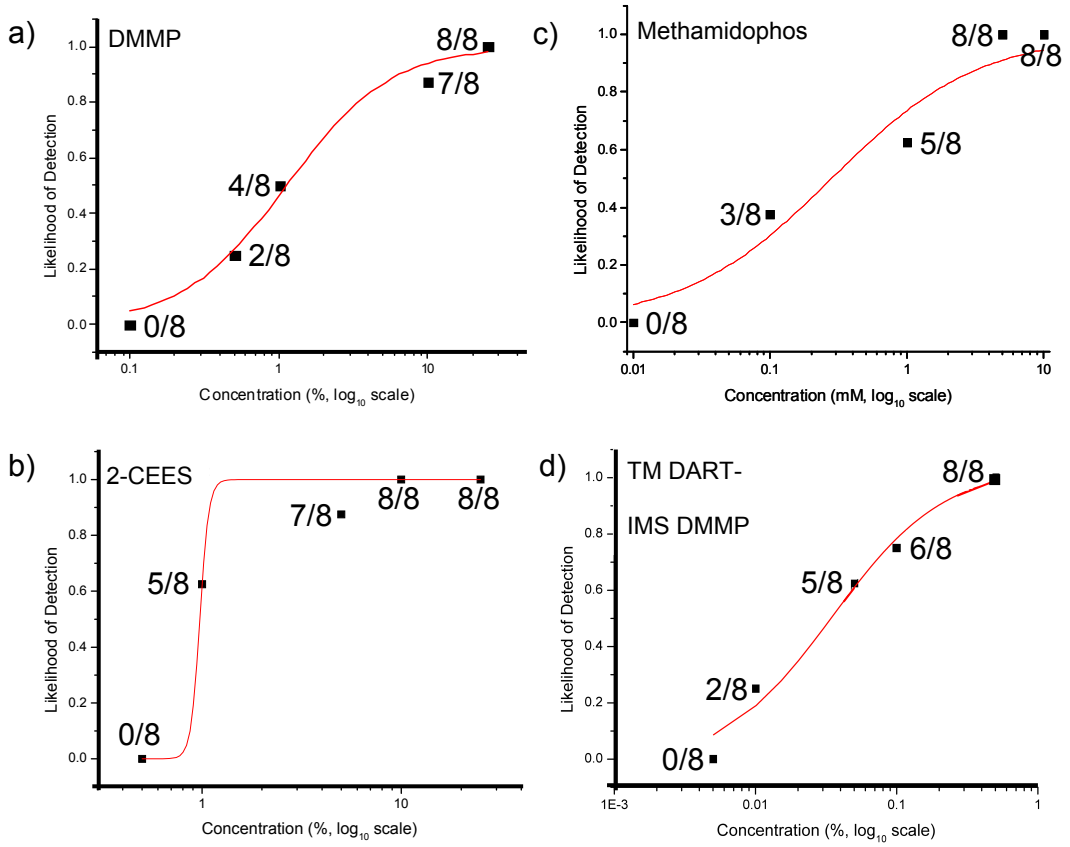

Figure 5.5: Probability of detection (POD) curves for a) DMMP, b) 2-CEES, c) methamidophos and d) TM DART analysis of DMMP tested at various concentration levels (n = 8 at each concentration level).

5.6. Transmission-Mode DART-DTIMS

To maintain the advantages of nitrogen-based operation, such as low operational costs and the ability of using higher electric fields for increased IM resolving power while simultaneously improving the 95% POD values, a TM DART geometry[148] was implemented in the same instrument. For this purpose, the front-end of the IM instrument was outfitted with a stainless steel mounting bracket to hold a sample sorbent screen (Figure 5.1 inset). TM DART experiments were conducted with DMMP, as in previous experiments this was the target analyte with the highest POD levels. For TM DART, the calculated DMMP 95% POD was 0.28 % (v/v) (Figure 5.5d), an improvement of almost

two orders of magnitude (~97.6 %) respect to the previous baseline experiments. This increase in sensitivity allowed recording mobility spectra during the first minute, not the second, as with the previous method. This 50 % reduction in detection time was the result of the screen being placed directly in front of the DART gas stream, instead of being placed above the heated flow, as with the glass capillary. The more uniform heating efficiently desorbed the analyte molecules from the screen, enabling more sensitive and rapid detection. More uniform analyte distribution onto the screen may also have played a role in the improved detection capabilities. The porous graphitized carbon black material (Carbopack X) used to coat the stainless steel screen allows formation of a more uniform, thinner, layer of the target compound, further facilitating thermal desorption. An additional factor explaining this improvement is the electrostatic and fluid dynamic focusing possible in the TM geometry via the application of an electrostatic potential directly to the sorbent mesh, and directing the DART gas jet through the mesh holder.

5.7. Reliability of Detection of Conventional and TM DART-DTIMS

At the calculated 95% POD levels, 24 replicate experiments for each analyte resulted in positive detection for all trials (Figure 5.6). The average drift time, and reduced mobility for DMMP sampled from a glass capillary were 36.0 ± 0.25 ms and 1.38 ± 0.01 cm^2 V^{-1} s^{-1}, respectively. TM DART-DTIMS experiments with DMMP yielded an average drift time of 36.0 ± 0.20 ms and K_0 of 1.38 ± 0.01 cm^2 V^{-1} s^{-1}, respectively. These values match the literature value for the protonated DMMP dimer.[140, 142] The average drift time and reduced mobility for 2-CEES were 36.8 ± 0.24 ms and 1.35 ± 0.01 cm^2 V^{-1} s^{-1}, respectively. The average drift time and reduced mobility for

methamidophos were 37.7 ± 0.2 ms and 1.32 ± 0.01 $cm^2 V^{-1} s^{-1}$, respectively, but no literature value were available for comparison.

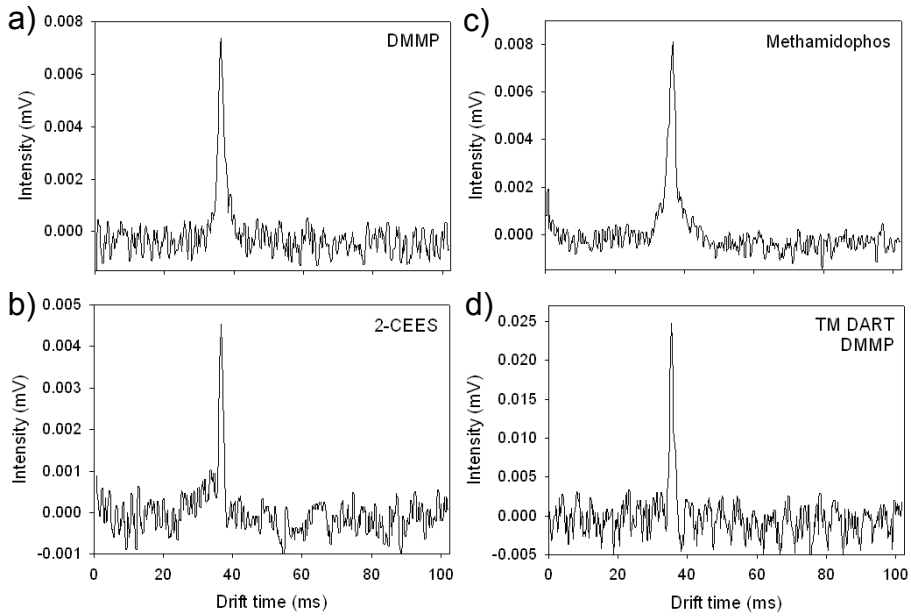

Figure 5.6: Sample spectra collected at the 95% POD with corresponding average drift time values (n = 24) for a) DMMP, b) 2-CEES, c) methamidophos and d) TM DART analysis of DMMP. Four hundred sweeps were averaged in every case.

To ensure that the detected species were indeed different and not the product of carry-over in the system, the drift times of each analyte were compared in a box plot (Figure 5.7), and were found to be statistically different from each other.

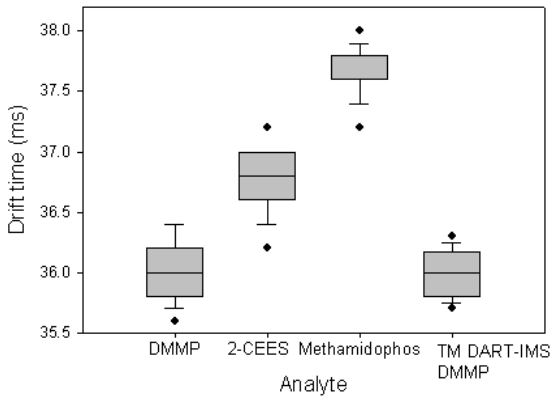

Figure 5.7: Box plot of the interquartenary ranges of recorded drift times of each analyte at their POD concentration levels (n = 24). Solid lines inside the boxes are the median values and the dots are outlier values.

5.8. Sensitivity Gains Obtained From Multiplexed DART-DTIMS

An alternative method to increase sensitivity is to modify the method for gating ions into the drift tube by multiplexing the ion injection scheme. In the previous set of experiments, data was acquired in what is commonly known as "signal averaging" mode which carries the drawback of a very low duty cycle. For instance, with an ion gate pulse width of 400 μs (one element) and a 102.4 ms run (a 256-element sequence), the theoretical duty cycle (the temporal ratio of the pulse width to experiment length) is ~0.4 %. In this scenario, >99 % of the ions generated by the DART ion source are not gated into the drift tube. In multiplexed DTIMS, multiple packets of ions are gated successively throughout the sequence. The recorded spectrum is convoluted, but by knowing the gate pulse width, and the number and index of open elements in the binary ion gating sequence, the original spectrum can be deconvoluted.

Multiplexed IMS also offers more flexibility in terms of ion injection approaches than classical IM experiments. In a signal averaged DTIMS experiment, the gate opens in the beginning of each sweep and then closes until the ion swarm reaches the detector. If a hypothetical 16-elements sequence was used for ion injection, only the first element would represent an open gate (Figure 5.8). Therefore, the duty cycle would be 6.25 %. A multiplexed approach adds more open gate events to the sequence to increase the total amount of ions introduced into the drift tube. Ions could be injected for 2, 4 or 8 elements selected randomly along the 16-element sequence representing duty cycles of 12.5, 25 and 50 %, respectively. The total number of injection sequences with identical duty cycle is therefore dependent on the length of the sequence (n) and the number of open gate elements (r), as defined by (eq. 5.5):

$$\#Sequences = \frac{n!}{r!(n-r)!} \qquad \text{(eq. 5.5)}$$

Therefore, for the previous example, there are 120, 1820, and 12870 different possible ion injection sequences when 2, 4, or 8 elements in the sequence are open ion gate states, respectively. We refer to this approach as "digital multiplexing".[139]

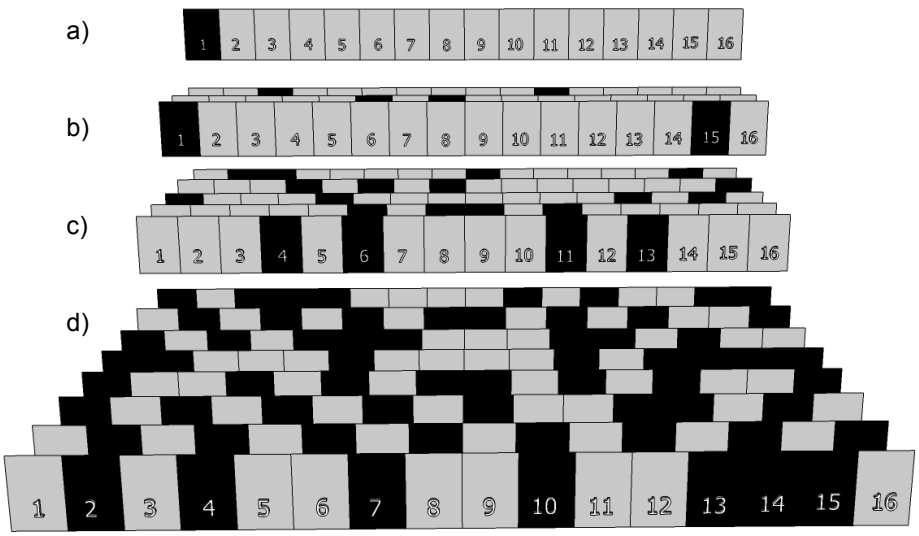

Figure 5.8: Illustration describing multiplexing theory using a basic 16 element sequence as an example. a) In conventional signal averaging mode, the gate is opened only for the first element (r = 1) and ions travel until they are detected (6.25 % duty cycle). In digitally-multiplexed methods, ions can be injected any place along the sequence for a predetermined amount of elements: b) three potential sequences (12.5 % duty cycle) out of a possible 120 total sequences, c) ions are injected during four elements (25 % duty cycle) five of a total of different 1820 sequences are shown, d) ions are injected for eight elements (50 % duty cycle) eight of 12870 different sequences are shown above.

In order to investigate the feasibility of performing DART-DTIMS in conjunction with a digital multiplexing, DMMP at the 95% POD level was used as a test case. A signal averaged run with a ~0.4 % duty cycle and a 400 μs gate pulse produced a SNR of 5.6 (Figure 5a), whereas digitally multiplexed spectra recorded with 5, 10, 30 and 50 % duty cycles showed improved SNR values of 8.7, 7.4, 10.7 and 11, respectively (Figure 5c, d, e and f).

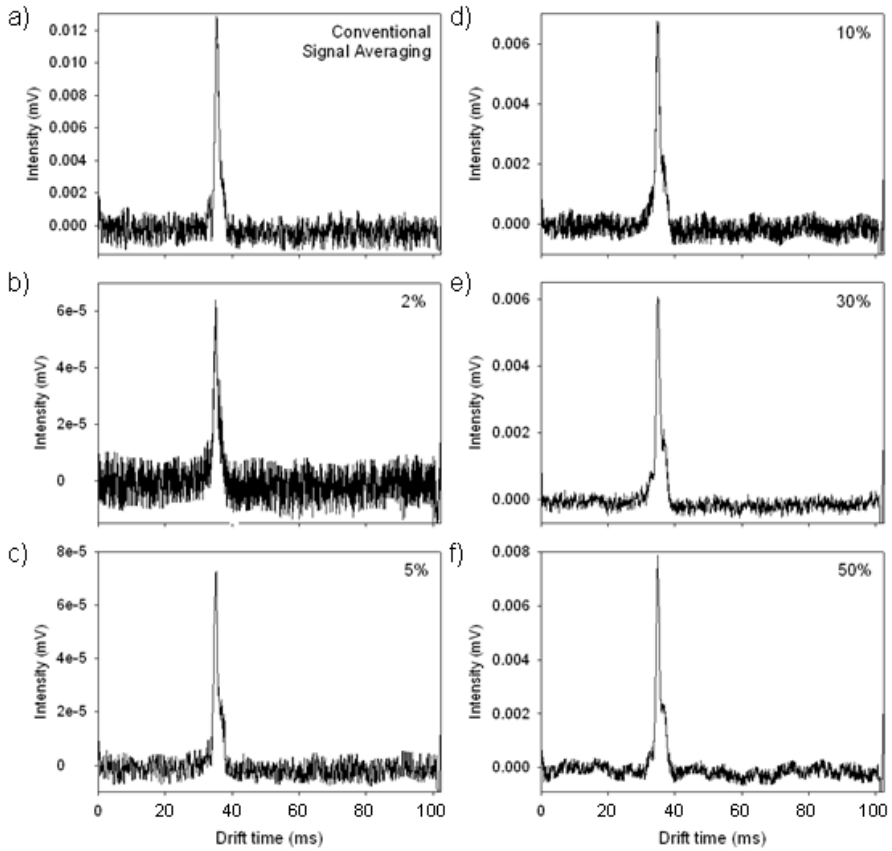

Figure 5.9: Comparison of DMMP spectra at the 95% POD concentration level acquired with a 400 µs gate pulse width: a) conventional signal averaging (~0.4 % duty cycle), and digital sequences with duty cycles of b) 2 %, c) 5 %, d) 10 %, e) 30 % and f) 50 % (400 sweeps averaged).

A conventional experiment using a 200 µs ion gate pulse width resulted in a SNR of 3.2 (Figure 5.10). Corresponding digitally multiplexed spectra recorded at 2, 5, 10, 30 and 50 % duty cycles also showed improved SNRs of 4.6, 5.8, 5, 9.2 and 4.9, respectively (Figure 5.10).

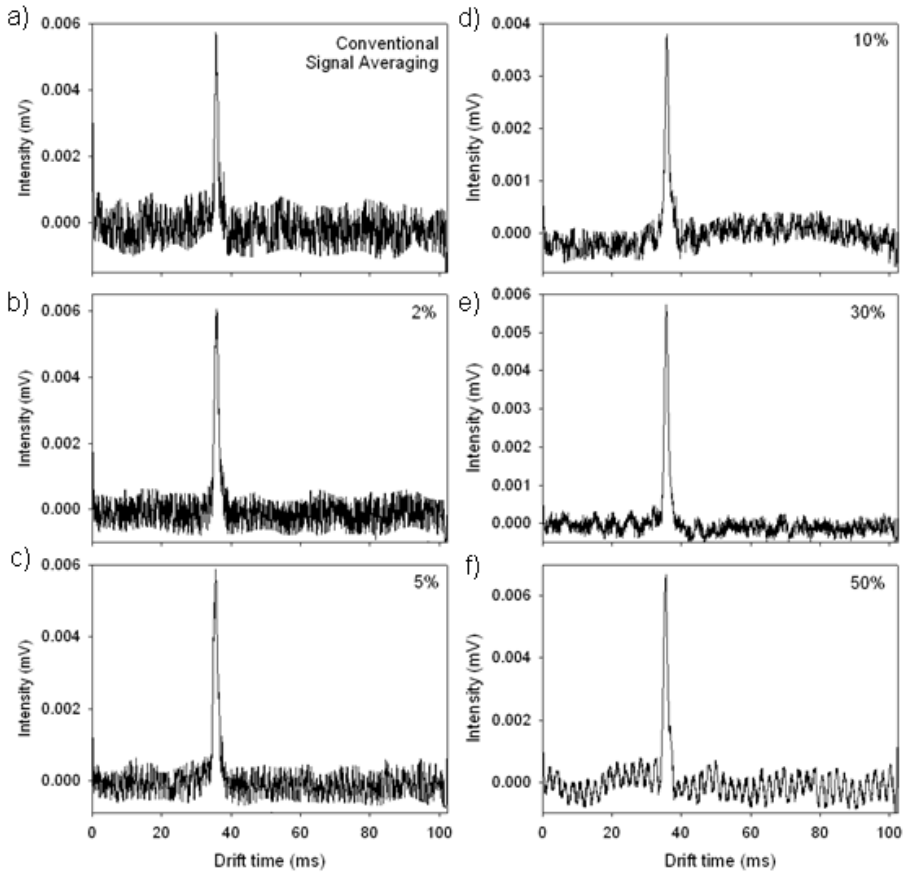

Figure 5.10: Comparison of DART-DTIMS spectra of DMMP at the POD level with 200 µs gate pulse width. Spectrum collected using a) conventional signal averaging (~0.4 % duty cycle) and arbitrary digital sequences with duty cycles of b) 2 %, c) 5 %, d) 10 %, e) 30 % and f) 50 %. All experiments consisted of 400 sweeps.

A summary of the observed multiplexing gains for experiments using 200 and 400 µs gates and 20-400 sweeps is presented in Figure 5.11, showing that gains greater than 1 were observed in most cases. The highest observed gains compared to traditional signal averaging mode were observed for 20-sweep acquisitions carried out with 30 % 200 µs (3-fold gain) and 10 % 400 µs (4.5-fold gain) sequences.

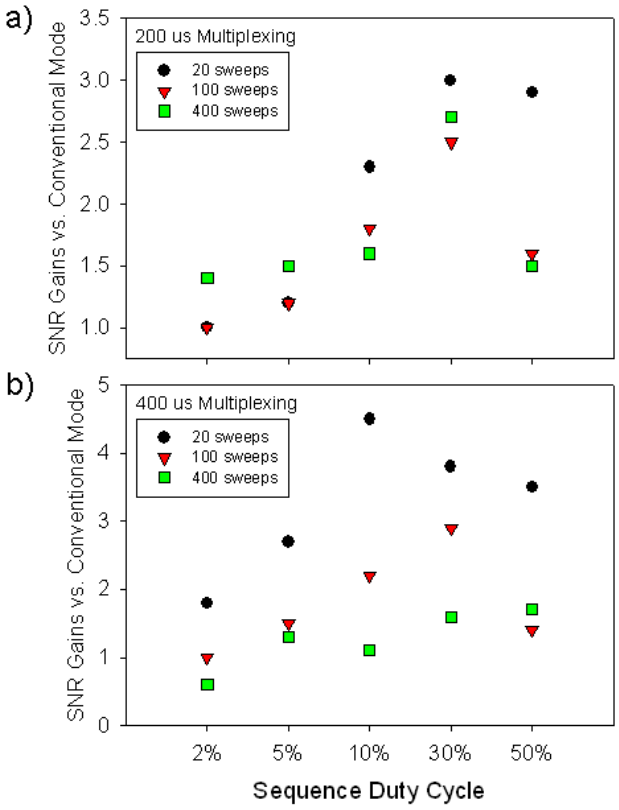

Figure 5.11: Signal-to-noise ratio gains observed for digitally-multiplexed experiments over traditional signal averaging mode during the DART-DTIMS analysis of DMMP at the 95% POD concentration level carried out with a) 200 µs and b) 400 µs gate pulse widths and 20 (●), 100 (▼) or 400 (■) averaged sweeps.

The reason behind these findings was probably due to the short period of time where the signal was collected in 20-sweep experiments. During this time segment, the ion source temperature remained essentially steady, which was a central requirement to correct implementation of multiplexing approaches.[149] The only case where SNR gains were not observed was the 400 µs 2% duty cycle digital sequence which showed a SNR of 3.6 (Figure 5.9b). This phenomenon has been previously documented and was attributable to the specific distribution of gating events in the particular sequence selected to run the experiment, which was one out of $>8.8 \cdot 10^9$ possible combinations.[139]

In the previous experiments, it was also noted that 50 % duty cycle experiments resulted in lower than expected gains for 400 spectral sweeps. Therefore, an alternative

50 % duty cycle method was implemented utilizing Hadamard Transform (HT) multiplexing.[139, 150-152] For both 200 and 400 μs gate widths in 20, 100 and 400 sweep runs, HT sequences showed SNR gains over conventional signal averaging experiments, as expected (Figure 5.12). The greatest gains were observed for 100 sweep runs with 200 μs gates, with a gain of 3.3x over conventional mode (Figure 5.12a).

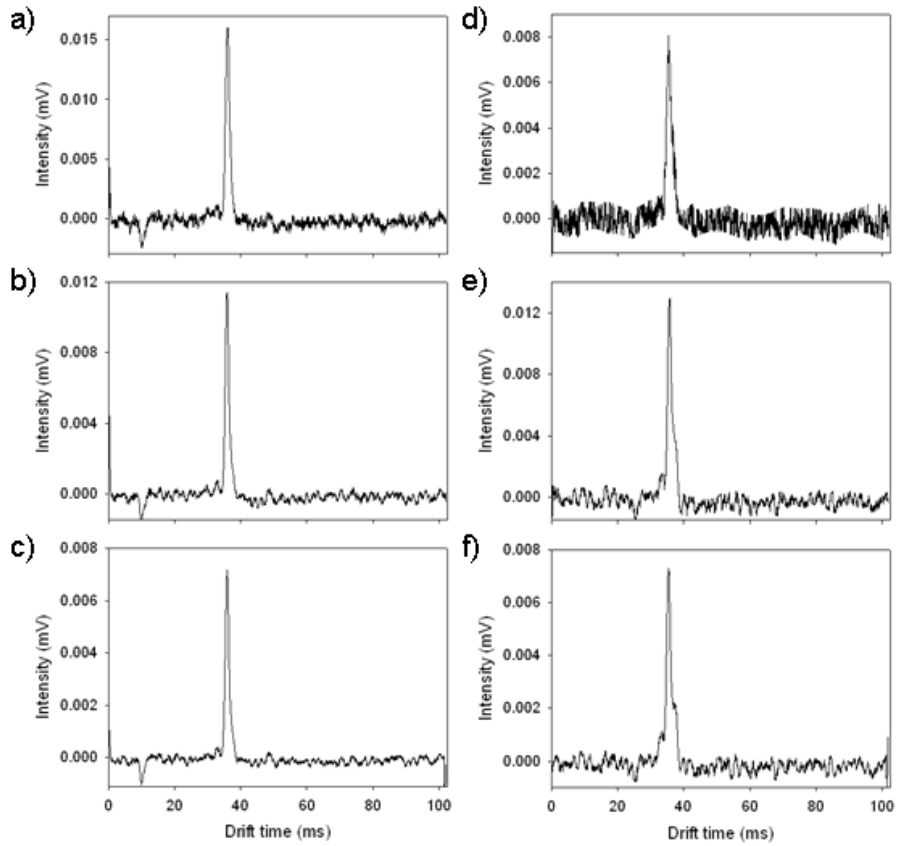

Figure 5.12: DART-DTIMS spectra acquired using HT multiplexing. Spectra acquired with 200 μs gate pulse widths for a) 20 sweeps, b) 100 sweeps and c) 400 sweeps. Spectra acquired with 400 μs gate pulse widths for d) 20 sweeps, e) 100 sweeps and f) 400 sweeps. SNR gains over conventional signal averaging mode runs were a) 2.6x, b) 3.3x, c) 3.2x, d) 1x, e) 1.4x and f) 1.5x.

The gain for this HT experiment over the 50 % digital multiplexing experiment was 1.6x. However, accompanying this gain were spectral defects in the acquired HT spectra. These defects were most noticeable with the 200 μs gates appearing as negative

peaks at drift times of 10.5, 9.9 and 10.1 ms for the 20, 100 and 400 sweep averaged runs, respectively (Figure 5.12a, b and c). Smaller defect peaks were observed with 400 μs gates at drift times of 25.0, 25.3 and 25.4 ms for 20, 100 and 400 sweeps, respectively (Figure 5.12 d, e and f). Defect peaks are due to imperfect ion swarms released into the drift tube. Contributing to the shape of the ion swarm are phenomena such as space charge, thermal diffusion,[153] "gate ringing" of the applied waveform[154] and ion depletion in the region immediately preceding the ion gate.[150] All these effects contribute to decreases in SNR gains and the appearance of defect (i.e. ghost or echo) peaks.

5.9. Conclusion

The results presented here demonstrate the ability to detect and identify toxic substances including CWA simulants and low vapor pressure chemicals using a DART-DTIMS platform. The use of nitrogen for both the DART reactive gas and the DTIMS drift gas keeps operational costs lower compared to helium gas. Additionally, the all nitrogen system allowed for a high electrical field to be used, maximizing IM resolving power. However, the use of nitrogen as the DART gas also resulted in lower sensitivity than with standard helium operation. Two avenues to compensate for this reduction in sensitivity were successfully tested. First, it was found that sampling in transmission mode geometry reduced the 95% probability of detection level by almost two orders of magnitude compared to sampling from a melting point capillary tube. Secondly, digital and HT multiplexing techniques were utilized leading to 3-4.5 fold improvements in SNR over conventional signal averaging experiments.

CHAPTER 6. AMBIENT METASTABLE-INDUCED CHEMICAL IONIZATION IN TRANSMISSION AND IMAGING MODES

6.1. Abstract

An attractive feature for ambient ionization techniques, in particular DART, is the enclosureless set-ups and open-air access to samples and the ionization region. This allows for novel ways to perform challenging experiments of delicate or odd-shaped samples. In one case, a TM geometry was developed to allow reactive gas species to flow through the sample (e.g. insecticide-treated nets) Introduction of the sample at this fixed geometry eliminates the need for optimizing sample position and allows spectra based on factors such as metastable gas temperature and flow to be systematically evaluated. In another application, the metastable-gas stream from a DART source was coupled to laser ablation for imaging and targeted MS experiments (infrared laser ablation metastable-induced chemical ionization, IR-LAMICI). The laser ablation allowed for spatially resolved sampling of a sample's surface by ablating material into the reactive metastable plume facilitating gas-phase chemical ionization. IR-LAMICI was explored by imaging pharmaceutical tablets, screening counterfeit drugs, and probing algal tissue surfaces for natural products.

6.2. Alternate Implementations of Direct Analysis In Real Time

6.2.1. Transmission-Mode Geometry

The DART analysis of an object's macroscopic surface requires the sample to be held in a position which allows for the reactive DART gas stream to flow tangentially to the surface, and avoid blocking the flow of desorbed analyte ions into the MS.[18] In the case of applications involving liquids, they are analyzed by first dipping the end of a

melting point tube into the sample and then holding it within the ionizing gas stream, which causes rapid drying and ionization. New commercial versions of the DART ion source allow the angle of the incident metastable gas stream to be adjusted for optimization, however, detailed reports of the effect of sampling angle on sensitivity and reproducibility have yet to be published. A TM DART methodology was developed as an alternative sampling strategy for DART MS. Qualitative and quantitative TM-DART MS analysis of insecticide-treated nets (ITN) coated with pyrethroid pesticides is shown as an example of the type of applications that can benefit from this approach. ITNs are widely used in control and prevention of malaria transmission in endemic countries, and are a central component of national malaria programs. A custom-designed sample holder was fabricated to rapidly and reproducibly place the bed nets normal to the ionizing metastable gas stream.

6.2.2. IR-LAMICI

Plasma-based ambient ion generation techniques such as DART and FAPA[155] make use of a gaseous flux of electronic and/or vibronicly-excited metastable helium or nitrogen formed in a distal electrical discharge. These metastable species are directed through the ionization source where they can be heated to enhance desorption and/or isolated by a grid electrode to limit the exposure of the sample to ions and electrons. Under standard conditions, these metastables react with atmospheric water, oxygen, or other air components to produce reactive protonated water clusters. With the exception of micro-hollow cathode discharges, most plasma-based ambient ionization sources produce a reactive stream of at least several millimeters in diameter, preventing their use for direct mass spectrometry imaging (MSI). Recognizing this limitation, Hieftje and co-workers[156]

coupled FAPA to Nd:YAG laser ablation in an enclosed configuration. Although not carried out in the open air, such two-step desorption/ionization experiment has the advantage of not being limited by the lateral resolution provided by a diverging liquid jet. Herein, we report the first results obtained using a new open air technique named IR-LAMICI.

6.3. Experimental

6.3.1. Instrumentation

For the TM-DART analyses, a custom-made sample holder was fabricated in-house (Figure 6.1). Benet sections were sandwiched between two 57 mm × 3.2 mm × 19 mm MACOR slides each containing a centered 5 mm-diameter hole. This assembly was placed onto an aluminum holder and mounted in between the DART ion source gas outlet and the mass spectrometer inlet orifice, exposing a 20 mm^2 bed net area to the metastable gas stream. Notches in the sides of the aluminum sample holder allowed for it to easily be slid on and off custom-made screws mounted into pre-threaded holes of the DART ion source.

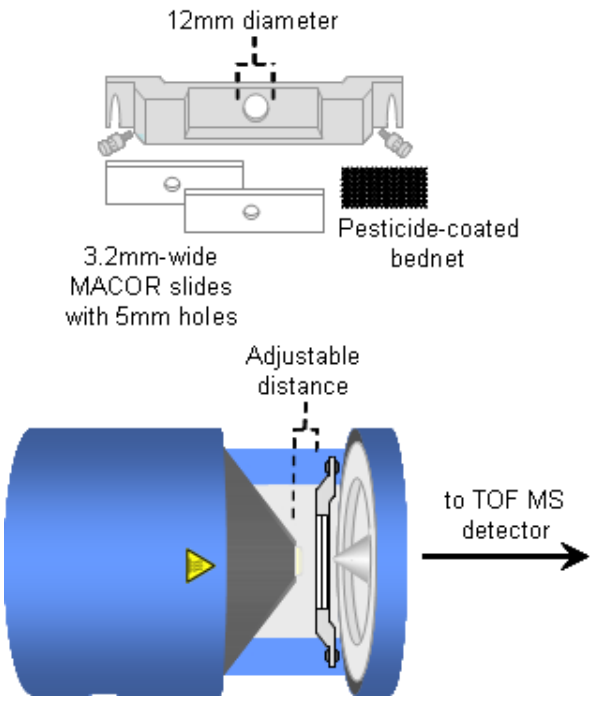

Figure 6.1: Schematics of the custom-made sample holder used for TM-DART analysis. Top: exploded view of the sample holder. Bottom: top-view of the sample holder assembly mounted in the ionization region of the TM-DART time of flight (TOF) mass spectrometer interface.

The IR-LAMICI source (Figure 6.2) consisted of a custom-made metastable generation chamber[18] equipped with a 90° bent glass nozzle (o.d. 0.3 cm) mounted in front of the mass spectrometer sampling inlet. Laser ablation was achieved with a Nd:YAG laser-driven optical parametric oscillator (OPO, Vibrant IR, Opotek Inc., Carlsbad, CA) operated at 2940 nm with a pulse length of 4 ns at 20 Hz frequency, and 2 mJ per pulse. The laser pulses impinged orthogonally from above on the sample surface with quasi-circular focal spots of ~300 μm diameter. A fraction of the ablated sample material was directed towards the mass spectrometer capillary inlet by the flow of the metastable plume in which gas-phase chemical ionization of analyte molecules occurred, generating protonated or deprotonated species in positive and negative ion modes, respectively.

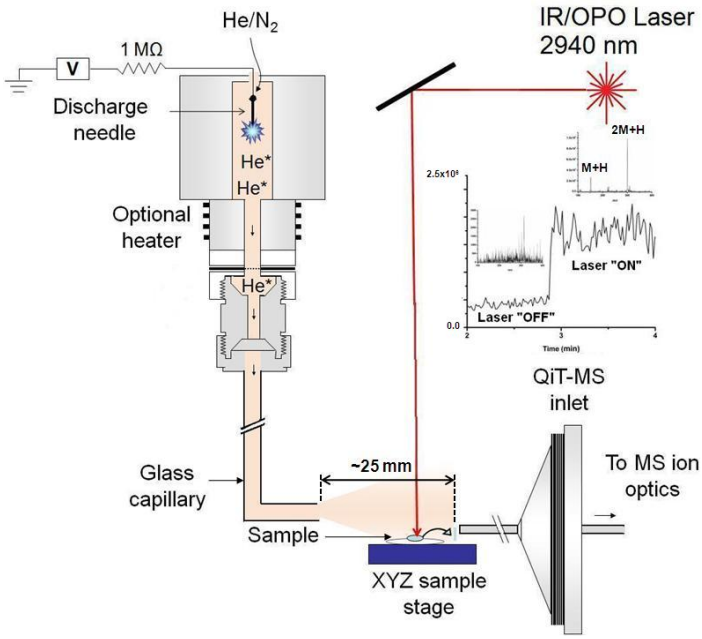

Figure 6.2: Schematic of the IR-LAMICI ion source coupled to a quadrupole ion trap mass spectrometer. The inset shows the total ion current trace observed for the analysis of an acetaminophen tablet with the laser turned off and on.

6.3.2. Computer Simulations

A three-dimensional design geometry file was created depicting the accurate dimensions of the DART gas exit nozzle, sample capillary and MS inlet orifice with the computer-aided design program within the COMSOL Multiphysics® (COMSOL, Inc., Burlington, MA, USA) finite element analysis environment. The modeled flow rates, gases and sample holder spacing matched those used in the DART experiments. All models were built in the absence of electric fields and without regard to the influence of reduced pressure transport originating at the inlet of the mass spectrometer. Transient (200 ms) simulations were performed on a dual Intel Xeon quad core (2.66 GHz) computer with 8 GB memory and 1.5 GB video memory. Simulations required between 0.75 and 12.5 hours to complete depending on the chosen conditions, with higher flow rates requiring longer due to the increased complexity of the fluid dynamics.

6.3.3. Procedure

The TM-DART source (IonSense, Danvers, MA) was coupled to a JMS-T100LC (AccuTOF™) orthogonal TOF mass spectrometer (JEOL, USA, Peabody, MA) for high-accuracy mass measurement experiments performed in positive ion mode using either helium or nitrogen gas. The flow rate of helium gas was varied between 0.55 and 2.0 L min^{-1} to determine its effect on the resulting spectra. The flow rate of nitrogen gas was held at 7.0 L min^{-1}, as lower flow rates did not produce a stable and reproducible baseline signal. Therefore, the effect of varying the nitrogen gas flow could not be evaluated. The distance between the exit of the DART ion source and the sample holder was examined at two positions: (a) in contact with one another and (b) 4 mm apart. These distances were used to compare the spectra obtained from varying gas flow rates. The gas heater temperature was varied between 100 °C and 225 °C to determine the effects of temperature on the resulting spectra. The glow discharge needle voltage of the DART source was set to 3500 V and the discharge and grid electrode voltages were 150 V and 250 V, respectively. The TOF mass spectrometer ion optics settings were as follows: inlet orifice voltage: 20 V for helium DART and 30 V for nitrogen DART; ring electrode voltage: 5 V; orifice 2: 5 V; ion guide bias voltage: 29 V; ion guide peaks voltage: 300 V for helium DART and 500 V for nitrogen DART. The detector voltage was set to 2750 V. Mass calibration was performed by placing a 1.5 mm o.d. × 90 mm-long glass capillary tube dipped in a concentrated PEG solution in the metastable gas stream for 30 s and obtaining a reference mass spectrum. Mass spectral data acquisition, processing, calibration and background subtraction were performed using the built-in mass spectrometer software, MassCenter 1.3.

The IR-LAMICI was interfaced to a LCQ Deca *XP+* ion trap mass spectrometer (Thermo Finnigan, San Jose, CA). Without laser illumination, no salient ionic species were observed in the mass spectrum as the metastable flux was not in direct contact with the sampled surface (Insert, Figure 6.2). However, when laser pulsing was started, intense analyte peaks were observed, suggesting that ions are produced by direct interaction of neutral aerosol particles with gas-phase reactive species. The base peak ion intensity was observed to be largely dependent on the energy of the laser beam and the position of the inlet capillary. Optimum signal intensity was observed for the mass spectrometer inlet capillary positioned ~1 mm above the sampling surface and ~25 mm away from the metastable gas nozzle.

6.4. Comparison of Helium and Nitrogen TM DART

Helium and nitrogen-induced DART MS spectra of neat deltamethrin (Figure 6.3) and permethrin (Figure 6.4) standards deposited on a melting point capillary were obtained in positive ion mode to first identify mass spectral peaks specific to these pyrethroid insecticides. Figures 6.3 (a-b) and 6.4 (a-b) show helium DART MS spectra of neat deltamethrin and permethrin standards, respectively, at 225 °C (a) and 150 °C (b) at a flow rate of 1.5 L min^{-1}.

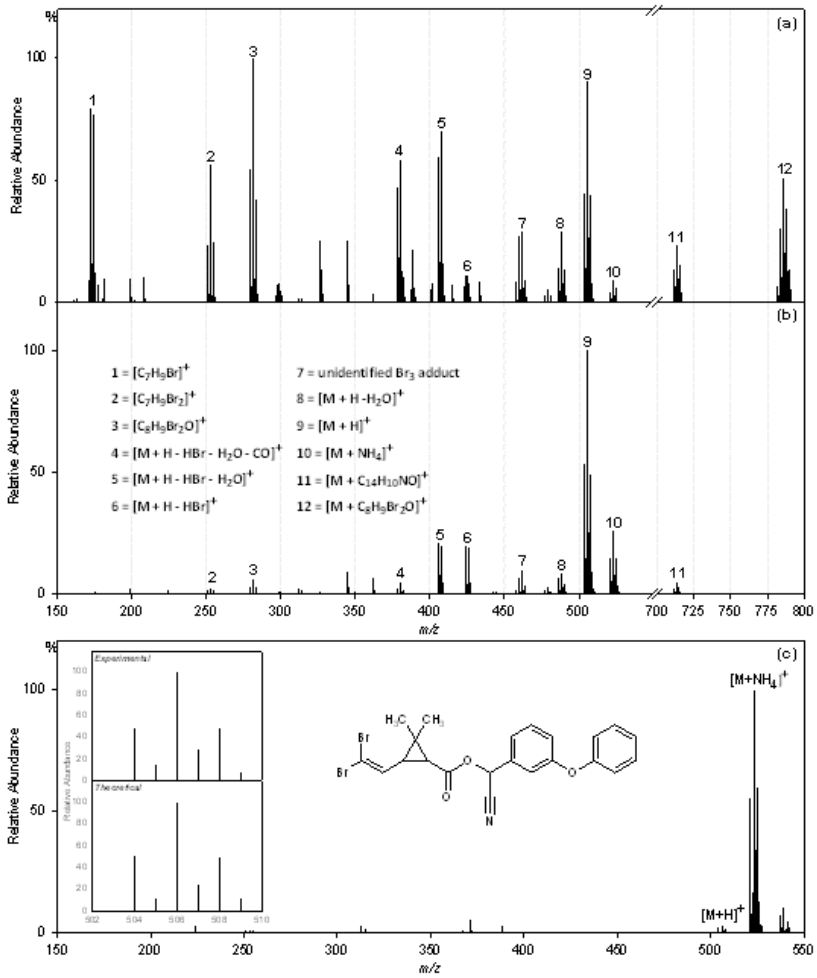

Figure 6.3: Helium DART MS spectra of a neat deltamethrin standard obtained at 225°C (a) and 150°C (b) with 1.5 L min^{-1} gas flow rate. Fragmentation is observed when helium is used as the ionizing gas, increasing with increasing temperature. The nitrogen-induced mass spectrum shown in (c) presents a predominant $[M+NH_4]^+$ ion with little-to-no fragmentation (225°C, 7.0 L min^{-1}). The insets in panel (c) show the experimental and theoretical isotopic structures of the deltamethrin $[M+H]^+$ ion observed in the helium-induced spectra.

Figures 6.3c and 6.4c show their nitrogen DART MS spectra obtained at 225°C and 7.0 L min^{-1}. In the case of deltamethrin it was observed that helium at 150 °C yielded a higher abundance of the protonated molecule (peak 9) while producing less fragmentation in comparison to helium analysis at 225 °C. Also, intense fragment ions pertaining to mono- (peak 1) and di-brominated (peak 2) fragment ions arising from alpha-cleavage, ester bond cleavage (peak 3), and dehydration (peaks 4, 5, and 8), among

others, were observed at 225 °C. In addition, adducts of thermally-induced fragment ions with neutral precursor molecules were observed. Peaks 11 and 12 corresponded to neutral deltamethrin molecules adducted with the cyano-containing benzyl cation, $[C_{14}H_{10}NO]^+$, and the doubly-brominated cation indicated as peak 3, respectively. Conversely, nitrogen DART performed at 225 °C resulted in low intensities of fragment ions and protonated molecules. The base peak was the ammonium adduct ion (peak 10) as commonly observed for compounds containing carbonyl functional groups.[157] The presence of bromine atoms in the deltamethrin molecule yielded characteristic Br_{1-2} isotopic patterns, which aided in the identification of ionic species. As an example, the inset in Figure 6.3c shows the experimental isotopic distribution of the protonated deltamethrin monomer, which was consistent with the expected theoretical distribution.

The helium DART analysis of permethrin yielded fewer fragment ions and only a slight increase in their abundance when increasing gas temperature from 150 °C to 225 °C (Figure 6.4). The identities of the fragment and adduct ions of permethrin were similar to some of those identified in the deltamethrin case for both helium and nitrogen, but with some interesting differences. The ions observed for helium experiments were a result of alpha-cleavage (peak 1), $[C_{13}H_{11}O]^+$ benzyl cations (peak 2), ester bond cleavage (peak 3), HCl and H_2O losses from the protonated molecule (peaks 4 and 5, respectively), and the protonated (peak 7) and ammoniated (peak 8) adduct ions. Interestingly, the permethrin $[M]^{+\bullet}$ molecular ion (peak 6) was observed, which was not the case for deltamethrin. The absence of the stabilizing effect caused by the cyano functional group in permethrin, resulted in a low abundance of its protonated molecular ion (peak 7), the base peak instead corresponding to the HCl neutral loss (peak 4).

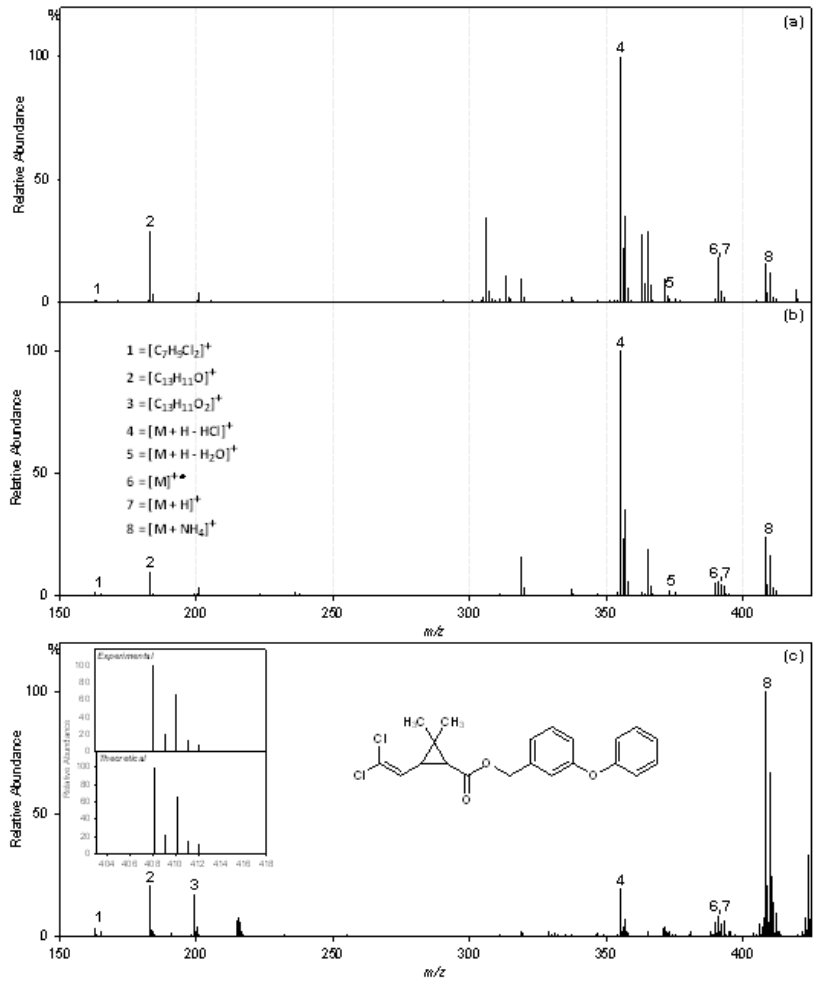

Figure 6.4: Helium induced DART MS spectra of a neat permethrin standard obtained at 225°C (a) and 150°C (b) with 1.5 L min^{-1} gas flow rate. Significant fragmentation exists when helium is used as the ionizing gas, increasing only slightly with increasing temperature. The nitrogen induced (225°C, 7.0 L min^{-1}) mass spectrum (c) results in an abundant $[M+NH_4]^+$ ion but also considerable fragmentation compared to that of deltamethrin (see Figure 2). Insets in panel (c) show the chemical and isotopic (experimental and theoretical) structures of the permethrin pesticide. The inset showing the isotopic distribution corresponds to the $[M+NH_4]^+$ ion of the nitrogen-induced spectra.

Helium DART MS analysis of cypermethrin, the chlorinated analog of deltamethrin, showed the same relative fragment intensities and adduct ions as for deltamethrin, reinforcing the notion of a stabilization effect driven by the cyano moiety (data not shown). Similar to deltamethrin, the ammonium adduct (peak 8) of permethrin was the base peak in the nitrogen spectrum (Figure 6.4c), with only a small relative

amount of fragment ions present. The lower-energy of nitrogen metastables and the lower thermal conductivity of nitrogen are believed to be the reasons behind the reduced fragmentation observed in nitrogen when compared to helium. Interestingly, a relatively larger degree of fragmentation was observed in the nitrogen spectra of permethrin when compared to deltamethrin, likely due to a lack of charge stabilization of the $[M+H]^+$ ion via the cyano group. As expected, chlorine atoms present in permethrin were responsible for the characteristic Cl_{1-2} isotopic patterns, shown in the inset in Figure 6.4c, which details the experimental and theoretical isotopic distributions of the ammoniated permethrin monomer ion.

6.5. Effect of Flow Rates on TM DART

As indicated in Figure 6.1, the sample holder and DART ion source configuration allows for the distance between the gas outlet of the DART source and the bed net to be adjusted. TM-DART analyses of a bed net conventionally-treated with 55 mg m^{-2} deltamethrin were conducted at 150 °C by varying the helium gas flow. At each flow rate, two positions of the sample holder were tested: in contact with the ion source gas nozzle (▲) and 4 mm apart (×) from it (Figure 6.5). With the exception of the data point at 1.5 L min^{-1}, it was observed that when the ion source outlet was in contact with the sample holder, the ion intensity increased with the gas flow rate. It is not clear as to why the data point at 1.5 L min^{-1} deviated from the upward trend, but it is possible that it was caused by improper placement of the holder. The opposite effect was observed at a source-to-holder distance of 4 mm, where the ion intensity showed a downward trend with increased flow rate.

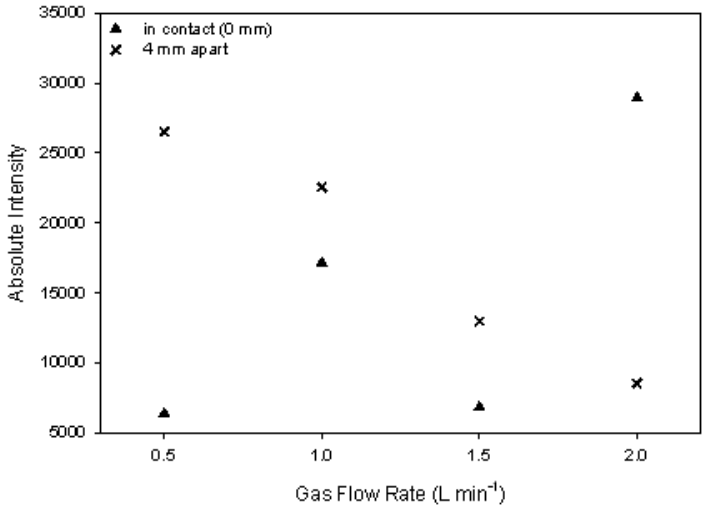

Figure 6.5: Effect of helium gas flow rate on the absolute intensity of the deltamethrin $[M+H]^+$ ion during TM-DART analysis of a 55 mg m^{-2} conventionally-treated bed net. The adjustable distance between the gas exit of the DART source and the sample holder (see Figure 6.1) allowed two settings to be examined at various gas flow rates: in contact with one another (▲) and 4 mm apart (×). Set gas temperature was 150°C in all cases.

The trends seen in Figure 6.5 are supported by computational fluid dynamic (CFD) simulations of the ionization region. When the sample holder is 4 mm away from the DART gas nozzle, the reactive gas stream collides into the peripheral regions of the Macor sample opening, deflecting some of the reactive gas plume away from the bed net (Figure 6.6). When the gas flow rate is set to 0.5 and 1.0 L min^{-1} (Figure 6.6 a and b, respectively), the deflection is fairly homogenous with respect to the sample hole opening. As the gas flow rate increases to 1.5 and 2.0 L min^{-1} (Figure 6.6 c and d, respectively), the deflected gas travels further away from the sample entrance and in more sporadic directions. Although the overall gas velocity remains high, the presence of fewer reactive species passing through the net may account for the lower intensity observed as the gas flow rate is increased in this configuration.

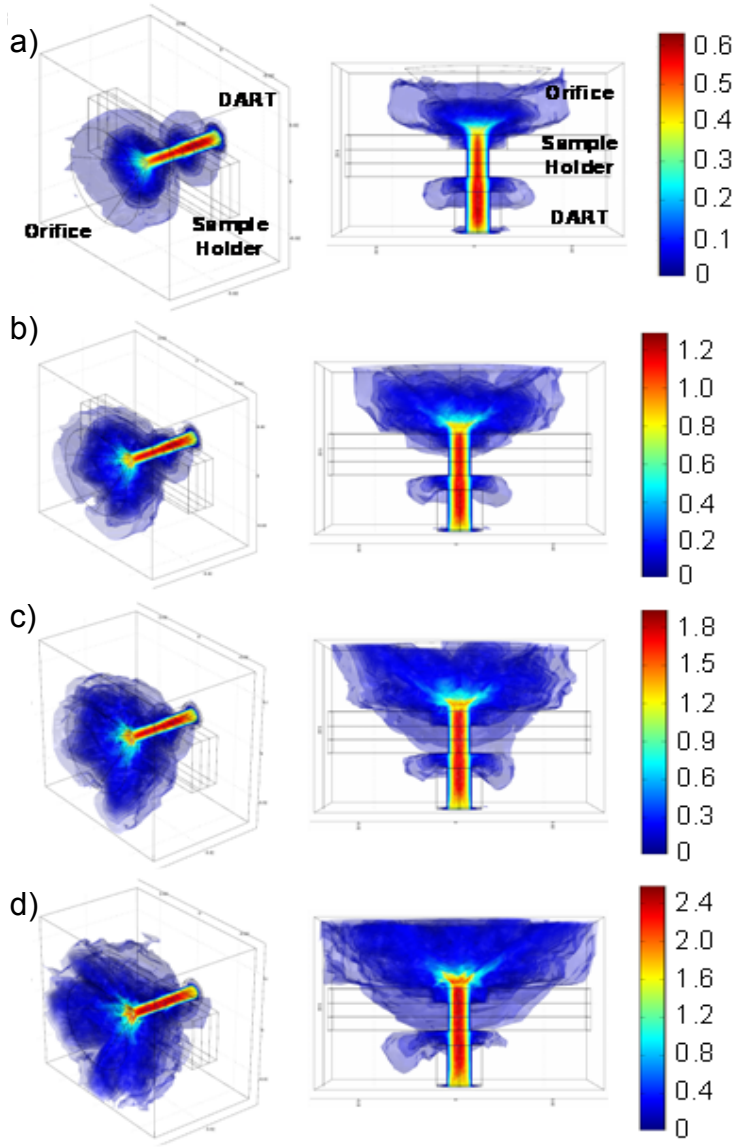

Figure 6.6: CFD simulations at a) 0.5, b) 1.0, c) 1.5 and d) 2.0 L min^{-1} helium at 150 ºC when the DART gas nozzle is positioned 4 mm away from the sample holder. The images on the left show a 3D perspective of the system, the middle images show the gas flow from above, and the heat map scales on the right are the gas velocities in m s^{-1}.

Conversely, when the DART gas nozzle is directly in contact with the sample holder opening, the high velocity reactive gas is forced through the bed net without gas deflection (Figure 6.7).

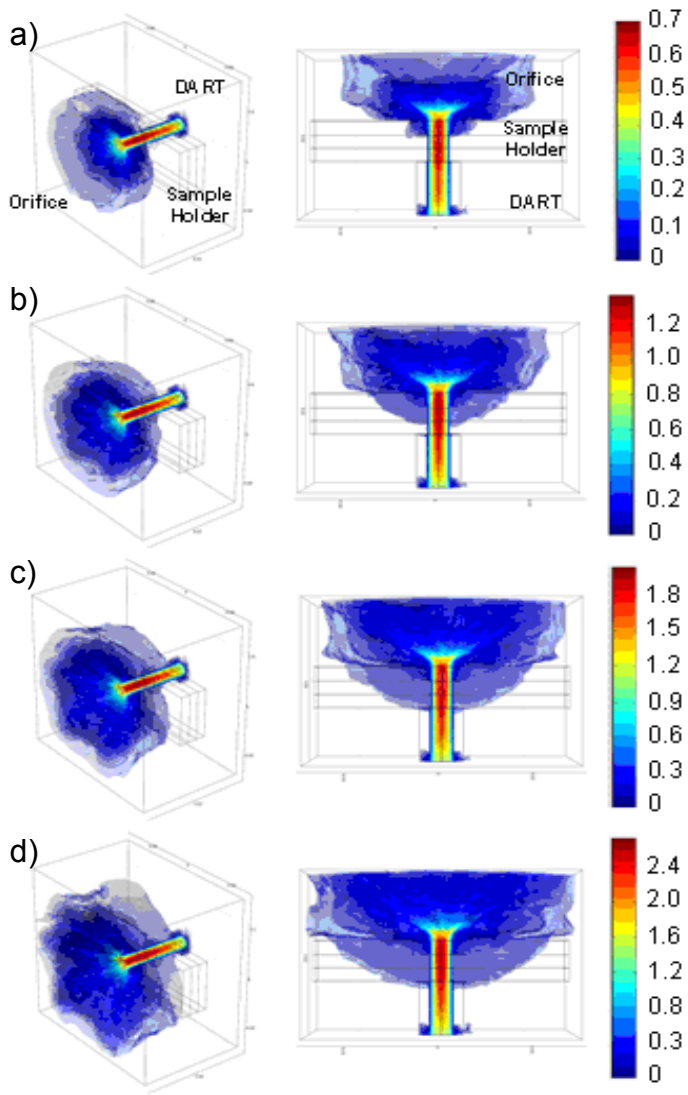

Figure 6.7: CFD simulations at a) 0.5, b) 1.0, c) 1.5 and d) 2.0 L min^{-1} helium at 150 ºC when the DART gas nozzle is positioned in contact with sample holder. The images on the left show a 3D perspective of the system, the middle images show the gas flow from above, and the heat map scales on the right are the gas velocities in m s^{-1}.

The overall gas velocities are very similar to those in the previous configuration, but the presence of more reactive species hydrodynamically focused to contact the net may account for the higher experimental sensitivity observed.

6.6. Quantitative Assessment of TM DART

Extracted ion chronograms obtained from TM-DART analyses of bed nets conventionally-treated with increasing levels of deltamethrin are shown in Figure 6.8. The conditions chosen for each analysis were those that overall yielded the highest abundances of the protonated ion (using helium) or ammonium adduct ion (using nitrogen) based on the results shown in Figures 6.3 and 6.4.

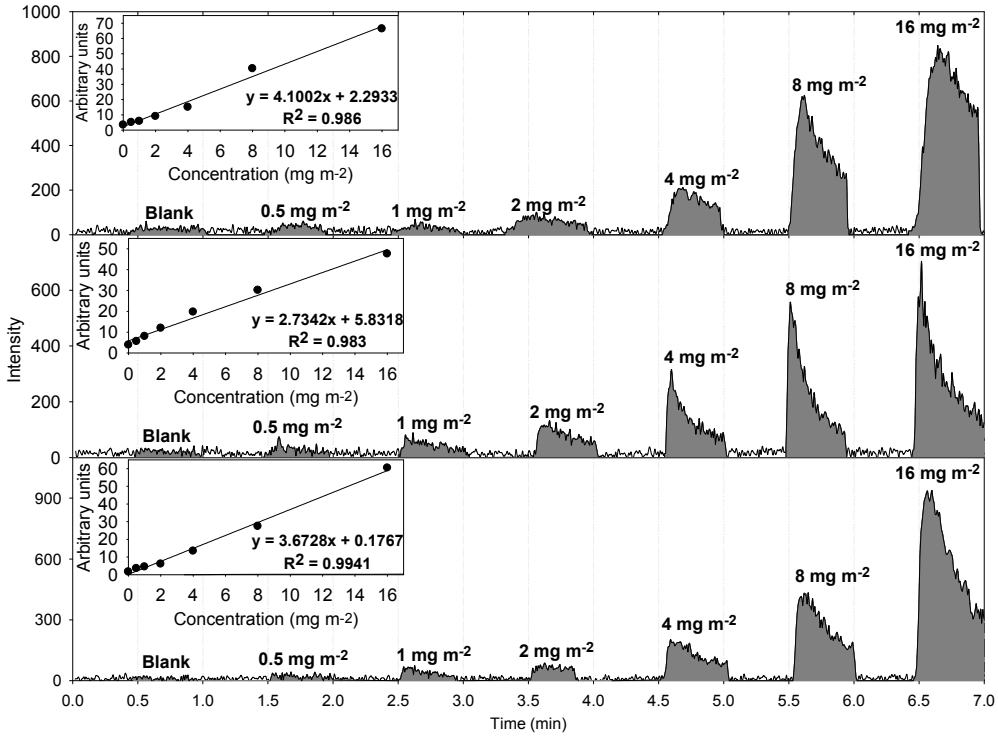

Figure 6.8: Extracted ion chronograms for the DART analysis of bed nets coated with increasing levels of deltamethrin using the custom-made sample holder. Experiments were performed using helium (0.5 L min^{-1} (top) and 2.0 L min^{-1} (center) at 150°C) and nitrogen (7.0 L min^{-1} at 225°C (bottom)). Insets show integrated peak areas as a function of bed net insecticide concentration. The $[M+H]^+$ and $[M+NH_4]^+$ ions are plotted for helium and nitrogen, respectively.

Analysis with helium was performed at 150°C, 0.5 L min^{-1}, and 4-mm source-to-holder distance (Figure 6.8, top), or 150°C, 2.0 L min^{-1} and the source in contact with the holder (Figure 6.8, center). Nitrogen analysis was performed at 225°C and 7.0 L min^{-1}

with a source-to-holder distance of 4 mm (Figure 6.8, bottom). Bed nets treated at various concentration levels (blank-16 mg m^{-2}) were sampled for approximately 30 s. The shaded regions represent the areas integrated for each concentration level, which are plotted in the insets. The observed linearity (R^2 = 0.983 or better) suggests that TM-DART has potential for semi-quantitative determination of pesticides in ITNs, and that levels as low as 0.5 mg m^{-2} of deltamethrin can be detected with either helium or nitrogen used to effect ionization. With a sampling area of approximately 20 mm^2, this is equivalent to a detection limit of approximately 10 ng of deltamethrin.

6.7. Investigating the Fluid Dynamic Contributions to IR-LAMICI

To better understand the atmospheric transport of the ablated particles, a time resolved (t = 200 ms) three-dimensional CFD simulation with particle tracing was created with COMSOL Multiphysics® (COMSOL, Burlington, MA). The simulated setup consisted of the metastable gas glass nozzle, a typical pharmaceutical tablet, and the inlet capillary. Due to convergence limitations, the models were constructed without electric fields and the reduced pressure transport influence of the inlet capillary. Particle trajectories originating on the tablet surface and extending upwards every 10 μm from five points on a laser spot size of 300 μm in diameter (total of 150 particles) were simulated (Figure 6.9a). The simulated gas velocity map depicts the high velocity gas jet deflecting slightly upwards above the tablet surface and the inlet capillary (Figure 6.9b). The upward gas flow affects particle flow sending a large part of the simulated particles above the inlet capillary (Figure 6.9c). Gas flow recirculation directing some particles backwards towards the gas capillary was also observed, a phenomenon previously

predicted for DART MS.[18] These simulations indicate that further improvement of ion transmission in IR-LAMICI could result in large gains in sensitivity.

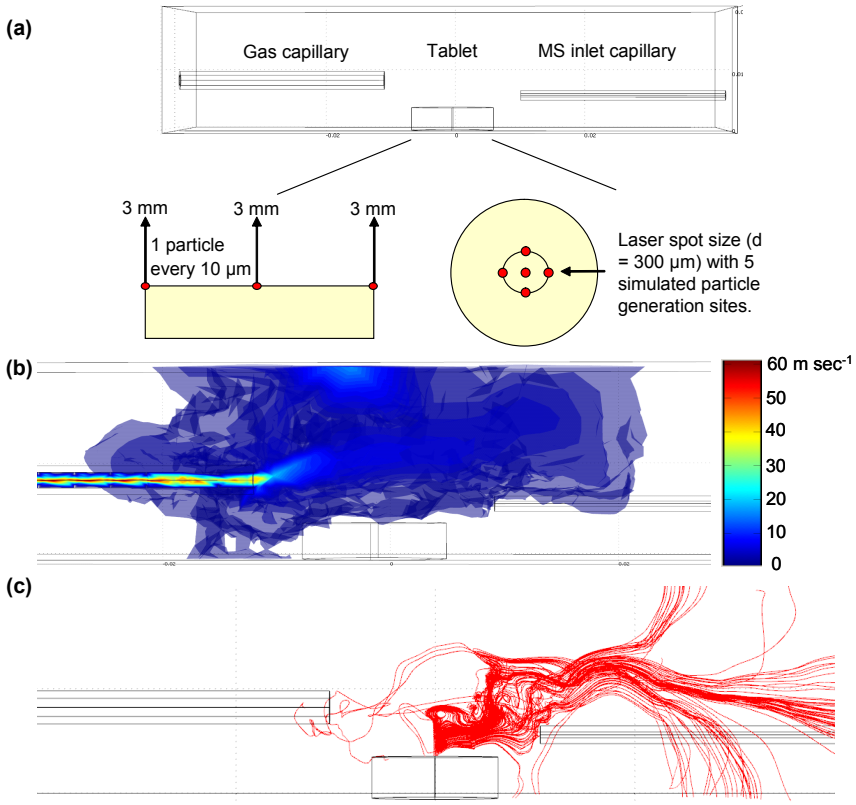

Figure 6.9: Three-dimensional CFD simulations of the IR-LAMICI setup: (a) 150 particles were simulated originating from a 300 µm-diameter laser spot; (b) gas velocity map and velocities; (c) particle trajectories originating from the positions outlined in (a). The laser spot diameter was measured by taking an optical image (Olympus BX41, optical microscope) of a single shot laser ablation spot.

6.8. Direct Analysis With IR-LAMICI

The potential of IR-LAMICI for direct MS analysis and imaging was investigated by using a variety of samples previously tested in our laboratory by DART and/or DESI. Figure 6.10a shows the IR-LAMICI spectrum obtained for a counterfeit artesunate antimalarial tablet collected in the Republic of Cameroon. The signal at *m/z* 320 was identified as the protonated chloroquine molecule, a wrong active ingredient previously detected in this sample by both DART and DESI. This assignment was verified by the

observed isotopic abundance pattern (shown as inset) and by MS/MS experiments (data not shown). The signal at *m/z* 247 resulted from the loss of $C_4H_{11}N$. Peaks corresponding to the correct active ingredient, artesunic acid, were not detectable.

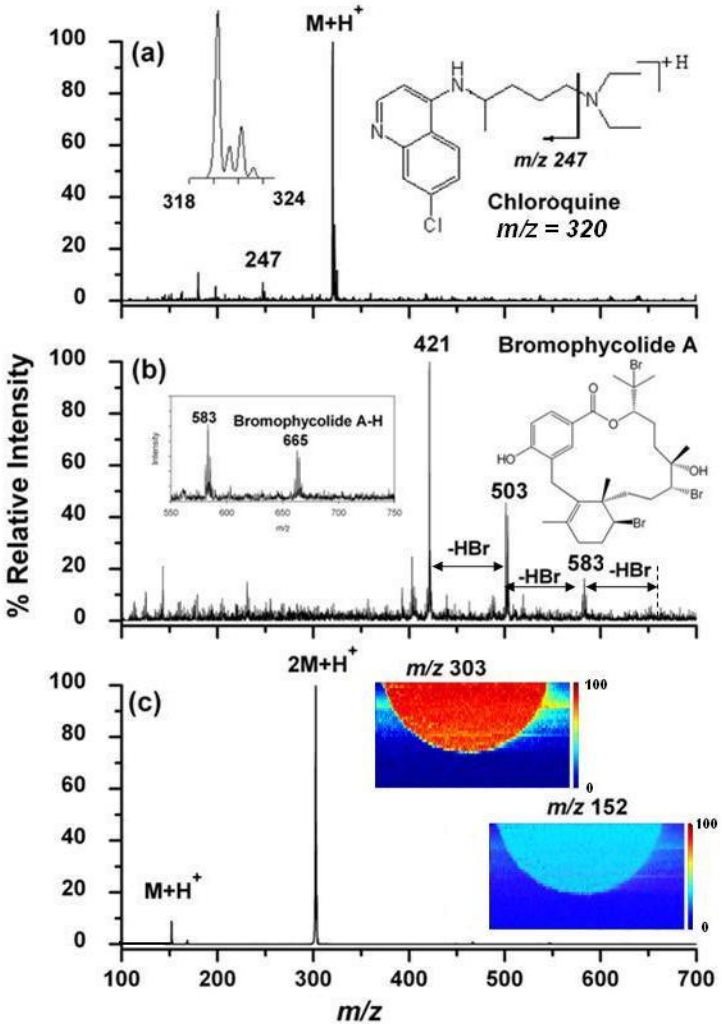

Figure 6.10: IR-LAMICI MS analyses of (a) a counterfeit artesunate antimalarial drug tablet collected in Cameroon; (b) a red macroalga, *Callophycus serratus*, showing the presence of bromophycolides; and (c) a Tylenol® tablet (325 mg acetaminophen). The inset in (b) shows a typical negative ion mode DESI MS spectrum of a similar tissue sample, with the peak at *m/z* 665 corresponding to [bromophycolide A/B - H]$^-$ and the peak at *m/z* 583 to [bromophycolide A/B - HBr]$^-$ and/or [bromophycolide E - H]$^-$). The insets in (c) show false-color scale IR-LAMICI MS images of the distribution of acetaminophen monomer and dimer ions on the tablet.

In a separate set of experiments, tissue samples of the red macroalga *Callophycus serratus* previously investigated by DESI[158] were probed by negative ion mode IR-

LAMICI (Figure 6.10b). The obtained mass spectrum shows the presence of several ionic fragments originating from HBr losses from the deprotonated bromophycolide A molecule, a secondary metabolite involved in surface-mediated chemical defense mechanisms. Comparison with a typical DESI MS spectrum of similar tissue (insert) where the intact bromophycolide $[M-H]^-$ was readily observed, suggested that during IR-LAMICI the amounts of internal energy deposited on analyte molecules are larger than in DESI. However, a more extensive optimization of the numerous variables involved in IR-LAMICI (e.g. laser pulse length, laser power, metastable flux) would be necessary for a more thorough comparison to other, more established, ambient MSI techniques.

6.9. Mass Spectrometry Imaging Utilizing IR-LAMICI

The full potential of IR-LAMICI was best showcased in MSI experiments. The successful coupling of IR-laser ablation with metastable-induced chemical ionization resulted in a truly-ambient plasma-based small molecule imaging platform for MS. The IR-LAMICI spectrum of a Tylenol® (325 mg) tablet showed peaks at *m/z* 152 and 303, corresponding to the protonated acetaminophen molecule and dimer, respectively (Figure 6.10c). The protonated dimer was found to be more intense than the protonated monomer, likely due to two factors. First, laser ablation generates significantly large amounts of neutral sample material off the sample surface, thus favoring the formation of dimeric species at higher acetaminophen concentrations. Secondly, the use of an ambient temperature metastable flux, rather than a heated one as in DART, coupled to collisional cooling, promotes more extensive clustering. Similar effects have been observed when comparing atmospheric pressure and MALDI.[159] Assuming uniform distribution of acetaminophen in the tablet and a 10 μm laser depletion layer, the limit of detection was

estimated to be 15-30 pg. The insert in Figure 6.10c shows chemical images constructed from the signals at *m/z* 152 and 303, corresponding to the protonated acetaminophen monomer and dimer, respectively. Images were constructed from individual surface raster scans with an in-house written MATLAB program (Ver. R2008a, Math-Works, Inc., Natick, MA). The total image construction time which includes, image data collection and processing was approximately 40 minutes for a 14 mm x 7 mm area. The images show a relatively uniform distribution of acetaminophen on the tablet surface, indicative of a good tablet formulation practice. The left-to-right streaking effect seen beyond the curved edge boundaries of the tablet images was a result of some of the ablated unionized material depositing on the inner walls of the mass spectrometer inlet capillary. This material was ionized while scanning the subsequent surface pixel. Despite this secondary effect, lateral resolution in these images was sufficiently high to accurately describe the sharply curved tablet edges. The main advantage of IR-LAMICI was that the resolution of a chemical image was determined by the crater size produced with each laser pulse, but not by the size of the metastable gas jet. This was important in acquiring spatially-resolved chemical information for micron-sized surface features.

6.10. Conclusion

The results reported here demonstrate TM-DART as an alternative sampling strategy versus traditional methods of probing sample surfaces for DART MS analysis, with particularly interesting application to the analysis of insecticide treated bed nets. The cavity of the custom-made holder creates an ion tunneling effect directly affecting the spectral appearance, following changes in metastable gas temperature and flow rate, and the distance between the gas outlet and the sample being analyzed. Reproducible, quick,

and easy mounting/dismounting of the sample holder assembly to a fixed position within the ionization region allows a systematic approach to analyzing ITN samples, providing highly-selective semi-quantitative analysis capabilities with throughputs of 60 samples per hour.

We expect that IR-LAMICI will make small molecule ambient MSI more accessible to the end user and enable new applications in the life sciences. Additionally, the use of IR laser ablation to desorb analytes may lead to future implementations of DART for higher molecular weight compounds. As shown by finite element simulations, much improvement is still possible in terms of ion transmission, which should result in greater sensitivity and better detection limits.

CHAPTER 7. CONCLUSIONS AND OUTLOOK

7.1. Abstract

This chapter presents a summary of the results encompassing the fundamental characterization of ambient sampling/desorption ionization MS techniques and the applications presented in this dissertation. This chapter concludes with a discussion of potential future directions and perspective to further expand this work.

7.2. Accomplishments In the Characterization and Implementation of Ambient Sampling/Desorption Ionization Techniques

7.2.1. Fundamental Insights

It is safe to say that our understanding of DART has improved greatly through the efforts presented in this dissertation. Paramount to these findings was the use of finite element method simulations and carefully designed experiments to yield insight into the ionization region.[18] The first finite element simulation models of a home built DART-type ion source which provided spatial and temporal representation of the thermal gradients, particle trajectories and fluid dynamics in the ionization region and within the hardware itself. Models and temperature probe experiments suggested that thermal dissipation into the surrounding atmosphere contributed to heating of the sample before its introduction into the ionizing plume. Depending on the sample properties, this initial heating may contribute to premature thermal desorption before ionization. Therefore, sensitivity loss is a major concern prior to or during sample positioning. Additionally, various sample geometries and spatial orientations have a drastic effect on the fluid dynamic stream lines resulting in turbulent gas flow and particle trajectories.

Investigations of the DART internal energy distribution has led to a better understanding of the energetic contributions of desorption and ionization.[160] It was revealed that internal energy increases with higher gas flow rates and temperature. This proceeds through several pathways with the major factor being the proton transfer reactions during ionization. During this process, the excess energy that was released was sufficient enough to fragment labile molecules. Other important contributions include collision-induced dissociation from the added pressure from the high flow gas flow rates of DART into the first differentially-pumped region of the mass spectrometer. Additional factors like direct Penning-ionization and pyrolysis had small impacts, however, they could become significant under different operational conditions.

One of the most important findings was the study of the DART reactivity in space series of experiments which explored multiple experimental effects such as sensitivity, reproducibility, dynamic range and ion suppression in a spatial manner. Depending on the concentration of the sample, there were distinct "hot spots" in the ionization region where sensitivity was highest. For instance lower concentrations (<100 μM) the best sampling position is in the middle of the ionization region in line with the DART gas nozzle and the inlet capillary of the mass spectrometer. This position provided a hot enough environment for thermal desorption and minimized losses from ion transmission. Conversely, at higher concentrations (>500 μM) the best position was directly in front of the DART gas nozzle where the higher temperature thermally desorbed more analyte mitigating any losses during ion transport.

This study also demonstrated the susceptibility of DART to ion suppression. Regardless of position and temperature, ion suppression was significant between two

analytes with the same boiling point but different proton affinities with suppression levels greater than 15x for most conditions. The same effect but to a lesser degree (<4x) was observed for the reverse situation with molecules of the same proton affinities but different boiling points. The problem of ion suppression was exacerbated if the same analytes were positioned in different sampling points in space. Suppression several orders of magnitude greater than if sampled in the same spot was observed. Although the experiments used continuous infusion of liquids to acquire steady-state signals, it was expected that solid samples and conventional quick screening methods would show similar if not higher ion suppression due to matrix composition and instabilities in the ionization region.

7.2.2. Instrument Development and Applications

There were three significant instrumental and application advances with DART demonstrated in this dissertation: TM sampling for reproducible sample placement, ion mobility spectrometry (IMS) coupling to detect toxic chemicals and chemical warfare agent simulants and coupling to laser ablation for MS imaging (IR-LAMICI).

TM DART analysis mitigated concerns of positioning the sample material and its effect on ion transmission. With the insecticide-treated bed nets, the holes in the screen allowed for the reactive gas flux to travel through the sample. This enabled a greater surface area of analyte to be thermally desorbed and ionized. Compared to solvent extraction methods coupled to chromatography, TM DART throughputs of up to 1 sample min^{-1} with just a single screen holder showed that comparable analysis could be obtained with DART in a more high-throughput manner. Implementations of TM DART

with an automated sample rail system and 96 “well” sampling array are now commercially available.[161]

Coupling TM DART with IMS provided a reproducible sampling strategy to detect toxic chemicals and chemical warfare agent simulants.[162] The advantage of IMS as the detection platform over MS was that IMS does not require reduced or vacuum conditions, thereby reducing the instrumental complexity in a potential field portable platform. The metalized screens used in this study were coated with an absorbent graphitized carbon material (Carbopack X) which was believed to provide better adhesion of sample to the solid substrate. Limits and probability of detection were both improved using these substrates over conventional sample analysis on a melting point capillary. Additionally, the IMS platform was used in a multiplexed acquisition mode. Multiplexing improved the duty cycle of the instrument resulting in signal-to-noise ratio gains for most tested sequences ranging from 3-5x over conventional acquisition.

The IR-LAMICI source circumvented the spatial resolution limitations of the DART reactive gas flux out of the source by using laser ablation to raster a sample’s surface. The DART reactive gas then targeted the neutral plume generated by the ablation. As a result, open-air small molecule imaging with a plasma-based ionization source was possible and advantageous for those in the life sciences to use. Besides the imagining capabilities, this two-step desorption/ionization process negated the need for thermal desorption by DART. This could lead to analysis of compounds above the upper mass limit of DART (800-1000 Da). Paramount to the development of this technique is improving the ion transmission. Simulations suggested that the majority of the neutral plume was blown away from the entrance of the mass spectrometer. Using lower gas

flow rates and replacing the traditional entrance ceramic capillary with a flared capillary should improve sensitivity.

7.3. Proposed Future Directions

7.3.1. Fundamental Insight Awaiting To Be Explored and Exploited

Moving forward, there are many projects that should be explored to gain a better understanding of the DART fundamental processes. First, a follow-up study on the dynamic range, sensitivity in space and ion suppression experiments should be duplicated using nitrogen as the DART gas. Nitrogen will shift to be primary choice for reactive gas due to the rising costs and difficult accessibility of purified helium. Nitrogen's thermal conductivity is lower than helium which makes desorption of higher molecular weight compounds more difficult. Also, some of the gas-phase reactive chemistry with nitrogen is different from helium. However, costs will become an overriding factor for future screening and detection platforms. Jumping ahead of the curve and performing these fundamental studies will make the transition faster.

Another fundamental project that should be pursued is an in-depth investigation into TM DART gas dynamics and mesh/screen material properties. Similar fundamental studies performed on TM DESI substrates facilitated a better understanding of strand composition, optimal dimensions and distances to use for reproducible analysis. Additionally, absorptive and selective coatings on these materials will greatly improve the capabilities of TM DART. As indicated earlier with the Carbopack X coatings, the interaction between reactive species and sample desorption is intimately tied to the surface functionality. Some potential directions for these studies could begin with traditional solid phase extraction and column chromatography coatings/stationary-phases

and grow towards selective binding on the substrates with molecular imprinted polymers, aptamer and antibody coating. It would not be hard to imagine fabrication of surface selective screen materials which would greatly enhance ionization efficiencies and lower suppression for targeted low abundance compounds from biological fluids.

7.3.2. Direction For Current Applications

MS imaging with IR-LAMICI will grow to be a complementary imaging tool to other established techniques like MALDI imaging. Then major benefit of IR-LAMICI is its open-air format enabling the imaging of awkwardly shaped samples. The major factor that it must overcome is the limited mass range of ionization. Laser ablation can help extend this mass range 500-1000 Da for singly-charged molecules if pursued. However, much larger biomolecules like proteins will be not be sampled.

One of the biggest potential markets for DART will be in the homeland security field. DART is a simple ionization technique to operate and the primary ions formed are singly charged which make them easy for identification. The capabilities to shrink the size of DART are available which would decrease both the power required and the amount of gas needed for operation. Both these merits would make DART a more field-friendly platform to couple to miniature ion mobility and mass spectrometers. Most importantly, DART is a simple and safe ionization technique that government and military employees could operate with little training.

7.3.3. Emerging Applications

One of the most promising emerging applications with DART is metabolomic screening. Our group has begun investigating ovarian cancer serum for biomarkers for an early diagnosis protocol.[101, 102] This project began with sampling processed serum off of

melting point capillaries. To improve sensitivity and reprocibility it has been transitioned toward TM sampling. However as mentioned previously, fundamental studies into TM DART substrates have not been conducted yet. Sampling off of plain metal screen meshes is likely not the optimal protocol since they are difficult to heat and may quench the metastables in the reactive gas. Passing a current through the steel mesh to rapidly heat the surface is a possible approach to improve desorption. Other variables like sample deposition methods must also be thoroughly investigated before this approach is fully adopted. From experience, sample deposition and drying methods were more flexible with the Carbopack X coated screens than the plain stainless steel meshes. This may have been due to the added surface roughness and porosity of the substrate.

APPENDIX A. Application of Direct Analysis In Real Time Mass Spectrometry to Pharmaceutical Forensics

A.1. Abstract

A vital component of malaria control rests on the availability of good quality artemisinin-derivative based combination therapy (ACT) at the correct dose. However, there have been increasing reports of poor quality and counterfeit medicines being distributed for the treatment of malaria. This is a significant public health concern that challenges the capabilities of both the pharmaceutical industry and the governments of developing countries. Collaborations across many agencies and institutes have led to a comprehensive assessment of tablets with an assortment of analytical techniques. However, at the core of these studies are high-throughput MS screening tools utilizing ambient sampling/ionization techniques. DART and DESI provide the first tier of advanced screening approaches to monitor the contents of field collected samples in a time-scale that is orders of magnitude faster than direct infusion ESI, liquid chromatography or other analytical detection platforms. Described in this chapter are examples taken from several studies where DART and other direct ionization tools have helped tackle the spread of counterfeits in developing countries.

A.2. Substandard and Counterfeit Antimalarials

A.2.1. Outline of Counterfeit Drugs' Impact on Society

Drug counterfeiting is a well-recognized public health problem. It accounts for an estimated $35 billion/year financial impact to the pharmaceutical industry alone, without considering the enormous disease and financial burden placed on patients and healthcare

systems.[163, 164] The current definition of counterfeit medicines used by WHO since 1992 states that: *"A counterfeit medicine is one which is deliberately and fraudulently mislabeled with respect to identity and/or source. Counterfeiting can apply to both branded and generic products and counterfeit products may include products with the correct ingredients, wrong ingredients, without active ingredients, with insufficient quantity of active ingredient or with fake packaging"*. Hence counterfeit drugs are, by definition, the products of criminals.

Counterfeit drugs are drugs sold illegally, where the identity of the source is deliberately and fraudulently mislabeled in a way that it is suggested to be the genuine product. Counterfeit drugs may include those without the expected active ingredient, with an insufficient quantity of the active ingredient, with wrong active ingredients, or with fake packaging very closely resembling the genuine product.[165] The World Health Organization (WHO) estimates that about 10% of all pharmaceutical products sold worldwide are counterfeit, but these figures should only be regarded as estimates.[19] It is believed that counterfeits probably comprise approximately a large portion of those drugs sold over the Internet from pharmacies that conceal their physical address.[166]

In developed countries, counterfeit drugs most commonly reach consumers through dubious internet "pharmacies". For example, in June 2010 the US Food and Drug Administration issued a warning of a fake version of the flu treatment Tamiflu (oseltamivir) being sold online that could be dangerous to people allergic to penicillin.[167] The so called "generic Tamiflu" contained cloxacillin, a penicillin that could cause unexpected and inexplicable severe allergic reactions. This type of counterfeit drugs containing "wrong" active pharmaceutical ingredients (APIs), are nowadays the norm

rather than the exception, not only leaving the patient's condition untreated, but also potentially engendering drug resistance and triggering unexplained adverse reactions. For these reasons, it is important not only to distinguish fake from genuine drugs, but also to characterize the chemical composition of the latter.

A.2.2. Counterfeit Antimalarials

Artesunate, first developed in the People's Republic of China, is an antimalarial derivative of artemisinin considered vital for the treatment of this disease.[168] It is widely used as part of mono- or combination therapies in South East Asia and increasingly in Africa for the treatment of *Plasmodium falciparum* malaria. Its relatively high cost and demand has made it a preferred target for counterfeiters.[169] Counterfeit artesunate was first found in Cambodia in 1998 when relatively inexpensive tablets were discovered.[170] A recent stratified random survey of the proportion of poor quality oral artesunate sold at medicine outlets in the Lao PDR showed that 90% was counterfeit.[171] In 2008, a multidisciplinary forensic international team tracked the origin of a subclass of counterfeit artesunate tablets using various complementary analytical techniques which included: liquid chromatography, ambient MS, X-ray diffraction spectroscopy, stable isotope ratio MS, gas chromatography, and palynological analysis.[172] Despite the success of this investigation, the ever-growing sophistication of counterfeit drugs prompts for the constant development of increasingly more in-depth pharmaceutical analysis approaches for investigating their composition and origin.

A.3 Experimental

A.3.1. DART MS Analysis

A DART-type[173] or commercial DART ion source interfaced to a time-of-flight mass spectrometer (JEOL AccuTOF™, Peabody, MA) was used in all cases. All experiments were performed in positive ion mode. Ion optics settings were as follows: inlet orifice voltage 30 V, ring electrode voltage 5 V, orifice-2 5 V, ion guide bias voltage 29 V, ion guide peaks voltage 300 V. The detector voltage was set to 2,650 V. The DART ion source settings were as follows: high-purity He (99.999% ultrahigh purity helium, Airgas, Atlanta, GA) flow rate 2-6 L min^{-1}, heater temperature 200 ºC, glow discharge needle voltage 1.5-3 kV, grid electrode voltage 50-200 V, distance between ion source and MS orifice 1.5-3 cm. Mass calibration for accurate mass determinations was performed before and after each sample by placing a 1.5 mm o.d. x 90 mm long glass capillary dipped in polyethylene glycol 600 (PEG, Sigma Aldrich, St. Louis, MO) in front of the DART source for 30 s, and obtaining a reference mass spectrum. Sample tablets were held in the ionization region with stainless steel tweezers and data was acquired for 30 s. Mass spectral data processing, calibration and background subtraction were performed using the built-in mass spectrometer software (MassCenter, v. 1.3). DART MS data were exported in ASCII format as JEOL-DX centroided spectra and searched against an in-house library of potential $[M+H]^+$ ions and related fragment ion species, derived from 238 common drugs found in the List of Essential Drugs supplied by the WHO.[161] A match was considered positive if the difference between the experimental and theoretical accurate masses was less than 5 mmu.

A.4. Detection of Counterfeit Medicines Acquired In South East Asia and Cameroon

In an on-going project in the Fernández group, funded by the Bill and Melinda Foundation and in collaboration with the Centers for Disease Control (CDC) and Prevention (Atlanta, GA), the London School of Tropical Medicine and Hygiene (LSHTM) and the Mahosot Hospital in Vientiane (Laos) assessed the severity of antimalarial counterfeiting in SE Asia and Africa by both DART MS and DESI MS. Analysis of a genuine Mekophar artesunate tablets by DART MS generated peaks corresponding predominantly to artesunic acid fragment species. Suspected counterfeit samples showed a peak at *m/z* 320.1891 assigned as a proton bound adduct of an unknown species, presumably a API. No peaks corresponding to artesunic acid species could be observed in this spectrum. The isotope pattern of the peak corresponding to this unknown AI, has a relative abundance of 100.00 % for the $[M+H]^+$ ion and 32.27 % for the $[M+H+2]^+$ ion, a ratio of approximately 3:1 indicating the presence of a single Cl atom in the molecule (the relative isotope abundance of ^{35}Cl is 75.77 % and that of ^{37}Cl is 24.23%) (Figure A.1). The DART spectrum was then imported into the MS tools software and elemental composition calculations suggested that the primary candidate corresponded to chloroquine. DESI-MS confirmed this identity indicating the samples were counterfeits.

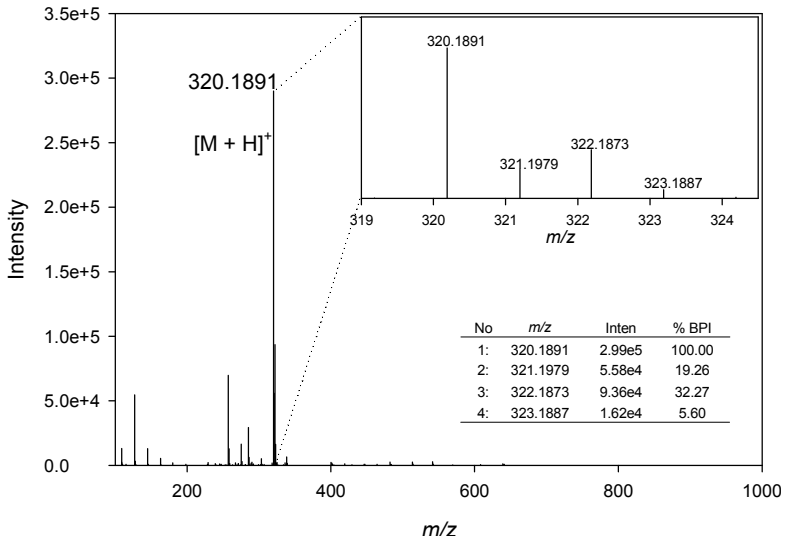

Figure A.1: Positive mode DART spectrum of sample Cam S5/07. The insert shows the isotopic signature of the ion at *m/z* 320.1891.

Duocotexcin samples, a synergistic artemisinin combination therapy, were collected from China. Analysis of a sample by DART-MS showed predominantly peaks corresponding to dihydroartemisinin and piperaquine fragment species. No peaks corresponding to intact analyte species could be detected in the spectrum. Another sampled tablet resulted in no identification of peaks by DART-MS. Direct infusion by ESI TOF-MS showed peaks at *m/z* 475.4125 and *m/z* 949.4418 after internal mass drift correction against NaTFA. The ESI-TOF spectrum was then imported into the MS tools software, and the monositopic mass was used to do a search for the possible elemental formulas corresponding to these masses. One of the primary hits matched Sildenafil (Viagra®). DESI-MS and MS/MS analysis of the samples and standards confirmed the identification of Sildenafil with a standard.

A.5. Combining Two-Dimensional Diffusion-Ordered Nuclear Magnetic Resonance Spectroscopy, Imaging Desorption Electrospray

Ionization Mass Spectrometry and Direct Analysis In Real Time Mass Spectrometry for the Integral Investigation of Counterfeit Pharmaceuticals.

A collaboration with the Biomedical NMR Laboratory at the University of Paul Sabatier (France) and the Wallace H. Coulter Department of Biomedical Engineering at Georgia Tech (Atlanta) focused on a multi-faceted investigation of counterfeit pharmaceuticals combining two-dimensional diffusion-ordered nuclear magnetic resonance spectroscopy (2D DOSY ^{1}H NMR), imaging DESI MS and DART MS. Although methods of identification had been established for both DART MS and DESI MS, this study provided graphical representation of DOSY ^{1}H NMR results which aided in classifying groups of samples by examining polymeric excipients which were undetected by MS (Figure A.2). In addition, this was the first study to utilize DESI MS in an imaging mode for pharmaceutical analysis revealing information on sample homogeneity and impurities which were difficult to detect by NMR and DART MS.

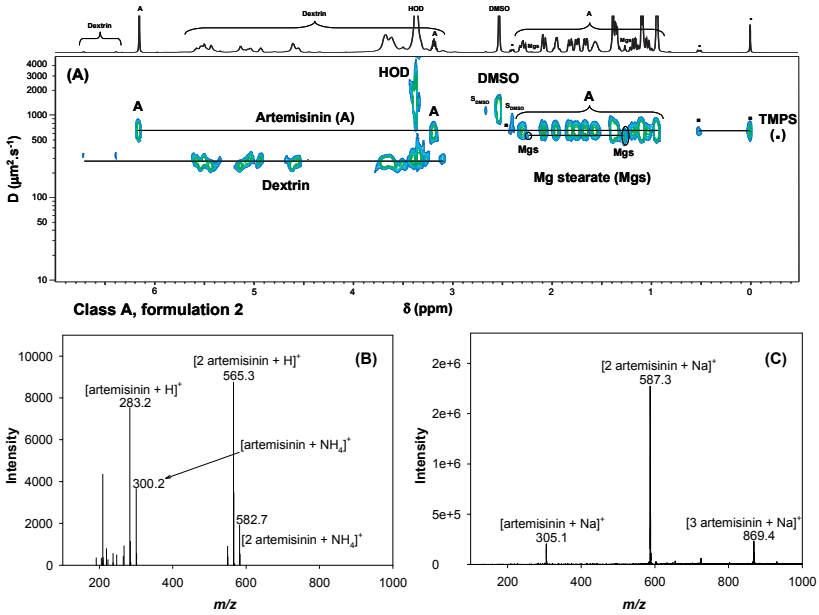

Figure A.2: Analyses of a sample by: (A) 2D DOSY 1H NMR in DMSO-d_6 with TMPS as internal reference standard (S_{DMSO} represents DMSO satellite signals), (B) DART MS in positive ion mode and (C) DESI MS in positive ion mode.

A.6. Conclusion

A greater investment is required to ensure the quality of antimalarials in Africa and South East Asia. Despite the developments listed in this Appendix and other pursued by the labs of our collaborators, criminals continue their assault on public health by producing diverse harmful antimalarial counterfeits. Drug resistant strains of the malaria parasite are expected to grow due to the presence of substandard and/or degraded medicines and of counterfeits containing sub-therapeutic amounts of active ingredients. In addition, sub-therapeutic levels of active ingredients may result in persistent sickness and death of many patients. Looking ahead, the methods applied to the antimalarial field should be extended to other pharmaceuticals, particularly those targeted towards diseases prevalent in developing countries like tuberculosis, HIV/AIDS and tropical diseases.

APPENDIX B. Enhanced Direct Ambient Analysis By Differential Mobility-Filtered Desorption Electrospray Ionization Mass Spectrometry

B.1. Abstract

Although little to no sample pretreatment procedures are required, DESI may suffer poor sensitivity and/or selectivity due to the lack of chromatographic separation prior to analysis and limited ion transmission. In order to improve sensitivity and selectivity, a differential mobility spectrometry (DMS) separation-based ion filtration unit was successfully interfaced to a DESI ionization source. The new platform can operate in two modes, DMS-off mode and DMS-on mode allowing for direct comparisons between the conventional DESI and DMS-DESI. The performance of the new platform was tested with several samples including counterfeit pharmaceuticals, binary mixtures and isobaric chemicals. With DMS-on, mass spectral signal-to-noise ratios were improved by ~2 fold. For the analysis of near isobaric compounds, baseline mobility separation was successfully obtained. Furthermore, these results demonstrated that the addition of the DMS coupled with in-source ion activation provided tandem MS-like spectra in a single stage MS instrument.

B.2. Introduction

B.2.1. Desorption Electrospray Ionization

DESI makes use of a pneumatically-assisted charged jet which is directed onto the sample surface where the analytes are present. This jet desorbs a very small part of the sample which is carried by secondary charged droplets that are scattered off the surface, and immediately sampled by a mass spectrometer equipped with a suitable atmospheric pressure interface. DESI shares a key characteristic with ESI, which is to enable the analysis of materials over a large mass range without significant fragmentation. Computational fluid dynamics simulations have shown three consecutive stages in DESI: a) the formation of a thin liquid film on the sample surface by impacting droplets, b) extraction of the solid-phase analytes into the thin film, and c) collision of primary droplets with the thin film, producing secondary droplets taking up part of the analyte-containing liquid.[174] These secondary droplets undergo ESI-like ionization processes on their way to the mass spectrometer.

Although little to no sample pretreatment procedures are required, DESI may suffer from limited sensitivity and/or selectivity due to less-than-optimal droplet/ion transmission, and typical chemical interferences found also in ESI. For example, our efforts with counterfeit drug detection have shown the need for more advanced technologies to aid in combating this ever growing public health problem.[175, 176] The presence of isobaric species and chemically-interfering species is a common scenario in both pharmaceutical analysis[177] and other quality control applications.[178] In resource-limited environments where there is not access to tandem MS instrumentation, new

instrumental methods that allow structural elucidation by selective in-source fragmentation without relying on chromatographic separations would be beneficial.

B.2.2. Differential Mobility Spectrometry

Differential mobility spectrometry (DMS, also called Field Asymmetric-Waveform Ion Mobility Spectrometry, FAIMS) is a gas-phase ion mobility separation technique based on differences between ion mobilities as a function of a time-dependent asymmetric high electrical field, operated at or near atmospheric pressure.[179] DMS is quasi-orthogonal to MS which affords higher selectivity and specificity versus standalone MS.[180] Key among the beneftis of DMS operation with MS detection are improved signal-to-noise ratio (SNR) gains and separation of isobaric species and structural isomers without time-consuming chromatographic methods. Also, the ability to perform collision induced dissociation (CID) of pre-selected ions leaving the DMS cell allows for highly informative tandem MS-like fragmentation info to be obtained in a single-staged mass spectrometer.

B.3. Experimental

B.3.1. DESI Instrumentation Settings

The DESI-DM-MS system encompasses a custom-made DESI source,[181] a modified Sionex Corporation (Bedford, MA) microDMX differential mobility sensor, and an orthogonal TOF mass spectrometer (JEOL AccuTOF, Tokyo, Japan). The DESI source was built around a joystick-controlled motorized microscope XY stage (Prior Scientific, Rockland, MA) for automatic and manual sample positioning in the x-y and z coordinates, respectively. The DESI sprayer was mounted on a MicroBlock 3-axis positioner (Thorlabs, Newton, NJ) for manual adjustment of the emitter position in the x-

y-z coordinates with respect to the TOF orifice inlet, and fitted with a high precision rotation mount (Thorlabs, Newton, NJ) for manual adjustment of the spray impact angle. The DESI operating parameters were as follows: spray voltage 3.6 kV, ion transfer capillary voltage 128 V, methanol solvent flow rate 5-8 μL min^{-1}, desolvation (nitrogen) gas flow 2.5 L min^{-1}, tip-to-surface distance 1.5-3 mm, spray incident angle 55°, and collection angle 30°.

B.3.2. DMS-TOF MS Instrumentation Settings

The differential mobility unit consists of a desolvation chamber, DM electrode housing and a DM assembly holder. The DESI-DM assembly holder (Figure B.1) mounts this module to the orifice 1 plate of the AccuTOF instrument.

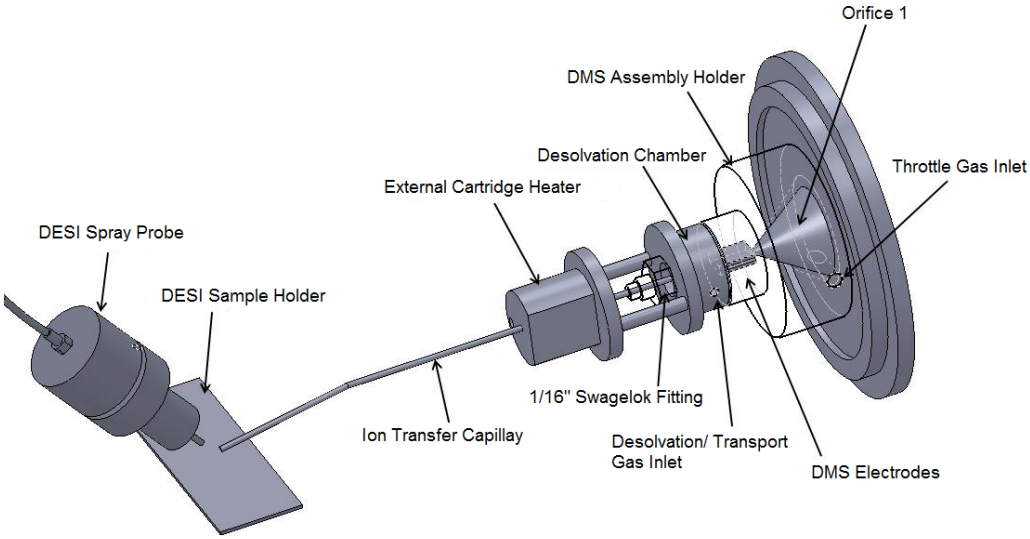

Figure B.1: DESI-DM-TOF MS mounting assembly composed of the DESI spray probe, heated transfer region, DMS assembly, and TOF MS orifice.

The AccuTOF orifice 1 voltage was 128 V, ring electrode 5 V, orifice 2 voltage 18 V and transfer hexapole bias 27 V. The DM assembly holder has a side port for throttle gas (ultra pure nitrogen, Airgas, Atlanta, GA) supply at an optimum flow rate of

0.5 L min^{-1}. Isopropanol is fed as a dopant (~5000 ppm) into the DM desolvation chamber in combination with heated (~80˚C) nitrogen at a flow rate of 0.2 L min^{-1}. The DESI ion transfer capillary (250 mm long, OD: 1.58 mm, ID: 0.6 mm) was attached to the entrance of the DM desolvation chamber by using a vacuum sealable 1/16" Swagelok® fitting. Sufficient vacuum suction to enhance ion/droplet transport from the DESI sampling stage through the DM unit to the MS orifice 1 inlet was achieved by vacuum sealing each component of the DM unit with PTFE-based Gore-Tex® washers. Additional heating (~250 ˚C) was provided to improve ion desolvation during transit through the ion transfer capillary via an external heater block. The voltages applied to the DMS cell were as follows: separation voltage (SV) 500-1500 V, compensation voltage (CV) -42-15 V, CV scan steps 100-150, CV step duration 100 ms. The DM unit was independently controlled by the Sionex microDMX (v2.4.0) software interface, while MS data were collected and analyzed by JEOL AccuTOF Mass Center (v1.3.0) application software.

B.4. Improving the Signal-to-Noise Ratio

As mentioned above, the DESI-DM-MS platform can operate in two modes: fly-through "DMS-off" mode or "DMS-on" mode. In DMS-off mode, the voltages on the DM electrodes were turned off, and ions were allowed to fly-through the DM module. This mode was exclusively used for the optimization of the ion transmission through the DESI-DM interface without mobility separation. Figure B.2a shows the analysis of a counterfeit antimalarial pharmaceutical tablet in DMS-off mode. The two predominant peaks in the spectrum (*m/z* 407.108, and 365.106) were assigned to [artesunic acid + $Na]^+$ and [lactose + $Na]^+$, respectively. Analysis of the same pharmaceutical tablet by DESI-

MS in a previous study [formulation 4],[177] revealed the presence of the same chemical components. One major difference between the two spectra is that the relative abundance of lactose in the DESI-DM-MS spectrum is higher than DESI-MS. The peak at *m/z* 443.233 corresponds to 50 µL of 1 mM Rhodamine 6G (R6G), a chemical tag spotted on the tablet surface. R6G is a pre-charged ionic species that served as a simulated concomitant background ion, and was used for ion transmission optimization and mass drift correction.

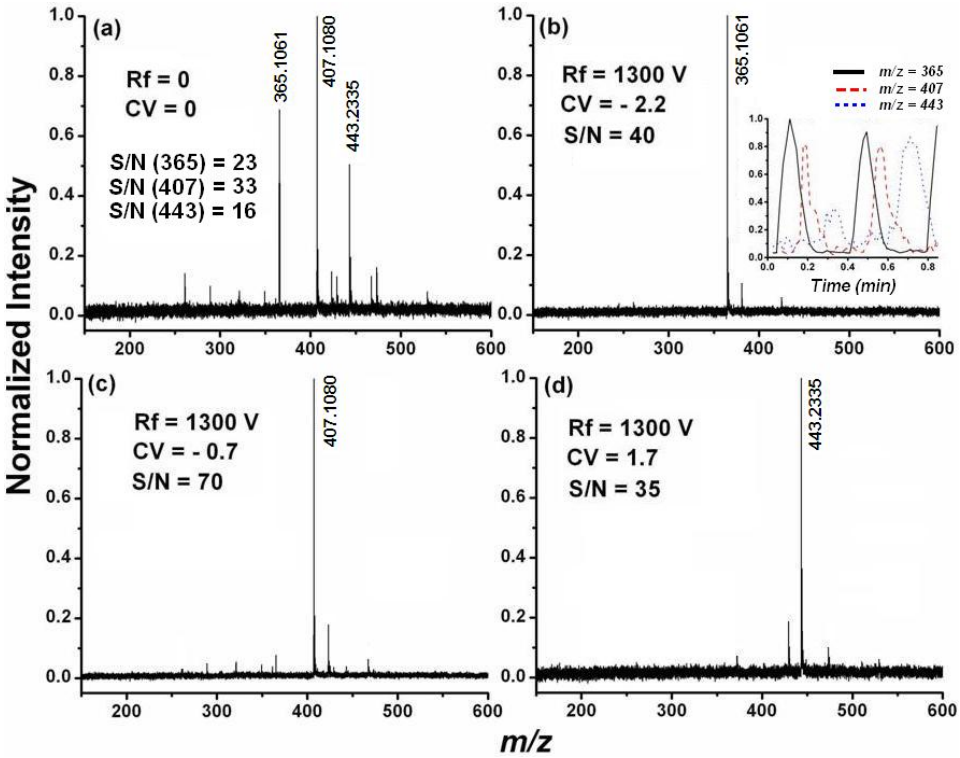

Figure B.2: Analysis of a counterfeit antimalarial pharmaceutical tablet by DESI-DM-MS: (a) DMS-off mode (no voltages applied) and DMS-on mode for the isolation of: (b) sodiated lactose excipient (*m/z* = 365.1061, SV = 1300 V, CV = -1.7 V), (c) sodiated artesunic acid (*m/z* = 407.1082, SV = 1300 V, CV = -0.7 V), and (d) R6G (*m/z* = 443.2335, SV = 1300 V, CV = 1.7 V). The inset shows the normalized selected ion trace for each ion in the MS acquisition time scale with a CV sweep rate of 0.25 V $step^{-1}$.

In DMS-on mode, an asymmetric RF voltage, often referred to as separation voltage (SV), and a counterbalancing DC potential, called the compensation voltage (CV)

are simultaneously applied on the DM unit electrodes. Figures B.2b-d illustrate the separation of the three major chemical species, sodiated lactose (*m/z* 365.106), sodiated artesunic acid (*m/z* 407.108) and R6G (*m/z* 443.233), from the tablet surface. Mobility separation was performed at a fixed SV (1300 V), with three different CVs (-2.2 V, -0.7 V and +1.7 V, respectively). In this mode, prior estimation of SV and CV is required for the best differential mobility separation. For this purpose, the SV was first scanned between 500 and 1500 V, with no CV applied. This was necessary for the optimization of the SV to transmit the analytically relevant *m/z* range. After optimization of the SV, the CV was ramped between -20 V and 5 V. During CV ramping, the optimized SV (1300 V) was applied across the electrodes, perpendicular to the direction of ion transmission. Based on their ionic mobilities under low and high field conditions, these ions migrate toward the ground electrode, but in three different trajectories. These ion trajectories are corrected by when the appropriate CV is applied during the CV ramp. In the DMS-on mode, only the ions of interest were allowed to transmit through the system, one at a time. The orthogonal separation capability of DMS allowed discrimination and simplification of the spectra by filtering the unrelated background chemical noise. This resulted in improved S/N (Figure B.2b-d). The inset in Figure B.2b shows the normalized selected MS ion chromatograms. Although the ionic species were not base line separated, they were easily distinguished from each other. In order to improve the DM resolution, a mixture of nitrogen (80%) and helium (20%, V/V) was introduced as the transport gas. In the presence of helium, peak widths were ~30% narrower than in the case of pure nitrogen (Figure B.3).

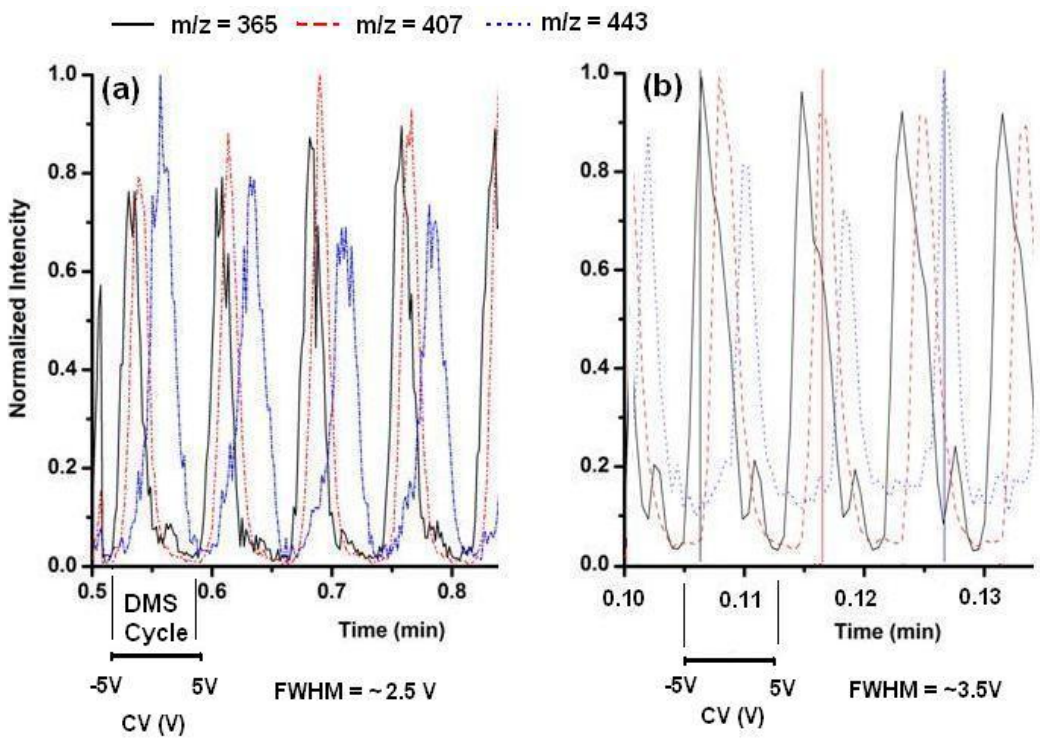

Figure B.3: Separation of a mixture of sodiated lactose (*m/z* 365.106), sodiated artesunic acid (*m/z* 407.108) and R6G (*m/z* 443.233) in the presence of a) 20 % helium in nitrogen and b) pure nitrogen as the transport gas.

Additional characterization of the DESI-DM-MS system was performed by depositing chemical standards on PTFE surfaces. In Figure B.4a, analysis of a mixture of 0.5 mM pyrimethamine (moni-isotopic MW = 248.083) and 1 mM polyethylene glycol (PEG 400) in DMS-off mode is illustrated. Higher concentration of PEG was deliberately added to the mixture in order to introduce a higher chemical background. The peak at *m/z* = 249.091 corresponds to protonated pyrimethamine with a S/N of 7. However, when analyzed in DMS-on mode (SV = 1300 V, CV = 1.2 V), the chemical background induced by PEG is completely eliminated and the pyrimethamine ion S/N increased from 7 to 20 (improvement ~2.9x). The chemical background pre-filtering effect is highly encouraging, especially for future analysis of complex chemical mixtures, and imaging purposes.

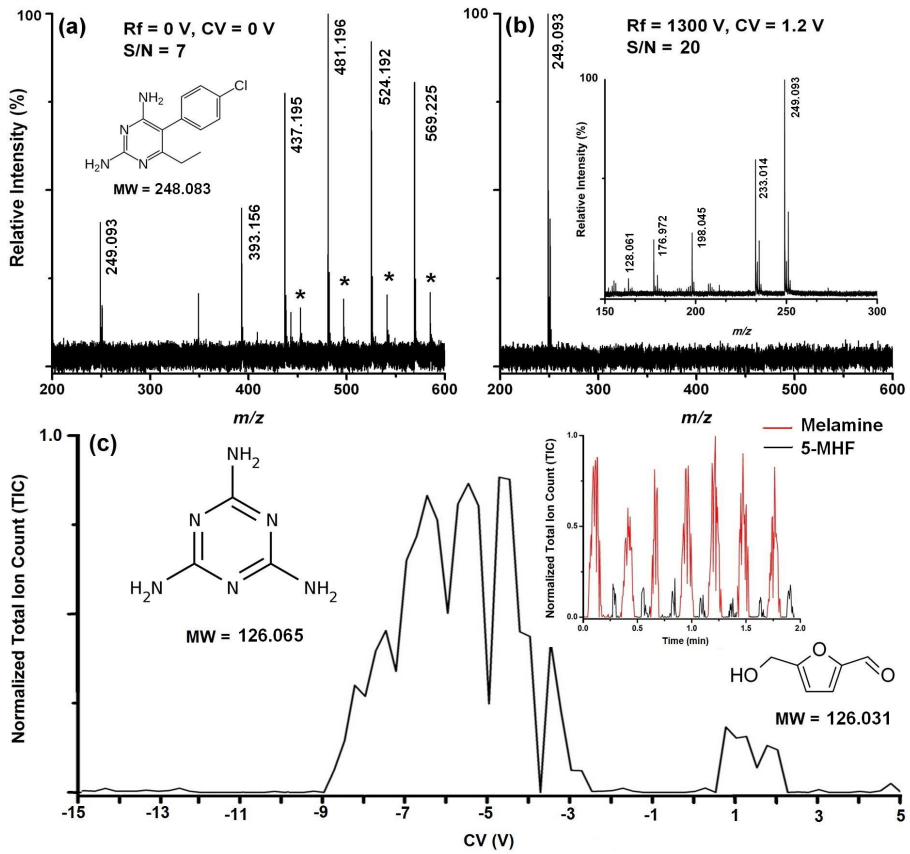

Figure B.4: Application of DESI-DM-MS to the analysis of chemical standards on PTFE surfaces. Mixture of 0.5 mM pyrimethamine (mono-isotopic MW = 248.083) and 1 mM polyethylene glycol (PEG 400): (a) DMS-off (no voltages applied), and (b) DMS-on mode (SV = 1300, CV = 1.2V). The inset of (b) shows the DESI-DM-CID-MS mode of operation at orifice voltage of 120 V. (c) The analysis of a binary mixture of pyrimethamine (100 µM) and 5-HMF (100 µM) in DMS-on mode (SV = 900 V, CV = -15 V to 5 V). Inset shows the total ion trace in the MS time scale, while the CV was scanned.

B.5. Incorporating Collision Induced Dissociation With DMS Separation

The ability of performing CID of pre-selected ions leaving the DM unit was tested by activating the protonated pyrimethamine precursor ion. In this mode, ion dissociation is achieved by first selecting the ions of interest in the DM unit and then passing them into the mass spectrometer with additional activation energy provided by collisions in the

first differentially pumped region. To induce ion dissociation, the orifice 1 voltage was raised while the other instrument parameters were kept constant. The Figure B.4b inset shows the DESI-DM-CID-MS spectrum of the pyrimethamine $[M+H]^+$ at an orifice 1 voltage of 120 V. The extensive fragmentation observed is highly informative, and similar to previously reported ESI-MS/MS spectra.[183] DESI-DM-CID-MS thus provides higher selectivity and specificity than DESI-MS, and can be viewed as a low-cost alternative to higher performance tandem mass spectrometers.

B.6. DMS Separation of Isobaric Ions

The performance of the DESI-DM-MS platform was tested for the separation and detection of near-isobaric compounds. For example, 5-hydroxymethylfurfural (5-HMF) which is formed as a result of heating dried milk powder,[182] produces a protonated ion (theoritaical *m/z* = 127.039) that is challenging to distinguish from protonated melamine (theoretical *m/z* 127.073) by using low-resolution mass spectrometers. Recent attempts of detecting trace amounts of melamine in dairy products triggered the exploration of new, low-cost, and rapid analysis techniques for their detection. However, almost all of these detection methods required high-resolution mass spectrometry and/or tandem mass spectrometry to eliminate possible false positives.[42] In this study, an equimolar mixture (50 μL of 100 μM solutions in methanol) of melamine and 5-HMF were deposited on a PTFE surface and analyzed by DESI-DM-MS. As shown in Figure B.4c, the two nearly isobaric compounds were successfully base line resolved (SV = 900), and positively identified based on their appearance time in the CV spectrum.

B.7. Conclusion

For the first time, a hybrid DESI-DM-MS platform was successfully implemented on a commercial mass spectrometer. DESI-DM-MS was found to be effective in suppressing/eliminating chemical noise and separating interfering ions of similar mass-to-charge ratio that were produced by DESI. In-source ion activation was achieved by increasing the orifice 1 voltage, allowing additional tandem MS-like capability. This type of hybrid instrumentation could successfully be utilized in analyzing complex sample mixtures by DESI in their native states while improving S/N ratios for enhanced sensitivity and selectivity.

REFERENCES

(1) Takats, Z.; Wiseman, J. M.; Gologan, B.; Cooks, R. G. (**2004**). "Mass Spectrometry Sampling under Ambient Conditions with Desorption Electrospray Ionization", *Science*, 306(5695), pp. 471-473.

(2) Cody, R. B.; Laramee, J. A.; Durst, H. D. (**2005**). "Versatile New Ion Source for the Analysis of Materials in Open Air under Ambient Conditions", *Analytical Chemistry*, 77(8), pp. 2297-2302.

(3) Cooks, R. G.; Ouyang, Z.; Takats, Z.; Wiseman, J. M. (**2006**). "Ambient Mass Spectrometry", *Science*, 311(5767), pp. 1566-1570.

(4) Harris, G. A.; Nyadong, L.; Fernandez, F. M. (**2008**). "Recent Developments in Ambient Ionization Techniques for Analytical Mass Spectrometry", *Analyst*, 133(10), pp. 1297-1301.

(5) Venter, A.; Nefliu, M.; Cooks, R. G. (**2008**). "Ambient Desorption Ionization Mass Spectrometry", *TrAC, Trends in Analytical Chemistry*, 27(4), pp. 284-290.

(6) Van Berkel, G. J.; Pasilis, S. P.; Ovchinnikova, O. (**2008**). "Established and Emerging Atmospheric Pressure Surface Sampling/Ionization Techniques for Mass Spectrometry", *Journal of Mass Spectrometry*, 43(9), pp. 1161-1180.

(7) Chen, H.; Gamez, G.; Zenobi, R. (**2009**). "What Can We Learn from Ambient Ionization Techniques?", *Journal of the American Society for Mass Spectrometry*, 20(11), pp. 1947-1963.

(8) Ifa, D. R.; Jackson, A. U.; Paglia, G.; Cooks, R. G. (**2009**). "Forensic Applications of Ambient Ionization Mass Spectrometry", *Analytical and Bioanalytical Chemistry*, 394(8), pp. 1995-2008.

(9) Alberici, R. M.; Simas, R. C.; Sanvido, G. B.; Romao, W.; Lalli, P. M.; Benassi, M.; Cunha, I. B. S.; Eberlin, M. N. (**2010**). "Ambient Mass Spectrometry: Bringing MS into the "Real World"", *Analytical and Bioanalytical Chemistry*, 398(1), pp. 265-294.

(10) Green, F. M.; Salter, T. L.; Stokes, P.; Gilmore, I. S.; O'Connor, G. (**2010**). "Ambient Mass Spectrometry: Advances and Applications in Forensics", *Surface and Interface Analysis*, 42(5), pp. 347-357.

(11) Huang, M.-Z.; Yuan, C.-H.; Cheng, S.-C.; Cho, Y.-T.; Shiea, J. (**2010**). "Ambient Ionization Mass Spectrometry", *Annual Review of Analytical Chemistry*, 3 pp. 43-65.

(12) Ifa, D. R.; Wu, C.; Ouyang, Z.; Cooks, R. G. (**2010**). "Desorption Electrospray Ionization and Other Ambient Ionization Methods: Current Progress and Preview", *Analyst*, 135(4), pp. 669-681.

(13) Weston, D. J. (**2010**). "Ambient Ionization Mass Spectrometry: Current Understanding of Mechanistic Theory; Analytical Performance and Application Areas", *Analyst*, 135(4), pp. 661-668.

(14) Nicol, G.; Sunner, J.; Kebarle, P. (**1988**). "Kinetics and Thermodynamics of Protonation Reactions - $H_3O+(H_2O)_h + B = BH^+(H_2O)_b + (h - b + 1)H_2O$, Where B Is a Nitrogen, Oxygen or Carbon Base", *International Journal of Mass Spectrometry and Ion Processes*, 84(1-2), pp. 135-155.

(15) Cooks, R. G.; Ast, T.; Mabud, A. (**1990**). "Collisions of Polyatomic Ions with Surfaces", *International Journal of Mass Spectrometry and Ion Processes*, 100 pp. 209-265.

(16) Chen, H.; Zheng, J.; Zhang, X.; Luo, M.; Wang, Z.; Qiao, X. (**2007**). "Surface Desorption Atmospheric Pressure Chemical Ionization Mass Spectrometry for Direct Ambient Sample Analysis without Toxic Chemical Contamination", *Journal of Mass Spectrometry*, 42(8), pp. 1045-1056.

(17) Kpegba, K.; Spadaro, T.; Cody, R. B.; Nesnas, N.; Olson, J. A. (**2007**). "Analysis of Self-Assembled Monolayers on Gold Surfaces Using Direct Analysis in Real Time Mass Spectrometry", *Analytical Chemistry*, 79(14), pp. 5479-5483.

(18) Harris, G. A.; Fernandez, F. M. (**2009**). "Simulations and Experimental Investigation of Atmospheric Transport in an Ambient Metastable-Induced Chemical Ionization Source", *Analytical Chemistry*, 81(1), pp. 322-329.

(19) Fernandez, F. M.; Cody, R. B.; Green, M. D.; Hampton, C. Y.; McGready, R.; Sengaloundeth, S.; White, N. J.; Newton, P. N. (**2006**). "Characterization of Solid Counterfeit Drug Samples by Desorption Electrospray Ionization and Direct-Analysis-in-Real-Time Coupled to Time-of-Flight Mass Spectrometry", *ChemMedChem*, 1(7), pp. 702-705.

(20) Curtis, M.; Minier, M. A.; Chitranshi, P.; Sparkman, O. D.; Jones, P. R.; Xue, L. (**2010**). "Direct Analysis in Real Time (DART) Mass Spectrometry of Nucleotides and Nucleosides: Elucidation of a Novel Fragment $[C_5H_5O]^+$ and Its In-Source Adducts", *Journal of the American Society for Mass Spectrometry*, 21(8), pp. 1371-1381.

(21) Lapthorn, C.; Pullen, F. (**2009**). ""Soft"or "Hard" Ionisation? Investigation of Metastable Gas Temperature Effect on Direct Analysis in Real-Time Analysis of Voriconazole", *European Journal of Mass Spectrometry*, 15(5), pp. 587-593.

(22) Cody, R. B. (**2009**). "Observation of Molecular Ions and Analysis of Nonpolar Compounds with the Direct Analysis in Real Time Ion Source", *Analytical Chemistry*, 81(3), pp. 1101-1107.

(23) Song, L.; Gibson, S. C.; Bhandari, D.; Cook, K. D.; Bartmess, J. E. (**2009**). "Ionization Mechanism of Positive-Ion Direct Analysis in Real Time: A Transient Microenvironment Concept", *Analytical Chemistry*, 81(24), pp. 10080-10088.

(24) Song, L.; Dykstra, A. B.; Yao, H.; Bartmess, J. E. (**2009**). "Ionization Mechanism of Negative Ion-Direct Analysis in Real Time: A Comparative Study with Negative Ion-Atmospheric Pressure Photoionization", *Journal of the American Society for Mass Spectrometry*, 20(1), pp. 42-50.

(25) Grange, A. H. (**2009**). "Rapid Semi-Quantitative Surface Mapping of Airborne-Dispersed Chemicals Using Mass Spectrometry", *Environmental Forensics*, 10(3), pp. 183-195.

(26) Edison, S. E.; Lin, L. A.; Gamble, B. M.; Wong, J.; Zhang, K. (**2011**). "Surface Swabbing Technique for the Rapid Screening for Pesticides Using Ambient Pressure Desorption Ionization with High-Resolution Mass Spectrometry", *Rapid Communications in Mass Spectrometry*, 25(1), pp. 127-139.

(27) Maleknia, S. D.; Vail, T. M.; Cody, R. B.; Sparkman, D. O.; Bell, T. L.; Adams, M. A. (**2009**). "Temperature-Dependent Release of Volatile Organic Compounds of Eucalypts by Direct Analysis in Real Time (DART) Mass Spectrometry", *Rapid Communications in Mass Spectrometry*, 23(15), pp. 2241-2246.

(28) Nilles, J. M.; Connell, T. R.; Durst, H. D. (**2010**). "Thermal Separation to Facilitate Direct Analysis in Real Time (DART) of Mixtures", *Analyst*, 135(5), pp. 883-886.

(29) Perez, J. J.; Harris, G. A.; Chipuk, J. E.; Brodbelt, J. S.; Green, M. D.; Hampton, C. Y.; Fernandez, F. M. (**2010**). "Transmission-Mode Direct Analysis in Real Time and Desorption Electrospray Ionization Mass Spectrometry of Insecticide-Treated Bednets for Malaria Control", *Analyst*, 135(4), pp. 712-719.

(30) Haunschmidt, M.; Klampfl, C. W.; Buchberger, W.; Hertsens, R. (**2010**). "Determination of Organic Uv Filters in Water by Stir Bar Sorptive Extraction and Direct Analysis in Real-Time Mass Spectrometry", *Analytical and Bioanalytical Chemistry*, 397(1), pp. 269-275.

(31) Jagerdeo, E.; Abdel-Rehim, M. (**2009**). "Screening of Cocaine and Its Metabolites in Human Urine Samples by Direct Analysis in Real-Time Source Coupled to Time-of-Flight Mass Spectrometry after Online Preconcentration Utilizing Microextraction by Packed Sorbent", *Journal of the American Society for Mass Spectrometry*, 20(5), pp. 891-899.

(32) Jones, R. W.; Reinot, T.; McClelland, J. F. (**2010**). "Molecular Analysis of Primary Vapor and Char Products During Stepwise Pyrolysis of Poplar Biomass", *Energy & Fuels*, 24(9), pp. 5199-5209.

(33) Eberherr, W.; Buchberger, W.; Hertsens, R.; Klampfl, C. W. (**2010**). "Investigations on the Coupling of High-Performance Liquid Chromatography to Direct Analysis in Real Time Mass Spectrometry", *Analytical Chemistry*, 82(13), pp. 5792-5796.

(34) Yu, S.; Crawford, E.; Tice, J.; Musselman, B.; Wu, J. T. (**2009**). "Bioanalysis without Sample Cleanup or Chromatography: The Evaluation and Initial Implementation of Direct Analysis in Real Time Ionization Mass Spectrometry for the Quantification of Drugs in Biological Matrixes", *Analytical Chemistry*, 81(1), pp. 193-202.

(35) Nilles, J. M.; Connell, T. R.; Stokes, S. T.; Dupont Durst, H. (**2010**). "Explosives Detection Using Direct Analysis in Real Time (DART) Mass Spectrometry", *Propellants, Explosives, Pyrotechnics*, 35(5), pp. 446-451.

(36) Bevilacqua, V. L.; Nilles, J. M.; Rice, J. S.; Connell, T. R.; Schenning, A. M.; Reilly, L. M.; Durst, H. D. (**2010**). "Ricin Activity Assay by Direct Analysis in Real Time Mass Spectrometry Detection of Adenine Release", *Analytical Chemistry*, 82(3), pp. 798-800.

(37) Nilles, J. M.; Connell, T. R.; Durst, H. D. (**2009**). "Quantitation of Chemical Warfare Agents Using the Direct Analysis in Real Time (DART) Technique", *Analytical Chemistry*, 81(16), pp. 6744-6749.

(38) Bennett, M. J.; Steiner, R. R. (**2009**). "Detection of Gamma-Hydroxybutyric Acid in Various Drink Matrices Via AccuTOF-DART", *Journal of Forensic Sciences*, 54(2), pp. 370-375.

(39) Vaclavik, L.; Zachariasova, M.; Hrbek, V.; Hajslova, J. (**2010**). "Analysis of Multiple Mycotoxins in Cereals under Ambient Conditions Using Direct Analysis in Real Time (DART) Ionization Coupled to High Resolution Mass Spectrometry", *Talanta*, 82(5), pp. 1950-1957.

(40) Ackerman, L. K.; Noonan, G. O.; Begley, T. H. (**2009**). "Assessing Direct Analysis in Real-Time-Mass Spectrometry (DART-MS) for the Rapid Identification of Additives in Food Packaging", *Food Additives and Contaminants*, 26(12), pp. 1611-1618.

(41) Vaclavik, L.; Rosmus, J.; Popping, B.; Hajslova, J. (**2010**). "Rapid Determination of Melamine and Cyanuric Acid in Milk Powder Using Direct Analysis in Real

Time-Time-of-Flight Mass Spectrometry", *Journal of Chromatography A*, 1217(25), pp. 4204-4211.

(42) Dane, A. J.; Cody, R. B. (**2010**). "Selective Ionization of Melamine in Powdered Milk by Using Argon Direct Analysis in Real Time (DART) Mass Spectrometry", *Analyst*, 135(4), pp. 696-699.

(43) Jeckelmann, N.; Haefliger, O. P. (**2010**). "Release Kinetics of Actives from Chewing Gums into Saliva Monitored by Direct Analysis in Real Time Mass Spectrometry", *Rapid Communications in Mass Spectrometry*, 24(8), pp. 1165-1171.

(44) Haunschmidt, M.; Klampfl, C. W.; Buchberger, W.; Hertsens, R. (**2010**). "Rapid Identification of Stabilisers in Polypropylene Using Time-of-Flight Mass Spectrometry and Dart as Ion Source", *Analyst*, 135(1), pp. 80-85.

(45) Rothenbacher, T.; Schwack, W. (**2010**). "Rapid Identification of Additives in Poly(Vinyl Chloride) Lid Gaskets by Direct Analysis in Real Time Ionisation and Single-Quadrupole Mass Spectrometry", *Rapid Communications in Mass Spectrometry*, 24(1), pp. 21-29.

(46) Rothenbacher, T.; Schwack, W. (**2009**). "Rapid and Nondestructive Analysis of Phthalic Acid Esters in Toys Made of Poly(Vinyl Chloride) by Direct Analysis in Real Time Single-Quadrupole Mass Spectrometry", *Rapid Communications in Mass Spectrometry*, 23(17), pp. 2829-2835.

(47) Domin, M. A.; Steinberg, B. D.; Quimby, J. M.; Smith, N. J.; Greene, A. K.; Scott, L. T. (**2010**). "Routine Analysis and Characterization of Highly Insoluble Polycyclic Aromatic Compounds by Direct Analysis in Real Time Mass Spectrometry (DART)", *Analyst*, 135(4), pp. 700-704.

(48) Borges, D. L. G.; Sturgeon, R. E.; Welz, B.; Curtius, A. J.; Mester, Z. (**2009**). "Ambient Mass Spectrometric Detection of Organometallic Compounds Using Direct Analysis in Real Time", *Analytical Chemistry*, 81(23), pp. 9834-9839.

(49) Curtis, M. E.; Jones, P. R.; Sparkman, O. D.; Cody, R. B. (**2009**). "Determination of the Presence or Absence of Sulfur Materials in Drywall Using Direct Analysis in Real Time in Conjunction with an Accurate-Mass Time-of-Flight Mass Spectrometer", *Journal of the American Society for Mass Spectrometry*, 20(11), pp. 2082-2086.

(50) Nyadong, L.; Harris, G. A.; Balayssac, S.; Galhena, A. S.; Malet-Martino, M.; Martino, R.; Parry, R. M.; Wang, M. D.; Fernandez, F. M.; Gilard, V. (**2009**). "Combining Two-Dimensional Diffusion-Ordered Nuclear Magnetic Resonance Spectroscopy, Imaging Desorption Electrospray Ionization Mass Spectrometry, and Direct Analysis in Real-Time Mass Spectrometry for the Integral

Investigation of Counterfeit Pharmaceuticals", *Analytical Chemistry*, 81(12), pp. 4803-4812.

(51) Steiner, R. R.; Larson, R. L. (**2009**). "Validation of the Direct Analysis in Real Time Source for Use in Forensic Drug Screening", *Journal of Forensic Sciences*, 54(3), pp. 617-622.

(52) Helmy, R.; Schafer, W.; Buhler, L.; Marcinko, S.; Musselman, B.; Guidry, E.; Jenkins, H.; Fleitz, F.; Welch, C. J. (**2010**). "Ambient Pressure Desorption Ionization Mass Spectrometry in Support of Preclinical Pharmaceutical Development", *Organic Process Research & Development*, 14(2), pp. 386-392.

(53) Navare, A. T.; Mayoral, J. G.; Nouzova, M.; Noriega, F. G.; Fernandez, F. M. (**2010**). "Rapid Direct Analysis in Real Time (DART) Mass Spectrometric Detection of Juvenile Hormone Iii and Its Terpene Precursors", *Analytical and Bioanalytical Chemistry*, 398(7-8), pp. 3005-3013.

(54) Zhou, M.; McDonald, J. F.; Fernandez, F. M. (**2010**). "Optimization of a Direct Analysis in Real Time/Time-of-Flight Mass Spectrometry Method for Rapid Serum Metabolomic Fingerprinting", *Journal of the American Society for Mass Spectrometry*, 21(1), pp. 68-75.

(55) Zhou, M.; Guan, W.; Walker, L. D.; Mezencev, R.; Benigno, B. B.; Gray, A.; Fernandez, F. M.; McDonald, J. F. (**2010**). "Rapid Mass Spectrometric Metabolic Profiling of Blood Sera Detects Ovarian Cancer with High Accuracy", *Cancer Epidemiology, Biomarkers and Prevention*, 19(9), pp. 2262-2271.

(56) Jones, R. W.; Cody, R. B.; McClelland, J. F. (**2006**). "Differentiating Writing Inks Using Direct Analysis in Real Time Mass Spectrometry", *Journal of Forensic Sciences*, 51(4), pp. 915-918.

(57) Haefliger, O. P.; Jeckelmann, N. (**2007**). "Direct Mass Spectrometric Analysis of Flavors and Fragrances in Real Applications Using Dart", *Rapid Communications in Mass Spectrometry*, 21(8), pp. 1361-1366.

(58) Morlock, G.; Ueda, Y. (**2007**). "New Coupling of Planar Chromatography with Direct Analysis in Real Time Mass Spectrometry", *Journal of Chromatography A*, 1143(1-2), pp. 243-251.

(59) Petucci, C.; Diffendal, J.; Kaufman, D.; Mekonnen, B.; Terefenko, G.; Musselman, B. (**2007**). "Direct Analysis in Real Time for Reaction Monitoring in Drug Discovery", *Analytical Chemistry*, 79(13), pp. 5064-5070.

(60) Pierce, C. Y.; Barr, J. R.; Cody, R. B.; Massung, R. F.; Woolfitt, A. R.; Moura, H.; Thompson, H. A.; Fernandez, F. M. (**2007**). "Ambient Generation of Fatty

Acid Methyl Ester Ions from Bacterial Whole Cells by Direct Analysis in Real Time (DART) Mass Spectrometry", *Chemical Communications*, (8), pp. 807-809.

(61) Vail, T.; Jones, P. R.; Sparkman, O. D. (**2007**). "Rapid and Unambiguous Identification of Melamine in Contaminated Pet Food Based on Mass Spectrometry with Four Degrees of Confirmation", *Journal of Analytical Toxicology*, 31(6), pp. 304-312.

(62) Li, Z.; Wang, H. (**2003**). "Drag Force, Diffusion Coefficient, and Electric Mobility of Small Particles. II. Application.", *Physical Review E: Statistical, Nonlinear, and Soft Matter Physics*, 68 pp. 061206.

(63) Lin, S. Y.; Huang, M. Z.; Chang, H. C.; Shiea, J. (**2007**). "Using Electrospray-Assisted Laser Desorption/Ionization Mass Spectrometry to Characterize Organic Compounds Separated on Thin-Layer Chromatography Plates.", *Analytical Chemistry*, 79 pp. 8789-8795.

(64) Appelhans, A. D.; Dahl, D. A. (**2005**). "Imion Ion Optics Simulations at Atmospheric Pressure.", *International Journal of Mass Spectrometry*, 244 pp. 1-14.

(65) Lai, H. M.; McJunkin, T. R.; Miller, C. J.; Scott, J. R.; R., A. J. (**2008**). "The Predictive Poser of Simion/Sds Simulation Software for Modeling Ion Mobility Spectrometry Instruments.", *International Journal of Mass Spectrometry*, 276(1), pp. 1-8.

(66) Dahl, D. A. (**2000**). "Simion 3d Version 7.0 User's Manual", *SIMION 3D Version 7.0 User's Manual*, Rev. 5

(67) Lawrence, A. H.; Nanji, A. A.; Taverner, J. (**1988**). "Skin-Sniffing/Ion Mobility Spectrometric Analysis: A Potential Screening Method in Clinical Toxicology.", *Journal of Clinical Laboratory Analysis*, 2(2), pp. 101-107.

(68) Felippa, C. A. (**2001**). "A Historical Outline of Matrix Structural Analysis: A Play in Three Acts.", *Computers and Structures*, 79(14), pp. 1313-1324.

(69) Ackroyd, R. T. (**1981**). "The Why and How of Finite Elements", *Annals of Nuclear Energy*, 8 pp. 539-566.

(70) Gosz, M. R. *Finite Element Method: Applications in Solids, Structures, and Heat Transfer*; Taylor & Francis Group, **2006**.

(71) Iannelli, J. *Characteristics Finite Element Methods in Computational Fluid Mechanics*; Springer, **2006**.

(72) Kenttamaa, H. I.; Cooks, R. G. (**1985**). "Internal Energy Distributions Acquired through Collisional Activation at Low and High Energies", *International Journal of Mass Spectrometry and Ion Processes*, 64 pp. 79-83.

(73) Vekey, K. (**1996**). "Internal Energy Effects in Mass Spectrometry", *Journal of Mass Spectrometry*, 31 pp. 445-463.

(74) Gabelica, V.; De Pauw, E. (**2004**). "Internal Energy and Fragmentation of Ions Produced in Electrospray Sources", *Mass Spectrometry Reviews*, 24 pp. 566-587.

(75) Katritzky, A. R.; Watson, C. H.; Dega-Szafran, Z.; Eyler, J. R. (**1990**). "Collisionally-Activated Dissociation of N-Alkylpyridinium Cations to Pyridine and Alkyl Cations in the Gas Phase", *Journal of the American Chemical Society*, 112 pp. 2471-2478.

(76) Wysocky, V. H.; Kenttamaa, H. I.; Cooks, R. G. (**1987**). "Internal Energy Distributions of Isolated Ions after Activation by Various Methods", *International Journal of Mass Spectrometry and Ion Processes*, 75(2), pp. 181-208.

(77) Vekey, K.; Brenton, A. G.; Beynon, J. H. (**1986**). "Electron Capture Induced Decomposition of the Benzene $C_6h_6^{2+}$ Ion", *Journal of Physical Chemistry*, 90(16), pp. 3569-3577.

(78) Collette, C.; De Pauw, E. (**1998**). "Calibration of the Internal Energy Distribution of Ions Produced by Electrospray", *Rapid Communications in Mass Spectrometry*, 12 pp. 165-170.

(79) Collette, C.; Drahos, L.; De Pauw, E.; Vekey, K. (**1998**). "Comparison of the Internal Energy Distributions of Ions Produced by Different Electrospray Sources", *Rapid Communications in Mass Spectrometry*, 12 pp. 1673-1678.

(80) Nefliu, M.; Smith, J. N.; Venter, A.; Cooks, R. G. (**2008**). "Internal Energy Distributions in Desorption Electrospray Ionization (DESI)", *Journal of the American Society for Mass Spectrometry*, 19 pp. 420-427.

(81) Peng, W. P.; Goodwin, M. P.; Chen, H.; Cooks, R. G.; Wilker, J. (**2008**). "Thermal Formation of Mixed-Metal Inorganic Complexes at Atmospheric Pressure", *Rapid Communications in Mass Spectrometry*, 22(22), pp. 3540-3548.

(82) Gabelica, V.; Pauw, E. D.; Karas, M. (**2004**). "Influence of the Capillary Temperature and the Source Pressure on the Internal Energy Distribution of Electrospray Ions", *International Journal of Mass Spectrometry*, 231 pp. 189-195.

(83) Drahos, L.; Heeren, R. M. A.; Collette, C.; De Pauw, E.; Vekey, K. (**1999**). "Thermal Energy Distribution Observed in Electrospray Ionization", *Journal of Mass Spectrometry*, 34 pp. 1373-1379.

(84) Fisenko, S. P.; Wang, W. N.; Lenggoro, I. W.; Okyuama, K. (**2006**). "Evaporative Cooling of Micron-Sized Droplets in a Low-Pressure Aerosol Reactor", *Chemical Engineering Science*, 61 pp. 6029-6034.

(85) Campbell, V. L.; Guan, Z.; Laude, J., D.A. (**1994**). "Selective Generation of Charge-Dependent/Independent Ion Energy Distributions from a Heated Capillary Electrospray Source", *Journal of the American Society for Mass Spectrometry*, 5 pp. 221-229.

(86) Kebarle, P. (**2000**). "A Brief Overview of the Present Status of the Mechanisms Involved in Electrospray Mass Spectrometry", *Journal of Mass Spectrometry*, 35 pp. 804-817.

(87) Kebarle, P.; Peschke, M. (**2000**). "On the Mechanisms by Which the Charged Droplets Produced by Electrospray Lead to Gas Phase Ions", *Analytica Chimica Acta*, 406 pp. 11-35.

(88) Cody, R. B. (**2009**). "Observation of Molecular Ions and Analysis of Nonpolar Compounds with the Direct Analysis in Real Time Ion Source", *Analytical Chemistry*, 81 pp. 1101-1107.

(89) Laramee, J. A.; Cody, R. B. "Chemi-Ionization and Direct Analysis in Real Time (DART) Mass Spectrometry. ", In *Encyclopedia of Mass Spectrometry*; Gross, M. L., Caprioli, R. M., Eds.; Elsevier: Amsterdam, **2007**; Vol. 6: Ionization Methods, pp 377-387.

(90) Milligan, D. B.; Wilson, P. F.; Freeman, C. G.; Mautner, M. M. N.; McEwan, M. J. (**2002**). "Dissociative Proton Transfer Reaction of H_3^+, N_2h^+, and H_3o^+ with Acyclic, Cyclic, and Aromatic Hydrocarbons and Nitrogen Compounds, and Astrochemical Implications", *Journal of Physcial Chemistry A*, 106 pp. 9745-9755.

(91) Schmidt, A.; Bahr, U.; Karas, M. (**2001**). "Influence of Pressure in the First Pumping Stage on Analyte Desolvation and Fragmentation in Nano-Esi-Ms", *Analytical Chemistry*, 73 pp. 6040-6046.

(92) Kurahashi, M.; Yamauchi, Y. (**2000**). "Metastable Helium Atom Stimulated Desoprtion of H+ Ion", *Physical Review Letters*, 84(20), pp. 4725-4728.

(93) Kurahashi, M.; Yamauchi, Y. (**2000**). "Observation of H^+ Desorption Stimulated by the Impact of Metastable Helium Atoms", *Surface Science*, 454-456 pp. 300-304.

(94) Galhena, A. S.; Harris, G. A.; Nyadong, L.; Murray, K. K.; Fernandez, F. M. (**2010**). "Small Molecule Ambient Mass Spectrometry Imaging by Infrared Laser

Ablation Metastable-Induced Chemical Ionization", *Anal Chem*, 82(6), pp. 2178-2181.

(95) Nyadong, L.; Harris, G. A.; Balayssac, S.; Galhena, A. S.; Malet-Martino, M.; Martino, R.; Parry, R. M.; Wang, M. D.; Fernandez, F. M.; Gilard, V. (**2009**). "Combining Two-Dimensional Diffusion-Ordered Nuclear Magnetic Resonance Spectroscopy, Imaging Desorption Electrospray Ionization Mass Spectrometry, and Direct Analysis in Real-Time Mass Spectrometry for the Integral Investigation of Counterfeit Pharmaceuticals", *Anal Chem*, 81(12), pp. 4803-4812.

(96) Yu, S.; Crawford, E.; Tice, J.; Musselman, B.; Wu, J. T. (**2009**). "Bioanalysis without Sample Cleanup or Chromatography: The Evaluation and Initial Implementation of Direct Analysis in Real Time Ionization Mass Spectrometry for the Quantification of Drugs in Biological Matrixes", *Anal Chem*, 81(1), pp. 193-202.

(97) Bevilacqua, V. L.; Nilles, J. M.; Rice, J. S.; Connell, T. R.; Schenning, A. M.; Reilly, L. M.; Durst, H. D. (**2010**). "Ricin Activity Assay by Direct Analysis in Real Time Mass Spectrometry Detection of Adenine Release", *Anal Chem*, 82(3), pp. 798-800.

(98) Nilles, J. M.; Connell, T. R.; Durst, H. D. (**2009**). "Quantitation of Chemical Warfare Agents Using the Direct Analysis in Real Time (DART) Technique", *Anal Chem*, 81(16), pp. 6744-6749.

(99) Nilles, J. M.; Connell, T. R.; Stokes, S. T.; Dupont Durst, H. (**2010**). "Explosives Detection Using Direct Analysis in Real Time (DART) Mass Spectrometry", *Propellants, Explos., Pyrotech.*, 35(5), pp. 446-451.

(100) Harris, G. A.; Kwasnik, M.; Fernandez, F. M. (**2011**). "Direct Analysis in Real Time Coupled to Multiplexed Drift Tube Ion Mobility Spectrometry for Detecting Toxic Chemicals", *Anal Chem*, 83(6), pp. 1908-1915.

(101) Zhou, M.; Guan, W.; Walker, L. D.; Mezencev, R.; Benigno, B. B.; Gray, A.; Fernandez, F. M.; McDonald, J. F. (**2010**). "Rapid Mass Spectrometric Metabolic Profiling of Blood Sera Detects Ovarian Cancer with High Accuracy", *Cancer Epidemiol Biomarkers Prev*, 19(9), pp. 2262-2271.

(102) Zhou, M.; McDonald, J. F.; Fernandez, F. M. (**2010**). "Optimization of a Direct Analysis in Real Time/Time-of-Flight Mass Spectrometry Method for Rapid Serum Metabolomic Fingerprinting", *J Am Soc Mass Spectrom*, 21(1), pp. 68-75.

(103) Reiter, S. M.; Buchberger, W.; Klampfl, C. W. (**2010**). "Rapid Identification and Semi-Quantitative Determination of Polymer Additives by Desorption Electrospray Ionization/Time-of-Flight Mass Spectrometry", *Anal Bioanal Chem*.

(104) Rothenbacher, T.; Schwack, W. (**2010**). "Rapid Identification of Additives in Poly(Vinyl Chloride) Lid Gaskets by Direct Analysis in Real Time Ionisation and Single-Quadrupole Mass Spectrometry", *Rapid Commun Mass Spectrom*, 24(1), pp. 21-29.

(105) Shelley, J. T.; Hieftje, G. M. (**2010**). "Ionization Matrix Effects in Plasma-Based Ambient Mass Spectrometry Sources", *Journal of Analytical Atomic Spectrometry*, 25 pp. 345-350.

(106) Sangster, T.; Spence, M.; Sinclair, P.; Payne, R.; Smith, C. (**2004**). "Unexpected Observation of Ionsuppression in a Liquid Chromatography/Atmospheric Pressure Chemical Ionization Mass Spectrometric Bioanalytical Method", *Rapid Commun Mass Spectrom*, 18 pp. 1361-1364.

(107) Harris, G. A.; Hostetler, D. M.; Hampton, C. Y.; Fernandez, F. M. (**2010**). "Comparison of the Internal Energy Deposition of Direct Analysis in Real Time and Electrospray Ionization Time-of-Flight Mass Spectrometry", *Journal of the American Society for Mass Spectrometry*, 21(5), pp. 855-863.

(108) Tabrizchi, M.; Shooshtari, S. (**2003**). "Proton Affinity Measurements Using Ion Mobility Spectrometry", *The Journal of Chemical Thermodynamics*, 35(6), pp. 863-870.

(109) http://webbook.nist.gov/chemistry/.

(110) Nicol, G.; Sunner, J.; Kebarle, P. (**1988**). "Kinetics and Thermodynamics of Protonation Reactions: $H_3o^+ (H_2o)_H + B = Bh^+ (H2o)_B + (H - B + 1) H_2o$, Where B Is a Nitrogen, Oxygen or Carbon Base", *International Journal of Mass Spectrometry and Ion Processes*, 84(1-2), pp. 135-155.

(111) Chang, H. C.; Wu, C. C.; Kuo, J. L. (**2005**). "Recent Advances in Understanding the Structures of Medium-Sized Protonated Water Clusters", *International Reviews in Physical Chemistry*, 24(3-4), pp. 553-578.

(112) Shi, Z.; Ford, J. V.; Wei, S.; Castleman Jr., A. W. (**1993**). "Water Clusters: Contributions of Binding Energy and Entropy to Stability", *Journal of Chemical Physics*, 99(10), pp. 8009-8015.

(113) Magnera, T. F.; David, D. E.; Michl, J. (**1991**). "The First Twenty-Eight Gas-Phase Proton Hydration Energies", *Chemical Physics Letters*, 182(3-4), pp. 363-370.

(114) Black, R. M. (**2010**). "History and Perspectives of Bioanalytical Methods for Chemical Warfare Agent Detection", *Journal of Chromatography B*, 878 pp. 1207-1215.

(115) Cotte-Rodriguez, I.; Justes, D. R.; Nanita, S. C.; Noll, R. J.; Mulligan, C. C.; Sanders, N. L.; Cooks, R. G. (**2006**). "Analysis of Gaseous Toxic Industrial Compounds and Chemical Warfare Agent Simulants by Atmospheric Pressure Ionization Mass Spectrometry", *Analyst*, 131 pp. 579-589.

(116) Kim, P.; Albarella, J. D.; Carey, J. R.; Placek, M. J.; Sen, A.; Wittrig, A. E.; McNamara III., W. B. (**2008**). "Towards the Development of a Portable Device for the Monitoring of Gaseous Toxic Industrial Chemicals Based on a Chemical Sensor Array", *Sensors and Actuators B: Chemical*, 134 pp. 307-312.

(117) Borowsky, J.; Collins, G. E. (**2007**). "Chemical and Biological Threat-Agent Detection Using Electrophoresis-Based Lab-on-a-Chip Devices", *Analyst*, 132 pp. 958-962.

(118) Diakowski, P. M.; Xiao, Y.; Petryk, M. W. P.; Kraatz, H. B. (**2010**). "Impedence Based Detection of Chemical Warfare Agent Mimics Using Ferrocene-Lysine Modified Carbon Nanotubes", *Analytical Chemistry*, 82 pp. 3191-3197.

(119) Loui, A.; Ratto, T. V.; Wilson, T. S.; McCall, S. K.; Mukerjee, E. V.; Love, A. H.; Hart, B. R. (**2008**). "Chemical Vapor Discrimination Using a Compact and Low-Power Array of Piezoresistive Microcantilevers", *Analyst*, 133 pp. 608-615.

(120) Ohira, S. I.; Toda, K. (**2008**). "Micro Gas Analyzers for Environmental and Medical Applications", *Analytica Chimica Acta*, 619 pp. 143-156.

(121) Zygmunt, B.; Zaborowska, A.; Swiatlowska, J.; Namiesnik, J. (**2007**). "Solid Phase Microextraction Combined with Gas Chromatography - a Powerful Tool for the Determination of Chemical Warfare Agents and Related Compounds", *Current Organic Chemistry*, 11 pp. 241-253.

(122) Kendler, S.; Zifman, A.; Gratziany, N.; Zaltsman, A.; Frishman, G. (**2005**). "A New Method and Apparatus for on-Site Detection of Trace Levels of Chemical Warfare Agents", *Analytica Chimica Acta*, 548 pp. 58-65.

(123) Wood, M.; Laloup, M.; Samyn, N.; Fernandez, M. M. R.; de Bruijn, E. A.; Maes, R. A. A.; Boeck, G. D. (**2006**). "Recent Application of Liquid Chromatography-Mass Spectrometry in Forensic Science", *Journal of Chromatography A*, 1130 pp. 3-15.

(124) Eiceman, G. A.; Karpas, Z. *Ion Mobility Spectrometry*; CRC Press, Inc.: Boca Raton, **1994**.

(125) Beegle, L. W.; Kanik, I.; Matz, L.; Hill, H. H. (**2001**). "Electrospray Ionization High-Resolution Ion Mobility Spectrometry for the Detection of Organic Compounds, 1. Amino Acids", *Analytical Chemistry*, 73 pp. 3028-3034.

(126) Tabrizchi, M.; Khayamian, T.; Taj, N. (**2000**). "Design and Optimization of a Corona Discharge Ionization Source for Ion Mobility Spectrometry", *Review of Scientific Instruments*, 71(6), pp. 2321-2328.

(127) Dong, C.; Wang, W.; Li, H. (**2008**). "Atmospheric Pressure Air Direct Current Glow Discharge Ionization Source for Ion Mobility Spectrometry", *Analytical Chemistry*, 80 pp. 3925-3930.

(128) Steiner, W. E.; Clowers, B. H.; English, W. A.; Hill, H. H. (**2004**). "Atmospheric Pressure Matrix-Assisted Laser Desorption/Ionization with Analysis by Ion Mobility Time-of-Flight Mass Spectrometry", *Rapid Communications in Mass Spectrometry*, 18 pp. 882-888.

(129) Pershenkov, V. S.; Tremasov, A. D.; Belyakov, V. V.; Razvalyaez, A. U.; Mochkin, V. S. (**2006**). "X-Ray Ion Mobility Spectrometer", *Microelectronics Reliability*, 46 pp. 641-644.

(130) Borsdorf, H.; Neitsch, K.; Eiceman, G. A.; Stone, J. A. (**2009**). "A Comparison of the Ion Chemistry for Mono-Substituted Toluenes and Anilines by Three Methods of Atmospheric Pressure Ionization with Ion Mobility Spectrometry", *Talanta*, 78 pp. 1464-1475.

(131) Van Berkel, G. J.; Pasilis, S. P.; Ovchinnikova, O. (**2008**). "Established and Emerging Atmospheric Pressure Surface Sampling/Ionization Techniques for Mass Spectrometry", *Journal of Mass Spectrometry*, 43 pp. 1161-1180.

(132) Harry, E. L.; Reynolds, J. C.; Bristow, A. W. T.; Wilson, I. D.; Creaser, C. S. (**2009**). "Direct Analysis of Pharmaceutical Formulations from Non-Bonded Reversed-Phase Thin-Laye Chromatography Plates by Desorption Electrospray Ionisation Ion Mobility Mass Spectrometry", *Rapid Communications in Mass Spectrometry*, 23 pp. 2597-2604.

(133) Kaur-Atwal, G., Weston, D. J., Green, P. S., Crosland, S., Bonner, P. L. R., Creaser, C. S. (**2007**). "Analysis of Tryptic Peptides Using Desorption Electrospray Ionization Combined with Ion Mobility Spectrometry/Mass Spectrometry", *Rapid Communications in Mass Spectrometry*, 21 pp. 1131-1138.

(134) Weston, D. J.; Bateman, R.; Wilson, I. D.; Wood, T. R.; Creaser, C. S. (**2005**). "Direct Analysis of Pharmaceutical Drug Formulations Using Ion Mobility Spectrometry/Quadrupole-Time-of-Flight Mass Spectrometry Combined with Desorption Electrospray Ionization", *Analytical Chemistry*, 77(23), pp. 7572-7580.

(135) Williams, J. P.; Scrivens, J. H. (**2008**). "Coupling Desorption Electrospray Ionisation and Neutral Desorption/Extractive Electrospray Ionisation with a

Travelling-Wave Based Ion Mobility Mass Spectrometer for the Analysis of Drugs", *Rapid Communications in Mass Spectrometry*, 22(2), pp. 187-196.

(136) Myung, S.; Wiseman, J. M.; Valentine, S. J.; Takats, Z.; Cooks, R. G.; Clemmer, D. E. (**2006**). "Coupling Desorption Electrospray Ionization with Ion Mobility/Mass Spectrometry for Analysis of Protein Structure: Evidence for Desorption of Folded and Denatured States", *Journal of Physical Chemistry B*, 110 pp. 5045-5051.

(137) D'Agostino, P. A.; Chenier, C. L. (**2010**). "Desorption Electrospray Ionization Mass Spectrometric Analysis of Organophosphorus Chemical Warfare Agents Using Ion Mobility and Tandem Mass Spectrometry", *Rapid Communications in Mass Spectrometry*, 24 pp. 1617-1624.

(138) Kwasnik, M.; Fuhrer, M.; Gonin, M.; Barbeau, K.; Fernandez, F. M. (**2007**). "Performance, Resolving Power, and Radial Ion Distribution of a Prototype Nanoelectrospray Ionization Resistive Glass Atmospheric Pressure Ion Mobility Spectrometer", *Analytical Chemistry*, 79 pp. 7782-7791.

(139) Kwasnik, M.; Caramore, J.; Fernandez, F. M. (**2009**). "Digitally-Multiplexed Nanoelectrospray Ionization Atmospheric Pressure Drift Tube Ion Mobility Spectrometry", *Analytical Chemistry*, 81(4), pp. 1587-1594.

(140) Eiceman, G. A.; Nazarov, E. G.; Stone, J. A. (**2003**). "Chemical Standards in Ion Mobility Spectrometry", *Analytica Chimica Acta*, 493 pp. 185-194.

(141) Laakia, J.; Pedersen, C. S.; Adamov, A.; Viidanoja, J.; Sysoev, A.; Kotiaho, T. (**2009**). "Sterically Hindered Phenols in Negative Ion Mobility Spectrometry-Mass Spectrometry", *Rapid Communications in Mass Spectrometry*, 23 pp. 3069-3076.

(142) Viitanen, A.-K.; Mauriala, T.; Mattila, T.; Adamov, A.; Pedersen, C. S.; Mäkelä, J. M.; Marjamäki, M.; Sysoev, A.; Keskinen, J.; Kotiaho, T. (**2008**). "Adjusting Mobility Scales of Ion Mobility Spectrometers Using 2,6-D*t*BP as a Reference Compound", *Talanta*, 76 pp. 1218-1223.

(143) Thomas, C. L. P.; Rezgui, N. D.; Kanu, A. B.; Munro, W. A. (**2002**). "Measuring the Temperature of the Drift Gas in an Ion Mobility Spectrometer: A Technical Note", *International Journal of Ion Mobility Spectrometry*, 5 pp. 31-36.

(144) Eiceman, G. A.; Kelly, K.; Nazarov, E. G. (**2002**). "Nitric Oxide as a Reagent Gas in Ion Mobility Spectrometry", *International Journal of Ion Mobility Spectrometry*, 5 pp. 22-30.

(145) Song, L.; Gibson, S. C.; Bhandari, D.; Cook, K. D.; Bartmess, J. E. (**2009**). "Ionization Mechanism of Positive-Ion Direct Analysis in Real Time: A Transient Microenvironment Concept", *Analytical Chemistry*, 81 pp. 10080-10088.

(146) (**1999**). "Nondestructive Evaluation System Reliability Assessment", *Department of Defense Handbook*, MIL-HDBK-1823.

(147) Georgiou, G. A. (**2006**). "Probability of Detection (POD) Curves: Derivation, Applications and Limitations", *Jacobi Consulting Limited Health and Safety Executive Research Report*, 454 .

(148) Perez, J. J.; Harris, G. A.; Chipuk, J. E.; Brodbelt, J. S.; Green, M. D.; Hampton, C. Y.; Fernandez, F. M. (**2010**). "Transmission-Mode Direct Analysis in Realt Time and Desorption Electrospray Ionization Mass Spectrometry of Insecticide-Treated Bednets for Malaria Control", *Analyst*, 135(4), pp. 712-719.

(149) Kimmel, J. R.; Yoon, O.; Zuleta, I. A.; Trapp, O.; Zare, R. N. (**2005**). "Peak Height Precision in Hadamard Transform Time-of-Flight Mass Spectra", *Journal of the American Society for Mass Spectrometry*, 16(7), pp. 1117-1130.

(150) Clowers, B. H.; Siems, W. F.; Hill, H. H.; Massick, S. M. (**2006**). "Hadamard Transform Ion Mobility Spectrometry", *Analytical Chemistry*, 78(1), pp. 44-51.

(151) Szumlas, A. W.; Ray, S. J.; Hieftje, G. M. (**2006**). "Hadamard Transform Ion Mobility Spectrometry", *Analytical Chemistry*, 78(13), pp. 4474-4481.

(152) Clowers, B. H.; Belov, M. E.; Prior, D. C.; Danielson III, W. F.; Ibrahim, Y.; Smith, R. D. (**2006**). "Hadamard Transform Ion Mobility Spectrometry", *Analytical Chemistry*, 78 pp. 4474-4481.

(153) Mariano, A. V.; Su, W.; Guharay, S. K. (**2009**). "Effect of Space Charge on Resolving Power and Ion Loss in Ion Mobility Spectrometry", *Analytical Chemistry*, 81 pp. 3385-3391.

(154) Kimmel, J. R.; Fernandez, F. M.; Zare, R. M. (**2003**). "Effects of Modulation Defects on Hadamard Transform Time-of-Flight Mass Spectrometry (HT-TOFMS)", *Journal of the American Society of Mass Spectrometry*, 14 pp. 278-286.

(155) Shelley, J. T.; Wiley, J. S.; Chan, G. C. Y.; Schilling, G. D.; Ray, S. J.; Hieftje, G. M. (**2009**). "Characterization of Direct-Current Atmospheric-Pressure Discharges Useful for Ambient Desorption/Ionization Mass Spectrometry", *Journal of the American Society for Mass Spectrometry*, 20(5), pp. 837-844.

(156) Shelley, J. T.; Ray, S. J.; Hieftje, G. M. (**2008**). "Laser Ablation Coupled to a Flowing Atmospheric Pressure Afterglow for Ambient Mass Spectral Imaging", *Analytical Chemistry*, 80(21), pp. 8308-8313.

(157) Cody, R. B. (**2009**). "Observation of Molecular Ions and Analysis of Nonpolar Compounds with the Direct Analysis in Real Time Ion Source", *Analytical Chemistry*, 81(3), pp. 1101-1107.

(158) Lane, A. L.; Nyadong, L.; Galhena, A. S.; Shearer, T. L.; Stout, E. P.; Parry, R. M.; Kwasnik, M.; Wang, M. D.; Hay, M. E.; Fernandez, F. M.; Kubanek, J. (**2009**). "Desorption Electrospray Ionization Mass Spectrometry Reveals Surface-Mediated Antifungal Chemical Defense of a Tropical Seaweed", *Proceedings of the National Academy of Sciences of the United States of America*, 106(18), pp. 7314-7319.

(159) Karas, M.; Krüger, R. (**2003**). "Ion Formation in MALDI: The Cluster Ionization Mechanism", *Chemical Reviews*, 103(2), pp. 427-440.

(160) Harris, G. A.; Hostetler, D. M.; Hampton, C. Y.; Fernandez, F. M. (**2010**). "Comparison of the Internal Energy Deposition of Direct Analysis in Real and Electrospray Ionization Time-of-Flight Mass Spectrometry", *J Am Soc Mass Spectrom*, 21(5), pp. 855-863.

(161) *http://www.ionsense.com/*

(162) Harris, G. A.; Kwasnik, M.; Fernandez, F. M. (**2011**). "Direct Analysis in Real Time Coupled to Multiplexed Drift Tube Ion Mobility Spectrometry for Detecting Toxic Chemicals", *Analytical Chemistry*, 83(6), pp. 1908-1915.

(163) Newton, P. N.; Green, M.; Fernandez, F. M.; Day, N. P. J.; White, N. J. (**2006**). "Counterfeit Anti-Infective Drugs", *Lancet Infectious Diseases*, 6 pp. 602-612.

(164) Fernandez, F. M.; Newton, P. N.; Green, M. (**2008**). "Prevalence and Detection of Counterfeit Pharmaceuticals: A Mini Review", *Industrial & Engineering Chemistry Research*, 47 pp. 585-590.

(165) Wondemagegnehu, E. (**1999**). "Counterfeit and Substandard Drugs in Myanmar and Vietnam", *WHO Report. WHO/EDM/QSM/99.3.*

(166) Weiss, A. M. (**2006**). "Buying Prescription Drugs on the Internet: Promises and Pitfalls", *Cleveland Clinic Journal of Medicine*, 73(3), pp. 282-288.

(167) FDA Sounds Alarm on Phony Tamiflu. http://www.fda.gov/ForConsumers/ConsumerUpdates/ucm216009.htm

(168) White, N. J. (2008). "Qinghaosu", *Science*, **320** pp. 330-334.

(169) Newton, P.; Proux, S.; Green, M.; Smithuis, F.; Rozendaal, J.; Prakongpan, S.; Chotivanich, K.; Mayxay, M.; Looareesuwan, S.; Farrar, J.; Nosten, F.; White, N. J. (**2001**). "Fake Artesunate in Southeast Asia", *The Lancet*, 357 pp. 1948-1950.

(170) Rozendaal, L. (**2000**). *Bull. Mekong Malaria Forum*, 7 pp. 62-68.

(171) Sengaloundeth, S.; Green, M. D.; Fernandez, F. M.; Manolin, O.; Phommavong, K.; Insixiengmay, V.; Hampton, C. Y.; Nyadong, L. N.; Mildenhall, D.; Khounsaknalath, L.; Syhakhang, L.; Newton, P. N. (**2009**). "A Stratified Random Survey of the Proportion of Poor Quality Oral Artesunate Sold at Medicine Outlets in the Lao PDR – Implications for Therapeutic Failure and Drug Resistance", *Malaria Journal*, submitted.

(172) Newton, P. N.; Fernandez, F. M.; Plancon, A.; Mildenhall, D. C.; Green, M. D.; Ziyong, L.; Christophel, E. M.; Phanouvong, S.; Howells, S.; McIntosh, E.; Laurin, P.; Blum, N.; Hampton, C. Y.; Faure, K.; Nyadong, L.; Soong, C. W.; Santoso, B.; Zhiguang, W.; Newton, J.; Palmer, K. (**2008**). "A Collaborative Epidemiological Investigation into the Criminal Fake Artesunate Trade in South East Asia", *PLoS Med.*, 5(2), pp. e32.

(173) Harris, G. A.; Fernandez, F. M. (**2009**). "Simulations and Experimental Investigation of Atmospheric Transport in an Ambient Metastable-Induced Chemical Ionization Source", *Analytical Chemistry*, 81 pp. 322-329.

(174) Costa, A. B.; Cooks, R. G. (**2007**). "Simulation of Atmospheric Transport and Droplet-Thin Film Collisions in Desorption Electrospray Ionization", *Chemical Communications*, (38), pp. 3915-3917.

(175) Fernandez, F. M.; Green, M. D.; Newton, P. N. (**2008**). "Prevalence and Detection of Counterfeit Pharmaceuticals: A Mini Review", *Industrial and Engineering Chemistry Research*, 47 pp. 585-590.

(176) Kaur, H.; Green, M. D.; Hostetler, D. M.; Fernandez, F. M.; Newton, P. N. (**2010**). "Antimalarial Drug Qualtiy: Methods to Detect Suspect Drugs", *Therapy*, 7 pp. 49-57.

(177) Nyadong, L.; Harris, G. A.; Balayssac, S.; Galhena, A. S.; Malet-Martino, M.; Martino, R.; Parry, R. M.; Wang, M. D.; Fernandez, F. M.; Gilard, V. (**2009**). "Combining Two-Dimensional Diffusion-Ordered Nuclear Magnetic Resonance Spectroscopy, Imaging Desorption Electrospray Ionization Mass Spectrometry, and Direct Analysis in Real-Time Mass Spectrometry for the Integral Investigation of Counterfeit Pharmaceuticals", *Analytical Chemistry*, 81 pp. 4803-4812.

(178) Keller, B. O.; Suj, J.; Young, A. B.; Whittal, R. M. (**2008**). "Interferences and Contaminants Encountered in Modern Mass Spectrometry", *Analytica Chimica Acta*, 627(1), pp. 71-81.

(179) Krylov, E. V.; Nazarov, E. G.; Miller, R. A. (**2007**). "Differential Mobility Spectrometer: Model of Operation", *International Journal of Mass Spectrometry*, 266(1-3), pp. 76-85.

(180) Schneider, B. B.; Covey, T. R.; Coy, S. L.; Krylov, E. V.; Nazarov, E. G. (**2010**). "Planar Differential Mobility Spectrometer as a Pre-Filter for Atmospheric Pressure Ionization Mass Spectrometry", *International Journal of Mass Spectrometry*, 298(1-3), pp. 45-54.

(181) Nyadong, L.; Green, M. D.; De Jesus, V. R.; Newton, P. N.; Fernandez, F. M. (**2007**). "Reactive Desorption Electrospray Ionization Linear Ion Trap Mass Spectrometry of Latest-Generation Counterfeit Antimalarials Via Noncovalent Complex Formation", *Analytical Chemistry*, 79(5), pp. 2150-2157.

(182) Groux, M. (**1974**). "Chemical Alterations of Heat Treated Concentrated Skim Milk", *Journal of Dairy Science*, 57(2), pp. 153-155.

(183) Storme, M. L.; Jansen, F. H.; Goeteyn, W.; Van Bocxlaer, J. F. (**2006**). "Simultaneous Quantitative Analysis of the Antimalarials Pyrimethamine and Sulfamethoxypyrazine in Plasma Samples Using Liquid Chromatography/Tandem Mass Spectrometry", *Rapid Communications in Mass Spectrometry*, 20(19), pp. 2947-2953.

LIST OF PUBLICATIONS

Chapters 1 and 7

- **Harris, Glenn A.**; Nyadong, Leonard; Fernandez, Facundo M. "Recent developments in ambient ionization techniques for analytical mass spectrometry." *Analyst* (2008), 133, 1297-1301.

- **Harris, Glenn A.;** Galhena, Asiri S., Fernandez, Facundo M. "Ambient sampling/ionization mass spectrometry: applications and current trends." Invited review for *Analytical Chemistry* (2011), In Press.

Chapter 2

- **Harris, Glenn A.**; Fernandez, Facundo M. "Simulations and experimental investigation of atmospheric transport in an ambient metastable-induced chemical ionization source." *Analytical Chemistry* (2009), 81, 322-329.

Chapter 3

- **Harris, Glenn A.**; Hostetler, Dana M.; Hampton, Christina Y.; Fernandez, Facundo M. "Comparison of the internal energy deposition of direct analysis in real time and electrospray ionization time-of-flight mass spectrometry." *Journal of the American Society for Mass Spectrometry* (2010), 21, 855-863.

Chapter 4

- **Harris, Glenn A.;** Falcone, Caitlin E; Fernandez, Facundo M. "Ion yield and ion suppression 'hot-spots' in direct analysis in real time mass spectrometry." In preparation for *Analytical Chemistry*.

Chapter 5

- **Harris, Glenn A.**; Kwasnik, Mark; Fernandez, Facundo M. "Direct analysis in real time coupled to multiplexed drift tube ion mobility spectrometry (DART-DTIMS) for detecting toxic chemicals." *Analytical Chemistry*, (2011), 83, 1908-1915.

- **Harris, Glenn A.**; Kwasnik, Mark; Fernandez, Facundo M. "Multiplexed Ion Mobility Spectrometry and Ion Mobility-Mass Spectrometry." *Ion Mobility – Mass Spectrometry: Theory and Applications* by Charles L. Wilkins and Sarah Trimpin (2010).

Chapter 6

- Perez, Jose J.; **Harris, Glenn A.**; Chipuk, Joseph E.; Brodbelt, Jennifer S.; Green, Michael D.; Hampton, Christina Y.; Fernandez, Facundo M. "Transmission-mode direct analysis in real time and desorption electrospray ionization mass spectrometry of insecticide-treated bednets for malaria control." *Analyst* (2010), 135, 712-719.

- Galhena, Asiri S.; **Harris, Glenn A.**; Nyadong, Leonard; Murray, Kermit K.; Fernandez, Facundo M. "Small molecule ambient mass spectrometry imaging by infrared laser ablation metastable-induced chemical ionization." *Analytical Chemistry* (2010), 82, 2178-2181.

Appendix A

- Nyadong, Leonard*; **Harris, Glenn A.***; Balayssac, Stephane*; Galhena, Asiri S.*; Malet-Martino, Myriam; Martino, Robert; Parry, R. Mitchell; Wang, May Dongmei; Fernandez, Facundo M.; Gilard, Veronique. "Combining two-dimensional diffusion-ordered nuclear magnetic resonance spectroscopy, imaging desorption electrospray ionization mass spectrometry, and direct analysis in real-time mass spectrometry for the integral investigation of counterfeit pharmaceuticals." *Analytical Chemistry* (2009), 81, 4803-4812.

- Newton, Paul A.; Green, Michael D.; Mildernhall, Dallas C.; Plancon, Aline; Nettey, Henry; Nyadong, Leonard; Hostetler, Dana M.; Swamidoss, Isabel; **Harris, Glenn A**.; Powell, Kristen; Wolff, Jean-Claude; Timmermans, Ans E.; Amin, Abdinasir A.; Hiiti, Sillo; Opuni, Stephen K.; Muhairwe, Apollo; Barbareu, Serge; Faurant, Claude; Eckers, Christine; Smith, Stephen; Soong, C. W. Ray; Faure, Kevin; Thevanayagam, Jonarthan; Fernandes, Peter; Kaur, Harparkash; Angus, Brian; Carter, Neil M.; Fernandez, Facundo M. "Poor quality vital antimalarials in Africa-a disaster in the making?" Submitted to *Lancet of Infectious Diseases*.

Appendix B

- Galhena, Asiri S.; **Harris, Glenn A.**; Kwasnik, Mark; Fernandez, Facundo M. "Enhanced direct ambient analysis by differential mobility-filtered desorption electrospray ionization-mass spectrometry." *Analytical Chemistry*, (2010), 82, 9159-9153.

Other publications at the Georgia Institute of Technology

- **Harris, Glenn A.;** Yuan, Cheng-Hui; Wollnik, Hermann; Eiceman, Gary A.; Fernandez, Facundo M. "Screening of genuine and counterfeit solid

pharmaceutical by electrospray-assisted laser desorption ionization atmospheric pressure drift tube ion mobility spectrometry." In preparation for *Analyst.*

- Malhotra, U.; Rakita, R.; Fernandez, Facundo M.; **Harris, Glenn A.;** Arguin, P.; Bronzan, R.; Slutsker, L.; Green, Michael D.; Townes, D. "Hepatitis temporally associated with an herbal supplement containing artemisinin-Washington, 2008." *Morbidity and Mortality Weekly Report* (2009), 58, 854.

- Rhodes, Scott D.; Fernandez, Facundo M.; Leichliter, Jami, S.; Vissman, Aaron, T; Montaño, Jaime; Duck, Stacy; O'Brien, Mary Claire; Miller, Cindy; Wilkin, Aimee M.; **Harris, Glenn A.**; Hostetler, Dana M.; Bloom, Fred R. "Medications for sexual health available from non-medical sources: A need for increased access to healthcare and education among immigrant Latinos in the rural Southeastern USA." *Journal of Immigrant and Minority Health*, Accepted.

VITA

Glenn A. Harris was born in Oak Lawn, Illinois. He moved to his hometown Clearwater, Florida and attended public school in Pinellas County, Florida. In the fall of 2003 he enrolled at the University of South Florida in Tampa, and graduated in Spring 2007 with degrees in Biology (B.S.) and Chemistry (B.A.). In fall 2007, he moved to Atlanta, Georgia to pursue a Doctorate in Analytical Chemistry from the Georgia Institute of Technology. When he is not working on his research, Glenn enjoys cooking, baking, eating, working out, spending time outdoors and listening to music.